

University of Strathclyde
Department of Biomedical Engineering

Development of an In-Dressing Wound Infection
Sensor

Aiden James Hannah BSc (Hons)

2022

A thesis presented in the fulfilment of the requirements for the
degree of Doctor of Engineering.

This thesis is the result of the author's original research. It has been composed by the author and has not been previously submitted for examination which has led to the award of a degree.

The copyright of this thesis belongs to the author under the terms of the United Kingdom Copyright Acts as qualified by University of Strathclyde Regulation 3.50. Due acknowledgement must always be made of the use of any material contained in, or derived from, this thesis.

Signed:

Date:

ABSTRACT

Infection can be detrimental to the wound healing process, prolonging healing times and potentially leading to severe consequences. Current gold-standard methods of infection detection rely upon lengthy laboratory-based culturing procedures, typically taking at least 48 hours. Rapid detection of wound infection and determination of the causative pathogens are vital to ensuring timely, targeted treatment. In this study, the development of an in-dressing electrochemical sensor that can detect wound infection in real time was advanced.

Different screen-printed sensor materials were explored with the aim of determining the most suitable for rapid bacterial detection. The Ag/AgCl sensors studied were unsuitable: both bactericidal properties and instability during measurement were observed. Conversely, for both the carbon and platinised carbon electrodes (PCE) studied, wound pathogens were detected within 30 minutes in culture medium. Normalised impedance signatures characteristic of bacterial growth were uncovered. Due to their superior response, it was concluded that the PCE sensors were most appropriate for this application.

Artificial wound bed models were created, further evidencing the suitability of the PCE sensor in particular for bacterial detection in the wound environment. These models incorporated factors such as a simulated wound fluid, a collagen gel matrix and a range of wound dressings.

Finally, different algorithmic approaches were used to analyse the large volume of impedance data obtained. A rate of change based approach was developed to support bacterial concentration estimation. Further, artificial neural networks enabled bacterial detection and species identification.

To advance this device, future research should include conducting clinical studies to test the sensors with real wound samples and in a real wound environment. This would reveal their suitability for adoption into a future medical device. Additionally, using this clinical data and added laboratory data the bacterial detection and identification algorithms could be advanced.

ACKNOWLEDGEMENTS

I would like to first thank my supervisor, Trish, for all her help and guidance throughout this project. I am very grateful for all her support and encouragement. My thanks also go to Andy, for helping me to grasp the fundamentals of bacterial electrochemistry and providing many creative suggestions. Many thanks also to Brian for his continuous support in the lab. I am also very grateful to Sean for listening to the ins and outs of my research on a daily basis and being a great sounding board for ideas. Thanks also to my clinical collaborators, Dr Helen McDevitt and Dr Neil Patel for their enthusiasm for this project and their clinical insight.

I am grateful to the EPSRC and Strathclyde University for funding and hosting this multidisciplinary Doctoral Training Programme. My fellow EngD students have been a pleasure to work with and a great source of support.

Thank you very much also to all my family for their continuous support and encouragement. Finally, I would like to thank my amazing wife Amy for her love, patience and understanding throughout my doctorate. I am very grateful for all of your support and many hours of proof-reading papers.

LIST OF PUBLICATIONS

The work reported within this thesis has resulted in the following peer-reviewed publications:

1. Ward A.C.*, Hannah A.J.*, Kendrick S. L., Tucker N. P., MacGregor G. & Connolly P. (2018) Identification and characterisation of *Staphylococcus aureus* on low cost screen printed carbon electrodes using impedance spectroscopy. In: Biosensors and Bioelectronics. 110, pp 65-70. <https://doi.org/10.1016/j.bios.2018.03.048>
*Authors contributed equally to the paper.
2. Hannah A.J., Ward A.C., Connolly P. (2021) Rapid detection of wound pathogen *Proteus mirabilis* using disposable electrochemical sensors. In: Proceedings of the 7th World Congress on Electrical Engineering and Computer Systems and Sciences (EECSS'21). DOI: 10.11159/icbes21.105. Paper presented at ICBES'21, part of EECSS'21 (www.international-aset.com).
3. Hannah A.J., Ward A.C., Connolly P. (2021) Rapidly Detected Common Wound Pathogens via Easy-to-Use Electrochemical Sensors. In: Journal of Biomedical Engineering and Biosciences. 8, pp11-20. <https://jbeb.avestia.com/2021/002.html>.

Signed:

Date:

SYMBOLS

a_i	Output from neuron i
A	Area
b	Bias
c_i	Concentration of ion species i
C	Capacitance
C_{dl}	Double layer capacitance
C_{GC}	Gouy-Chapman capacitance
C_H	Helmholtz capacitance
C_O	Bulk concentration of oxidised species
C_R	Bulk concentration of reduced species
C_S	Stern capacitance
d	Distance
D_i	Coefficient of diffusion
ε	Dielectric constant
ε_0	Permittivity of free space
E	Electric field
$E^{0'}$	Standard electrode potential
E_{eq}	Equilibrium potential
f	Frequency
f_n	False negative
f_p	False positive
F	Faraday constant
g	Activation function
h	Hypothesis
i	Current
i_0	Exchange current
i_d	Diffusion current
i_m	Migration current
in_j	Input to neuron j
I	Current (Complex)
$IP_{normalised}$	Normalised impedance parameter
$IP_{t=0}$	Starting impedance value

$IP_{t=n}$	Impedance value at time n
j	$\sqrt{-1}$
J_i	Flux of ion species i
k_B	Boltzmann's constant
L	Diffusion length
M	Matrix element
η	Viscosity
η	Overpotential
n	Number of electrons
$\emptyset(x)$	Potential
r_i	Radius of ion
R	Universal gas constant
R	Resistance
R_{ct}	Charge transfer resistance
R_S	Solution resistance
σ	Charge density
σ_M	Charge density on electrode surface
σ_S	Charge density from solution
σ_i	Charge density from adsorbed ions
σ_d	Charge density from diffuse layer
θ	Phase angle
t	Time
t_i	Transference number
t_n	True negative
t_p	True positive
T	Absolute temperature
u	Ion mobility
V	Voltage (Complex)
ω	Angular frequency
w_{ij}	Neuron weight
W	Warburg impedance
W_o	Finite space (open) Warburg impedance
X_E	End circuit element value
X_S	Start circuit element value

z	Charge (of ion)
Z	Complex impedance
Z'	Real part of impedance
Z''	Imaginary part of impedance

ABBREVIATIONS

AI	Artificial Intelligence
AMR	Antimicrobial Resistance
ANN	Artificial Neural Network
ATP	Adenosine Triphosphate
CE	Counter Electrode
CFU	Colony Forming Units
CPE	Constant Phase Element
CSV	Comma Separated Variable
CV	Crystal Violet
DL	Deep Learning
DNA	Deoxyribonucleic Acid
ECG	Electrocardiogram
ECM	Equivalent Circuit Model
EIS	Electrochemical Impedance Spectroscopy
EIT	Electrical Impedance Tomography
ELISA	Enzyme-Linked Immunosorbent Assay
EPS	Extracellular Polymeric Substances
FBS	Foetal Bovine Serum
FFC	Flat Flexible Cable
FPC	Flat Printed Circuit
GUI	Guided User Interface
HAI	Healthcare Associated Infection
IHP	Inner Helmholtz Plane
LB	Lennox Broth
LFI	Lateral Flow Immunochromatography
MALDI-TOF MS	Matrix-assisted Laser Desorption Ionisation Time-of-flight Mass Spectrometry
MIC	Minimal Inhibitory Concentration
ML	Machine Learning
MLP	Multi-Layer Perceptron
MRSA	Methicillin Resistant <i>Staphylococcus aureus</i>
MSC	Microbiology Safety Cabinet
NPWT	Negative Pressure Wound Therapy

OCP	Open Circuit Potential
OHP	Outer Helmholtz Plane
PC	Personal Computer
PCE	Platinised Carbon Electrode
PCR	Polymerase Chain Reaction
PET	Polyethylene Terephthalate
PHMB	Polyhexamethylene Biguanide
RNA	Ribonucleic Acid
rRNA	Ribosomal-Ribonucleic Acid
ROC	Rate of Change
SCV	Small Colony Variant
SSI	Surgical Site Infection
SWF	Simulated Wound Fluid
dWBM	Double-sensor Wound Bed Model
WBM	Wound Bed Model
WE	Working Electrode

TABLE OF CONTENTS

ABSTRACT.....	iii
ACKNOWLEDGEMENTS.....	iv
LIST OF PUBLICATIONS.....	v
SYMBOLS.....	vi
ABBREVIATIONS.....	ix
TABLE OF CONTENTS.....	xi
1. WOUND INFECTION AND APPROACHES TO BACTERIAL DETECTION.....	1
1.1 Introduction.....	2
1.2 The Skin and Wounds.....	2
1.2.1 Layers of the Skin.....	2
1.2.2 Types of Wounds.....	4
1.2.3 Wound Healing.....	7
1.3 Wound Infection.....	8
1.3.1 The Microflora of Human Skin.....	9
1.3.2 The Development of Infection.....	10
1.3.3 Causes of Infection and Risk Factors.....	11
1.3.4 The Microflora of Infected Wounds.....	12
1.4 Wound Management.....	15
1.4.1 The TIME Framework and Wound Management.....	15
1.4.2 Wound Care Products.....	17
1.5 Detection Approaches for Wound Infection.....	20
1.5.1 Signs of Wound Infection.....	21
1.5.2 Current Detection of Infection in Clinical Practice.....	22
1.5.3 Rapid Techniques in Clinical Microbiology.....	23
1.5.4 Biomarkers and Biosensors Supporting <i>in situ</i> Detection of Wound Infection	26
1.6 Detecting Bacteria using Impedance Spectroscopy.....	28
1.6.1 Biological Tissues- An Electrical Perspective.....	29
1.6.2 The Impact of Bacteria Upon Electrochemical Impedance.....	30
1.6.3 Impedance Experiments for the Detection of Bacteria.....	32
1.6.4 Impedance Spectroscopy in Wound Monitoring.....	36
1.7 Conclusion.....	37
1.8 Project Objectives.....	38
2. BACKGROUND THEORY.....	39

2.1	Introduction.....	40
	Fundamental Microbiology Concepts Underpinning this Research	40
2.2	40
2.2.1	Prokaryotic Cell Structure.....	40
2.2.2	Bacterial Growth.....	43
2.2.3	Cell Metabolism.....	44
2.2.4	Bacterial Biofilms	44
2.2.5	Bacterial Species of Interest.....	46
2.3	Fundamental Electrochemistry Concepts Underpinning this Research	48
2.3.1	Electrochemical Cell Reactions	48
2.3.2	Ion Solvation.....	49
2.3.3	Mechanisms of Mass Transfer	50
2.3.4	The Electrode/Electrolyte Interface	52
2.3.5	Faradaic and Non-Faradaic Processes.....	55
2.3.6	The Nernst Equation and Electrochemical Kinetics	57
2.3.7	Complex Electrical Impedance	58
2.3.8	Capacitance and Dielectric Materials.....	60
2.3.9	Electrochemical Impedance Spectroscopy (EIS).....	62
2.3.10	Impedance Data Modelling and Analysis	63
2.4	Fundamental Machine Learning Concepts Underpinning this Research	66
2.4.1	Supervised vs Unsupervised Learning.....	67
2.4.2	Artificial Neural Network Fundamentals.....	68
2.4.3	Scikit-learn’s MLP Classifier Neural Network.....	71
3.	MATERIALS AND METHODS.....	73
3.1	Introduction.....	74
3.2	Bacterial Culture	75
3.2.1	Bacterial Strains	75
3.2.2	Culture Media	75
3.2.3	Cell Washing.....	77
3.2.4	Colony Counting.....	77
3.2.5	Crystal Violet Staining.....	78
3.3	Electrode Types.....	79
3.4	Electrochemical Impedance Spectroscopy (EIS) Measurements and Data Analysis.....	81
3.4.1	Impedance Measurements.....	81
3.4.2	Spectrum Normalisation and Analysis.....	85

3.5	Ag/AgCl Electrode Methods.....	86
3.5.1	Ag/AgCl Electrode Experimental Assembly	86
3.5.2	Ag/AgCl Electrode Characterisation.....	87
3.5.3	Ag/AgCl Electrode LB Medium Growth Experiments.....	87
3.5.4	Ag/AgCl Sensor Zone of Inhibition.....	88
3.5.5	Minimal Inhibitory Concentration of Silver	88
3.5.6	Ag/AgCl Electrode Wound Bed Model Development.....	89
3.6	Carbon Electrode Methods.....	91
3.6.1	Carbon Electrode Assembly and Conditioning.....	91
3.6.2	Carbon Electrode LB Medium Growth Experiments.....	92
3.6.3	Carbon Electrode SWF Experiments	93
3.6.4	Carbon Electrode Wound Bed Model Adaption	94
3.6.5	Carbon Electrode Saline Experiments	94
3.6.6	Equivalent Circuit Modelling.....	95
3.7	Platinised Carbon Electrode Methods.....	96
3.7.1	PCE Sensor Assembly and Conditioning.....	97
3.7.2	PCE LB Medium Growth Experiments	98
3.7.3	Dry Sensor Preparation Method.....	99
3.7.4	PCE SWF Growth Experiments.....	100
3.7.5	Wound Bed Model Adaption and Double Sensor Model Development..	100
3.7.6	Incorporating Wound Dressings into the WBM	103
3.7.7	PCE Saline Experiments	104
3.7.8	Equivalent Circuit Modelling.....	104
3.7.9	Effects of Bacterial Concentration upon Impedance Response During Growth	106
3.7.10	Neural Network Development for Bacterial Detection.....	106
4.	ASSESSING THE SUITABILITY OF Ag/AgCl ELECTRODES FOR THE DETECTION OF WOUND PATHOGENS	110
4.1	Introduction.....	111
4.2	Ag/AgCl Electrode Voltage-Induced Instability in Saline Solution	111
4.3	Ag/AgCl Electrode Detection of Bacteria in LB Medium is Impacted by Applied Measurement Voltage	115
4.3.1	200 mV Inhibits Bacterial Growth in LB.....	115
4.3.2	20 mV Permits Bacterial Growth In LB	117
4.4	The Ag/AgCl Electrode Surface Causes a Zone of Inhibition	120
4.5	Calculation of the Minimal Inhibitory Concentration of Ag ⁺	121

4.6	Wound Bed Model Development for the Assessment of Ag/AgCl Sensor Bacterial Detection in a Wound Environment	122
4.6.1	20 mV Detection of Bacteria in SWF	123
4.6.2	Collagen Matrix WBM Assessment at 20 mV	124
4.6.3	The Presence of a Collagen Matrix Enables Bacterial Growth at 200 mV 128	
4.7	Discussion and Summary	129
5.	ASSESSING THE SUITABILITY OF CARBON ELECTRODES FOR THE DETECTION OF WOUND PATHOGENS	131
5.1	Introduction	132
5.2	Carbon Electrode Detection of Bacteria in LB Medium	132
5.3	Carbon Electrode Detection of Bacteria in SWF	140
5.4	Carbon Electrode Detection of Bacteria in the Wound Bed Model	146
5.5	The Influence of Direct Cell/Electrode Processes Upon the Measured Carbon Electrode Impedance Signatures	149
5.5.1	Effects of Washed Cells in Saline Over Time Upon Impedance	150
5.5.2	<i>S. aureus</i> Cell Concentration Dependent Effects Upon Impedance	152
5.6	Exploration of the Mechanisms Underpinning the Bacterial Impedance Signatures via Equivalent Circuit Modelling	154
5.6.1	<i>P. mirabilis</i> Circuit Modelling Results	155
5.6.2	<i>S. aureus</i> Circuit Modelling Results	156
5.7	Discussion and Summary	158
6.	ASSESSING THE SUITABILITY OF PLATINISED CARBON ELECTRODES FOR THE DETECTION OF WOUND PATHOGENS	160
6.1	Introduction	161
6.2	PCE Detection of Bacteria in LB Medium	161
6.2.1	Using a Sterile Normalisation Point	161
6.2.2	Using a Non-Sterile Normalisation Point	164
6.3	Evaluation of a Dry PCE Sensor Preparation Method	168
6.4	PCE Detection of Bacteria in SWF	171
6.5	PCE Detection of Bacteria in Model Wound Environments	175
6.5.1	Detection of Bacteria in the WBM	176
6.5.2	Detection of Bacteria in the dWBM	182
6.6	The Impact of Wound Dressings Upon Impedance and Bacterial Growth	192
6.6.1	Acticoat Dressing	192
6.6.2	Advazorb Dressing	194
6.6.3	N-A [®] Ultra Dressing	196

6.6.4	Activon Tulle Dressing	198
6.6.5	Mepitel® Dressing	201
6.7	The Influence of Direct Cell/Electrode Processes Upon the Measured PCE Impedance Signature.....	204
6.7.1	Effects of Washed Cells in Saline Over Time	204
6.7.2	<i>S. aureus</i> Cell Concentration Dependent Effects	207
6.8	Exploration of the Mechanisms Underpinning the Bacterial Impedance Signatures via Equivalent Circuit Modelling.....	209
6.8.1	Modelling the LB Medium Data.....	209
6.8.2	Modelling the 0.9% w/v NaCl Data.....	211
6.9	Bacterial Concentration Estimation via Rate of Normalised Impedance Change	212
6.10	Development of Neural Networks for the Detection and Identification of Bacteria	218
6.10.1	Training Dataset Overview	219
6.10.2	Model Feature Selection and Rationale	220
6.10.3	ANN1 Model Creation for Detecting Infection	222
6.10.4	ANN2 Model Creation for Bacterial Species Identification	225
6.11	Discussion and Summary	227
7.	DISCUSSION.....	229
7.1	Introduction.....	230
7.2	Electrode Materials - Assessment and Selection	230
7.2.1	Ag/AgCl Sensor Conclusions	230
7.2.2	Carbon Sensor Conclusions	233
7.2.3	PCE Sensor Conclusions.....	238
7.2.4	Summary - Electrode Material Selection in the Context of the Project Objectives	242
7.3	The Relevance and Importance of the WBM Used to Assess Sensor Performance	243
7.3.1	Bacterial Growth Detection in SWF	243
7.3.2	Bacterial Growth Detection in the WBM.....	246
7.3.3	The dWBM and Gravitational Influence Upon Single Species Signatures	250
7.3.4	Multispecies Bacterial Detection in the WBM and Gravitational Influence	253
7.3.5	The Influence of Wound Dressings Upon Bacteria and Impedance	255
7.3.6	Summary – Impact of the WBM Studies upon the Project Objectives	258

7.4	Evaluating the Algorithmic Approaches to Bacterial Signature Differentiation	259
7.4.1	Concentration Dependent Signature Differentiation.....	259
7.4.2	Using Artificial Neural Networks for Bacterial Detection and Identification	261
7.4.3	Summary – Algorithmic Approaches to Bacterial Detection in the Context of the Project Objectives.....	264
7.5	Conclusions and Future Work.....	265
7.5.1	Project Conclusions.....	265
7.5.2	Future Research Recommendations.....	265
8.	REFERENCES	268
9.	APPENDIX.....	298
9.1	Appendix A.....	299

LIST OF FIGURES

Figure 1.1	Key layers and features of the skin.....	3
Figure 1.2	Pressure ulcer on an individual’s sacrum	5
Figure 1.3	Ulcer on the lower leg and foot due to ischemia	6
Figure 1.4	The four stages of wound healing.....	7
Figure 1.5.	The four key phases of infection development.....	10
Figure 1.6.	(A) Image of trauma wound to leg that is healing successfully and (B) image of an infected amputation wound.	11
Figure 1.7.	Prevalence of different pathogens in HAI	13
Figure 1.8.	Resistance of gram-positive bacteria isolated from wound infections to selected antibiotics.....	14
Figure 1.9.	Summary of common wound dressing properties.	19
Figure 1.10.	Summary of the infection detection methods introduced within Section 1.5.	21
Figure 1.11.	A selection of key wound infection symptoms.....	21
Figure 1.12.	Potential biomarkers of wound infection for biosensor exploitation.....	26
Figure 1.13.	Dielectric spectra of biological tissue containing the α -, β -, and γ -dispersion regions.....	30
Figure 1.14.	Potential mechanisms via which bacteria alter electrochemical impedance.....	31
Figure 1.15.	Diagram of the hypothesised future in situ wound infection monitoring device.....	38

Figure 2.1. Taxonomic rank in biological classification	40
Figure 2.2. Key prokaryotic cell features.....	41
Figure 2.3. Cell wall structure and Gram staining for Gram positive and Gram negative bacteria.....	42
Figure 2.4 Image of <i>P. mirabilis</i> swarming pattern formation on an agar plate.	43
Figure 2.5. Bacterial growth curve.....	43
Figure 2.6. Bacterial biofilm formation lifecycle.....	45
Figure 2.7. Scanning electron microscope image of <i>Alcaligenes xylosoxidans</i> biofilm formation within a central venous catheter	46
Figure 2.8. A simple electrochemical cell.....	48
Figure 2.9. Key factors influencing electrochemical reaction rate.	49
Figure 2.10. Ion solvation shell.....	50
Figure 2.11. Structure of the electrical double layer.....	54
Figure 2.12. Current vs potential plots for an (A) non-polarisable and (B) polarisable electrode.....	56
Figure 2.13. A resistor contains only a real component of impedance.	59
Figure 2.14. A capacitor contains only an imaginary component of impedance.	60
Figure 2.15. The impedance of an electrochemical system typically has both resistive and capacitive components	60
Figure 2.16. Diagram of a charged capacitor.....	61
Figure 2.17. The relationship between current and voltage for a hypothetical electrochemical system, with a localised region of linearity highlighted.	63
Figure 2.18. Basic equivalent circuit model for EIS data.	64
Figure 2.19. EIS data presentation and circuit modelling	65
Figure 2.20. Nyquist plots for Randle's ECM containing a Warburg element.....	66
Figure 2.21. Defining artificial intelligence concepts.....	67
Figure 2.22. Comparison of supervised and unsupervised ML applications	68
Figure 2.23. A simplistic representation of a neuron	69
Figure 2.24. Diagram representing an ANN.....	70
Figure 3.1. Outline of key areas investigated with each sensor.	74
Figure 3.2. Colony counting procedure.	78
Figure 3.3. Crystal violet staining example.	78
Figure 3.4. Image of the Ag/AgCl WoundSense electrode (with dimensions overlaid).....	79
Figure 3.5. Carbon electrode manufacturing.	80

Figure 3.6. Image of a PCE sensor (with dimensions overlaid).....	81
Figure 3.7. Image of the Solartron SI1260 impedance gain/phase analyser used for impedance measurements.	82
Figure 3.8. Electrode measurement control overview	83
Figure 3.9. Use of the experiment GUI.....	84
Figure 3.10. GUI plotting options selection.....	85
Figure 3.11. Ag/AgCl sensor plate assembly.....	86
Figure 3.12. Image of crystal violet leakage from chamber after 24 hours (during sealant pattern testing).	86
Figure 3.13. Zone of inhibition experimental set up.....	88
Figure 3.14. Depiction of a Ag/AgCl sensor wound bed model well.	90
Figure 3.15. Image of the Ag/AgCl sensor automated WBM measurement set-up.....	90
Figure 3.16. Carbon electrodes assembled into an array of 8 sensor wells.....	91
Figure 3.17. Carbon electrode conditioning effects.	92
Figure 3.18. Carbon electrode assembly and cable harness connection.	93
Figure 3.19. The simple equivalent circuit model used to fit carbon sensor data.	95
Figure 3.20. Example Nyquist plot obtained using a carbon sensor.	96
Figure 3.21. Acrylic wall secured onto PCE sensor to create a well.	97
Figure 3.22. Effect of the NaOH chemical conditioning process upon the PCE sensors.	97
Figure 3.23. Assembly of PCE sensors for automated multiplexer measurements.	98
Figure 3.24. Diagram of the PCE WBM configuration (side view).	100
Figure 3.25. Image of a PCE sensor with the individual working electrodes used in the WBM experiments highlighted.....	101
Figure 3.26. Assembly of the double sensor wound bed model (dWBM).....	102
Figure 3.27. Diagram (side view) of the double sensor wound bed model (dWBM).	103
Figure 3.28. Assembly for dressing studies conducted in the WBM.....	103
Figure 3.29. Example Nyquist plot for a PCE sensor.	105
Figure 3.30. Equivalent circuit model used to fit selected PCE sensor data.....	105
Figure 3.31. Circuit used to approximate Warburg element values for low frequency data.	106
Figure 3.32. Flowchart describing the development of the ANN predictive model.	108
Figure 4.1. Impedance spectra obtained through repeated measurements of 0.9% w/v NaCl in dH ₂ O with Ag/AgCl electrodes.....	113
Figure 4.2. The effects of using different perturbation voltages upon impedance	114

Figure 4.3. Impedance response associated with the inoculation of LB medium with <i>P. aeruginosa</i> (PA14) and performing measurements with a 200 mV perturbation voltage over 24 hours.....	116
Figure 4.4. Impedance response associated with the inoculation of LB medium with <i>P. aeruginosa</i> (PA14) and performing measurements with a 20 mV perturbation voltage over 24 hours.....	118
Figure 4.5. Impedance response associated with the inoculation of LB media with <i>S. aureus</i> (NCTC8325) and performing measurements with a 20 mV perturbation voltage over 24 hours.....	119
Figure 4.6. Ag/AgCl electrode zone of inhibition experiments performed with <i>P. aeruginosa</i> (PA14).....	120
Figure 4.7. Assessing the MIC of AgNO ₃	121
Figure 4.8. Impedance response associated with the inoculation of SWF with <i>S. aureus</i> (NCTC8325) and performing measurements with a 20 mV perturbation voltage.....	124
Figure 4.9. Image of the Ag/AgCl sensor WBM from above and below.	125
Figure 4.10. Impedance response associated with the inoculation of the WBM with <i>S. aureus</i> (NCTC8325) and performing measurements with a 20 mV perturbation voltage over 24 hours.....	126
Figure 4.11. Image from below of the WoundSense assembly after 72 hours of PA14 growth in the WBM (20 mV voltage used for measurements).	127
Figure 4.12. Impedance response associated with the inoculation of the WBM with <i>P. aeruginosa</i> (PA14) and performing measurements with a 20 mV perturbation voltage over 72 hours.....	127
Figure 4.13. Image from below of the WoundSense assembly after 24 hours of PA14 growth in the WBM with a 200 mV voltage used for measurements.	128
Figure 4.14. Impedance response associated with the inoculation of the WBM with <i>P. aeruginosa</i> (PA14) and performing measurements with a 200 mV perturbation voltage over 24 hours.....	129
Figure 5.1. Raw impedance plots associated with the inoculation of LB medium with <i>S. aureus</i> (NCTC8325) and performing measurements over 24 hours with carbon sensors. ...	133
Figure 5.2. Normalised impedance signatures obtained following the inoculation of LB medium with <i>S. aureus</i> (NCTC8325) and performing 200 mV measurements with the carbon sensors over 24 hours.....	134
Figure 5.3. <i>S. aureus</i> (NCTC8325) growth in LB medium time-based plots.	136

Figure 5.4. Impedance response associated with the growth of <i>S. epidermidis</i> (NCTC11964) in LB medium to an average concentration of 3.8×10^7 CFU/mL after 24 hours.	137
Figure 5.5. Impedance response associated with the growth of <i>P. mirabilis</i> (DSM4479) in LB medium over 24 hours.	139
Figure 5.6. CV staining images resulting from bacterial growth experiments performed in LB medium.	140
Figure 5.7. The baseline (A) modulus and (B) absolute phase plots obtained using the carbon sensors in sterile SWF.....	141
Figure 5.8. Impedance response associated with the growth of <i>S. aureus</i> (NCTC8325) in SWF.	142
Figure 5.9. Impedance response associated with the growth of <i>P. aeruginosa</i> (PA14) in SWF.	144
Figure 5.10. Impedance response associated with the growth of <i>P. mirabilis</i> (DSM4479) in SWF.	145
Figure 5.11. The baseline (A) modulus and (B) absolute phase plots obtained using the carbon sensors in a sterile WBM (n = 4, shading depicts +/- 1 standard deviation).....	146
Figure 5.12. Impedance response associated with the growth of <i>S. aureus</i> (NCTC8325) in the WBM.	147
Figure 5.13. Impedance response associated with the growth of <i>P. aeruginosa</i> (PA14) in the WBM.	149
Figure 5.14. Impedance response associated with measurements of <i>P. mirabilis</i> (DSM4479) in 0.9% v/w NaCl over 24 hours.....	151
Figure 5.15. Impedance response associated with measurements of <i>S. aureus</i> (NCTC8325) in 0.9% v/w NaCl over 2.5 hours.....	152
Figure 5.16. Measurements of <i>S. aureus</i> (NCTC8325) at increasing concentrations (denoted as multiplication factors, MF) in 0.9% w/v NaCl.....	154
Figure 5.17. <i>P. mirabilis</i> (DSM4479) growth in LB medium circuit fitting results.	155
Figure 5.18. <i>P. mirabilis</i> (DSM4479) in 0.9% w/v NaCl circuit fitting results.	156
Figure 5.19. <i>S. aureus</i> (NCTC8325) growth in LB medium circuit fitting results.	157
Figure 5.20. <i>S. aureus</i> (NCTC8325) in 0.9% w/v NaCl circuit fitting results.	157
Figure 5.21. Timeline of influence for bacterial mechanisms impacting impedance signatures.	159
Figure 6.1. Impedance response associated with the growth of <i>S. aureus</i> (NCTC8325) in LB medium	162

Figure 6.2. Normalised impedance response associated with the growth of <i>S. aureus</i> (NCTC8325) in LB medium	163
Figure 6.3. <i>S. aureus</i> (NCTC8325) growth in LB medium over 24 hours, time-based plots	164
Figure 6.4. Normalised impedance response associated with the growth of <i>S. aureus</i> (NCTC8325) in LB medium	165
Figure 6.5. Normalised impedance response associated with the growth of <i>P. aeruginosa</i> (PA14) in LB medium.	167
Figure 6.6. A sample of CV staining images resulting from PCE bacterial growth experiments performed in LB medium	168
Figure 6.7. Flow diagram outlining PCE preparation methods A and B	169
Figure 6.8. Characterisation of the PCE response associated with the preparation method A vs proposed new method B	170
Figure 6.9. The baseline impedance plots obtained using the PCE sensors in sterile SWF.	171
Figure 6.10. Impedance response associated with the growth of <i>S. aureus</i> (NCTC8325) and <i>P. aeruginosa</i> (PA14) separately but simultaneously in SWF.....	172
Figure 6.11. Impedance response associated with <i>E. coli</i> (DSM30083) growth in SWF....	174
Figure 6.12. Impedance response associated with the growth of <i>P. mirabilis</i> (DSM4479) in SWF.	175
Figure 6.13. The baseline (A) modulus and (B) absolute phase plots obtained using the PCE sensors in sterile WBM.....	176
Figure 6.14. Image of a WBM chamber	177
Figure 6.15. Impedance response associated with the growth of <i>S. aureus</i> (NCTC8325) and <i>P. aeruginosa</i> (PA14) separately but simultaneously in the PCE WBM.....	178
Figure 6.16. Comparison of SWF and WBM experiment bacterial/surface arrangements..	179
Figure 6.17. Impedance response associated with the growth of <i>S. aureus</i> (NCTC8325) and <i>P. aeruginosa</i> (PA14) and a polymicrobial NCTC8325 and PA14 culture in the PCE WBM.	181
Figure 6.18. Images of the WBM chambers following the PCE polymicrobial experiment.	182
Figure 6.19. The baseline impedance plots obtained for the dWBM.....	183
Figure 6.20. Impedance response associated with the growth of <i>S. aureus</i> (NCTC8325) and <i>P. aeruginosa</i> (PA14) separately but simultaneously in the PCE dWBM.....	185
Figure 6.21. <i>S. aureus</i> (NCTC8325) and <i>P. aeruginosa</i> separate growth in the dWBM over 24 hours time-based plots.	187

Figure 6.22. Impedance response associated with the growth of <i>S. aureus</i> (NCTC8325), <i>P. aeruginosa</i> (PA14) and a co-culture of these species (Poly) in the PCE dWBM.....	189
Figure 6.23. <i>S. aureus</i> (NCTC8325), <i>P. aeruginosa</i> and co-culture of these bacteria (Poly) grown in the dWBM time-based plots.	191
Figure 6.24. Acticoat absorbent dressing images.	192
Figure 6.25. The baseline (A) modulus and (B) absolute phase plots observing the initial impact of the Acticoat absorbent with SILCRYST™ dressing upon the WBM.....	193
Figure 6.26. Impedance response associated with the growth of <i>S. aureus</i> (NCTC8325) in the PCE WBM	194
Figure 6.27. Advazorb foam dressing images.....	195
Figure 6.28. The baseline (A) modulus and (B) phase plots observing the initial impact of the Advazorb foam dressing upon the WBM.	195
Figure 6.29. Impedance response associated with the growth of <i>S. aureus</i> (NCTC8325) in the PCE WBM	196
Figure 6.30. N-A Ultra silicone coated knitted dressing images.	197
Figure 6.31. The baseline (A) modulus and (B) absolute phase plots observing the initial impact of the N-A Ultra dressing upon the WBM.	197
Figure 6.32. Impedance response associated with the growth of <i>S. aureus</i> (NCTC8325) in the PCE WBM	198
Figure 6.33. Activon Tulle Manuka honey dressing images	199
Figure 6.34. The (A) modulus and (B) absolute phase plots assessing the initial impact of the Activon Tulle dressing upon the WBM baseline impedance.....	199
Figure 6.35. Impedance response associated with the growth of <i>S. aureus</i> (NCTC8325) in the PCE WBM	201
Figure 6.36. Mepitel soft silicone dressing images.....	202
Figure 6.37. The (A) modulus and (B) phase plots assessing the initial impact of the Mepitel dressing upon the WBM baseline impedance	202
Figure 6.38. Impedance response associated with the growth of <i>S. aureus</i> (NCTC8325) in the PCE WBM.	203
Figure 6.39. Impedance response associated with the introduction of washed <i>S. aureus</i> and <i>P. aeruginosa</i> cells into 0.9% w/v NaCl.	205
Figure 6.40. Impedance response associated with measurements of <i>S. aureus</i> (NCTC8325) and <i>P. aeruginosa</i> (PA14) in 0.9% v/w NaCl over 24 hours.	206
Figure 6.41. Measurements of <i>S. aureus</i> (NCTC8325) at increasing concentrations.	208

Figure 6.42. Circuit fitting results for <i>S. aureus</i> (NCTC8325) growth in LB medium over 24 hours.....	210
Figure 6.43. Circuit fitting results for <i>P. aeruginosa</i> (PA14) growth in LB medium over 24 hours.....	211
Figure 6.44. Circuit fitting results for washed <i>S. aureus</i> (NCTC8325) and <i>P. aeruginosa</i> (PA14) cell settlement in 0.9% w/v NaCl over 24 hours.	212
Figure 6.45. Normalised impedance response associated with the growth of different concentrations of <i>S. aureus</i> (NCTC8325) in LB medium.....	214
Figure 6.46. Mean rate of change as a function of time for (A) normalised modulus at 1 Hz and (B) normalised (absolute) phase at 200Hz.	215
Figure 6.47. Calibration curves obtained for absolute rate of change as a function of concentration.....	216
Figure 6.48. Mean rate of change as a function of time for the test data	217
Figure 6.49. Summary of the dataset collated for ANN training.	220
Figure 6.50. Justification of normalised modulus 1 Hz and 1 kHz feature selection.....	221
Figure 6.51. Justification of normalised (absolute) phase 1 Hz, 100 Hz and 1 kHz feature selection.	222
Figure 7.1. Summary of the unique dWBM factors believed to be influential in the quality of experimental results.....	251
Figure 7.2. Summary of the final ANN1 (bacterial detection) and ANN2 (bacterial identification) key characteristics and average validation scores.....	261
Figure 7.3. Summary of the key considerations for new digital and data driven health technologies.....	264
Figure 7.4. Overview of key areas identified for future research.....	266

LIST OF TABLES

Table 1.1 Different layers of the skin and their roles.....	3
Table 1.2 Definitions of wound thickness classifications.....	4
Table 1.3 Common neonatal and paediatric wound types	7
Table 1.4. A selection of wound care products linked to the TIME framework.....	17
Table 1.5. Wound sampling techniques.....	22
Table 1.6. Key label free bacterial impedance spectroscopy studies.....	33
Table 2.1. Summary of bacterial species central to this thesis.....	47

Table 2.2. Overview of MLP Classifier model parameters.	71
Table 3.1. Screen printer settings for carbon electrode printing.	80
Table 3.2. Ag/AgCl electrode characterisation measurement voltages.	87
Table 3.3. Electrode preparation methods used to test the new dry sensor preparation technique.	100
Table 3.4. Details of the wound dressings studied in the <i>S. aureus</i> WBM experiments.	103
Table 6.1. Sensor preparation parameters.	168
Table 6.2. Cell densities for <i>S. aureus</i> and <i>P. aeruginosa</i> over the simultaneous SWF growth experiment.	173
Table 6.3. Cell densities for the <i>S. aureus</i> and <i>P. aeruginosa</i> simultaneous WBM experiment.	177
Table 6.4. Cell densities for <i>S. aureus</i> and <i>P. aeruginosa</i> in the polymicrobial WBM experiment.	180
Table 6.5. Cell densities for the <i>S. aureus</i> and <i>P. aeruginosa</i> simultaneous dWBM experiment.	184
Table 6.6. Cell densities for <i>S. aureus</i> and <i>P. aeruginosa</i> in the polymicrobial dWBM experiment.	188
Table 6.7. Estimates of the average <i>S. aureus</i> cell density present in test samples, obtained using the rate of change method.	218
Table 6.8. ANN1 number of neurons optimisation for a 2 hidden layer network.	223
Table 6.9. ANN1 number of hidden layers optimisation.	223
Table 6.10. ANN1 learning type and rate exploration.	223
Table 6.11. Optimising the maximum number of iterations for ANN1.	224
Table 6.12. ANN1 final algorithm classification report.	224
Table 6.13. ANN2 number of neurons optimisation for a 2 hidden layer network.	225
Table 6.14. Optimisation of the number of hidden layers for ANN2.	225
Table 6.15. Exploration of learning type and rate for ANN2.	226
Table 6.16. Results of altering the maximum number of iterations for ANN2.	226
Table 6.17. Classification report for the final ANN2 algorithm.	227
Table 7.1. Summary of key carbon electrode LB medium growth experiment impedance changes for the studied wound bacteria.	238
Table 7.2. Summary of key wound dressing WBM experiment findings.	256

1. WOUND INFECTION AND APPROACHES TO BACTERIAL DETECTION

1.1 Introduction

Wound healing is a complex, multi-stage process that requires careful management. A barrier to successful healing is infection: many bacteria thrive in the wound environment and can colonise the lesion, resulting in an infection. Detrimental to the healing process, infection can significantly prolong recovery times and potentially lead to serious complications and illnesses. Rapid detection of wound infection and identification of the responsible microorganisms are crucial to ensuring prompt and appropriate treatment.

Vulnerable individuals, such as neonates, the elderly and diabetics, are particularly susceptible to developing chronic wounds that are at high risk of infection. Further, the signs of this infection may not be as distinct as in healthy adults. Current clinical practice relies upon the observation of patient symptoms and time consuming culturing techniques. An *in situ* wound monitor capable of detecting infection in its early stages, whilst simultaneously providing an indication of the causative pathogens would be of great benefit. Such a device could also negate the need for unnecessary disturbances of the wound and its natural healing process by being positioned within the dressing.

1.2 The Skin and Wounds

1.2.1 Layers of the Skin

Skin is the cutaneous membrane, belonging to the integumentary system. It is critical to the protection of the body from many elements of the environment including chemicals, microorganisms and the sun's radiation (1). The adult skin contains multiple layers and typically covers a surface area of around 2 m². These multiple, distinct layers may be categorised into the epidermis, dermis and hypodermis (in order of increasing tissue depth, as seen in Figure 1.1), with these layers further subdivided (Table 1.1). The skin is a regenerative organ; the epidermis is replenished approximately every 4 weeks via differentiation, proliferation and migration of cells from the deeper layers of the epidermis to the outermost (2). This ensures that adequate protection of the dermis is maintained. Consisting of stratified squamous epithelial cells, the epidermis is avascular. Nutrients must, therefore, be supplied by diffusion from dermal blood vessels (1). Within Table 1.1 the key roles of each skin layer are detailed.

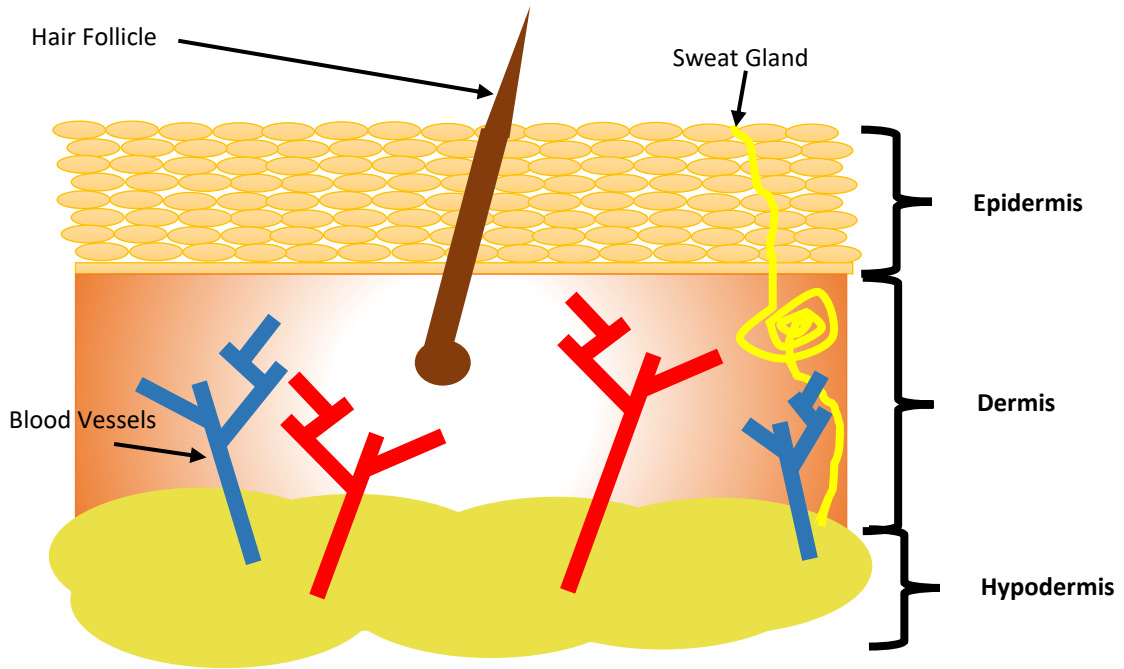


Figure 1.1 Key layers and features of the skin.

Table 1.1 Different layers of the skin and their roles (summarised from (1)).

Layer of Skin	Sub-Layers (in order of increasing depth)	Key Points
Epidermis	Stratum corneum	Exposed to environment, contains multiple layers of cells filled with keratin, strong protective barrier, relatively dry, water resistant
	Stratum lucidum (thick skin only)	Found in thick skin only such as palms
	Stratum granulosum	Most cells stopped dividing, makes keratin and keratohyalin
	Stratum spinosum	The daughter cells created following stem cell division are located here, “spiny” appearance, contains dendritic cells linked to immune response
	Stratum basale	Deepest layer of epidermis (separates it from dermis), attachment strength is key, contains basal cells (stem cells)

Dermis	Papillary layer	Areolar tissue, includes capillaries, lymphatic vessels and sensory neurons
	Reticular layer	Compact connective tissue consisting of collagen and elastic fibres

Of particular importance when considering tissue injury is the variation in skin properties that is observed. For example, the thickness of the epidermis can range from around 0.04 mm to 1.6 mm depending on body location (3). Age is a further factor that is known to affect the skin: the aging population display reduced skin thickness and an increased regeneration time; the premature neonatal population have greatly increased skin fragility and impaired skin function (3,4). Neonates typically lack a secure connection between the epidermal and dermal skin layers. Further, their underdeveloped strata cornea barrier functions lead to heat loss, water loss and a heightened risk of toxicity from absorption through the skin (5). A poorly formed stratum corneum additionally increases the infant’s risk of infection, as the skin’s normal barrier properties are impaired (6).

1.2.2 Types of Wounds

The combination of varying skin attributes and mechanisms of injury results in a vast assortment of wound types requiring care. Despite this, wounds can be broadly categorised into two distinct groups: acute and chronic. Whilst it is anticipated that acute wounds will heal within a foreseeable time frame, chronic wounds can take far longer to heal, can reoccur or be unable to heal (7). Typically wounds are classified as chronic if they fail to advance through the normal stages of healing within a time period of approximately 3 months; an estimated 1-2% of people in developed countries will acquire a chronic wound during their lifetime (8,9). Whereas acute wounds are commonly induced by an external source (for example a bite or surgical wound), chronic wounds are often linked to pre-existing conditions such as diabetes and obesity. As the incidences of these conditions are increasing, chronic wounds will likewise become an increasing problem. Additional modes of classification include wound age, origin and thickness (Table 1.2 defines the different thickness categories of wounds which are commonly referenced (10)).

Table 1.2 Definitions of wound thickness classifications.

Classification	Definition
Superficial	Injury to epidermis.

Partial thickness	Damage extending through epidermis into lower dermis.
Full thickness	Wound reaches through to subcutaneous tissue.

Pressure ulcers result from prolonged pressure to a localised area of skin (due to a lack of mobility or persistent medical device contact for example) and are the most prevalent form of hospital acquired skin injury (4). A key class of chronic wound, it often forms on an elderly or intensive care unit patient's sacrum, coccyx or heels (4,11) (Figure 1.2). Data has previously suggested that around 20% of hospital in-patients in Europe have a pressure ulcer, the vast majority of which are hospital acquired (9). Not only does treating pressure ulcers costs the NHS over £500 million per year, these wounds result in a 7% increase in mortality rate (9,12).



Figure 1.2 Pressure ulcer on an individual's sacrum (image sourced from www.medetec.co.uk).

A further common lesion is the foot ulcer (Figure 1.3). Approximately 19-34% of patients with diabetes will develop a foot ulcer in their lifetime (13). The occurrence of foot ulcers in these patients is associated with significantly increased 5- year mortality rates (14). Further, this wound is the most significant root of non-traumatic amputation in the developed world (15). Venous ulcers are a further concern. Most commonly affecting the lower leg, this condition is linked to venous hypertension (high venous pressure in the extremity). These ulcers are developed by 1% of the population, with higher prevalence in older age groups (16). Overall, chronic leg and foot ulcers are believed to require around one year to heal and subsequently reoccur in around two thirds of patients (9,17).



Figure 1.3 Ulcer on the lower leg and foot due to ischemia (image sourced from www.medetec.co.uk).

Burn injuries are another form of wound with high risk of mortality. For example, if a burn covers 80% of a young person's body, their probability of survival is only 50% (1). Leading causes of mortality following a burn wound are infection and sepsis, resulting in an approximate mortality rate of 1.5% for all burn patients (18,19). There are many possible origins of a burn wound, including chemical or thermal contact. Burn wounds may be classified as either 1st, 2nd or 3rd degree, a scale based upon increasing depth of skin damage as described in Table 1.2. In contrast to other types of wound, burns can result in extreme loss of blood plasma due to extensive capillary damage, resulting in large volumes of exudate (18).

It has been estimated that, in any given year, 10% of the UK's population will have a surgical procedure performed (20). Surgical wounds are therefore a very common type of injury, with severity varying widely depending on the procedure undergone. This type of wound can be particularly common amongst children with rare conditions who often require multiple surgical interventions. Furthermore, by means of a one-day audit of paediatric skin integrity in a children's hospital, it was found by Noonan et al. (2006) that 43% of inpatients had a wound (21). Premature neonates are among the most vulnerable patients; common wounds in this population include surgical wounds and pressure ulcers (5). A further common injury for this population is epidermal stripping, typically resulting from the removal of a wound dressing or skin-attached sensor. Due to the neonate's fragile dermal-epidermal junction, the detachment and removal of the outer layer of the child's skin can occur, causing significant damage (4). Within Table 1.3 a number of common neonatal and paediatric wounds are summarised.

Table 1.3 Common neonatal and paediatric wound types (summarised from Baharestani (2007) (5)).

Wound Type	Description
Surgical incisions	Wounds are the product of surgical intervention, frequent monitoring required to ensure appropriate healing
Pressure ulcers	Injury to skin most commonly resulting from sustained application of pressure, for example due to lack of mobility or continuous use of a medical device
Epidermal stripping	Commonly associated with the use of adhesives on the skin, causing detachment of the epidermis upon removal. Premature neonates particularly susceptible
Dermatitis	Most frequently linked to incontinence and can lead to <i>Candida albicans</i> infection
Chemical injuries	Increased permeability of neonatal skin can lead to irritation and toxicity issues arising from absorption of chemical agent applied to skin
Thermal injuries	The use of certain medical devices for instance could cause thermal damage to sensitive skin

1.2.3 Wound Healing

Upon injury, the body's natural response mechanisms initiate a series of vital processes to heal the wound. The four sequential, overlapping healing phases are: haemostasis, inflammation, proliferation and remodelling (Figure 1.4). These phases (described in detail by Guo and Dipietro (2010) (22)) and are summarised below.

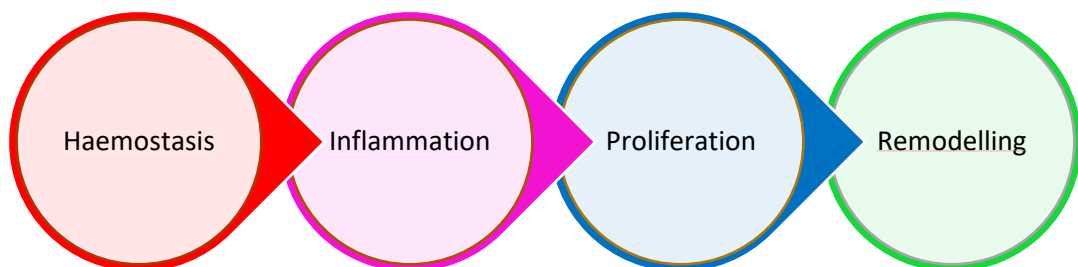


Figure 1.4 The four stages of wound healing.

When the skin integrity is compromised, the role of haemostasis is to prevent blood loss. Notably, vascular constriction restricts blood flow out of the wound and platelets are attracted

to the site, forming a plug to stop the bleeding. The blood's coagulation cascade then ultimately leads to the conversion of fibrinogen to fibrin, and the production of a stable fibrin clot (23). These complex processes involve numerous biochemical reactions. In the second phase- inflammation- neutrophils, monocytes and lymphocytes are recruited to clean the wound: cellular debris and microorganisms are removed, and wound exudate is secreted. The proliferation phase then occurs, including steps such as reepithelialisation and the formation of collagen and extracellular matrix. During this time the clot gradually dissolves through the action of plasmin. Finally, remodelling of the tissue occurs over an extended period whereby the wound is closed and scar tissue forms, strengthening in time (22).

There are numerous factors that impact the ability of a wound to heal effectively. For satisfactory healing, the four phases described above must occur in order and over an appropriate period of time (22). The type of wound leads to variation in healing time and success: the fluid loss associated with burns for example has a negative impact and the remodelling phase is often extended (1,18), and in chronic wounds healing is often disturbed by a persistent inflammatory phase (17). There are also numerous systemic factors which influence the wound healing process, for example: advancing age; stress; conditions such as diabetes; obesity; nutrition and alcohol intake (22). Furthermore, the local environmental conditions such as adequate oxygenation and moisture balance are equally vital (24,25). One of the most common causes of impaired healing is bacterial infection, a phenomenon visited in depth within the subsequent sections (4,17,18).

1.3 Wound Infection

Infection is a leading cause of disturbance to the natural, four-stage healing process of wounds. It can not only prolong healing times, but also provokes chronicity and can ultimately lead to serious complications such as sepsis, amputation and even death (26). Infection rates greatly vary between wound types: for example after approximately 2-3% of surgical procedures a skin or soft tissue infection will occur (27), whereas, over 50% of diabetes-related foot ulcers develop an infection (28). With the incidence of infection, healing is delayed or even prevented. Guest et al. (2020) found that infected chronic wounds had a healing rate of only 45%, compared to 59% for non-infected wounds (29). Further, infection leads to significant increases in treatment costs and resources (30).

1.3.1 The Microflora of Human Skin

At any given time, the body is host to around 10^{13} to 10^{15} bacteria (31), including on the skin and mucous membranes such as inside the mouth. Many factors affect which bacterial species will be present on the body and in which location, however, different species tend to have a preference for specific environmental conditions (32). The skin alone presents a variety of pH, nutrient and moisture levels, thus multiple niches and microbial species are present. Often these microorganisms are of benefit to the body (a symbiotic relationship) or are not harmful (commensal). Many microorganisms are believed to protect the skin from the invasion of more harmful pathogens, however, the introduction of different microorganisms or damage to the integrity of the epithelium can result in severe infection (33).

Over 180 different bacterial species exist on the human skin. The most frequent inhabitants of the skin's ecosystem are gram-positive bacteria: staphylococci, corynebacteria and propionibacteria account for around 50% of these (32). In particular, the coagulase-negative bacteria *Staphylococcus epidermidis* colonises many locations of the body and is the most commonly isolated microorganism from the skin (34). Gram-negative organisms such as *Klebsiella spp.* and *Escherichia coli* are present in certain regions of the skin, however, are far less abundant due to their limited ability to survive in dry environments (35,36). As previously stated, the skin microbiome varies across different sites of the body due to localised site conditions. Reasons for this topological variation include the presence of apocrine and eccrine glands, whose secretions attract certain microorganisms (33). Further, occluded areas of the skin such as the groin region are warmer and moister, providing an optimal environment for other bacteria such as species of corynebacteria.

Differences in normal microflora are also present between individuals. Infants for example host a wider range of bacteria, including a greater number of potentially harmful gram-negative organisms, whereas adults generally host fewer of these (32). For neonates, delivery method is linked to differences in skin microflora: babies delivered via Caesarean section are often colonised by *Staphylococcus* and *Corynebacterium* for example, and those delivered vaginally often acquire *Lactobacillus* and *Prevotella* (37). Sex further determines the variety of microorganisms located on the skin, as does local weather (33). Many species are common to all individuals, but proportional relationships can vary widely. The abundance of staphylococcal bacteria in the plantar heel region for example is extremely variable (38).

1.3.2 The Development of Infection

The epidermis functions as a barrier to protect the body from external pathogenic microorganisms. If its integrity is compromised, pathogens are given the opportunity to invade subcutaneous tissues. These tissues can possess desirable conditions, such as heat and moisture, which promote microbial growth. Guo and Dipietro (2010) describe four phases of infection, namely: contamination, colonisation, critical colonisation and invasive infection (22). The first, contamination, describes non-replicating bacteria existing within the lesion. Colonisation represents the transition of these bacteria to a replicating state, however, at this stage there is no destruction of, or significant response from, surrounding tissue. Critical colonisation (also termed local infection) defines a phase where the bacteria begin to evoke a reaction from neighbouring tissue. Finally, invasive infection is where the growing bacteria cause tissue damage and delay healing. Figure 1.5 summarises these phases of infection development. For comparison, Figure 1.6 contains both an example of a wound healing well (Figure 1.6A) and an infected wound (Figure 1.6B). A standard definition of bacterial load for a wound infection does not exist, however, it has been estimated that a bacterial load of $> 10^5$ CFU/g of tissue would constitute an infection (7). Converting this into an appropriate estimate in CFU/mL (units commonly used in bacterial studies), some researchers have acted on the assumption that 10^5 CFU/g is equivalent to 10^5 CFU/mL (39), whereas others have previously estimated equivalence to a lower concentration such as 10^3 CFU/mL from a swab (40).

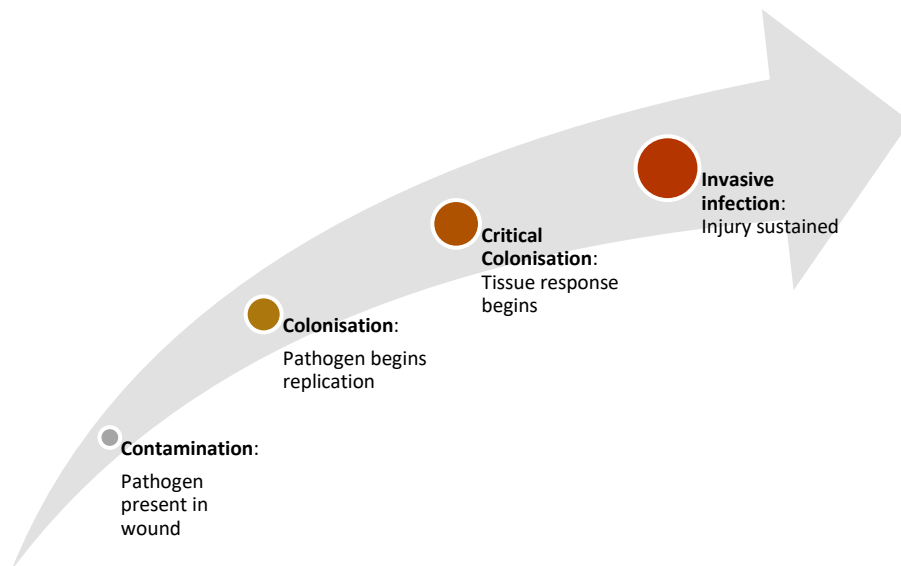


Figure 1.5. The four key phases of infection development.

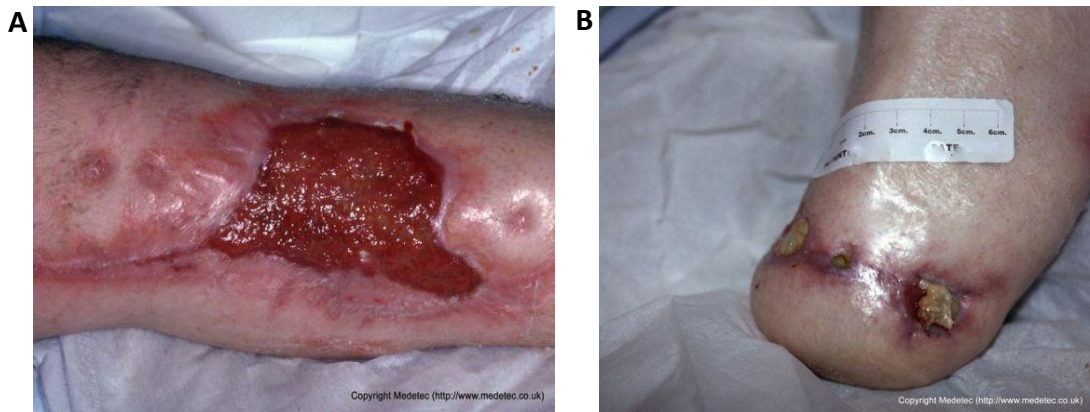


Figure 1.6. (A) Image of trauma wound to leg that is healing successfully and (B) image of an infected amputation wound. Images sourced from www.medetec.co.uk.

Following contamination, in around 6% of acute wounds and up to 80% of chronic wounds the colonising bacteria develop biofilms (41). In these cases, the bacteria are surrounded by a protective, self-produced matrix composed mainly of polysaccharides. Aggregations of microorganisms of this form are strikingly resistant to both antimicrobial agents and immune responses and, for this reason, can be particularly detrimental to the wound healing process (17,42). The formation of biofilms is discussed in detail within Section 2.2.

1.3.3 Causes of Infection and Risk Factors

Infection can form when pathogenic microorganisms breach the skin's protective barrier. Two key factors known to be important indicators of infection formation are: the presence of particular bacterial species on the skin; the overall bacterial density in and surrounding the wound (7). The infective pathogen may already be present within the skin's local microflora, may have spread from other areas of the body, or may be from external sources within the environment. Proactive wound management and hygiene practices such as cleansing and debridement are, therefore, crucial to the avoidance of infection (wound management practices are discussed within Section 1.4).

Of considerable concern is the risk of acquiring an infection whilst in a healthcare setting. Healthcare (or Hospital) Associated Infections (HAI) commonly originate from the use of invasive medical devices or form in wounds following surgery (43). In Scotland, data from

2016 revealed a ranging prevalence of HAI depending on the type of hospital. Notably, acute hospitals had an HAI prevalence of 4.6%, followed by non-acute hospitals with 3.2% and paediatric hospitals with 2.7% (44). Contaminated air conditioning systems, insufficient sterilisation and poor ward design amongst numerous elements leading to the spread of HAI (43).

Whilst every patient is at some risk of developing a wound infection, certain factors increase the probability. For example, Cheng et al. (2015) found the type of operation, history of diabetes or cancer, catheterisation and various other factors to increase an individual's risk of developing a surgical site infection (SSI) (45). Immunocompromised individuals such as neonates, and those with severe burn wounds also have an increased probability of infection development (18). Furthermore, the factors listed as affecting wound healing in Section 1.2.3 (such as obesity) can all delay healing times and thus increase the probability of exposure to invasive pathogens (22).

1.3.4 The Microflora of Infected Wounds

The pathogens responsible for wound infections vary, depending on the location of the wound and type of injury sustained for example. For wounds obtained out-with a clinical setting staphylococci and streptococci are generally the most prevalent colonising bacteria, whereas, in HAI such as SSI other strains can appear more frequently in line with the microflora of the patient's environment (46). By summarising HAI data reported to the USA's National Healthcare Safety Network, Sievert et al. (2013) found that, despite in excess of 80,000 different species of bacteria being found in the infections, over 80% of these belonged to one of eight microorganism categories (Figure 1.7) (27). Focusing on the microflora of wounds, Bessa et al. (2015) sampled 217 infected wounds of various types, finding 28 different species present (26). The most frequently occurring was *S. aureus*, present in 37% of sampled wounds, followed by *P. aeruginosa* (17%) and *P. mirabilis* (10%). The researchers also noted that in over one quarter of cases the wound had a polymicrobial infection, most commonly consisting of two bacteria: *S. aureus* and *P. aeruginosa*. Tong et al. (2015) similarly cite *S. aureus* as being the most dominant causative organism in SSI and cutaneous abscesses (42). In burn wound infections, *E. coli*, *P. aeruginosa* and other Gram-negative pathogens have been commonly associated (47).

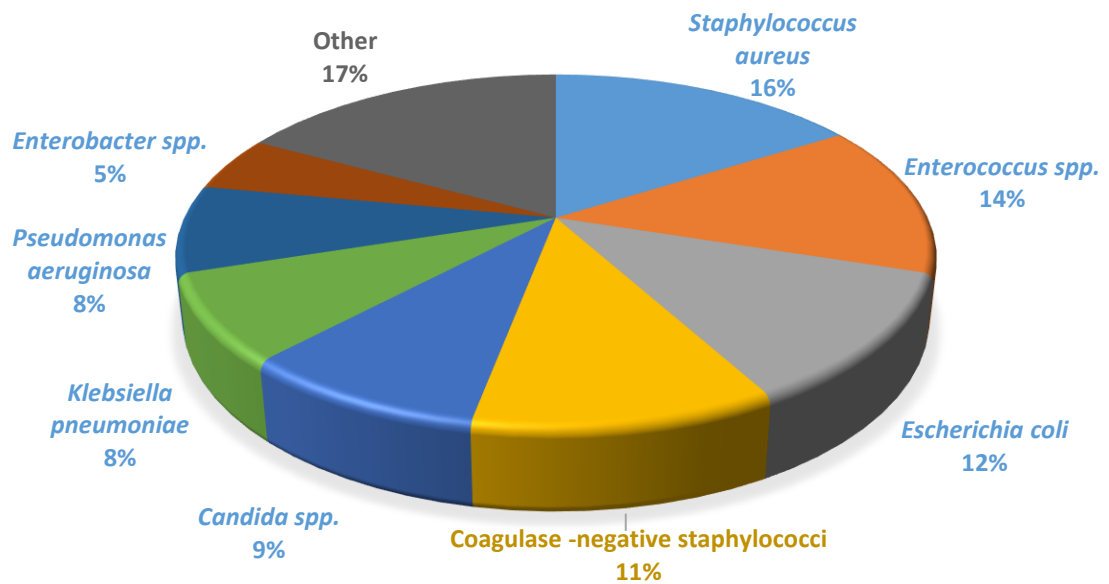


Figure 1.7. Prevalence of different pathogens in HAI, summarised from Sievert et al. (2013) (27).

The widespread use of antibiotics in settings such as healthcare and farming is driving a high rate of antimicrobial resistance (AMR), due to the selective pressure imposed upon bacteria and their consequent evolutionary reaction (48). Using 2016 data, it emerged that 1 in 3 hospital inpatients in Scotland received antimicrobial treatment (44). This high usage rate was noted to be of concern, due to the rising threat of antimicrobial resistance. The Review on Antimicrobial Resistance published a final report in 2016 which emphasised the importance of acting upon several key suggestions to help combat the problem, in order to negate an exponential rise in AMR associated fatalities by 2050 (49). Crucial examples include improving public knowledge of the issue, implementing stricter monitoring systems for antimicrobial usage and resistance, and encouraging the development of rapid diagnostic techniques that can help reduce unnecessary prescription of antimicrobials.

With increasing and varying frequencies across the globe, antibiotic-resistant strains are commonly being isolated from patient infections: Sievert et al. (2013) found from USA data that 20% of all bacteria isolated from HAIs could be classified as multiple drug resistant (27); a study conducted in Bangladesh by Alam et al. (2021) found over 67% of wound infection isolates to be multiple drug resistant (50). Further, Bessa et al. (2015) studied the susceptibility of wound infection isolates to a series of drugs, finding that large proportions of the bacteria displayed resistance to many of these (26). The antibiotics that the isolated bacteria showed the

highest resistances to are summarised in Figure 1.8. Vancomycin was amongst a minority of drugs largely successful in combating gram-positive bacteria in the wound infections studied, however, *Enterococcus* spp. resistance to this drug in particular is of growing concern and is estimated to have a very high resistance rates of up to 74% in certain African regions for example (51). Overuse of antibiotics can have very serious consequences, and future methods for the treatment of many infections are uncertain. The ESKAPE pathogens, namely *Enterococcus faecium*, *Staphylococcus aureus*, *Klebsiella pneumoniae*, *Acinetobacter baumannii*, *Pseudomonas aeruginosa* and *Enterobacter* species, have been identified as important bacteria of particular concern due to their growing antibiotic resistance (52).

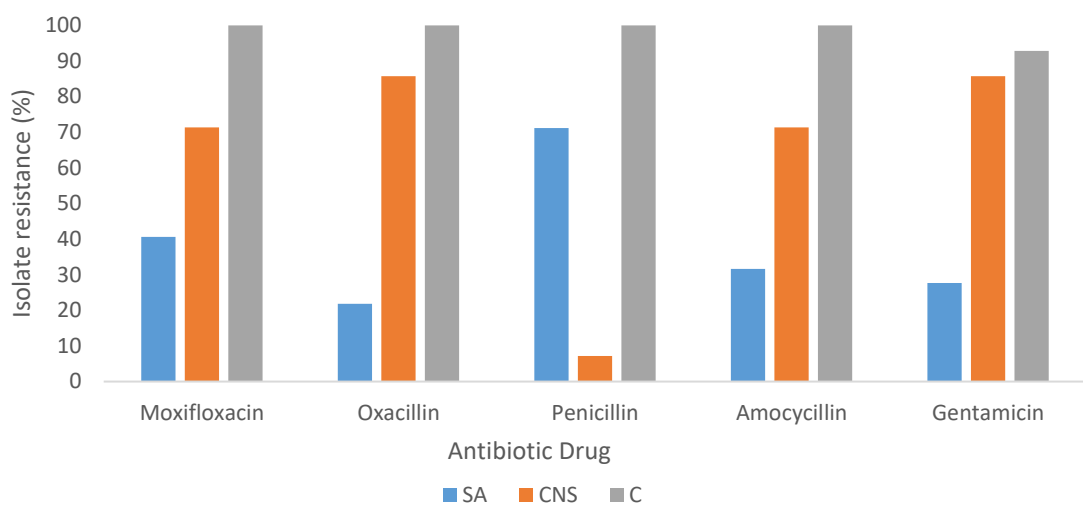


Figure 1.8. Resistance of gram-positive bacteria isolated from wound infections to selected antibiotics. Data summarised from Bessa et al. (2015) (26), with SA being *S. aureus*, CNS being coagulase negative staphylococci and C representing *Corynebacterium* spp..

Furthermore, it is apparent that both non-infected and infected wounds present varied microflora, with many species of bacteria originating from endogenous sources. In general, for mildly susceptible patients, greater than 50% of infectious diseases are caused by commensal or common environmental bacteria such as *Staphylococcus aureus*, *Staphylococcus epidermidis* and *Pseudomonas aeruginosa* (53). Opportunistic pathogens such as these are easily transferred in both healthcare and community environments by healthy individuals who are unaware of their presence. Wound management and the treatment of infection are, therefore, very complex disciplines that must continue to advance to achieve the best possible outcomes for patients.

1.4 Wound Management

Guest et al. (2020) estimated that around 7% of the UK's adult population received care from the NHS for a wound in 2017/2018, equating to an approximate annual cost of £8.3 billion (29). These values were significantly increased from the previous 2012/2013 estimates and highlighted the increasing burden of wounds upon limited NHS community resources in particular. Mirroring the complexity of wound healing, the management of both acute and chronic wounds can be complicated and there is no "one size fits all" approach. In an attempt to standardise the quality of wound care the "TIME" framework was created, providing healthcare practitioners with a systematic guide for the ongoing management and evaluation of wounds (54). As the financial burden associated with wound management is significant, treatment solutions aiming to both optimise patient outcomes and reduce their time spent in hospital or otherwise receiving care are, therefore, of vital importance.

1.4.1 The TIME Framework and Wound Management

Vital aspects of wound bed preparation were highlighted by Schultz et al. (2003) with an emphasis on the treatment of chronic wounds, where appropriate management guidelines were lacking (54). Crucially, a holistic assessment of the wound was encouraged and key clinical evaluation criteria were indicated. The acronym "TIME" was subsequently adopted, with each letter representing a key component of wound bed assessment: **T**issue, **I**nfection and inflammation, **M**oisture and **E**dge of wound (55). Whilst this concept has been widely adopted in clinical practice for many years, for the framework to remain relevant, many updates and revisions to the guidelines have been suggested (55–58).

Initiating a wound assessment, an examination of the local tissue must be made. The presence of non-viable (necrotic) tissue and debris for example is undesirable for effective healing and so debridement of the wound to remove these is recommended (54). Leaper et al. (2012) provide a summary of the different types of debridement available, such as: autolytic debridement, where necrotic tissue is removed by the individual's own enzymes and moisture; mechanical debridement, for example hydrotherapy; surgical debridement; enzymatic and chemical debridement. The benefits of frequent debridement and tissue cleaning have been noted (56).

An observation of infection or sustained inflammation is of similar clinical concern due to the healing impairment associated with each of these (54). Typically, infection is treated with the use of either topical or systemic antimicrobial agents (54). Antimicrobial agents applied topically can be used as part of the wound cleansing procedure, either as an ointment or impregnated into a dressing for example, to treat or help prevent infection. Despite the bactericidal effect of chemicals (such as silver and Manuka honey) on multiple pathogens, often they are not sufficient to eradicate an established infection and systemic antibiotics are instead required (46). Antibiotic efficacy is, however, limited due to their specificity to certain bacterial types and the rising microbial resistance to antibiotics (55). As discussed in Section 1.3, a key example of this is MRSA, a pathogen commonly isolated from SSIs (27,42). This species' ability to adapt to hostile environments and the overuse of antibiotics (β -lactam class) has led to its rising immunity to methicillin (59). Contributing to the multi-drug resistance of many species of bacteria is their propensity to form biofilms. These protect individual cells within a dense matrix from being affected by harmful agents; mechanisms to prevent the formation of these structures are of great interest. A concept central to this study, biofilms are described in detail within Section 2.2. Often drugs which are broadly effective against a range of pathogens (termed broad spectrum antibiotics) can be prescribed initially, with bacterial identification and susceptibility testing (introduced within Section 1.5) used to support more targeted antibiotic prescribing.

Further, the moisture balance of the wound must be assessed (54). It is now widely accepted that an appropriate level of moisture encourages healing, stemming from work by Winter (1962) that revealed a greatly increased epithelialisation rate for wounds healing in moist conditions when compared to those that were dry (60). Certain dressings may be applied to carefully control the moisture level, helping to prevent both desiccation (dryness) and maceration (harm due to too much moisture) in the wound (54). Of particular concern are premature neonates who, due to their underdeveloped epidermal layer, have heightened water loss through the skin (4,61). The volume of this trans-epidermal water loss is believed to increase with decreasing gestational age (61). Wound fluid (exudate) has a wide range of constituents including proteins (such as albumin), enzymes (such as matrix metalloproteinases) and blood products (62). Its content is varied, with particular differences between acute and chronic wounds for example: leukocytes and nutrients are abundant in acute wound exudate whereas chronic wound exudate contains more proteases and cytokines for example (55). Whilst exudate can be beneficial to healing, the high protease content of chronic wound exudate for example is believed to be harmful to the wound tissue (63). A careful moisture balance must, therefore, be struck.

The final element of TIME encourages an evaluation of the edge of the wound. A reduction in the dimensions of the lesion would indicate appropriate advancement through the healing process; poor condition of the skin at the edge of the wound may suggest a delay in its contraction and, therefore, healing (55).

By applying each of these components of the TIME acronym to the care of wounds, a comprehensive overview of the wound status is sought. This evaluation aims to enable the most appropriate treatment for each patient to be identified, improving patient outcomes. The most recently proposed update to this framework highlights the additional importance of considering the broader health of the patient during wound management (58). This new TIME CDST (TIME Clinical Decision Support Tool) proposed by Moore and Dowsett (2019) proposes additional, wider patient evaluation steps to optimise treatment delivery and outcomes. These include involving the patient’s multidisciplinary care team and treating the underlying causes of the wound. Ultimately, through periodic updates to the TIME framework as its limitations emerge, this framework has remained a key clinical wound management tool.

1.4.2 Wound Care Products

The wide range of products available on the market for wound care reflects the variety of wounds requiring management. Many of these products support adherence to the previously discussed TIME framework, ultimately protecting the wound and promoting healing (Table 1.4).

Table 1.4. A selection of wound care products linked to the TIME framework.

TIME Component	Possible Action	Examples of Supporting Products	References
Tissue	Debridement	Hydrocolloid or hydrogel dressings (autolytic debridement).	(55,64)
		Antiseptics (chemical debridement).	
Infection	Prevention of infection	Antiseptic agents such as potassium permanganate, acetic acid and iodine.	(56)
		Dressings incorporating medical grade honey or silver.	
Moisture	Moisture control	Dressings such as hydrogel, foam, hydrocolloid, hydrofiber and alginate.	(4,55,65)
Edge of wound	Laser therapy Ultrasound therapy	Specialist equipment required.	(55)

The use of traditional wet-to-dry gauze in the UK has decreased as it is believed, for example, to cause unwanted mechanical debridement of healthy tissue, excessive drying of the wound and be painful to remove (4,64). Currently more advanced dressings are often employed that optimise conditions to encourage healing, such as: retaining moisture, providing occlusion, allowing gas exchange, preserving temperature (64,66). In particular, these products can support re-epithelialisation, angiogenesis (due to a reduction in the level of oxygen accessing the wound bed) and the formation of key proteins such as collagen (67).

Hydrocolloid dressings are one of the most commonly applied; they are comprised of two layers and contain gel forming agents, elastomers and adhesives for instance (66). As semi-permeable dressings, they are permeable only to water vapour and protect the wound from pathogens (67). Due to their absorption and retention of wound exudate, they are not recommended for use on very moist wounds. They are, therefore, more suited to injuries such as minor burns and pressure sores, maintaining the appropriate moisture for the healing of these relatively dry lesions (66). These dressings may be worn over long time periods, however chronic ulcers that need frequent assessment would not benefit from this. A drawback to their use, the colour and odour when using these dressings can mimic the signs of infection (64).

Conversely, foam dressings are appropriate for use on wounds that have high levels of exudate (67). They can be extremely absorbent, allow gas exchange, and are suitable for use with leg ulcers for example. Foam products, however, cannot be worn for extended time periods (66). The Mepilex® foam dressing range by Molnlycke® (Gothenburg, Sweden) is amongst numerous foam dressings available on the market. This range highlights that a variety of properties can be achieved in this dressing type, with each individual dressing tailored for use with different types of wounds and different levels of exudate (<https://www.molnlycke.co.uk/products-solutions/mepilex/>). Many other wound dressing materials present a similar variety of properties; King et al. (2014) provide a visual summary of this which has been adapted to create Figure 1.9 (4). Notably, different dressing types have particular ranges of wound depths and exudate levels most suitable for their application.

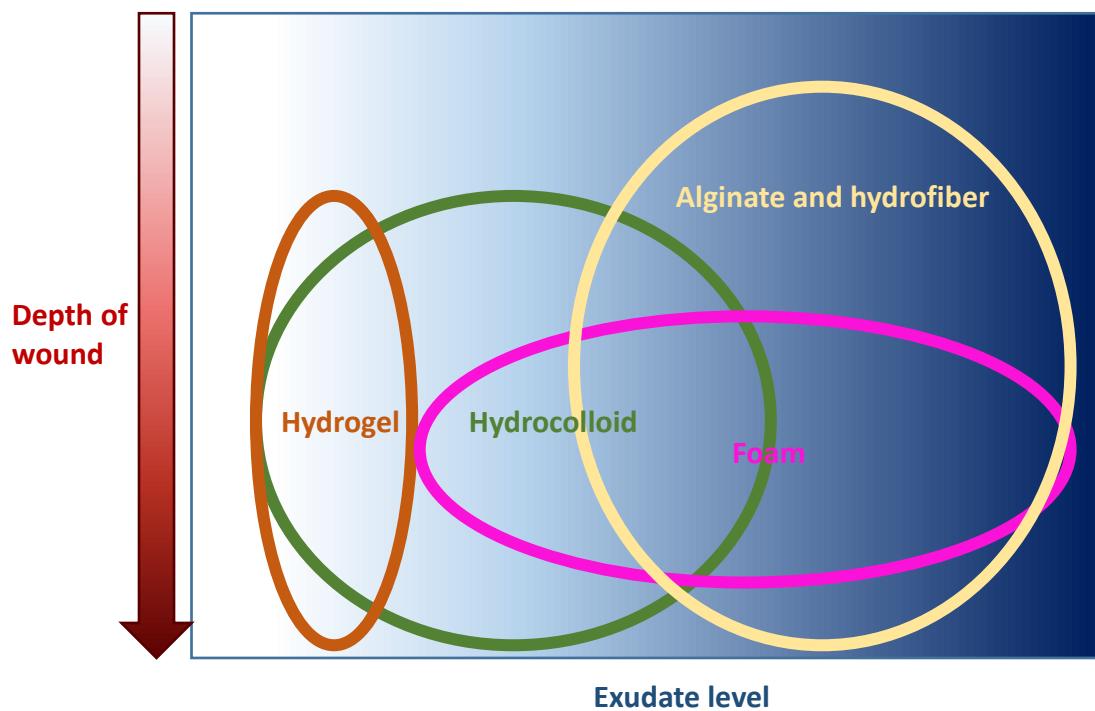


Figure 1.9. Summary of common wound dressing properties. Figure is adapted from King et al. (2014), with an increasing exudate level moving from left to right and an increasing depth of the wound moving from top to bottom (4).

Dressings specifically developed for the control of infection are also widely used. Incorporating chemical agents to counter bacterial growth, these are most commonly impregnated with silver, iodine, medical grade honey and polyhexamethylene biguanide (PHMB) (57). Although often associated with burn care, the ACTICOAT range for example (Smith & Nephew, London, UK) has incorporated silver nanotechnology to tackle infection in a range of wound types (including acute, chronic, burn and surgical wounds) (4). Silver ions are released from dressings in the presence of aqueous wound exudate; silver nitrate and silver sulfadiazine are amongst compounds frequently used for this purpose (57,68). Vital metabolic pathways are destroyed by the interaction of these ions with pathogen membranes, ultimately leading to bacterial cell death and infection prevention (68). The interaction of silver ions with bacteria is a concept of importance to this thesis, revisited on multiple occasions throughout Chapters 4-7. Dressings containing medical-grade honey similarly reduce wound bioburden (55,57). Pathogen growth is inhibited by: honey's sugar content, the presence of hydrogen peroxide (due to the enzyme glucose oxidase), and its acidic nature (69). In a study focused on burn wounds, Lindberg et al. (2015) found honey to be more beneficial than silver, finding it to reduce bacterial levels without the toxic effect on local tissue than can occur with silver (70). Conversely, Dumville et al. (2016) suggest that neither dressing, nor any other dressing type,

has stark evidence to support its use to reduce infection in surgical incisions (71). Evidence surrounding the use of these dressings, therefore, appears to be mixed. In general, antiseptic dressings are typically only recommended for use over a two-week period, after which their appropriateness use must be re-evaluated (55).

Whilst combinations of materials and agents for the cleansing or protection of a wound encompass the majority of wound care products, active devices for wound care have also been developed. One example of this is negative pressure wound therapy (NPWT), where a vacuum is created within a sealed dressing (commonly foam or gauze) using a pump, creating a closed, moist environment supportive of wound healing. This technique supports wound closure for a range of complex wounds, including chronic foot ulcers (72). A further key example are devices which supply an electric field directly to the wound to promote closure. These devices exploit the knowledge that wound healing events such as cell migration are enhanced by natural electrical stimulation by the body (73). It is hoped that, particularly in chronic wounds, an externally applied current could replicate and assist this natural process. A number of clinical trials to investigate this technology have been conducted, with electrical stimulation frequently found to be beneficial to both the success rate of, and time taken for, wound healing (74). A variety of approaches exist, for example many different direct current and pulsed current applications (73,74). A continuous direct current device, POSIFECT™ by BioFisica™, Hampshire, UK was reported to have positive results in the treatment of pressure ulcers; similarly, WoundEL®'s pulsed current approach was effective in leg ulcers (75,76). These devices used stimulating currents in the μA region (73). Furthermore, an increasingly broad and complex range of wound care products are available to support healing.

1.5 Detection Approaches for Wound Infection

Within this chapter so far, infection has been highlighted as a critical cause of delayed healing with potentially very serious consequences. It must, therefore, be detected and eradicated in a timely manner. The presence of clinical symptoms of infection often provokes further testing to confirm the diagnosis and suggest an appropriate, targeted treatment route via bacterial identification. Traditional gold-standard methods of bacterial detection are, however, time consuming. Many methods for the rapid identification of microorganisms have emerged, including technologies under development for *in situ* wound infection detection. The detection methods discussed in this section are summarised in Figure 1.10.

Gold Standard Techniques	Rapid Testing Technology	In situ Detection
<ul style="list-style-type: none"> • Observation of patient symptoms • Wound sampling, specimen culturing and testing 	<ul style="list-style-type: none"> • Process automation • Molecular microbiology (including real-time PCR, isothermal amplification) • Immunochemistry (including ELISA, LFI) • MALDI-TOF mass spectrometry 	<ul style="list-style-type: none"> • Artificial olfaction sensors • pH change detection • Other biochemical infection marker detection (often involving electrochemical techniques) • Impedance spectroscopy

Figure 1.10. Summary of the infection detection methods introduced within Section 1.5.

1.5.1 Signs of Wound Infection

There are a number of core symptoms which raise concern that a wound has developed an infection (Figure 1.11) (46,65). Whilst these signs may be overt in some patients, for individuals with comorbidities, the immunocompromised or the neonatal population, symptoms may be expressed more subtly or be delayed (55). Furthermore, the ability of classic signs such as pain, heat and swelling to predict infection in chronic wounds has been questioned (77). In addition to the key signs of infection noted within Figure 1.11, there are further clinical signs that bacterial biofilm formation has occurred within a wound. Indicators include ineffective antibiotics, the presence of an infection for over one month, and a viscous film of material on the surface of the wound that regenerates rapidly (78).

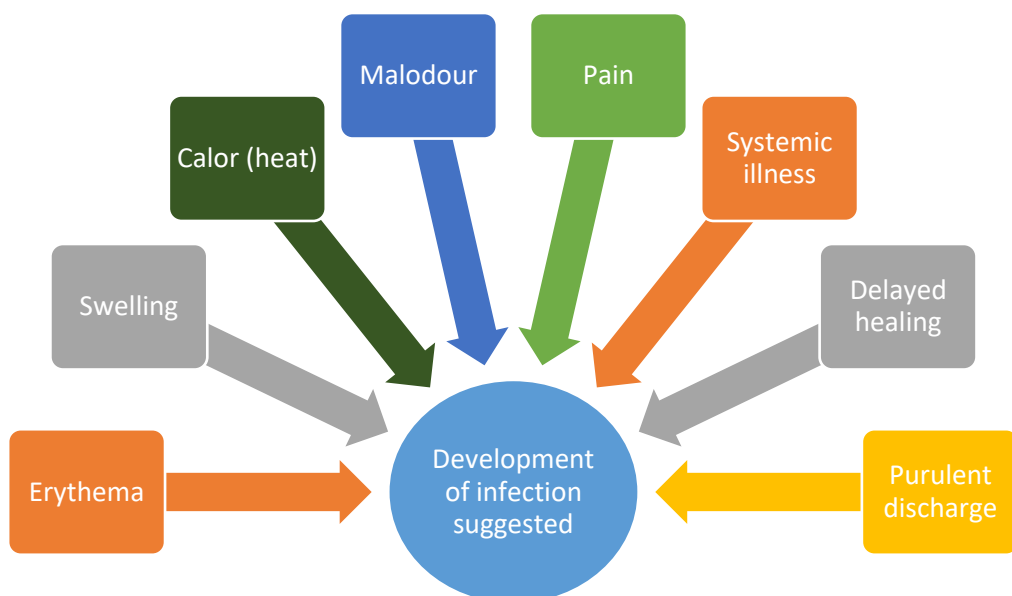


Figure 1.11. A selection of key wound infection symptoms.

1.5.2 Current Detection of Infection in Clinical Practice

Following observation of a number of the previously mentioned symptoms, to confirm the presence of infection, deduce which pathogens are responsible and determine an appropriate course of treatment, it is likely that the wound will be sampled and microbiological tests carried out. Due to limited hospital resources, it is not practical to swab all wounds. Furthermore, it is believed that limited insight can be gained from sampling a wound which is not clearly infected. It is, therefore, widely recommended that wound samples be collected only if a symptomatic diagnosis has been confirmed and that they be collected before antibiotic treatment commences (79). Whilst swabbing is an inexpensive, simple and common sampling technique, the preferred sampling method varies depending on the type and condition of a wound. Biopsy and needle aspiration of exudate for example are key alternative techniques for wound sampling (46). In Table 1.5 a number of advantages and disadvantages of each of these sampling techniques are noted (46,79,80). Further, the Levine swabbing technique (where a swab is rotated over a small area of the wound to extract fluid) was found to better sample the wound than the so-called “Z-swab” technique in a systematic review by Copeland-Halperin et al. (2016) (80). Their study further concluded that for initial tests swabbing was beneficial, however, for an assessment of antibiotic resistance and the effect of treatment biopsies were superior.

Table 1.5. Wound sampling techniques.

Method	Advantages	Disadvantages
Swabbing	Inexpensive, simple, non-invasive	May only reflect superficial microflora and not bacteria at greater depth
Biopsy	Allows for quantitative, sensitive, specific and accurate testing, valid even when debridement has been carried out	Invasive, complex, expensive, may deteriorate wound condition
Needle aspiration of exudate	Recommended method for sampling edge of ulcers	Confined fraction of wound sampled, may spread infection

Current gold standard clinical testing of wound infection involves the microbiological culture of these wound samples to identify the microorganisms present. This is a laborious, resource intense process, taking a minimum of 2-3 days and often longer if more detailed testing is required (81). For wound swabs, guidelines state that the specimen should first be rolled onto appropriate culture media, blood agar for example, and cultured at 35-37 °C for 40-48 hours (79). Guidelines additionally recommended that swabs be rolled onto anaerobe selective agar containing a 5 µg disc of metronidazole and incubated for 5 days in order to test for the presence

of anaerobic pathogens and their susceptibility to this drug (79). Other selective culture media and a variety of characterisation tests can then be utilised and, at each stage, microscopy is carried out to assess the morphology of cells and support identification (82). Gram-negative bacteria are known to be responsible for many serious infections, as are the Gram-positive streptococci and clostridia for example: a Gram stain test is often performed at an early stage to immediately exclude certain pathogens from further testing (79,83). Similarly, metabolic tests such as the coagulase test can be carried out to identify, for example, coagulase negative staphylococci (79). The susceptibility of bacteria to a range of other antimicrobial substances is also tested; bacterial response to specific antibiotics must be formally reported, for example *S. aureus* to flucloxacillin- a penicillin class drug which cannot act against MRSA (79). Ultimately, it is time consuming to obtain even a basic microbiological test result due to the nature of the culturing process.

1.5.3 Rapid Techniques in Clinical Microbiology

Whilst largely effective, these microbiological culture procedures are far from ideal. They do not produce rapid results for the clinician to act upon and a bias in results is evident: fastidious organisms are likely to be inadequately represented in cultures which are disproportionately dominated by other organisms (46). In a bid to reduce the time taken to obtain results and supplement culture results, NICE accredited NHS guidelines support the performance of more rapid testing methods that have been approved and validated (such as molecular techniques and matrix-assisted laser desorption ionisation time-of-flight mass spectrometry (MALDI-TOF MS), techniques detailed within this section) in addition to carrying out those described in Section 1.5.2 (79). To be able to conduct these methods, however, bacteria must still be cultured and isolated, a process that itself requires several hours and skilled laboratory staff (84).

Automation is a vital component of the drive to develop new techniques for timely and accurate identification of pathogens from patient samples. Increasing the efficiency of existing processes where possible can boost turn-around times (85). The BD Phoenix™ system (Franklin Lakes, NJ, USA) for example has automated the existing culturing processes of both bacterial identification and susceptibility testing, aiming to improve productivity and reduce the level of human error present in results. These culturing processes are, however, still limited by the lengthy incubation times required for sufficient bacterial growth. There have, therefore, emerged many new technologies for more rapid and accurate microbiological detection and analysis.

Molecular microbiology covers an array of different techniques for the analysis of microorganisms in a clinical laboratory, with a focus upon metabolites, DNA and proteins. Those involving nucleic acids such as the polymerase chain reaction (PCR), where very small quantities of specific DNA fragments are amplified using reagents and repeated heating and cooling cycles to enable subsequent detection and study, are one such example (81,86). Advancements enabling PCR to be carried out in real-time have emerged; this technology has been cited as fast, sensitive and simple to operate (86). A key example of real-time PCR use in clinical microbiology is for the detection of the COVID-19 virus (SARS-CoV-2) in throat/nasal swabs of potentially exposed individuals. This particular COVID-19 test is currently placed as the gold standard due to its high reliability, however this test does require laboratory processing and specific resources, impacting its turn-around-time and restricting its use to well-resourced healthcare settings (87). Commercial PCR systems include Thermo Fisher Scientific's TaqMan® Assays (Waltham, MA, USA), which evade the use of post-processing such as gel electrophoresis by using sophisticated fluorescent labelling during thermal cycling. As a result, it is possible to detect PCR amplification at a far earlier stage of the process and thus identify bacteria based on the quantification of DNA or RNA more rapidly. The GeneXpert® systems by Cepheid (Sunnyvale, CA, USA) can detect a variety of analytes by performing real-time PCR on target-specific cartridges; MRSA and *S. aureus* from skin infection samples for instance may be detected in under 60 minutes. Recent efforts to develop a more portable real-time PCR device has resulted in a large reduction in size for this instrument: Ahrberg et al. (2016) for example have developed a hand-held system that, after initial isolation and processing, can analyse two samples of interest in just over half an hour (88).

An alternative molecular technique, isothermal amplification (such as loop-mediated isothermal amplification), remains at one temperature instead of thermal cycling and can be adopted in simpler devices than basic PCR (81,89). Often isothermal amplification methods rely on the use of multiple enzymes (81). As the cost of next generation sequencing reduces, this technique is becoming more widely accessible (90). For example, microbiome studies, where the 16S rRNA (ribosomal-ribonucleic acid) gene is amplified and sequenced within a complex culture results in the ability to differentiate between species (91). Currently in clinical laboratories 16S rRNA PCR testing can successfully support the identification of bacteria which have failed to grow during culturing. This laboratory technique is, however, expensive to carry out: each positive result is estimated to cost over £550 and testing is commonly not able to be carried out on-site (92). Work is currently being done to develop a rapid, point of

care electrochemical device which detects DNA or RNA without the use of labels or amplification (93,94).

A further category of bacterial infection detection devices in the clinical laboratory is based upon immunochemistry (81). Antibodies produced by the body as a result of specific bacteria and their infections can be immobilised. This allows devices to be developed which detect bacteria via detection of the corresponding antigens on the surface of bacterial cells in a given sample. Most frequently, tests involve either enzyme-linked immunosorbent assays (ELISA) or lateral flow immunochromatography (LFI) to identify antigens associated with the pathogen (81,95). ELISA is often associated with the detection of foodborne bacteria, for example *Salmonella* spp. can be detected by a commercially available test from BIOLINE (96). The commonly adopted “sandwich” ELISA process first involves a primary antibody, to which the bacterial antigen binds. A second, enzyme-linked antibody then binds to this antigen (forming the characteristic “sandwich” formation). Subsequently, this enzyme interacts with an added chemical, resulting in a detectable change (such as colour). The various binding and washing steps involved may be carried out by automated devices such as the specialised DSX® and DS2® workstations by DYNEX Technologies (Chantilly, VA, USA) to increase productivity, however, they are still heavily dependent on a number of reagents, consumables and trained staff.

LFI testing is considered a simpler, cheaper alternative to ELISA which uses the lateral flow of a liquid sample through a test strip containing a number of membranes (with antibodies) to detect the presence of an analyte typically in under half an hour (96,97). Niu et al. (2014) for example used an immunochromatographic test strip incorporating gold nanoparticle labels to rapidly detect *S. aureus* in concentrations as low as 10^3 CFU/ml (98). The commercially available NADAL® test cassettes (nal von minden, Moers, Germany) exploit this technology to detect specific species of bacteria in urine or faeces for instance. Whilst portable, the technology does not yet allow for analysis of complex samples due to its specificity to single biomarkers (99). Lateral flow tests present a lower cost rapid alternative to PCR and have been widely deployed for community testing during the COVID-19 pandemic. Such tests are not, however, as accurate as PCR tests (100).

A further technology widely used in clinical laboratories to assist in the identification of bacteria is MALDI-TOF MS (84). Derived from traditional mass spectrometry, this technique allows microorganisms to be identified by first laser-ionising a sample covered by an organic acid (matrix) to produce a variety of charged particles. These are accelerated at different rates, depending on their charge and mass, through an electric field. Their subsequent time taken to

traverse a vacuum and be detected reveals these properties and enables a characteristic spectrum for each pathogen to be obtained. Whilst this process is rapid and has a high identification and differentiation power, there are several limitations associated with it. For example, the pathogen under investigation must first be freshly isolated using time consuming culturing, and the device is expensive to purchase (84).

In summary, a number of technologies support the fast detection of bacteria, however, the gold standard culturing techniques still prevail in clinical microbiology (79). Many drawbacks to these technologies still exist, in particular associated with cost and the time that must be spent processing samples before testing. Furthermore, the initial sampling and culturing process is responsible for much of the delay in obtaining results. A clear need for cheaper, simpler techniques that have the potential to be used *in situ*, evading sampling and unwanted disturbances of the wound has arisen.

1.5.4 Biomarkers and Biosensors Supporting *in situ* Detection of Wound Infection

There are a variety of biomarkers that have the potential to indicate wound infection development. Exploiting these to develop *in situ* wound infection monitors is an established area of research. Many of the key biomarkers under investigation are displayed in Figure 1.12 (65).

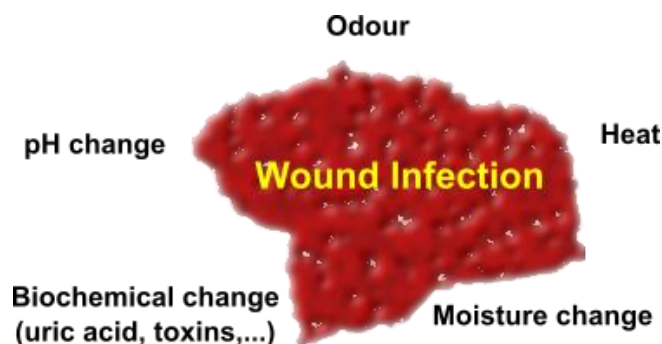


Figure 1.12. Potential biomarkers of wound infection for biosensor exploitation.

Artificial olfaction sensors, or electronic noses, aim to detect infection via changes in odour; as highlighted in Section 1.5.1, malodour is a clinical sign of an established wound infection. Often bacteria produce metabolites with distinctive odours (such as ammonia) that can allow the species to be identified (65). The airborne, volatile chemicals made by bacteria can be detected using an array of gas sensors which, combined, allow for differentiation between signals. Metal oxides and conducting polymers are key materials adopted for use in these detectors (101). An early, functional system is the AromaScan device (Osmetech plc, London,

UK) which was developed following successful detection of β -haemolytic *Streptococci* in venous leg ulcers utilising a conducting polymer array (101,102). Later, Boilot et al. (2002) were able to successfully detect a number of bacteria (including *S. aureus*, *E. coli* and *P. aeruginosa*) using the Cyranose 320 (Cyranose Sciences Inc., Pasadena, CA, USA) system which similarly relied on conducting polymers (103). The device did not, however, enumerate the bacterial samples. More recent developments include work by Sun et al. (2017) who created an electronic nose comprised of 30 gas sensors, each able to detect a variety of different common bacterial products, in a Teflon chamber (104). Different optimisation techniques were tested, resulting in pathogen identification rates of over 96% using complex computational analysis.

Several biosensors capable of detecting changes in wound pH have been reported, claiming to indicate the development of infection. In healthy subjects, the surface of the skin has the slightly acidic pH of 4.2-5.6; in local burn wound infection for example, this has been found to rise with the onset of infection (105). Sharp (2013) for example used uric acid as a pH-sensitive probe, pad-printing electrodes to contain a combination of uric acid and carbon (106). Using voltammetry, this device was able to successfully identify the pH of simulated wound fluid between pH 4-10. Tamayol et al. (2016) instead made use of hydrogel fibres to monitor wound pH (107). Dyes were integrated into these fibres to allow a visual and ultimately quantitative (through the use of image processing) map of pH to be created. Farooqui and Sharmin (2016) similarly developed a flexible, continuous pH monitoring device (11). Their device, inkjet-printed onto a bandage, could not only monitor changes in pH (using a resistive sensor), but also monitor irregular bleeding and physical pressure (with a capacitive sensor). A further prototype technology has been created by Chen et al. (2017) which is believed to have the capability of both detecting and reducing the development of wound infection, via pH and reactive oxygen species interactions coupled with Ciprofloxacin release (108). Whilst these devices all appear promising for the detection of wound infection, an ability to identify the responsible pathogen is lacking.

A variety of biochemical changes occur within a wound as an infection progresses; many of these markers have been extensively studied for their potential to be incorporated into continuous infection monitoring technology. Measurements of uric acid concentration in wound exudate is a key example of this: the concentration of uric acid is known to decrease due to the presence of bacterial infection (109). Kassal et al. (2015) describe the development of a sensor which uses adapted screen-printed carbon working electrodes containing urate oxidase enzymes for this purpose (110). Amperometric measurements indicating changes in

uric acid concentration could subsequently be wirelessly transmitted to mobile devices. Liu and Lillehoj (2017) were likewise able to detect uric acid with their amperometric sensor, which consisted of gauze knitted with carbon and silver/silver chloride coated thread (111). In a similar manner, the monitoring of myeloperoxidase activity in wound exudate has been studied also (112,113). Further, pyocyanin, a metabolite secreted during *P. aeruginosa* growth, can be used to identify proliferation of this pathogen via voltammetry for example (114,115).

Finally, changes in temperature and wound exudate levels can also be indicative of infection. Mehmood et al. (2015) developed a system which can measure both of these parameters to resolutions of 3.0% room humidity and 0.2 °C respectively using existing commercially available temperature and moisture sensors (116). Further, WoundSense (Ohmedics Ltd, Glasgow, UK) is a commercially available device which uses impedance measurements to assess the moisture level within a wound. It has been used to indicate that in current wound management practice many dressings are changed prematurely (117). By reducing the number of dressing changes occurring (in addition to detecting a known biomarker of infection) minimal disturbance of the site is caused and the risk of the wound being exposed to harmful pathogens is not unnecessarily increased. The application of the WoundSense electrodes to bacterial sensing is investigated within Chapter 4.

1.6 Detecting Bacteria using Impedance Spectroscopy

An alternative approach to bacterial detection, electrochemical impedance spectroscopy (EIS) has been used in several studies for the detection of microorganisms (118,119,128–131,120–127) and could, therefore, be a viable technique for use in an infection monitoring device. EIS is an analytical technique where resistance and reactance measurements of an electrochemical cell are collected over a range of AC frequencies to obtain a spectrum. The theory underpinning EIS is presented in Chapter 2, providing an understanding of the fundamental underlying principles. It has a variety of industrial applications, a prominent example of which is the characterisation of fuel cells. For example, EIS can be used to assess the performance of proton exchange membrane fuel cells (132,133), silicon solar cells (134) and lithium-ion batteries (135).

Further to this, the biological applications of EIS are wide ranging. Early uses include measurements of the resistance and capacitance of blood by Fricke and Morse (1925), and studies of muscle contractions by Dubuisson (1937) (136,137). Biological tissue characterisation using impedance has been the focus of many studies, aiming for example to

differentiate between different organs or between healthy and cancerous tissues (138–140). This work has led to the development of electrical impedance tomography (EIT), a novel medical imaging technique (141).

Of great importance to this study, the use of EIS to detect and monitor the growth of microorganisms will be discussed in depth within this section. Many recent bacterial detection experiments have evolved from work originally conducted in the 1970's (142,143), with commercial devices such as the Bactometer® being the culmination of these early studies (144). Importantly, the transient small amplitude signals applied during EIS measurements do not appreciably interfere with the bacteria (145).

1.6.1 Biological Tissues- An Electrical Perspective

When an electrical potential is applied to a biological tissue, the resulting ionic motion within the tissue produces a current which is dependent upon its conductivity (138). This electrical response is also time dependant, with features such as cell membranes and protein molecules causing dielectric behaviours. Electrical and dielectric properties vary both within a particular tissue and between distinct types of tissue; differences in conductivity and relative permittivity (concepts introduced in Chapter 2) can reveal valuable information about the material's attributes, with applications in cardiology for example.

Relaxation processes result in biological materials possessing a distribution of relative permittivities, varying with potential frequency (146). Three key dispersion regions exist within a plot of dielectric constant against frequency (Figure 1.13). The lowest frequency phenomenon, α -dispersion, has been linked to dipolar interactions at the membrane surfaces for example (138,139). In the mid-frequency range lies the β -dispersion. The focus of many early studies, this is associated with the structure of cell membranes: lipid membranes show capacitive charging (146). Finally, γ -dispersion exists at very high frequencies due to the polarisation of water molecules (138,146).

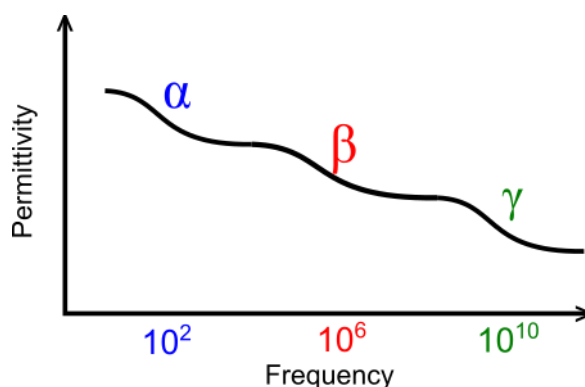


Figure 1.13. Dielectric spectra of biological tissue containing the α -, β -, and γ -dispersion regions. Image adapted from Schwan (1957) (146).

In addition to biological tissues, these dispersion regions have been further applied to the investigation of bacteria, with the β -dispersion region exploited in particular. For example, early β -dispersion measurements identified that *E. coli* cells possess membranes of low electrical conductivity (147). β -dispersion measurements have similarly been applied to bacterial biomass estimation, where the fall in capacitance experienced during the dispersion as frequency rises is used to calculate concentration (148). Similarities can be drawn between capacitors and bacterial cells: in general, at low frequencies cell membranes limit the current flow through cells due to the accumulation of ions both inside and outside the barrier, whereas at high frequencies the membrane displays a far lower impedance (149). Furthermore, the electric and dielectric properties of bacterial suspensions and, therefore, impedance are dependent upon frequency.

1.6.2 The Impact of Bacteria Upon Electrochemical Impedance

It has been hypothesised that there are numerous mechanisms by which bacteria can alter the impedance of an electrochemical system. Much of the literature focused on these changes has been aimed at developing more advanced technology for microbial fuel cells, where living organisms are harnessed as biocatalysts to generate electrical energy. The transfer of electrons from anode to cathode by bacteria is fundamental for their operation and, thus, the pathways via which this occurs are of critical importance. These same mechanisms are of equal importance when considering the changes caused by bacteria to impedance spectra in EIS and will, therefore, now be highlighted. In the context of microbial fuel cells, the processes have been broadly classified into two categories: direct electron transfer and mediated electron transfer (150). Whereas direct electron transfers result from direct contact between the bacterial cell and the electrode, mediated electron transfer is facilitated by bacterial metabolites

produced during growth (151). Furthermore, these categories are comprised of multiple mechanisms of charge transfer. For example, direct electron transfer may be a result of cell membrane contact with the surface of the electrode or due to contact of a membrane appendage with the electrode. In the context of bacterial impedance spectroscopy itself, Ward et al. (2014) highlighted 6 mechanisms via which bacteria can impact impedance (Figure 1.14) (118).

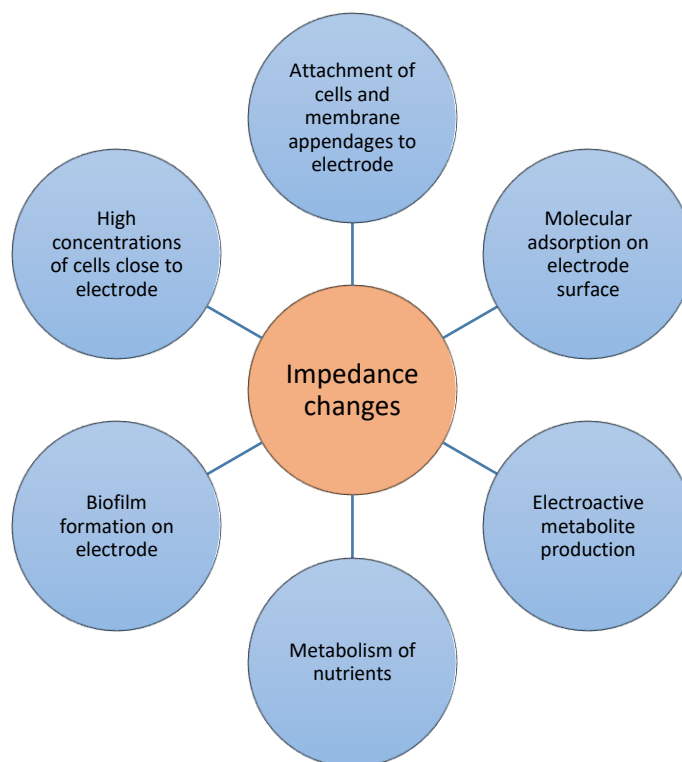


Figure 1. 14. Potential mechanisms via which bacteria alter electrochemical impedance.

As will be presented in Section 1.6.3, the attachment of bacteria to the surface of the electrode is perhaps one of the mechanisms most frequently attributed to changes in electrochemical impedance. Upon physical contact with the electrode surface, electrons within bacterial cells that have been created by metabolic redox reactions can be transferred to the electrode via integral membrane proteins (such as cytochromes) (151). Consequently, the flow of charge and, thus, the impedance is altered. This particular process can, however, only apply to the contacting monolayer of bacteria. *Shewanella oneidensis* and *Geobacter sulfurreducens* are among species capable of this; whilst these particular species have been extensively studied it is believed that many other species can similarly be classified as electroactive (152,153). Further, some species of bacteria possess electrically conducting pili or “nanowires” which

facilitate longer range electron transfer due to contact between the reaching nanowire and electrode surface (151,153). There are a variety of microorganism and electrode surface properties that effect the likelihood of adhesion such as electrode wettability, potential and charge (154). The bacterial adhesion is initially influenced by physical forces (such as electrostatics and van der Waals forces) and later by cellular attachment mechanisms (such as pili and binding proteins); adhesion is highly dependent upon the bacterial species (155). These direct contact processes, in addition to the consequences of electrode surface coverage by cells and biofilm matrix, have been widely investigated using impedance spectroscopy.

Bacteria metabolise several medium components during growth, altering the ionic content and, therefore, electrochemistry of the solution. Typically, high electrical conductivity molecules are produced from the metabolism of larger, lower conductivity molecules such as carbohydrates (143,150). In addition to the breakdown of nutrients, the production of new metabolites (and subsequent oxidation and reduction of these and reaction intermediaries) drives further conductivity changes (151). It has been found that the adsorption of macromolecules (such as those produced by bacteria during growth) to surfaces is most often irreversible, preventing bacterial attachment and permanently altering electron transport at the electrode/electrolyte interface (156). *Shewanella* for example has been found to produce riboflavin during growth, acting to increase electron transfer as both a media component and through adsorption to the electrode surface (157).

1.6.3 Impedance Experiments for the Detection of Bacteria

Within this section, key research investigating the way bacteria alter electrochemical impedance will be presented, giving insight into the current level of knowledge within this area. These studies are listed within Table 1.6. Most relevant to this project, only measurement systems where label-free electrodes have been used will be discussed. Whilst labelled electrodes such as those containing enzymes can benefit the sensitivity of measurements, there are a number of drawbacks to their use such as increased costs, increased preparation times and narrow range of use (158). This section will, therefore, focus upon reviewing label-free, biorecognition element-free impedance approaches which have the potential to enable real-time whole bacterial cell detection. As can be seen in Table 1.6, many of these studies employed the use of microelectrodes. Of a size smaller than (or equivalent to) the diffusion layer thickness (Chapter 2), these electrodes often show superior properties including higher mass transport and greater sensitivity (159). Microelectrodes are, however, subject to far

greater electrical interference, can be more complex to fabricate and less reproducible, and can be more greatly impacted by biofouling (160,161). For reasons such as these, many studies instead adopt macroelectrodes. Further, a wide range of different electrode materials were used in these studies. Each material possesses different characteristics, including: electrical conductivity; availability and cost; surface stabilities. Each electrode material used in this thesis will, therefore, be given an appropriate rationale within the relevant results Chapter (Chapters 4-6).

Table 1.6. Key label free bacterial impedance spectroscopy studies.

Study	Bacteria Detected	Electrode Type
Bayouth et al. (2008) (119)	<i>Pseudomonas stutzeri</i> , <i>Staphylococcus epidermidis</i>	Indium tin oxide plate
Bonetto et al. (2014) (128)	<i>Bacillus subtilis</i> , <i>Shewanella oneidensis</i>	Embedded gold micro-interdigitated electrodes
Cady et al. (1978) (142)	Microorganisms in urine samples	Gold plated, stainless steel
Farrow et al. (2012) (129)	<i>Staphylococcus aureus</i>	Silver- silver chloride on flexible polyethylene substrate
Goikoetxea et al. (2018) (162)	<i>Escherichia coli</i>	Titanium nitride microelectrode array
Kim et al. (2011) (123)	<i>Pseudomonas aeruginosa</i>	Platinum disk electrode
Muñoz-Berbel et al. (2006) (163)	<i>Pseudomonas aeruginosa</i>	Gold chip working electrode
Muñoz-Berbel et al. (2007) (120)	<i>Escherichia coli</i>	Platinum disk electrode (sputter coated on silicon nitride substrate)
Paredes et al. (2012) (125)	<i>Staphylococcus epidermidis</i>	Gold sputtered interdigitated microelectrode
Paredes et al. (2014) (126)	<i>Staphylococcus epidermidis</i>	Gold sputtered interdigitated microelectrode
Pires et al. (2013) (127)	<i>Pseudomonas aeruginosa</i>	Gold electrodes on cyclic olefin copolymer substrate
Settu et al. (2015) (121)	<i>Escherichia coli</i>	Interdigitated gold sputtered microelectrode
Ur and Brown 1975 (143)	<i>Escherichia coli</i> , <i>Klebsiella areogenes</i> , <i>Pseudomonas aeruginosa</i> , <i>Staphylococcus aureus</i> , <i>Streptococcus faecalis</i>	Glass capillary with gold plated electrodes

Van Duuren et al. (2017) (164)	<i>Pseudomonas aeruginosa</i>	xCELLigence RTCA SP instrument
Ward et al. (2014) (118)	<i>Pseudomonas aeruginosa</i> , <i>Staphylococcus aureus</i>	Screen printed carbon
Yang et al. (2004) (124)	<i>Salmonella typhimurium</i>	Indium tin oxide sputtered interdigitated microelectrodes
Zhu et al. (2010) (122)	<i>Porphyromonas gingivalis</i> , <i>Escherichia coli</i>	Fluidic electrodes with hydrodynamic focusing, KCl solution and Ag-AgCl wires
Zikmund et al. (2010) (131)	<i>Escherichia coli</i>	Tesla KB-12 sensor

A wide variety of different electrode and experimental configurations have been used to detect the attachment of bacteria to electrodes via EIS. Bayouhdh et al. (2008) attributed impedance magnitude reductions at low frequencies to the adhesion of bacteria to an indium tin oxide coated surface (119). Their flow chamber assembly was designed to control the hydrodynamic conditions within their experiment; consequently, they were able to assess the adherence of cells to the surface and remove any non-attached cells. By investigating both *Pseudomonas stutzeri* and *Staphylococcus epidermidis*, it was found that *P. stutzeri* had a faster rate of adhesion and enabled more charge transfer. Studies exploring the attachment of *E. coli* to an electrode surface have also been conducted. For example, Settu et al. (2015) used a gold-sputtered microelectrode to detect very low concentrations of this bacteria in urine samples (via low frequency impedance changes induced by surface attachment) (121). Further, Goikoetxea et al. (2018) attributed an increase in measured resistance to *E. coli* surface attachment (162). Muñoz-Berbel et al. (2007) found that their system could detect both the attachment of *E. coli* to sputter-coated platinum electrodes in real time and detect changes in its initial concentration in solution through variations in the double-layer capacitance of the system (120). The group found changes to impedance to be clearest at cell concentrations larger than 10^5 CFU/ml, speculating that the double layer capacitance was affected by both the influence of the cells on the structure of the double layer and a reduction in electrode area following adhesion. Further to this, increasing cell concentrations and sensor occlusion were also observed to have an effect by Zhu et al. (2010) and Zikmund et al. (2010) (122,131). Dielectric changes were also detected by Kim et al. (2011), who saw a reduction in double layer capacitance when studying *P. aeruginosa* cell adhesion and biofilm formation on alumina polished platinum electrodes (123). Their investigation intended to study only these processes by replacing the electrolyte with

fresh media prior to each measurement to remove any impedance changes mediated by metabolic processes. The xCELLigence real time cell analysis system (ACEA Biosciences Inc., USA) has also been used to assess *P. aeruginosa* biofilms in a 96-well plate arrangement (164). The surfaces of each of the plate's wells contain an array of gold microelectrodes onto which cells attach.

Focusing not on cellular adhesion but metabolism, Yang et al. (2004) attributed prominent impedance modifications at low frequencies for *Salmonella typhimurium* to growth-related mechanisms (124): indium-tin-oxide interdigitated microelectrodes detected an increase in double layer capacitance and overall reduction in impedance at 10 Hz. It was speculated that substances such as lactose were being converted into molecules of higher electrical charge, resulting in this response.

Many experiments have instead observed a combination of the mechanisms shown in Figure 1.14, with impedance changes arising due to both direct and mediated means (Section 1.6.2). Studying the impedance changes that may result from medical-device associated infections, Paredes et al. (2012) monitored the formation of biofilms by *S. epidermidis* on gold interdigitated microelectrodes at frequencies between 10 Hz and 100 kHz (125). Maximum impedance variations occurred 9 hours after inoculation; in resistance for example a 20% relative decrease at 7 kHz occurred. In general, a decrease in impedance magnitude here was correlated with an increase in the concentration of bacterial cells. Furthermore, low frequency changes were linked to processes such as cell attachment to the electrode, whereas higher frequency changes were associated with metabolic modifications. The research group later integrated the sensors into Petri dishes, finding that biofilm formation was best characterised by resistive changes at 10 Hz (126). Pires et al. (2013) likewise observed both metabolic and cellular related impedance changes, combining EIS and amperometric measurements to study *P. aeruginosa* biofilm formation and activity with gold electrodes (127). *P. aeruginosa* was also detected by Ward et al. (2014), and a characteristic impedance signature obtained for the species using screen-printed carbon electrodes (118). A key feature of the resistance spectra (evident at frequencies below 1 kHz) was shown to result from this species' production of pyocyanin, an electroactive phenazine. Furthermore, changes to impedance due to bacterial attachment to the electrode and biofilm formation were also observed and confirmed via epifluorescent microscopy.

Moreover, the variety of experimental set-ups used and bacteria under study have led to differing impedance observations. Whilst some changes in spectra such as a decrease in impedance magnitude appear more commonly, others are less widely reported and the exact

mechanisms behind many changes remain unclear. Some impedance changes arising from medium related electrode interactions over time (such as was observed in urine by Settu et al. (2015) (121)), and differences in sensor material, size and configuration may have introduced variation between studies. Within single studies, however, a number of results indicate that it may be possible to harness variations in observed impedance response to differentiate between microorganisms. Some studies indicate that it is possible to detect characteristic changes for different species, caused by distinct combinations of processes (118,128,162,165). For example, *Bacillus subtilis* was speculated by Bonetto et al. (2014) to cause early, low frequency modifications due to a specific cellular interaction with the electrode, whereas, later high frequency features were detected for *Shewanella oneidensis* which were more likely caused by its metabolism (128). Similarly, Goikoetxea et al. (2018) detected different resistance changes for *E. coli* strains that produced curli protein and those that did not. Further, differences in the measured impedance response of *S. aureus* and *P. aeruginosa* were reported by Ward et al. (2014) (118). Central to the work reported in this thesis, this particular result will be revisited. As the bacterial impedance spectra gained via EIS are highly specific to the experimental conditions under which they are obtained, it is vital to continue to investigate key spectrum features that arise to ensure reliable application of this technology in future.

1.6.4 Impedance Spectroscopy in Wound Monitoring

To indicate wound healing progression, the measurement of impedance has been suggested (166). Early work by Spence and Pomeranz (1996) for instance used silver electrodes incorporating saline to assess surgical incisions in rats, finding that an increasing wound resistance could be linked to healing. Combining key ideas from these investigations with the detection of bacteria using similar techniques, work has been done to apply label-free EIS to the detection of wound infection *in situ* (129,130,168).

Sheybani and Shukla (2017) developed a system incorporating two sensors: one to monitor the pH of the wound bed (an infection biomarker) and a second to detect bacterial cell adhesion (130). Different bacterial species, namely *Streptococcus pyogenes*, *S. aureus*, *P. aeruginosa* and *E. coli*, were detected *in vitro* at concentrations from 10^2 CFU/ml and above using thin film gold interdigitated electrodes. These sensors were coated with polymeric layers to promote bacterial cell adhesion and discourage other settlements. Cell concentration dependant impedance changes were observed, indicating the presence of the bacteria. Notably, variations in double-layer capacitance enabled the sensor response to be linked to cell size using the known cell concentration. The extent to which the polymeric coatings shielded the

measurements of any electrochemical changes resulting from metabolism of nutrients for example was not, however, assessed. Further, the system was tested in a simulated wound fluid, confirming the applicability of this system to wound infection monitoring.

Sheybani and Shukla's electrodes did not, however, have the simplicity, cost and manufacturing benefits that disposable screen-printed alternatives possess (169). Farrow et al. (2012) adopted disposable silver/silver chloride (Ag-AgCl) screen-printed electrodes in a system aiming to detect wound infection (129). The growth of *S. aureus* was monitored, however, impedance measurements conducted with these electrodes were found to inhibit bacterial growth. Use of a different electrode material such as carbon may, therefore, be more beneficial (118). Nevertheless, normalised impedance spectra containing distinct features relating to bacterial growth were obtained, for example phase angle peaks (129). The work by Farrow et al. (2012), in combination with that of Farrow (2010) where a wider range of experimental conditions were investigated, showed promise for the development of a device in future that is able to detect and differentiate between different bacterial species. Based upon the observed changes in normalised impedance signature, such a sensor could diagnose wound infection in real-time as part of an accessible and cost-effective system.

1.7 Conclusion

It is evident, therefore, that the development of infection acts as a critical barrier to the intricate process of wound healing. Due to the risks associated with wound infection and growing antibiotic resistance, accurate and rapid detection of infection is of vital importance. Whilst a wide range of bacteria can colonise wounds, certain species such as *S. aureus* and *P. aeruginosa* are particularly common to infected wounds. By identifying the bacteria responsible for an infection, the best course of treatment can be selected.

Current procedures for infection detection in clinical practice rely on culturing and specialist resources; these time-consuming processes can greatly delay targeted treatment selection. In turn, this can negatively affect patient outcomes and can result in the unnecessary prescription of broad-spectrum or ineffective antibiotics. Electrochemical impedance spectroscopy utilising label-free, screen-printed electrodes has emerged as a potentially viable technique for real-time, *in situ* wound infection monitoring. It has been established that a variety of mechanisms underlie the impedance changes caused by bacteria at an electrode interface. By understanding these, and obtaining characteristic signatures for a variety of bacteria, it is hoped that this

technology can successfully be incorporated into an infection monitoring device capable of bacterial identification in future.

1.8 Project Objectives

Ultimately, the project described within this thesis aimed to further the development of an electrochemical sensor that can detect wound infection in real time. The low cost and disposable nature of this sensor were seen as key features that would be crucial to a commercial device in future, therefore, label- and bio-recognition element-free screen-printed electrodes were investigated throughout the project. In theory, this sensor could be placed under a standard wound dressing and a handheld device connected when necessary to obtain an electrochemical impedance measurement (Figure 1.15). The device, which would ideally have wireless connectivity, would provide an indication of the infection status and, if infected, the level of infection and causative organisms.

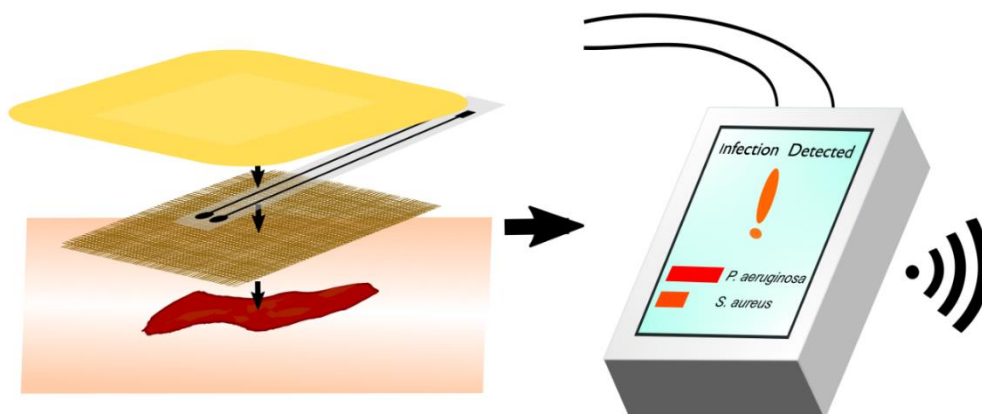


Figure 1.15. Diagram of the hypothesised future in situ wound infection monitoring device.

To aid the development of such a device, this project had the following key objectives:

1. Through testing different electrode materials, determine the most suitable for rapid bacterial detection.
2. Identify the key changes to impedance that occur during bacterial growth in culture media.
3. Develop and detect bacterial growth in a wound bed model which more accurately simulates a wound environment.
4. Determine methods of identifying infection, different bacterial species and concentrations through differences in the obtained impedance spectra.

2. BACKGROUND THEORY

2.1 Introduction

Within this stand-alone chapter, important areas of background theory that are fundamental to this multidisciplinary research are introduced, aiming to enable readers from a range of scientific disciplines to understand the work presented in this thesis.

2.2 Fundamental Microbiology Concepts Underpinning this Research

2.2.1 Prokaryotic Cell Structure

In biological taxonomy, there are numerous ranks of classification (Figure 2.1). Principally, there are three domains of life: Bacteria, Archaea and Eukaryotes (170). Both bacteria and archaea are prokaryotic cells: single-celled organisms with no membrane-bound organelles (such as nuclei). Distinctions between these two domains include differences in cell wall composition (32). By proceeding further down the taxonomic ranks, ultimately individual species can be identified and differentiated. The example provided in Figure 2.1 ultimately classifies *Staphylococcus aureus*, a species of bacteria. For each species, several different strains exist which can show slight phenotypic and genomic variations. The so called “Type strain” can be considered a consistent standard, having characteristics typical of the species.

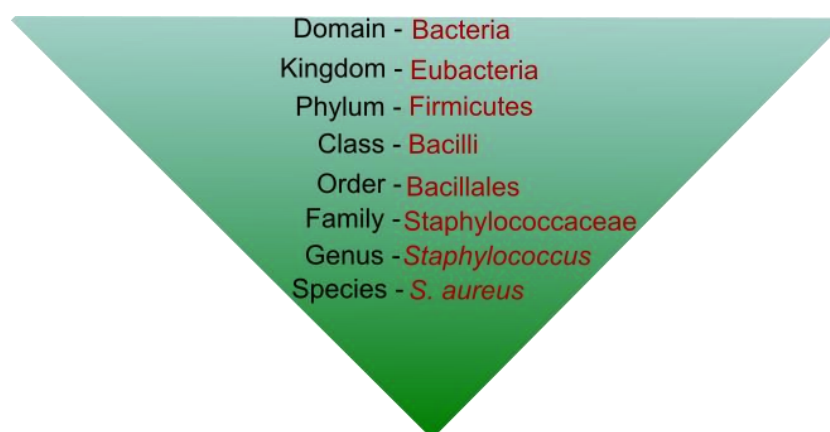


Figure 2.1. Taxonomic rank in biological classification. An example classification is provided.

A bacterial cell's cytoplasm contains macromolecules suspended in cytosol, a fluid containing water, salts and other molecules essential for survival. Unlike eukaryotic cells which have membrane bound nuclei, the genetic material of a bacterium (a single chromosome) is located in the undefined region within the cytoplasm termed the nucleoid (Figure 2.2) (32). A further macromolecule located within the cell cytoplasm, ribosomes perform protein synthesis.

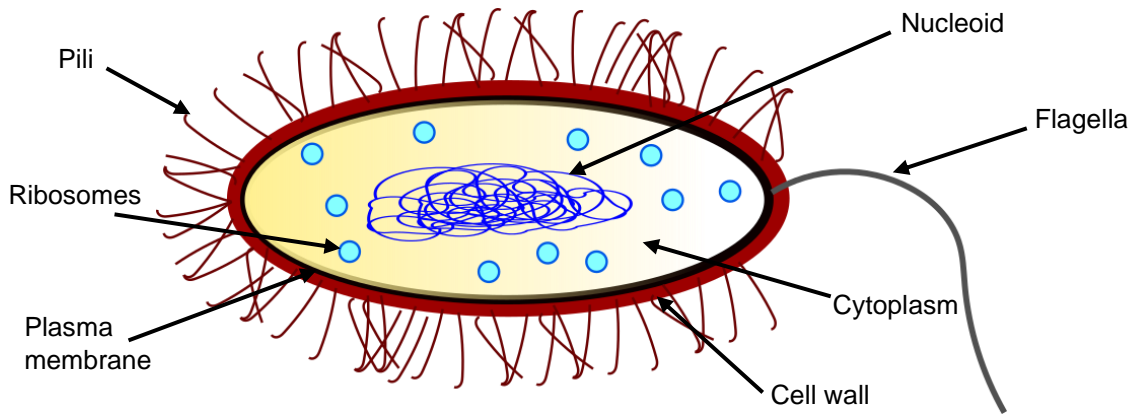


Figure 2.2. Key prokaryotic cell features.

Bacterial cells can also be categorised according to their shapes and morphology. Common cell shapes include cocci (spherical), rods (cylindrical) and spirals. The clustering of these cells due to division planes can be indicative of species, for example *Staphylococcus* clusters can be recognised by their grape-like appearance (32). It is believed that selective forces, such as nutrients and motility, have a role in the resulting bacterial shape (171). Individual cell sizes can range from around $0.02 \mu\text{m}^3$ to $400 \mu\text{m}^3$, with enzyme activity and protein synthesis being a limiting factor at the lower end of the scale and nutrient diffusion (governed by Fick's law) thought to limit the largest cell sizes (172).

Bacterial cells, as seen in Figure 2.2, possess plasma membranes and cell walls. The plasma membrane consists of a phospholipid bilayer which acts as a permeability barrier, whereas the cell wall contains peptidoglycans and is a more rigid, protective structure (32). A common method of classifying bacteria is the Gram stain- a test which differentiates bacteria based upon major differences in outer cell structure. The procedure involves staining the bacteria with crystal violet (primary stain) before adding an iodine solution to enhance the stain. The samples are then washed with alcohol, and a counterstain such as safranin added. For Gram positive bacteria the initial stain (blue/purple) is retained after washing with alcohol, whereas for Gram negative bacteria this stain is removed and the second (counter-) stain is instead taken (pink) (173). Structural differences are responsible for this outcome: after the inner plasma membrane, Gram positive bacteria possess a thick peptidoglycan cell wall (around $20 \text{ nm} - 80 \text{ nm}$), whereas Gram negative species have a thinner peptidoglycan cell wall (around $5 \text{ nm} - 10 \text{ nm}$) followed by an additional outer membrane composed of phospholipids and lipopolysaccharides

(174). The crystal violet is not retained by Gram negative bacteria due to this thin peptidoglycan layer not sufficiently encapsulating the dye during the dehydrating alcohol wash (32). These differences are highlighted in Figure 2.3.

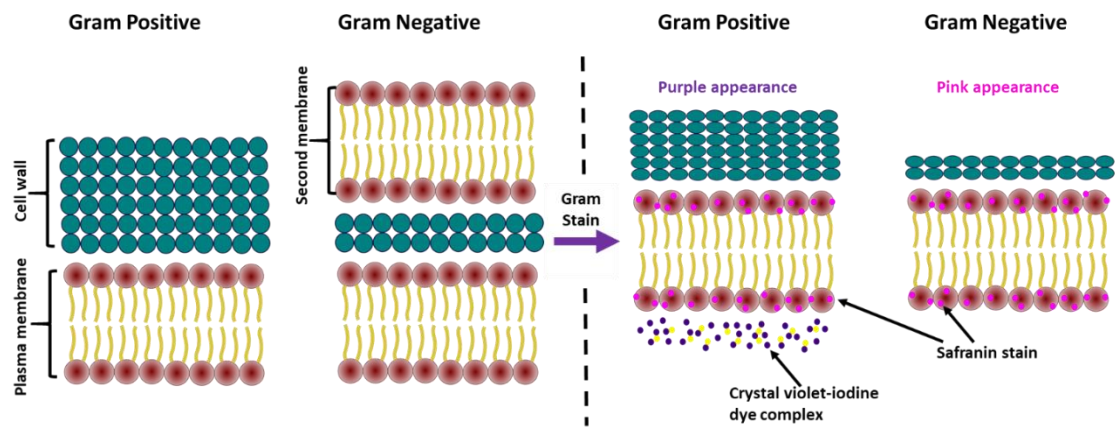


Figure 2.3. Cell wall structure and Gram staining for Gram positive and Gram-negative bacteria.

Many bacteria have filamentous appendages on their outer surface such as fimbriae, pili or flagella (32). A key function of fimbriae and pili is adhesion to other cells and surfaces, including host epithelial cells for example (175). Type IV pili have a specific role in the movement of certain species of bacteria, resulting in “twitching motility” (32). Flagella too play an important role in cell motility: these larger, whip-like appendages are themselves multi-structured, and are most commonly the source of movement for swimming bacteria. In species with swarming motility flagella are similarly involved, however, this case describes multicellular movement across a surface (176). A key example of swarming is the movement of *Proteus mirabilis* across a solid agar plate, as seen in Figure 2.4. Conversely, gliding bacteria move in a slower fashion along surfaces, aided for example by slime excretion (32). Bacterial locomotion allows cells to access other areas of their environment with, perhaps, more nutrients or favourable conditions. These movements can be in response to environmental gradients, for example chemotaxis.

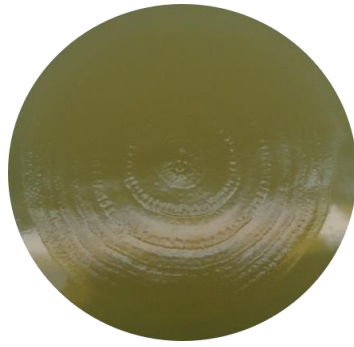


Figure 2.4 Image of *P. mirabilis* swarming pattern formation on an agar plate. The characteristic 'bullseye' shape is formed due to different phases of spreading elongated swarmer cells and more static dividing cells.

2.2.2 Bacterial Growth

As prokaryotes, bacterial cell division is undertaken via binary fission where one cell divides to produce two progeny cells (177). The generation time associated with a species is the period of time between successive cell divisions, and can range from around 30 minutes to 6 hours (32). Upon inoculation of an enclosed sample of medium with bacteria (batch culture), a growth cycle occurs (Figure 2.5). By plotting this growth curve, the generation time for the species under study can be visualised.

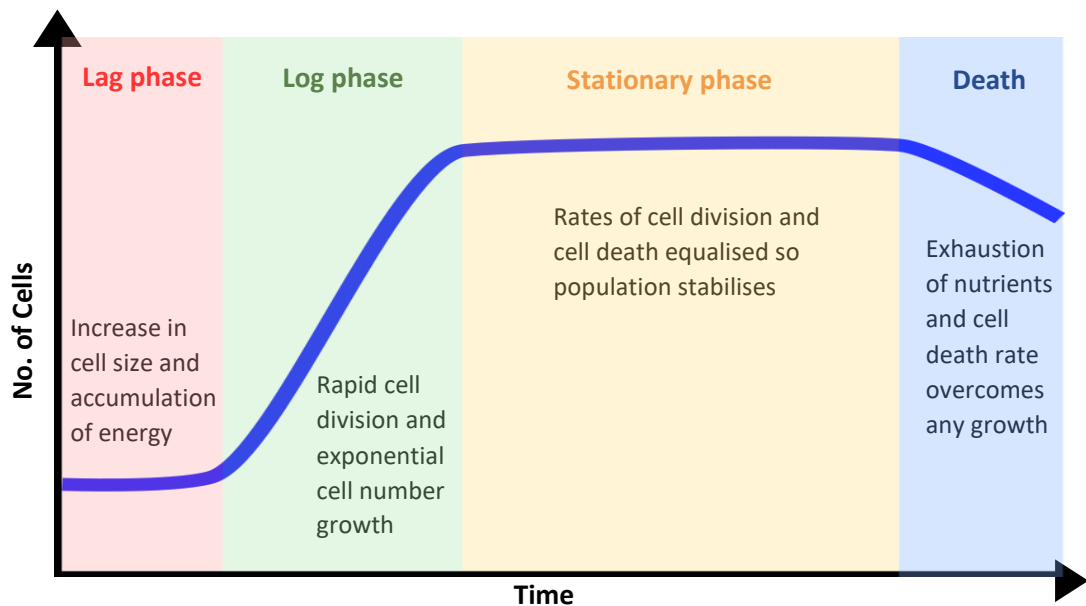


Figure 2.5. Bacterial growth curve.

During the initial lag phase of growth, bacteria adapt to their surroundings and produce complex molecules that enable exponential cell growth during the successive log phase. If there is a finite supply of essential nutrients, cell growth slows and is matched by the rate of cell

death during the stationary phase. Finally, after depletion of the available nutrients and accumulation of harmful waste products, the total viable cell number decreases during the cell death phase (32). In addition to nutrient availability, there are a variety of factors which influence cell proliferation. Crucial environmental factors include temperature, pH, moisture and oxygen availability.

2.2.3 Cell Metabolism

Metabolic reactions occur within cells to facilitate the use of energy and carbon to create the macromolecules essential for survival (biosynthesis). Energy, in the form of adenosine triphosphate (ATP) molecules can be generated through the metabolic processes of fermentation or respiration (178). During a process termed glycolysis, glucose is converted to pyruvate in the cytoplasm. Fermentation converts this into end products such as lactic acid and ethanol, and ATP is subsequently produced (32). If, however, oxygen is present, aerobic respiration occurs. Pyruvate is altered enzymatically and enters the Krebs cycle. Here, electrons are gathered and passed into the electron transport chain where their flow to the oxygen molecules (termed final electron acceptors) generates ATP and produces CO₂ and H₂O (179). Anaerobic respiration occurs in the absence of oxygen where an alternative, strongly electronegative molecule such as nitrogen is present and acts as the final electron acceptor. Furthermore, fats and proteins may also be used within the Krebs cycle, highlighting the range of different metabolic pathways available to bacteria (32). Exploiting this variety, numerous tests exist in the laboratory to categorise pathogens based on their metabolic activity (in particular, enzyme production such as catalase).

2.2.4 Bacterial Biofilms

Bacterial biofilms are defined as aggregates of cells which are surrounded by a self-produced protective extracellular matrix, often attached to solid surfaces (180). In this enclosed community, cells are given additional defence (against harsh environments and antibiotics for example) by the extracellular polymeric substances (EPS) that surround them.

The process of biofilm formation occurs in a series of steps, as depicted in Figure 2.6. Planktonic (or floating) cells first reversibly adhere to a surface; the propensity for cells to adhere is dependent upon surface properties such as roughness and wettability (156). This initial attachment activates gene expression required for the biosynthesis of cell surface polysaccharides, which in turn aid adherence and promote further, irreversible cell attachment

(32). In this colonisation stage, various intercellular signalling pathways are vital in the recruitment of cells and production of EPS (181). For example, in *Pseudomonas aeruginosa* acylated homoserine lactone molecules carry out quorum sensing- a process which enables communication between adjacent cells, alerting them of a growing biofilm population in this instance (32). Gene expression is regulated during quorum sensing by the production of autoinducers by bacteria. These signalling molecules alert neighbouring cells of the current cell density and prompt a specific response (182). In addition to biofilm formation, this process is involved in the regulation of numerous processes including cell virulence. Returning to biofilm formation, clusters of cells form (termed microcolonies) within the EPS matrix. This is composed mainly of polysaccharides such as alginate, and also includes other molecules such as proteins and nucleic acids (183). The composition of the matrix determines largely the shape and structure of the biofilm, however, in general biofilms are very heterogeneous and possess water channels which enable rapid nutrient diffusion (181). Their structure changes in time and, ultimately, cell dispersal occurs during biofilm maturation. This reverts some cells to a planktonic state, thus continuing the biofilm life cycle (Figure 2.6) (154).

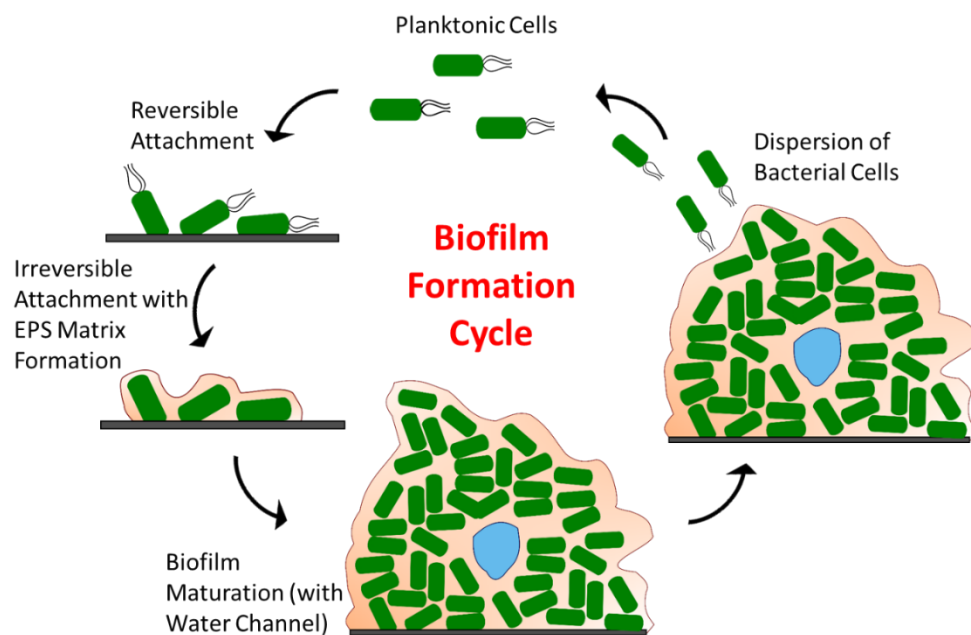


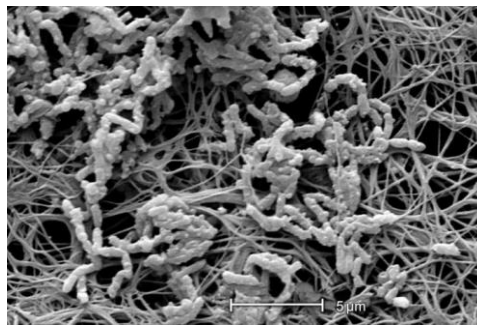
Figure 2.6. Bacterial biofilm formation lifecycle.

There are multiple reasons why biofilm formation is believed to occur. Crucially, formation of these structures is of great benefit to bacterial survival in nature. Key benefits are (32):

- **Self-Protection:** Embedded in the EPS matrix, cells are guarded from physical forces, toxic molecules (antibiotics for example) and cells of the immune system.
- **Environmental Stability:** Stable biofilm formation on a surface prevents the removal of cells from the nutrient rich environment.

- **Population Benefits:** By settling adjacent to a large number of other cells, bacterial signalling, survival and opportunities for genetic exchange are elevated.
- **Natural Mode of Growth:** In nature, it has been observed that biofilm formation is the natural arrangement for bacteria. This is likely due to the reduced nutrient availability in natural environments compared to idealistic laboratory investigations.

Biofilms play a significant role in a variety of clinical areas, from the formation of dental plaque and caries production, to medical implant infections (180). For example, Figure 2.7 provides an example of biofilm formation within a central venous catheter. Difficult to treat infections such as those formed in chronic wounds are commonly linked to the presence of biofilm material, which can be up to hundreds of micrometres in size (184). Due to the greatly decreased efficacy of antimicrobial agents upon bacteria in the presence of the EPS matrix, much research is ongoing to uncover novel mechanisms of action for future antibiotics (181).



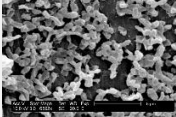

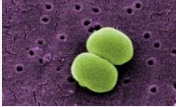


*Figure 2.7. Scanning electron microscope image of *Alcaligenes xylosoxidans* biofilm formation within a central venous catheter. Image source: <https://phil.cdc.gov>; photo credit Janice Haney Carr (2008).*

2.2.5 Bacterial Species of Interest

Within this thesis a number of bacterial species have been selected for use in experiments due to their clinical relevance to wound infection. A short summary of each of these organisms from a microbiological viewpoint is provided below in Table 2.1. Data is largely summarised from Madigan et al. (2018) (32). Each of these bacteria have an association with antimicrobial resistance and, therefore, are of global importance (Chapter 1). Further, each of these species is a facultative anaerobe and is commonly associated with biofilm formation.

Table 2.1. Summary of bacterial species central to this thesis. Scanning electron microscope images sourced from <https://phil.cdc.gov>.

Species	Gram stain	Shape	Motility	Common niche	Associated Infections	Notable Metabolites
<i>Escherichia coli</i> 	-	Rod	High motility via multiple flagella	Intestines	Digestive and urinary tract, surgical wounds, pressure sores	Characteristic foul smell a result of tryptophanase production and creation of indole
<i>Pseudomonas aeruginosa</i> 	-	Rod	High swimming motility via single polar flagellum	Moist environments - soil, airways, wounds.	Cystic fibrosis lungs, severe burns	Phezanines (important role in virulence and quorum sensing). Notably redox-active compound pyocyanin, gives characteristic blue/green pigment.
<i>Proteus mirabilis</i> 	-	Rod	High motility, swarming, high flagella densities	Gastrointestinal tract	Wounds, urinary catheters	Urease – causes alkalination of urine resulting in bladder/ kidney stones
<i>Staphylococcus aureus</i> 	+	Cocci	Non-motile	Human skin (anterior nares eg). Part of normal flora for ¼ of the population (34,42)	Wounds, urinary tract, catheters etc	Staphyloxanthin production gives characteristic yellow pigmentation. Catalase – can be used to differentiate from Streptococci. Coagulase – differentiates from other Staphylococci
<i>Staphylococcus epidermidis</i> 	+	Cocci	Non-motile	Human skin	Less virulent than <i>S. aureus</i> (185), but can cause infection in wounds, catheters etc.	Catalase- can be used to differentiate from Streptococci.

2.3 Fundamental Electrochemistry Concepts Underpinning this Research

Within this section, the basic electrochemical principles fundamental to this thesis are introduced. For further reading, please refer to more comprehensive texts such as Bard and Faulkner (2001) (186) or Orazem and Tribollet (2017) (187).

2.3.1 Electrochemical Cell Reactions

A basic electrochemical cell consists of two conductive electrodes separated by an electrolyte, such as is depicted in Figure 2.8. Whilst electrons act as charge carriers in the electrical circuit, ionic species carry charge in solution. When a voltage is applied across the electrodes (electrolytic cell), an electric field is induced in the solution. Electrostatic ion motion within the electrolyte results, and oxidation and reduction reactions occur at the electrode surface. These reactions would not occur spontaneously and are driven by the applied electrical potential. The result is a measurable net current flow through the electrochemical cell. Critical to electrochemistry, during these chemical reactions electrons are transferred between ions or molecules. Reduction and oxidation reactions always occur together, with the two individual half-reactions combining to balance an overall redox reaction both electrically and chemically.

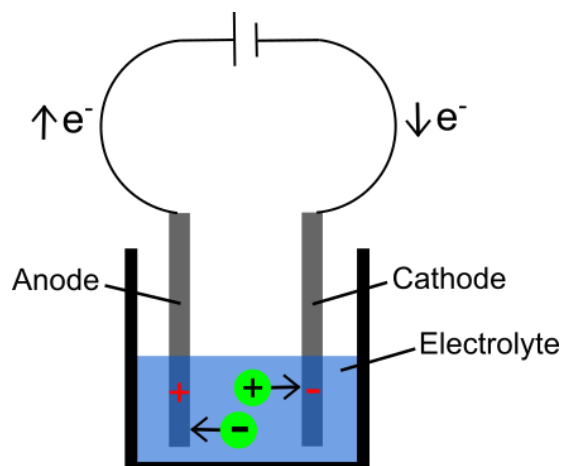


Figure 2.8. A simple electrochemical cell. When a voltage is applied, positive ions in the electrolyte are attracted towards the negatively charged cathode, and negative ions towards the positively charged anode.

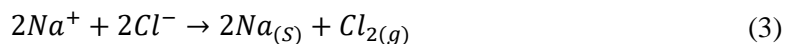
Given the configuration in Figure 2.8, imagine two inert carbon electrodes are immersed in a molten NaCl solution and a potential applied, initiating a reaction. Sodium ions (Na^+) are attracted towards the cathode where they are reduced, gaining an electron and forming atomic sodium:



Simultaneously, chloride ions (Cl^-) move towards the anode where they are oxidised, losing an electron and forming chlorine gas:



The overall, balanced redox reaction can therefore be written as:



In electrochemical systems, multiple reactions often occur simultaneously. Further, most commonly aqueous solutions are studied. For aqueous solutions the same processes apply, however, the reduction potential of each chemical constituent is important as this describes the tendency of the dissolved species to acquire electrons and be reduced. These values describe a hierarchy for redox reactions and enable redox reactions (and reaction products) to be predicted.

This is, however, a very simplistic description. In reality, the motion of ions in solution and the interactions occurring at the electrode/electrolyte interface are very complex. There are numerous electrochemical principles which govern these processes and the rate at which they occur. Figure 2.9 (adapted from (186)) summarises variables which influence the rates of electrochemical reactions.

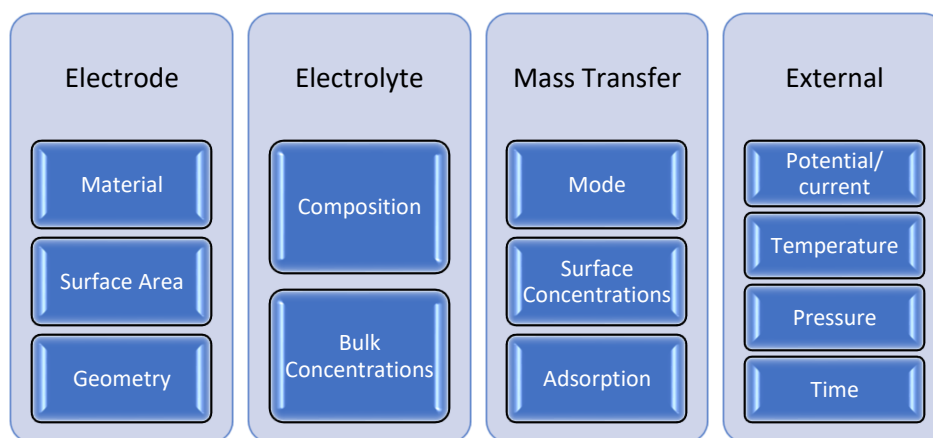


Figure 2.9. Key factors influencing electrochemical reaction rate (summarised from Bard and Faulkner (2001) (186)).

2.3.2 Ion Solvation

When dissolved in a solvent, ions become encircled by a shell of solvent molecules in a process termed solvation (Figure 2.10). In the case where the solvent is water (as is commonly the case

in bio-electrochemistry) this organisation is named hydration, and it results from strong interactions between the dipolar water molecules and the ion's electrostatic field (188). The formation of such a solvation shell around ions plays an important role in electrochemistry as it increases the effective radius of the ion and, therefore, effects its motion and the conductivity of the solution (189). Changes to solution properties resulting from solvation include variations in viscosity and diffusion coefficients (190).

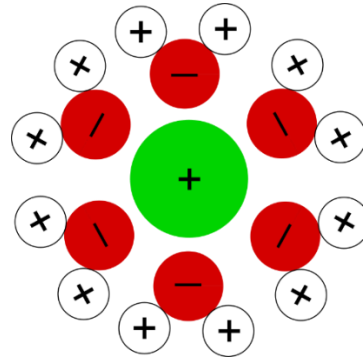


Figure 2.10. Ion solvation shell. Example given is a positive ion hydrated by water molecules.

2.3.3 Mechanisms of Mass Transfer

In an electrochemical cell, ionic species transport charge through the medium; it is the movement of these ions which results in a measurable current. There are three mechanisms of ionic mass transfer: diffusion, migration, and convection.

Diffusion is the movement of ions down a concentration gradient in the electrolyte, from areas of higher to lower concentration. Fick's first law describes diffusion for a steady-state system (in one dimension) (186):

$$J_i = -D_i \frac{dc_i}{dx} \quad (4)$$

Where J_i is the flux of ion species i , D_i is the coefficient of diffusion and $\frac{dc_i}{dx}$ is the concentration gradient for a concentration c_i of species i over distance x . Here, the negative sign indicates the movement of ions *down* the concentration gradient. Further, Fick's second law characterises systems which are instead transient and, therefore, the species concentration varies in both time (t) and space (x). For such systems (186):

$$\frac{\partial c_i}{\partial t} = D_i \left(\frac{\partial^2 c_i}{\partial x^2} \right) \quad (5)$$

Secondly, migration arises due to the application of an electric field resulting in the motion of charged ions. When a voltage is applied across the electrodes in solution, ions are either electrostatically attracted to, or repelled from, a given electrode based upon its polarity. The contribution to flux arising from migration is given by (186):

$$J_i = -\frac{z_i F}{RT} D_i c_i \frac{\partial \phi(x)}{\partial x} \quad (6)$$

Where z_i is the charge of species i (dimensionless), F the Faraday constant, R the universal gas constant, T the absolute temperature and $\frac{\partial \phi(x)}{\partial x}$ the potential gradient. Further, this can be written as:

$$J_i = \frac{z_i F}{RT} D_i c_i E \quad (7)$$

Where E is the electric field in one direction (x), given by:

$$E = -\frac{\partial \phi(x)}{\partial x} \quad (8)$$

The ability of ions to move in response to the applied force of the electric field is described by their mobility. This is dependent upon the number of collisions occurring between the different molecules in the electrolyte and is, therefore, electrolyte dependent. The Einstein-Smoluchowski equation links the mobility of ion species i (u_i) to the diffusion coefficient (186):

$$u_i = \frac{|z_i| F D_i}{RT} \quad (9)$$

Further, an appropriate estimate for the diffusion coefficient can be obtained using the Stokes-Einstein relation, which assumes that the ions are spherical and diffusing through a liquid (191):

$$D_i = \frac{k_B T}{6\pi r_i \eta} \quad (10)$$

Where k_B is Boltzmann's constant, η is the viscosity of the fluid and r_i is the radius of the ion.

Finally, convection is a hydrodynamic transport mechanism resulting from stirring for example. As the experiments within this thesis were conducted under static conditions, these effects were considered negligible.

Combining the effects of diffusion and migration (and neglecting convection) for a one-dimensional steady state system, the Nernst-Planck equation states that the total ionic flux is given by (186):

$$J_i = -D_i \frac{dc_i}{dx} + \frac{z_i F}{RT} D_i c_i E \quad (11)$$

For charged ions like those under consideration here, J_i is equivalent to current density and current can be calculated from this flux as:

$$-J_i = \frac{i_i}{z_i F A} \quad (12)$$

Where i_i is the current contribution from species i and A is cross-sectional area. The diffusion and migration currents may, in a similar manner to flux, be separated into individual contributions. In general, the total current is equal to:

$$i_i = i_d + i_m \quad (13)$$

With i_d representing the diffusion current and i_m the migration current. The relative contributions of these currents are dependent upon both time and position within the electrolyte. For example, migration dominates in the bulk electrolyte whereas both contributions are significant close to the electrode surface. At the electrode, the measured current is determined by reaction rate which, in turn, is governed by ionic flux and the rate of mass transfer (186). The relative contribution of each species to the total current is considered using the transference number t_i , with:

$$\sum_i t_i = 1 \quad (14)$$

Where the transference numbers are summed over all species.

2.3.4 The Electrode/Electrolyte Interface

In contrast to the arrangement of the bulk electrolyte, at the interface between the electrode and electrolyte phases a so called electrical double layer is formed which has properties analogous to a capacitor. The capacitance of this double layer is, however, dependent upon the applied potential (186). An accumulation of electrons at the electrode surface in the example depicted in Figure 2.11 creates a negatively charged surface which attracts dipolar water molecules, resulting in hydration of the electrode. In this layer, which is immediately adjacent to the electrode surface, some specifically adsorbed ions may also be present. This first layer is

termed the inner layer, and the Inner Helmholtz Plane (IHP) falls in line with the centre of the specifically adsorbed ions. Adjacent to this, hydrated ions are electrostatically drawn towards the electrode. This redistribution of charge balances the net charge at the interface, with each phase displaying equal and opposite charge. The Outer Helmholtz Plane (OHP) is the name given to the plane of closest approach, centred on these hydrated ions. Moving outwards into the solution from the OHP is the diffuse layer. This arises due to the interplay between long range electrostatic forces and thermal motion affecting the position of ions adjacent to the electrode. The thickness of the diffuse layer is dependent upon the ionic concentration within the electrolyte, and upon potential. Overall, the charge on the electrode surface is balanced by the combination of charges within the inner and diffuse layers:

$$-\sigma_M = \sigma_S = \sigma_i + \sigma_d \quad (15)$$

Where σ_M is the charge density on the electrode surface, σ_S the charge density from the adjacent solution, σ_i the charge density from specifically adsorbed ions in the inner layer and σ_d the charge density from the diffuse layer (186). Crucially, reaction rate at the electrode surface is impacted by the organisation of the double layer. Simplistically, in this configuration the electrode represents one capacitor plate and the wall of ions the other, with the water molecules in between acting as the dielectric for the charge barrier (Figure 2.11).

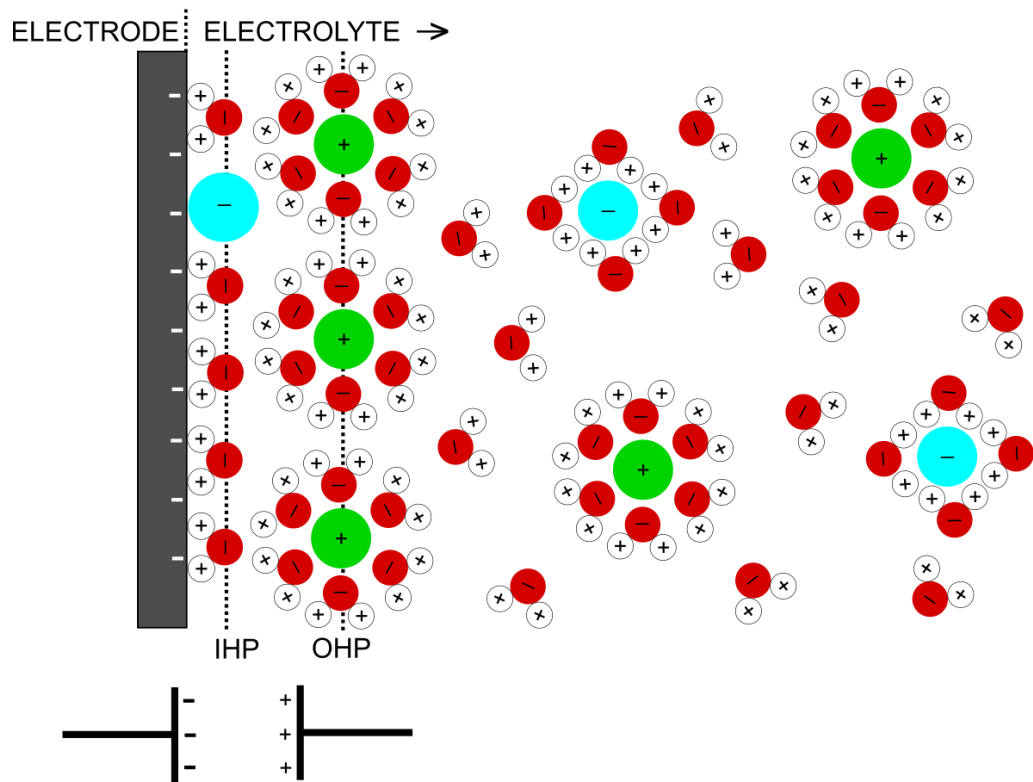


Figure 2.11. Structure of the electrical double layer. On the far left the electrode is depicted, with a negative surface charge shown. Solvent (water) molecules (red and white) from the electrolyte hydrate this surface and, with the addition of specifically adsorbed ions, this forms the Inner Helmholtz Plane (IHP). The Outer Helmholtz Plane (OHP) centred on the hydrated positively charged ions (green) at their location of closest approach is next depicted, before the neutral bulk solution. The structure of this double layer is akin to a capacitor.

Various models have been developed to describe this double layer, with the following key theories (summarised from Bard and Faulkner (2001) (186)) incrementally building upon each other to reach a model which approximates experimental observations. Firstly, Helmholtz theorised that the balancing charge in the electrolyte solution was located on the surface, in the same manner as it is on the surface of the electrode. This arrangement is identical to a parallel plate capacitor, with double layer capacitance therefore governed by:

$$C_H = \frac{\epsilon \epsilon_0}{d} \quad (16)$$

Where C_H is the differential capacitance predicted by Helmholtz, ϵ is the dielectric constant of the medium, ϵ_0 is the permittivity of free space, and d is the distance between the charged “plates” (186). This model predicts a constant value for capacitance and does not explain its dependencies upon potential and concentration that are observed experimentally. The Gouy-Chapman theory proposes a solution to this problem, by introducing the idea of the diffuse layer of charge in the solution. Instead of modelling the solution charge as a sheet of surface

charge, this theory suggests that a finite thickness of solution will be required to balance the electrode surface charge due to the combination of electrostatic and thermal effects. There is a potential drop across the diffuse layer; its structure impacts the profile of this. In this model capacitance is dependent upon potential and concentration as desired, with an increase in electrode potential causing a reduction in diffuse layer thickness and an increase in double layer capacitance for example. A full derivation of the Gouy-Chapman approximation for capacitance (C_{GC}) is out with the scope of this thesis and has, therefore, been omitted in favour of a qualitative description of the model. This model was, however, still found to be unable to accurately estimate values for double layer capacitance, in particular at high potentials. Stern attributed this failure to a lack of consideration for the finite radii of ions. When solvated, their radii increase further, and the distance of closest approach to the electrode surface must increase. This plane of closest approach is the Outer Helmholtz Plane. Stern's model predicts that at high potentials or concentrations, the diffuse layer is compressed to such an extent that the Helmholtz model dominates, with d in Equation 16 being the distance between the OHP and the electrode surface. Stated as a combination of capacitors in series, this final model specifies that:

$$\frac{1}{C_S} = \frac{1}{C_H} + \frac{1}{C_{GC}} \quad (17)$$

Where (C_S) is the Stern model double layer capacitance.

2.3.5 Faradaic and Non-Faradaic Processes

Processes occurring at the electrode/electrolyte interface can be categorised as either Faradaic or non-Faradaic (186). In the former, charge transfer takes place across the interface resulting in the occurrence of oxidation and reduction (redox) reactions that obey Faraday's law: the reaction product mass is proportional to the charge transferred. Conversely, in non-Faradaic processes no charge transfer across the electrode/electrolyte interface occurs. Instead, adsorption onto the electrode surface and the formation of the double layer are key. Variations in potential for example can result in the flow of transient non-faradaic current, which can be used to probe the structure of the interface. Both types of processes occur in electrochemical experiments, however, electrode choice is an important factor in determining which process type is favourable.

An ideal electrode which allows charge (electron) transfer across the electrode/electrolyte interface is termed "non-polarisable" as it prevents a change in potential at the interface, and

no charge separation at the interface exists (Figure 2.12A). This behaviour is analogous to that of a resistor. Whilst an ideal electrode does not exist, an example of an electrode with approximately non-polarisable properties is the Ag/AgCl electrode. This electrode material provides a stable electrode surface at which the redox reactions can occur. Non-polarizable electrodes are desirable for biomedical applications as they perform well even under non-static conditions and at low frequencies (192).

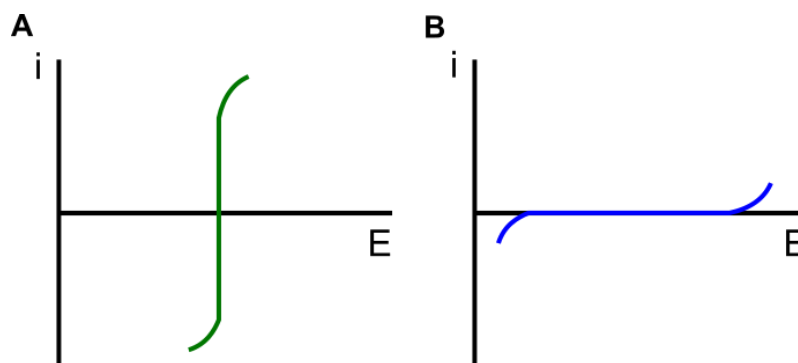


Figure 2.12. Current vs potential plots for an (A) non-polarisable and (B) polarisable electrode. Adapted from Bard and Faulkner (2001). This “ideal” behaviour in each case is exhibited within a limited potential window. For the non-polarisable electrode (analogous to a resistor), a change in potential is prevented during charge transfer across the interface. For the polarisable electrode (analogous to a capacitor), no charge transfer occurs over a range of potentials.

On the other hand, an “ideal polarisable electrode” prevents charge transfer across the electrode/electrolyte interface which is, therefore, equivalent to a capacitor (Figure 2.12B). Again, it is not possible to manufacture such an electrode, however, platinum electrodes in NaCl provide a good approximation of these characteristics. In reality, electrodes possess a limited potential range within which faradaic reactions are unfavourable and non-faradaic processes dominate. In particular for biomedical applications, there are many drawbacks to using polarizable electrodes and their performance is inferior to their non-polarizable counterparts (192). For example, the presence of motion artefacts and greater noise (192). In particular, polarisation effects negatively impact measurements performed using low frequency applied voltages (193). This is particularly important when performing electrochemical impedance spectroscopy (as will become clear in the subsequent sections). Efforts are, therefore, frequently made to minimise the electrode polarisation effects associated with double layer formation in biomedical measurements by altering the structure, geometry and roughness of the electrode for example (193–195).

In general, electrodes exhibit a combination of these characteristics, detecting both faradaic and non-faradaic process (192).

2.3.6 The Nernst Equation and Electrochemical Kinetics

A key concept in electrochemistry is the idea of an equilibrium at which no net faradaic current flows between an electrode and electrolyte (192). At equilibrium, oxidation and reduction reactions occur at an equal and opposite rate. The Nernst equation states the relationship between this equilibrium potential and the concentration of ions in solution (assuming unit activity coefficients) (186):

$$E_{eq} = E^{0'} + \frac{RT}{nF} \ln \left(\frac{C_o}{C_R} \right) \quad (18)$$

Where E_{eq} is the electrode potential at equilibrium, $E^{0'}$ is the standard electrode potential, R the universal gas constant, T is absolute temperature, n is the number of electrons transferred in the reaction, F is the Faraday constant and C_o and C_R the bulk concentrations of oxidised and reduced species respectively.

In the event of current flow, the electrode potential can be changed from this equilibrium value. This, as introduced in Section 2.3.5, is termed electrode polarisation. Overpotential (η) is used to quantify polarisation, and is equal to the difference between the measured potential when the current is flowing (E) and the zero current, reversible (Nernst) potential (E_{eq}) (186):

$$\eta = E - E_{eq} \quad (19)$$

The current flowing is dependent upon the rate of Faradaic reactions. The Tafel equation links overpotential to current (i) and, therefore, the reaction rate (186):

$$\eta = a + b \log i \quad (20)$$

Where a and b are constants. Plots of current (or current density) against voltage (or overpotential) are termed Tafel plots and can be useful tools in the study of complex electrode reactions (196).

Another key relation linking current to overpotential for an electrode is the Butler-Volmer equation. Neglecting mass transfer effects, it has the form (186):

$$i = i_0 [e^{-\alpha f \eta} - e^{(1-\alpha) f \eta}] \quad (21)$$

Where i_0 is the exchange current, α is the transfer coefficient and the constant $f = F/RT$. Broadly, it again describes the non-linear relationship between current and overpotential. This

more complex equation simplifies to a Tafel equation at large values of overpotential (197). Further, it can be simplified to regain the Nernst equation at equilibrium (186).

2.3.7 Complex Electrical Impedance

The concepts introduced so far have focussed upon the electrochemical processes occurring at an electrode/electrolyte interface. Before the core experimental measurement method - electrochemical impedance spectroscopy - is introduced, the concept of electrical impedance must first be described.

Consisting of both real and imaginary components, complex impedance is defined by Ohm's law as the ratio of potential to current:

$$Z = \frac{V}{I} \quad (22)$$

Where Z is complex impedance, V is complex potential and I is complex current. Impedance represents an opposition to the flow of electric charge (current) under the application of a potential. As a complex quantity, it may be written in the following Cartesian form:

$$Z = Z' + jZ'' \quad (23)$$

Where Z' and Z'' represent the real and imaginary parts of impedance respectively, namely resistance and reactance, and $j = \sqrt{-1}$. Note that in electrochemistry a negative sign is sometimes used in front of the imaginary term in the definition of Equation 23 (186). This convention enables positive values to be generally worked with as the imaginary contribution to impedance in electrochemistry is predominantly capacitive and, therefore, negative. To avoid any confusion, however, the standard definition of complex impedance is instead used in Equation 23. In polar form, this relation becomes:

$$Z = |Z|e^{j\theta} = |Z|(\cos(\theta) + jsin(\theta)) \quad (24)$$

Where $|Z|$ is the impedance magnitude, given by:

$$|Z| = \sqrt{(Z')^2 + (Z'')^2} \quad (25)$$

And θ is the phase angle between voltage and current in radians, such that:

$$\tan(\theta) = \frac{Z''}{Z'} \quad (26)$$

Consider an AC sinusoidal voltage of the form:

$$V = |V|\sin(\omega t) \quad (27)$$

Where $|V|$ is voltage amplitude (V), ω is angular frequency (rad s^{-1}) and t is time (s). For a pure resistance, the phase angle $\theta = 0$ such that current is equal to:

$$I = |I|\sin(\omega t) \quad (28)$$

With $|I|$ representing the current amplitude (A). Thus, the impedance of a resistor is (by definition) represented as a purely real, resistive quantity:

$$Z_R = \frac{V}{I} = \frac{|V|\sin(\omega t)}{|I|\sin(\omega t)} = \frac{|V|}{|I|} = R \quad (29)$$

Where R is resistance (Ω). This is visualised in Figure 2.13.

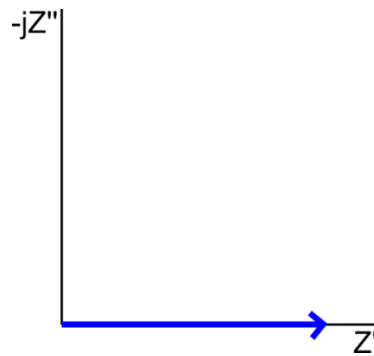


Figure 2.13. A resistor contains only a real component of impedance.

Conversely, for a capacitor the phase difference between voltage and current is $\frac{\pi}{2}$. We can derive this result by first writing potential across the capacitor as:

$$V = |V|e^{j\omega t} \quad (30)$$

The governing equations state that current is given by:

$$I = C \frac{dV}{dt} \quad (31)$$

Where C is capacitance (F). It can, therefore, be seen that:

$$I = C \frac{d}{dt} (|V|e^{j\omega t}) = j\omega C|V|e^{j\omega t} = \omega C|V|e^{j(\omega t + \frac{\pi}{2})} \quad (32)$$

Thus, current leads voltage by $\frac{\pi}{2}$ radians. It can also be said that voltage lags current by $\frac{\pi}{2}$ radians, and it is convention to quote the phase angle in this respect. The phase angle for a capacitor is, therefore, $\theta = -\frac{\pi}{2}$. Further, the impedance of a capacitor is:

$$Z_c = \frac{V}{I} = \frac{1}{j\omega C} = -\frac{j}{\omega C} \quad (33)$$

A perfect capacitor, therefore, is a purely imaginary, reactive component of impedance (Figure 2.14).

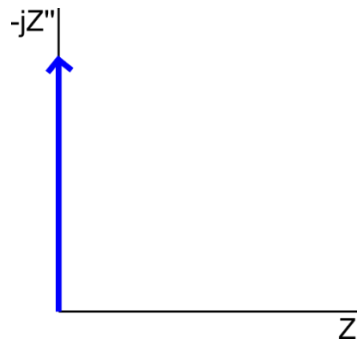


Figure 2.14. A capacitor contains only an imaginary component of impedance.

A similar derivation can be made for inductive impedance. In electrochemistry, however, inductance does not play a significant role in the observed impedance, and so a discussion of this component will be neglected here (187). Furthermore, in electrochemistry the phase angle typically lies in the range $-\frac{\pi}{2} \leq \theta \leq 0$. Electrochemical systems typically have a mixture of resistive and capacitive properties (Figure 2.15), in line with the combination of charge transfer (Faradaic) and polarisation (non-Faradaic) processes that occur (as was seen in Section 2.3.5).

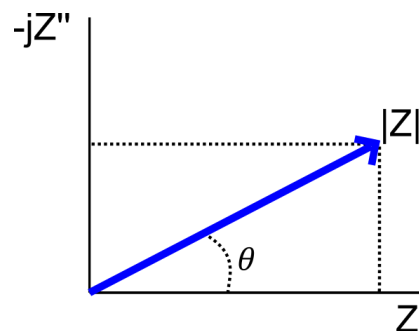


Figure 2.15. The impedance of an electrochemical system typically has both resistive and capacitive components, due to the combination of both charge transfer and polarisation processes.

2.3.8 Capacitance and Dielectric Materials

In its most basic form, a capacitor consists of two parallel plates (or conductors) separated by an insulating material termed a dielectric. When a potential difference is applied, an electric field is established between the plates due to the alignment of dipoles within the dielectric

material. Consequently, equal and opposite charges are present on the plates (Figure 2.16) (198). During this charging process, the voltage across the capacitor increases to a steady state value and the current exponentially decays to zero. When the applied potential is removed, the voltage across the capacitor decays to zero and a transient current in the opposite direction decays to zero once more. In the case of an alternating potential such as a sinusoid, however, current passage is permitted by the cyclic charging and discharging states stimulated.

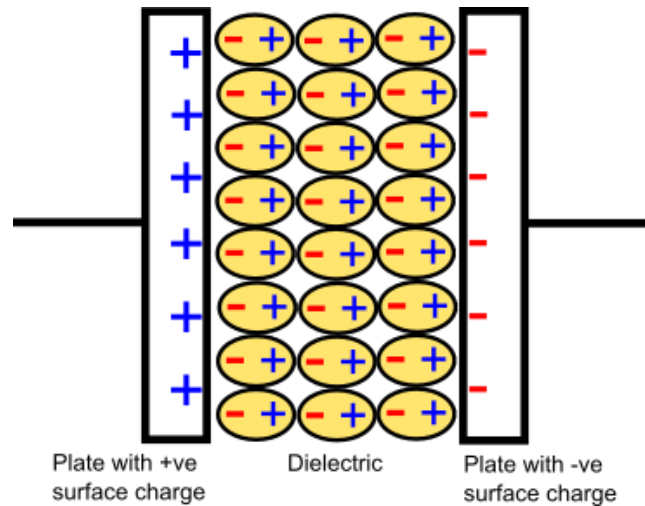


Figure 2.16. Diagram of a charged capacitor. Dipoles within the dielectric material are aligned with the electric field.

The permittivity of a dielectric is defined as the relationship between charge density (σ) and electric field strength (E) such that:

$$\frac{\sigma}{E} = \epsilon_0 \epsilon_r \quad (34)$$

Where ϵ_0 is the permittivity of free space and ϵ_r is the relative permittivity (or dielectric constant) of the dielectric (198). The dielectric constant is a unitless value quantifying the material's insulating properties, with $\epsilon_r = 1$ for a vacuum. Furthermore, capacitance can be quantified using the following equation:

$$C = \frac{\epsilon_0 \epsilon_r A}{d} \quad (35)$$

Where A is the area of a capacitor plate and d is the separation between plates.

Dipoles within the dielectric take some finite time to respond to an applied potential difference; this time is known as the relaxation time. For materials with a range of relaxation times, a frequency dependence emerges for dielectric constant termed dielectric dispersion. A decrease in capacitance is observed at high frequencies due to some relaxation times being too long for

the dipoles to respond, this is termed dielectric loss (186). Specific relaxation processes, such as those discussed in Section 1.6.1, are associated with dispersion. Investigating these material properties can provide useful insight, for example in the study of tissue properties as discussed in Section 1.6.1.

2.3.9 Electrochemical Impedance Spectroscopy (EIS)

Electrochemical Impedance Spectroscopy (EIS) is the fundamental measurement technique used throughout this research for the detection of bacteria. In this method, typically a small amplitude AC perturbation (in this case voltage) is applied, the current response measured, and the complex impedance of the system determined (Equation 22). In a single impedance “sweep”, the frequency of the perturbation voltage is changed over a wide range of values, and a measurement of impedance recorded at each step change. These impedance values are then plotted to obtain impedance spectra, which can provide valuable insight into the properties of the system under study. There are multiple scenarios where EIS is a particularly powerful technique, such as in studies of interfacial processes (for example adsorption and mass transfer), corrosion, coatings and biological membranes (132). Furthermore, EIS has emerged as a popular technique for biosensing applications (such as bacterial detection) due to: the volume of information obtainable through such measurements being higher than with other electrochemical methods; EIS not requiring the use of enzyme labels or redox probes; EIS not being a destructive technique (132,199). As described previously, numerous electrochemical and bacterial processes take place at the interface between an electrode and an electrolyte. These can impact the impedance of the system in different ways at different frequencies of applied potential.

Typically, in EIS small amplitude AC perturbations are used to drive electrochemical reactions. This keeps the system within the window for which the current vs potential relationship is linear and, therefore, follows Ohm’s law (Equation 22) (187). Whilst in general a non-linear relationship exists, localised regions of linearity can be found (Figure 2.17). In this region, the voltage magnitude does not impact the measured impedance and harmonics are not present in the output. Typically, a perturbation voltage amplitude between 10-100 mV is used for this reason (200). In addition to system linearity, EIS further assumes that the system is both stable and causal (200). The validity of these assumptions may be estimated by using a Kramers-Kronig transform, however, there are practical limitations to its use (in particular as a result of it only being possible to perform EIS measurements over a finite frequency range) (187). These relations will not, therefore, be discussed further in this thesis.

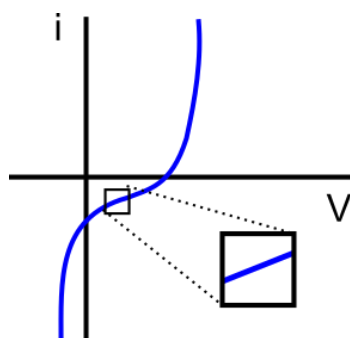


Figure 2.17. The relationship between current and voltage for a hypothetical electrochemical system, with a localised region of linearity highlighted.

Instrumentation is a crucial aspect to performing quality EIS measurements. Commercial impedance analysers have performance limitations (in particular low voltage and current detection limits) which should be respected when selecting measurement parameters. The number of electrodes used is also an important choice; typically, either two or three electrode set-ups are adopted. In the two-electrode arrangement, the potential applied between a working electrode (WE) and a counter electrode (CE) is studied. In this configuration, interfacial processes at both electrodes contribute to the measured impedance (200). Conversely, in a three-electrode arrangement a reference electrode is added which is ideally non-polarisable and enables only the working electrode interface to be measured. Further, reference electrodes provide a known reference potential which others may be measured in relation to (186). Whilst there are benefits to using a three-electrode configuration in many investigations (such as increased electrode stability in real-time DNA sensing (201)), using fewer electrodes minimises experimental complexity and can reduce unnecessary electrical artefacts (186,200). In comparison to the WE, a CE is typically designed to have a larger surface area. This both results in the relative contribution of the CE to the overall capacitance of the electrodes to be minimal, and means that the speed of reactions at the CE are not a limiting factor in the observation of WE processes (132). A further key instrumentation consideration is the influence of cable positioning. For example, cables can result in an increase in phase (inductance) at high frequencies. This can be mitigated by twisting the cables together (202).

2.3.10 Impedance Data Modelling and Analysis

Electrical circuits are frequently used to model EIS data. The electrochemistry of the system, described in Sections 2.3.1- 2.3.8, can be modelled using an electrical circuit which displays the same frequency dependant impedance behaviour. Circuit modelling can, therefore, greatly

increase understanding of the contributions of different physical processes occurring within the electrochemical cell (203). A generally accepted rule is that the circuit model should contain the minimum possible number of circuit elements to fit to the data, with each of those elements representing a known process within the electrochemical cell (187).

The simplest general circuit model which is the basis of all EIS data (and has components added to it to explain more complex behaviour) contains only resistors and a capacitor (Figure 2.18). This model is a simplified version of the Randle's circuit (detailed later in this section), and describes the scenario where an electrode is in contact with a solution (203). The resistor R_S represents the solution resistance between measuring electrodes, and is dependent upon the concentration and species of ions in the solution for example (132). The second resistor R_{ct} represents the charge transfer resistance. As described in Sections 2.3.5-2.3.6, this is determined by Faradaic reactions and associated concepts. The final circuit component, C_{dl} , is the double layer capacitance as described in Section 2.3.4.

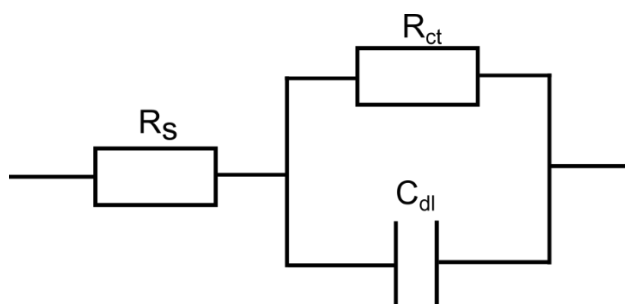


Figure 2.18. Basic equivalent circuit model for EIS data, containing solution resistance (R_S), charge transfer resistance (R_{ct}), double layer capacitance (C_{dl}).

Both EIS and equivalent circuit model (ECM) data are visualised using Bode and Nyquist plots. The former are logarithmic plots of impedance modulus and phase against frequency. Conversely, in a Nyquist plot the real and imaginary components of impedance are plotted against each other. To exemplify this, in Figure 2.19 the characteristic shape of these plots over a broad frequency range are shown for the circuit model in Figure 2.18 (which describes a basic electrochemical system) (132). Regions of these plots that reveal key information about the electrochemical system under study have been highlighted. Firstly, focusing on the bode plots in Figures 2.19A and 2.19B, it is clear that impedance varies significantly with frequency. The current path through the circuit is highlighted in Figure 2.19C and, from this, the low and high frequency impedance magnitudes can be approximated (Figure 2.19A). At low frequencies the impedance magnitude is maximal ($R_S + R_{ct}$) and at high frequencies it reaches a minimum (R_S). Further, the Nyquist plot shows the characteristic semi-circle shape that emerges for simple electrochemical systems such as this (Figure 2.19D). The location and shape of this trace can

once more be used to deduce the values of R_s and R_{ct} . A common modification to this circuit is the replacement of C_{dl} with a constant phase element (CPE), as is done within Chapter 5. A CPE is more appropriate to describe the non-ideal capacitive behaviour which is often observed in real systems, and frequently manifests as a depressed semi-circle when used in this ECM (186,203).

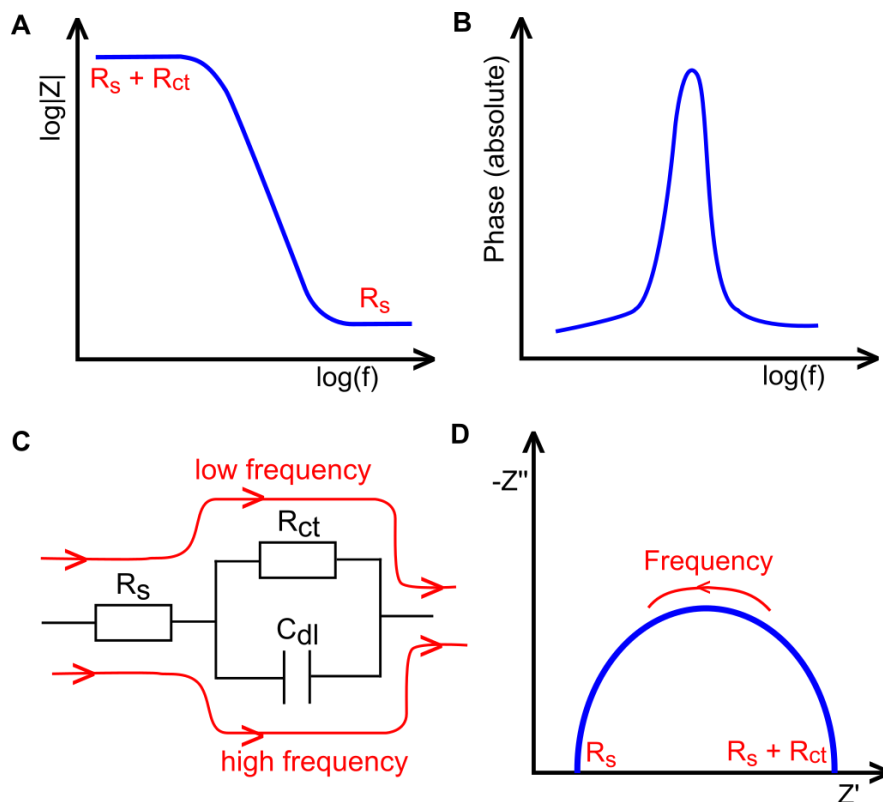


Figure 2.19. EIS data presentation and circuit modelling with: (A) the magnitude (modulus) Bode plot for the simple circuit model in Figure 2.18; (B) the corresponding absolute phase Bode plot (it should be noted that circuits are typically capacitive as is the case here and thus show negative phase, however, by plotting absolute phase positive values are generally worked with); (C) the current path through the ECM at low and high frequencies; (D) the corresponding Nyquist plot for the ECM.

This circuit does, however, neglect the effects of diffusion processes. The impedance of mass transfer is included in the full Randle's circuit by the addition of a Warburg element in series with R_{ct} (Figure 2.20A). This element does not have a direct electrical analogy. Crucially, there are different types of Warburg element, with the following descriptions summarised from Lasia (2014) (132). In the case of semi-infinite diffusion, a semi-infinite Warburg element is used. As shown in Figure 2.20B, this behaviour is characterised by a straight line at $-45^\circ (-\pi/2)$ phase in the Nyquist plot. At high frequencies the semi-circular shape representing kinetically controlled processes remains, however, this 45° low frequency tail emerges due to mass transfer

effects. For many real systems, however, it is more appropriate to use a finite-length Warburg element where the diffusion is bounded. For a transmissive boundary (also termed short circuit terminus), the Nyquist plot takes the form in Figure 2.20C, whereas for a reflective boundary (also termed open circuit terminus) the imaginary component of the low frequency tail continues to rise (Figure 2.20D). In each scenario the equation governing Warburg impedance varies, however, in each case it is concentration dependant. Further, the finite length forms are characterised by the parameter W-T, which has the form:

$$W - T = \frac{L^2}{D} \quad (36)$$

Where L is the diffusion length and D the diffusion coefficient.

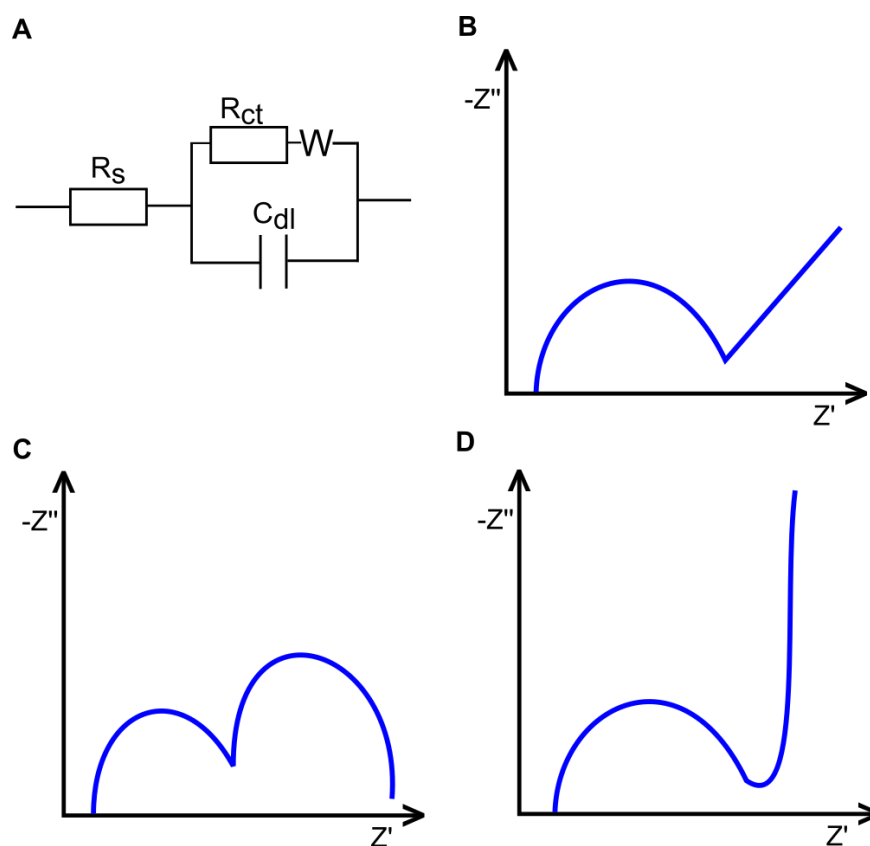


Figure 2.20. Nyquist plots for Randle's ECM containing a Warburg element. (A) displays the ECM and in (B) the Nyquist plot using a semi-infinite Warburg element is shown; in (C) a finite length transmissive (short) element is used; in (D) a finite length reflective (open) element is used.

2.4 Fundamental Machine Learning Concepts Underpinning this Research

Within this project the power of machine learning is exploited to the benefit of bacterial detection and identification using EIS data. The terms "artificial intelligence", "machine

learning” and “deep learning” are commonly used to describe technologically advanced algorithms, with some ambiguity existing around their use (204). For the purposes of this thesis, Artificial Intelligence (AI) is a broad term which refers to a computer program which can perform tasks that would traditionally be considered to need human intelligence. The term AI was first used in the 1950s, however, with the exponential increase in computational power in recent years it has come to the forefront of technological innovation (204,205). A subset of AI (Figure 2.21), Machine Learning (ML) algorithms are able to learn and improve their performance based on training data in order to accurately recognize patterns in the data (206). A powerful subset of ML is Deep Learning (DL) (Figure 2.21). In this technique, multiple layer Artificial Neural Networks (ANN) are used to process large volumes of data and extract patterns to form predictions for new data (205). The potential applications of AI in healthcare are wide ranging, from aiding clinical decisions and diagnosis, to public health monitoring and drug discovery (207).

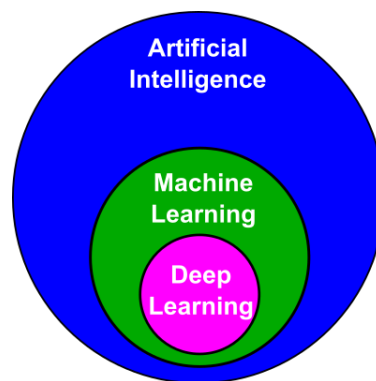


Figure 2.21. Defining artificial intelligence concepts.

2.4.1 Supervised vs Unsupervised Learning

A crucial distinction between categories of machine learning algorithms is made based upon their method of learning. Learning is the process used by the system to improve its performance based upon experience, without human reprogramming (204). Two of the most common modes of learning are supervised and unsupervised (207). In supervised learning the algorithm is trained using labelled data where both the input and output states are provided. The system uses this information to evaluate its performance and improve the accuracy of its output predictions. Conversely, unsupervised learning uses unlabelled data. Here the algorithm extrapolates patterns from the input data without a “correct” output providing feedback. Example applications of each of these modes of learning are provided in Figure 2.22 (summarised from Noorbakhsh-Sabet et al. (2019)).

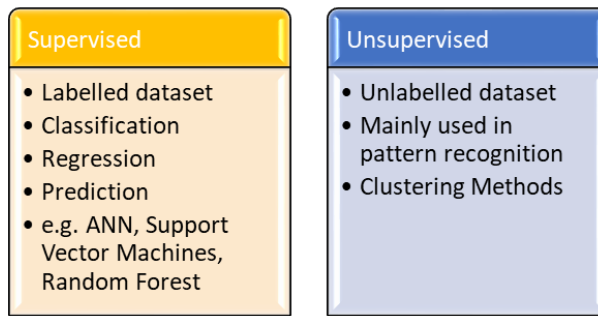


Figure 2.22. Comparison of supervised and unsupervised ML applications (summarised from Noorbakhsh-Sabet et al. (2019)).

Within this project it was appropriate to adopt supervised learning as clear data classifications (such as bacterial species) were known for training data, and a similar classification prediction desired for new data using the ML technique. Further, the ANN was chosen for its multiple category, high classification power using complex non-linear relationships (208).

2.4.2 Artificial Neural Network Fundamentals

Despite being one of the oldest AI models, artificial neural networks still remain one of the most commonly used ML methods (204). In the brain, the creation of neural networks are integral to the learning process (209). At the simplest level, neurons are interconnected by synapses which receive numerous input signals from other neurons and, in turn, pass an output signal on to other neurons. ANN are designed to mimic this architecture and are typically formed of numerous layers of computational units referred to as neurons. These units receive multiple inputs and, after processing these, transmit an output signal to subsequent neurons (Figure 2.23) (210). Like other ML algorithms, the ultimate goal of the ANN is to use training data to approximate a function termed a hypothesis (h) such that an unseen input (x) can be accurately mapped to its true output (y) (204):

$$y = h(x) \tag{37}$$

If the hypothesis can predict the output of unseen data with accuracy, it is said to “generalise well” (204).

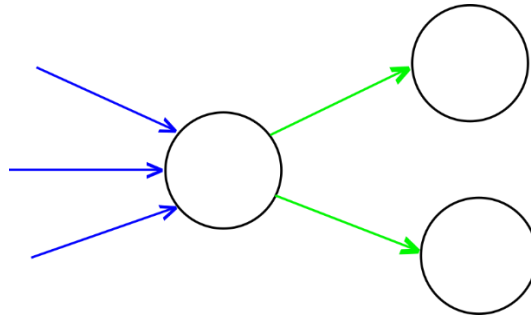


Figure 2.23. A simplistic representation of a neuron (either biological or computational) which receives multiple inputs (blue) and transmits an output (green) to subsequent neurons.

The first layer of neurons in an ANN is termed the input layer (Figure 2.24). The neurons in this initial layer receive their input from the external data, for example an image or experimental measurement values. This layer is succeeded by a number (n) of layers named “hidden layers”. The final layer, which provides the final output prediction, is termed the output layer. Neurons are connected to those in the adjacent layers by directional links (analogous to synapses). In a feedforward configuration, these links only permit information transfer in one direction, from the input to output layers (204). Links are characterised by weights which scale the input; the weight of a given link is representative of its relative importance. At each neuron, a weighted sum of inputs is calculated and then a non-linear activation function applied (as illustrated in Figure 2.24) (204):

$$a_j = g(in_j) = g\left(\sum_{i=0}^m w_{ij}a_i\right) \quad (38)$$

Where a_j is the output of neuron j , g is the activation function, in_j is the input to neuron j from m neurons in the previous layer, w_{ij} is the weight associated with the link between neurons i and j , and a_i is the output from neuron i . In its simplest form, this activation function provides a threshold below which the neuron output is 0 and above which the output is 1. More commonly, functions such as a sigmoid or hyperbolic tangent are now used as activation functions, resulting in the output of the neuron lying at any point between 0 and 1 (210). Further, the weight w_{0j} corresponds to $a_0 = 1$ and is termed a bias, b (204). Biases have the effect of shifting the activation function across the horizontal axis to adjust the threshold point (in contrast to weights which alter the shape of the slope) and add flexibility to the model. This process is repeated for each layer of the network, ultimately resulting in the determination of the probabilities associated with each output class.

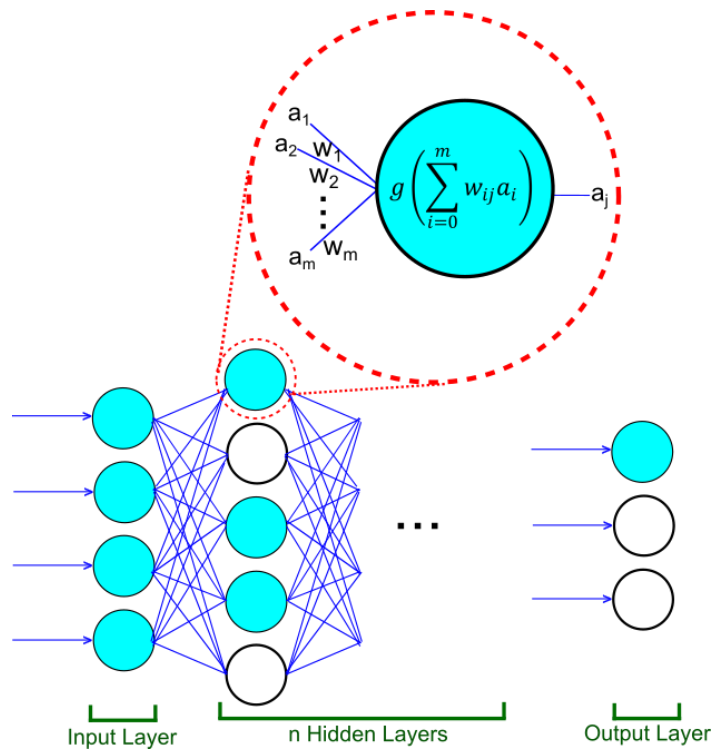


Figure 2.24. Diagram representing an ANN. The operation of a neuron, as described by Equation (38) is highlighted. Coloured neurons represent ones where the threshold is met, and they have a non-zero output to exemplify this process.

During learning these weights and biases are continually adjusted in a mathematical manner using feedback given by training data, to improve the accuracy of the function $h(x)$. This process is named backpropagation. The output of the algorithm is compared to the true output supplied by the training data, and derivatives (gradient) of the loss (error) function computed. These values are then used to update the weights and biases at each layer consecutively, working backwards from the output to the input layer (210). In this process of weight optimisation, a solver is used; the “Adam” solver was used in this thesis, as indicated in Section 2.4.3 (211).

There are several chosen parameters that characterise the ANN, termed hyperparameters. These affect the accuracy and validity of the generated model and are selected with a specific problem and dataset in mind. Crucial examples are the number of hidden layers and neurons per layer. Whilst initially increasing the numbers of each of these can improve the model’s power, if there are too many features in the architecture of ANN the algorithm is vulnerable to overfitting (204). When overfitting occurs, the model is too complex and its prediction accuracy is decreased for new data not involved in training. Commonly, trial and error methods are used to obtain the simplest structure that produces the most accurate ANN, however, it is generally

accepted that the number of features should be far fewer than the number of training examples employed (204,212). Ultimately, large volumes of data are required to train complex, powerful ANN (210). Further hyperparameters include the learning rate and maximum number of iterations.

To assess the performance of an ANN, validation methods are used. Commonly, as done in this thesis, the full dataset is randomly allocated into two categories- training data or test data. The fractional relationship between these two subsets is termed the test/train split. Whilst the paired inputs and outputs in the training dataset are used to adjust the weights and biases of the ANN as it learns, the test data is not involved in this process. Instead, the test data is used to assess the accuracy of the final constructed model and calculate values for sensitivity and specificity for example. Whilst performance metrics such as these can be quantified, ANNs are often described as a “black box” as it is not possible to ascertain the mathematical algorithm underpinning the predictions, in contrast to other ML methods which provide more transparency (206,208). This has raised both ethical (213) and medical device regulatory (207) concerns and is, therefore, a point of consideration in the discussion within Chapter 7.

2.4.3 Scikit-learn’s MLP Classifier Neural Network

As will be described in Chapter 3, the Python machine learning library “Scikit-learn” was used in this project to obtain ANNs for bacterial detection and identification (214). Within this library, the “MLP Classifier” neural network model was utilised. Key parameters of this model relevant to this thesis are detailed in Table 2.2 below.

Table 2.2. Overview of MLP Classifier model parameters.

Parameter	Description	Selection in this Project
Hidden layer sizes	Used to define the number of hidden layers and number of neurons in each.	Trial and error methods used to obtain the optimum sizes (Chapters 3, 6).
Activation function	Function applied to weighted sum of inputs at each neuron (Equation 38).	Default ReLU (rectified linear unit function) function was chosen, where $ReLU(x) = \max(0, x)$. This activation function performs well during the learning process of ANNs with multiple layers (210).

Solver	Used for weights optimisation during backpropagation.	Default 'adam' solver selected, for further details refer to Kingma et al. (2015) (211).
Learning rate	Controls how much the weights are changed by at each step during learning. The learning rate schedule defines whether the learning rate is constant or variable during learning, and the initial rate defines the starting step size.	Trial and error methods were once more used to select learning rate and schedule, with the default being a constant rate at 0.001. Alternative learning schedules trialled were "invscaling" where the rate is decreased during learning using an inverse exponent, and "adaptive" where the learning rate is reduced only if the training loss is not decreasing.
Maximum iterations	Defines how many iterations are used during learning i.e. the number of times each data point participates in the process.	Trial and error methods were used to select this, with variations from the default of 200 trialled.

3. MATERIALS AND METHODS

3.1 Introduction

As detailed in Section 1.8, the aim of this project was to further the development of a disposable electrochemical sensor capable of detecting wound infection in real time. Summarised in Figure 3.1, this involved assessing the suitability of different sensor materials for infection detection, by performing electrochemical impedance experiments using a range of wound pathogens and bacterial culture conditions. Algorithmic approaches to the detection of bacteria were then developed. Within this chapter the methods used will be described in detail.

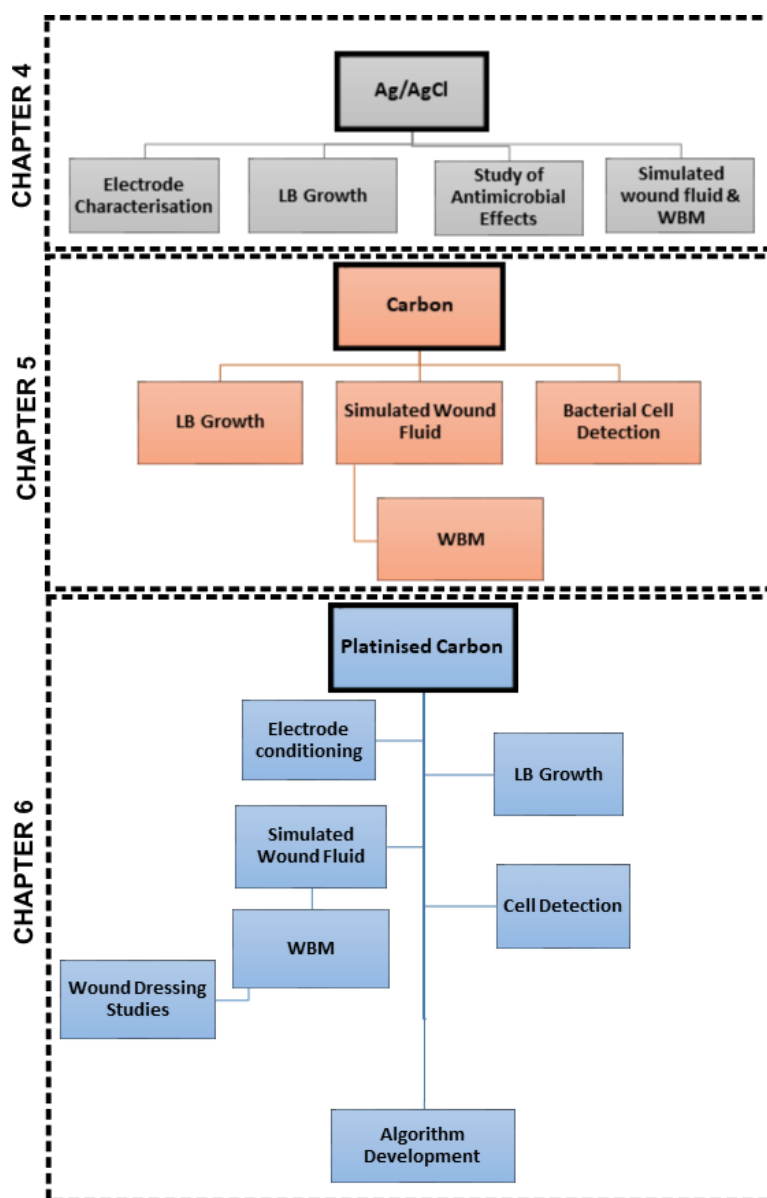


Figure 3.1. Outline of key areas investigated with each sensor. The corresponding results chapters are indicated.

3.2 Bacterial Culture

3.2.1 Bacterial Strains

In line with the key pathogens most commonly associated with wound infection (Chapter 1), the following bacterial species and strains were used throughout the course of this project:

- *Escherichia coli*, DSM30083
- *Proteus mirabilis*, DSM4479
- *Pseudomonas aeruginosa*, PA14
- *Staphylococcus aureus*, NCTC8325
- *Staphylococcus epidermidis*, NCTC11964

3.2.2 Culture Media

The following media were used in this project for the culture of bacteria:

- **LB Medium (Lennox Broth)**

This common laboratory culture medium was formed by mixing 10 g tryptone (Fisher Scientific, code 12787099), 5 g NaCl (Fisher Scientific, code 57653) and 5 g yeast extract (Acros Organics, code 451120010) in 1 L dH₂O (deionised water), and then autoclaving for 20 minutes at 121 °C. Stock bacterial cultures were obtained throughout this project by inoculating 10 mL of sterile LB medium with a single colony of the desired species and incubating for at least 16 hours at 37 °C, 150 rpm.

- ***S. aureus* Selective Medium**

To selectively grow *S. aureus* in polymicrobial experiments a Mueller-Hinton broth supplemented with salt was created from 21 g Mueller-Hinton broth (Oxoid, code CM0405) and 75 g NaCl (Fisher Scientific, code 57653) in 1 L dH₂O. This mixture was sterilised by autoclaving for 20 minutes at 121 °C.

- ***P. aeruginosa* Selective Agar**

Again used in polymicrobial experiments, *Pseudomonas* isolation agar was made by adding 45 g of *Pseudomonas* isolation agar medium (Fluka, code 17208) to 1 L dH₂O supplemented with 20 mL glycerol (Fisher Scientific, code 10021083). This mixture was again sterilised by autoclaving for 20 minutes at 121 °C.

- **Agar Plates**

To create solid agar plates from any broth, 2% w/v agar (Fisher Scientific, code A/1080/53) was added prior to autoclaving.

- **Simulated Wound Fluid (SWF)**

This wound exudate analogue was formed by mixing 50% v/v of foetal bovine serum (Biosera) with Solution A. The sterile foetal bovine serum (FBS) was heat-inactivated in a water bath at 56 °C for 30 minutes prior to use, in line with manufacturer instructions. Solution A is a physiological salt solution prepared from 142 mM NaCl (Fisher Scientific, code 57653), 2.5 mM CaCl₂·2H₂O (Sigma-Aldrich, code 223506) in dH₂O, and autoclaved for 20 minutes at 121°C. This SWF composition is based upon that used by Milne and Connolly (2014) for modelling the pH of the wound environment, however, with the equine serum replaced by FBS in this case (215). This SWF solution was believed to be similar to wound exudate in terms of protein content, ionic content and viscosity (215,216). A wide variety of SWF compositions of varying complexities have been used as part of in vitro wound studies, with these commonly containing both serum and salt components (217,218). The use of FBS in such solutions has been cited on a number of occasions, with successful bacterial culture in these broths reported (130,216). For this reason, therefore, the use of FBS as the serum component of the SWF was believed to be appropriate for this study.

- **Collagen Matrix Solution for WBM**

There are numerous complex elements of a wound bed, for example the bacterial content, host cells and matrix constituents, immune cells, and various chemical and physical properties (217). When modelling the wound bed, the compositional elements most relevant to the investigation must be incorporated. In studies of the bacterial colonisation of wounds, the inclusion of a collagen based matrix has proved important to modelling bacterial biofilm formation (216,217,219). A similar collagen matrix to that developed by Werthén et al. (2010) was included in the WBM within this study (216). The integral element of each WBM was the collagen matrix solution. This was formed by mixing 670 µL collagen I rat tail protein (Gibco, code A1048301, suspended in acetic acid at a concentration of 3 mg/mL) with 315 µL SWF and 15 µL filter sterilised 1 N NaOH (40 g NaOH (Sigma-Aldrich, code S5881) dissolved in 1 L dH₂O). This resulted in a 2 mg/mL collagen concentration in the matrix solution. When this solution was incubated at 37 °C, polymerisation of the gel occurred (due to the

neutralisation of the solution via the addition of the NaOH). The resulting 3D gel replicated the structure and type I collagen content of dermal tissue within a wound.

3.2.3 Cell Washing

For a number of experiments in this project, bacterial cells which lacked the conditions for growth were desired. These were obtained using the following cell washing process. Several 1 mL aliquots of stock bacterial cultures (in LB medium) were first centrifuged at 13,400 rpm for 5 minutes (Eppendorf Mini Spin). The supernatant was then replaced with sterile 0.9% w/v NaCl, and the cells re-suspended by repeated pipetting. Samples were then centrifuged once more, and the supernatant replaced with a further fresh aliquot of 0.9% w/v NaCl. This procedure resulted in washed bacterial cells suspended in 0.9% w/v NaCl which, therefore, lacked the necessary nutrients for growth.

3.2.4 Colony Counting

To enumerate the concentrations of bacteria present in a given sample, the drop plate method of colony counting was adopted. This was based upon the method detailed by Herigstad et al. (2001) (220). A 20 μL aliquot was first taken from the sample and added to 180 μL of sterile LB medium (10-fold dilution). A series of subsequent 10-fold dilutions were then made, ensuring to mix well by pipetting several times at each step. For a chosen number of these dilutions, ten 10 μL drops were then plated onto LB agar and the plates incubated for at least 16 hours at 37 °C (Figure 3.2). Visible colonies were subsequently counted at the dilution where 3 to 30 colonies per drop were present. Using the following relation, the concentration of bacteria in colony forming units per millilitre (CFU/mL) was calculated:

$$\text{Concentration} = \frac{n_{10} * 10}{10^{-d}} \quad (39)$$

Where n_{10} is the number of visible colonies summed over all ten drops (i.e. a number per 100 μL), d is the ten-fold dilution factor, and the multiple of 10 converts the units from CFU/100 μL to CFU/mL.

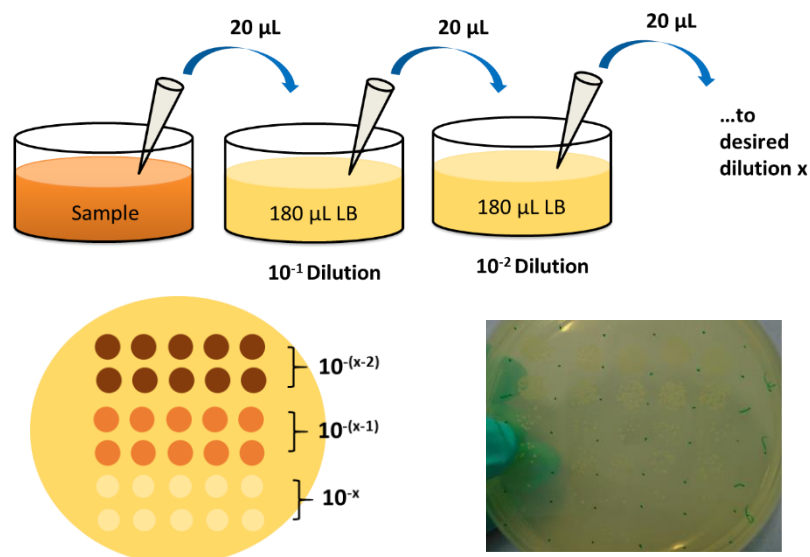


Figure 3.2. Colony counting procedure. A series of ten-fold dilutions were performed followed by plating ten 10 µL drops at a range of concentrations. Plates were then incubated overnight at 37°C, after which time visible colonies emerged (a photograph of *S. aureus* colony growth is provided as an example). Calculations were performed based upon these visible colonies.

3.2.5 Crystal Violet Staining

To visualise bacterial attachment to the electrodes via cellular adsorption and biofilm formation, at the end of a number of growth experiments crystal violet (CV) staining was performed. In a process similar to that described by Merritt et al. (221), electrodes were covered with 0.1% v/v CV in dH₂O for 10 minutes (diluted from 1% CV solution, Sigma-Aldrich, code V5265). This was then removed, and the sensors gently rinsed three times with dH₂O before leaving to air dry. Visual inspection was carried out to assess the level of staining, with darker regions indicating a greater bacterial presence (as illustrated in Figure 3.3 below).

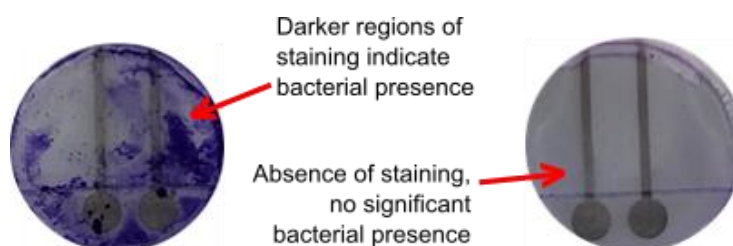


Figure 3.3. Crystal violet staining example.

3.3 Electrode Types

A key objective of this project was to test the suitability of different screen-printed electrodes for the rapid detection of bacteria. Screen-printed sensors have successfully been utilised in glucose detection for example, and they are capable of being manufactured on flexible substrates at a low cost, supporting *in situ* monitoring (222). The following three screen-printed sensors were investigated, each used in a two-electrode configuration:

- **Ag/AgCl WoundSense Electrodes**

These sensors are commercially available flexible electrodes used as part of the CE-marked WoundSense wound moisture monitoring device (Ohmedics Ltd, UK). For this study, Ohmedics Ltd supplied the sensors to enable their wider application to be investigated. The sensors consist of identical Ag/AgCl working and counter electrodes, screen printed onto a clear flexible polyethylene substrate. Key dimensions are provided in Figure 3.4.

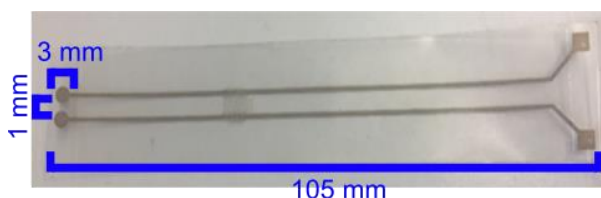


Figure 3.4. Image of the Ag/AgCl WoundSense electrode (with dimensions overlaid).

- **Carbon Electrodes**

The carbon electrodes used in this project were screen printed in-house (DEK 247 semi-automatic) onto a 0.3 mm Polyethylene Terephthalate (PET) substrate (Hi-Fi Films), as depicted in Figure 3.5A. For the first two layers, a solvent cure carbon ink (Electrodag PF-407A, Gwent) was pushed through two different masks to form the electrode pattern. For the final layer a dielectric insulating ink (D2020823D2, Gwent) was used with a third mask to outline the electrode area and insulate the electrode tracks. Table 3.1 outlines the printing parameters utilised. Additionally, prior to printing the first layer and after printing each subsequent layer, the electrode substrates were cured in a fan assisted box oven (Heratherm, Thermo Scientific) at 150°C for 30 minutes. The resulting electrodes (cut to size for experimental use) are shown in Figure 3.5B.

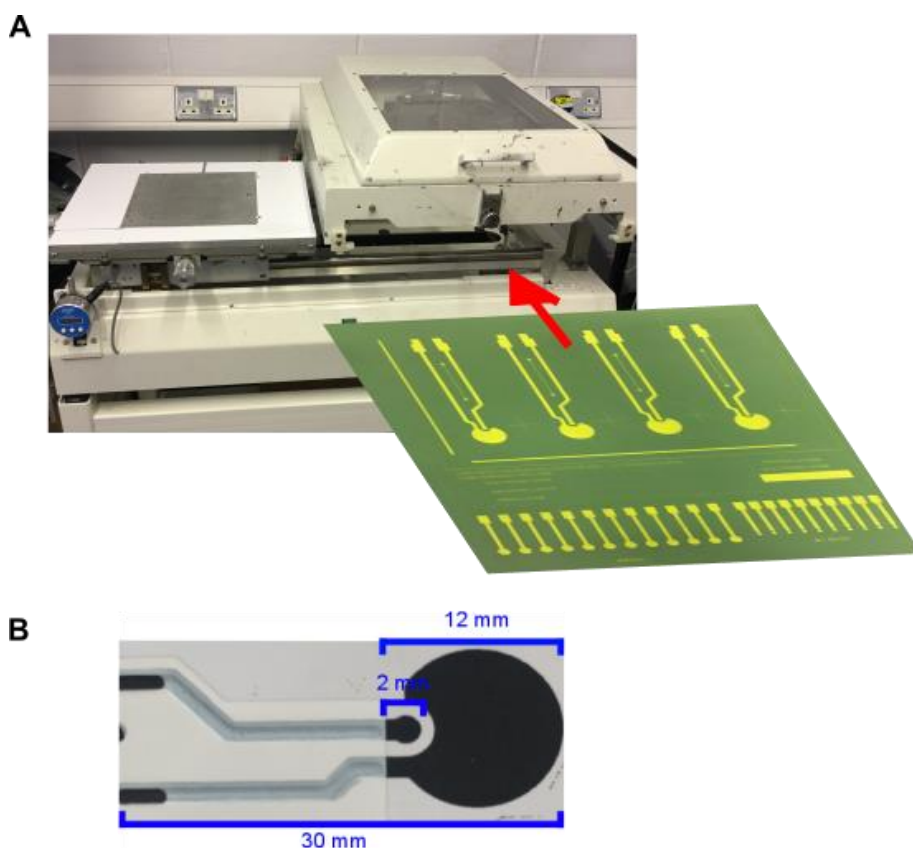


Figure 3.5. Carbon electrode manufacturing: (A) Screen printing of carbon electrodes; (B) Carbon electrode cut to size with dimensions overlaid.

Table 3.1. Screen printer settings for carbon electrode printing.

	Track Layer (1)	Electrode Layer (2)	Dielectric Layer (3)
Flood Speed	3	3	3
Print Speed	3	3	3
Print Height (mm)	-1.9	-1.9	-1.9
Right Stop (mm)	120	120	120
Left Stop (mm)	80	90	90
Squeegee Pressure	10	11	11
Print Settings	Print/print	Print/flood	Print/flood

- **Platinised Carbon Electrodes (PCE)**

These sensors were again provided by Ohmedics Ltd, who had recently developed them with the aim of applying them to bacterial detection. They were professionally manufactured by a UK printing company, via screen-printing platinised carbon ink onto a PET substrate. Each sensor contained a single large counter electrode and 8 smaller working electrodes (Figure 3.6). The counter electrode had a larger surface area than the previous carbon sensors, however, the circular working electrodes had the same diameter (2 mm). For experiments performed using the multiplexer system

(Section 3.4) a connection was established with a single central working electrode and the counter electrode only, with multiple sensors used to obtain multiple replicates. For other experiments, multiple working electrodes from a single sensor were measured to reduce the volumes of media required (detailed in the subsequent sections).

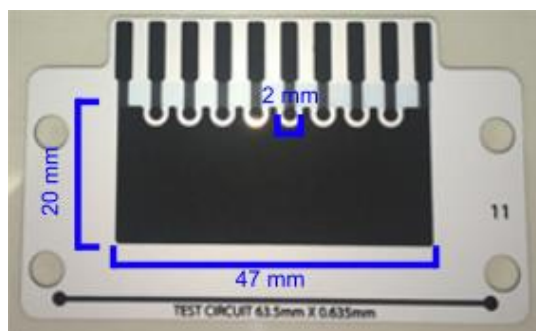


Figure 3.6. Image of a PCE sensor (with dimensions overlaid).

3.4 Electrochemical Impedance Spectroscopy (EIS) Measurements and Data Analysis

Throughout this project, impedance measurements of bacterial suspensions were performed over several hours using different sensors to determine the suitability of each sensor for real-time infection detection. The core measurement procedures common to all impedance experiments are detailed within this section. Throughout each step of the measurement process, a custom MATLAB based guided user interface (GUI) (which was developed previously by researchers within the group) was used for measurement and data management. The role of this interface will be highlighted where appropriate.

3.4.1 Impedance Measurements

Throughout this study, a Solartron SI1260 impedance gain/phase analyser (Solartron Analytical) was predominantly used to perform impedance measurements (Figure 3.7), with a 200 mV rms perturbation voltage (vs OCP) applied. As discussed in Chapter 2, typically a lower measurement voltage is applied in EIS to maintain system linearity. The suitability of this slightly higher voltage was explored in depth by Ward (2015) (223), who found that very large noise is present when lower voltages are adopted for EIS with screen printed sensors such as those used in this study. Instead, 200 mV provides an appropriate low noise, stable response which is desirable for bacterial investigations such as this (223). Due to this (and much previous work within the research group (168,224)), 200 mV was the default perturbation voltage

selected for use in this study. The impact of selecting this applied measurement voltage will, however, be revisited within Chapter 4.



Figure 3.7. Image of the Solartron SI1260 impedance gain/phase analyser used for impedance measurements.

EIS measurements were performed throughout the frequency range $0.1 - 1 \times 10^6$ Hz at 10 steps/decade. Due to equipment availability, for a number of Ag/AgCl sensor experiments only, a PalmSens 4 electrochemical interface (PalmSens) and associated PStace software was used to perform identical impedance measurements. By limiting the use of the PalmSens instrument to a small number of isolated experiments, any minor differences between the PalmSens and Solartron measurements will have had negligible impact upon the findings of this study. Any results obtained using the PalmSens instrument will be indicated, otherwise it can be assumed that the Solartron was used. The Solartron instrument was used for the majority of measurements within this project as its accuracy and reliability has been verified previously within the research group.

In conjunction with the Solartron impedance analyser, Z-Plot and Z-View (Scribner Associates) software packages were used to firstly initiate measurements, and then view the resulting Nyquist and Bode plots respectively (Figure 3.8A, 3.8B). In addition to performing experiments by manually connecting electrodes to the analyser via crocodile clips and subsequently initiating the measurement process one sensor at a time, an Arduino-based multiplexer system (developed previously by members of the research group) was used. This system enabled measurements of up to 16 sensors to be made consecutively in an automated manner over several hours (summarised in Figure 3.8C). Soldered cable harnesses made for each sensor type using flat printed circuit/ flat flexible cable connectors (FPC/FFC) connected the individual sensors to a small relay box which was, in turn, connected to the impedance analyser. The Arduino system interfaced with the PC and this relay box, switching consecutively between measurement channels as appropriate.

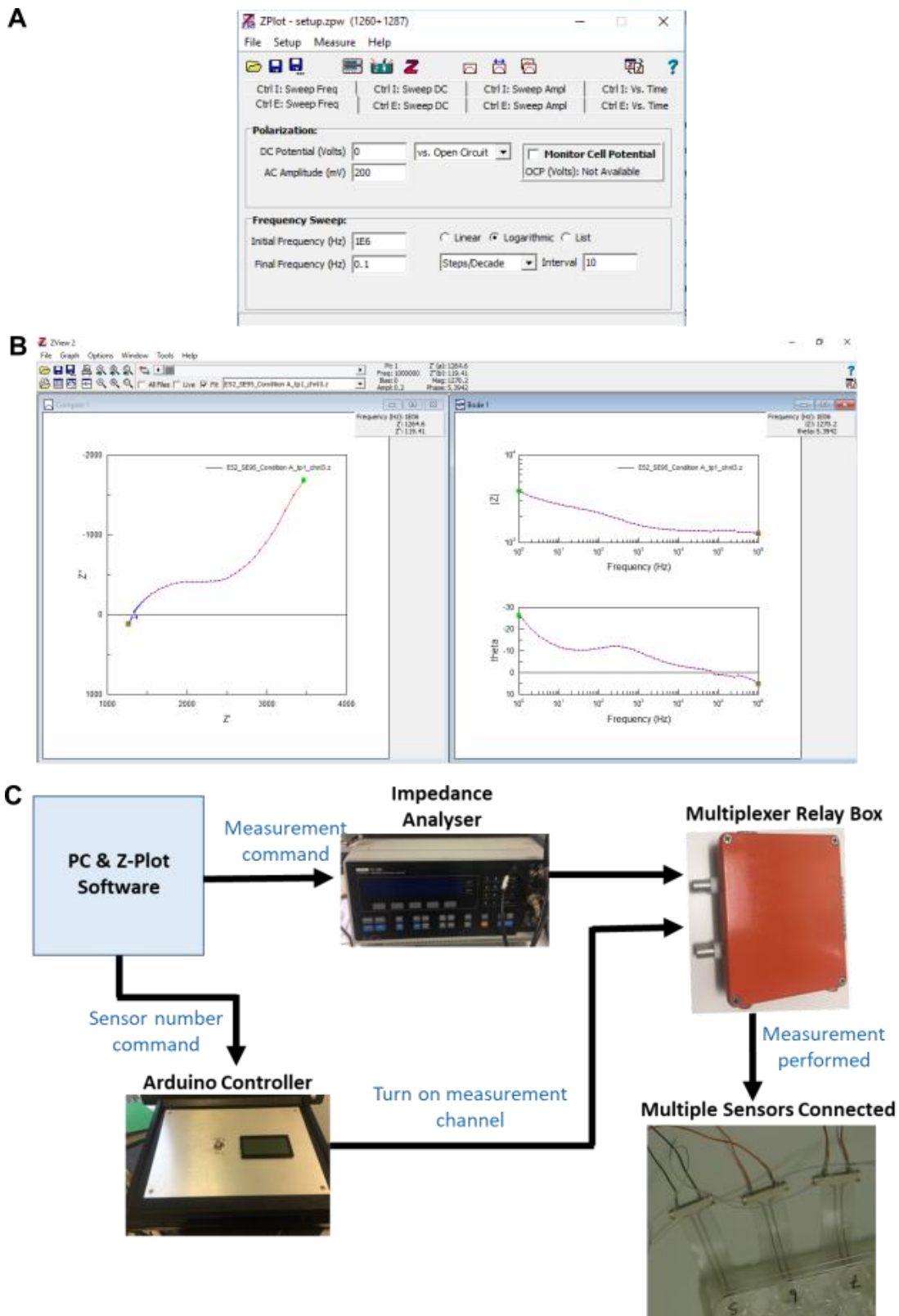


Figure 3.8. Electrode measurement control overview with: (A) showing the Z-Plot software used to control measurement parameters and run the experiment; (B) showing the Z-View software used to visualise the measurement data; (C) displaying a flow diagram of the multiplexer measurement process.

Using the custom MATLAB GUI, batch files that instructed multiple measurements at specific time intervals could be created (Figure 3.9A). These measurements were each labelled according to the experiment number, sensor number and measurement time point, and were loaded and run through the Z-Plot software “Measure” menu. Further, the GUI provided random electrode chamber assignment (for example sterile or infected). Automated measurements could, therefore, be performed without further manual input following the initial connection. At the end of an experiment, the GUI was further used to import the obtained data (Figure 3.9B) and store it in a PostgreSQL database (v9.6.3, The PostgreSQL Global Development Group) for later recall.

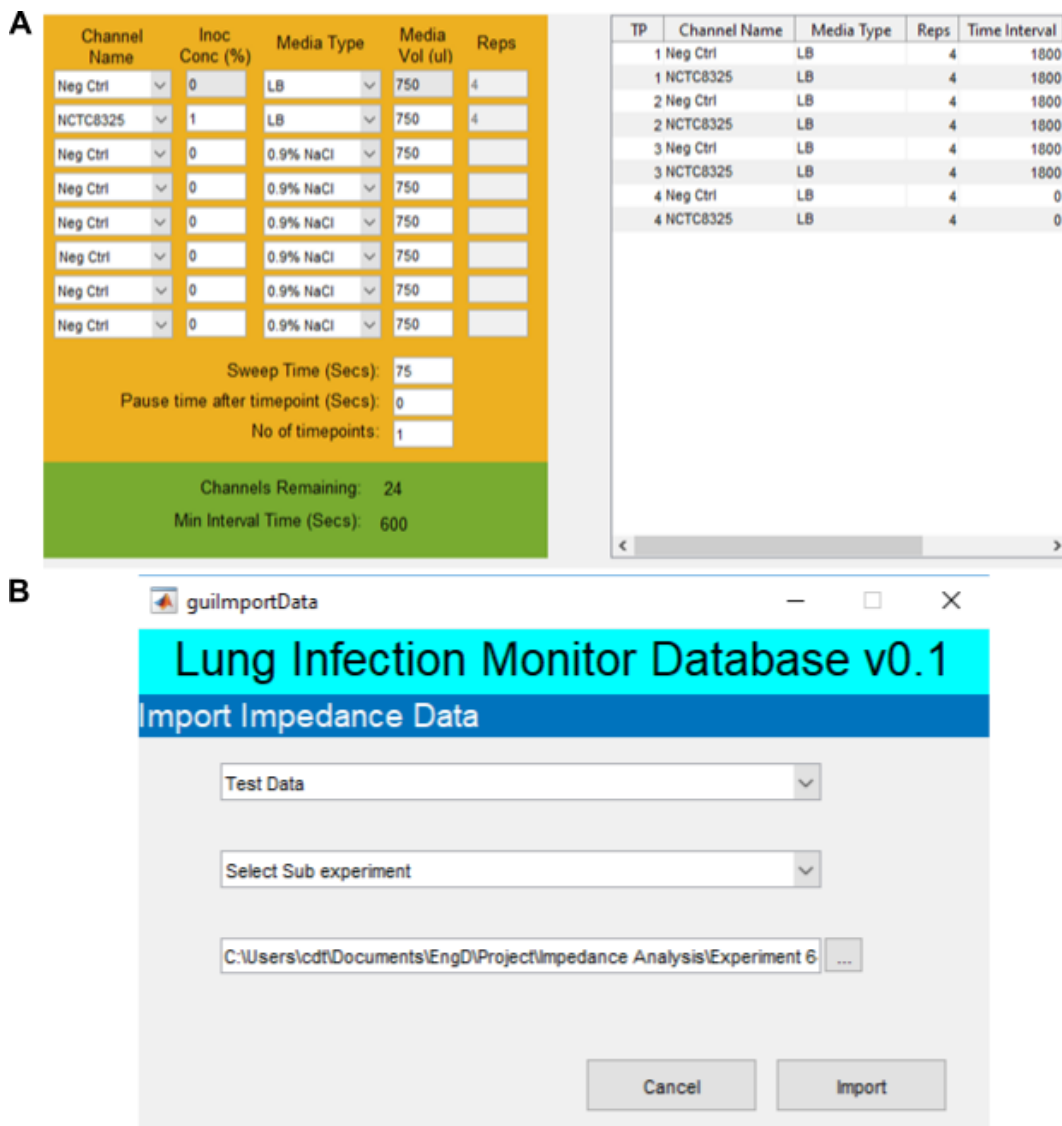


Figure 3.9. Use of the experiment GUI for: (A) measurement batch file creation; (B) data import.

3.4.2 Spectrum Normalisation and Analysis

Impedance data normalisation was carried out using a patented method for cell recognition, developed previously within the research group at Strathclyde University (224). Changes to the impedance spectra over time were highlighted using the following relation:

$$IP_{normalised} = \frac{IP_{t=n}}{IP_{t=0}} \quad (40)$$

Where $IP_{normalised}$ is the normalised impedance parameter, $IP_{t=n}$ is the impedance value at a given time n , and $IP_{t=0}$ is the starting impedance value. This normalisation process could be carried out within the MATLAB GUI, which additionally enabled plotting of both the raw (not normalised) and normalised data. Further, the data could be averaged, and standard deviations calculated for each experimental condition at each time point (Figure 3.10). Typically, each condition was tested with $n = 4$ replicates.

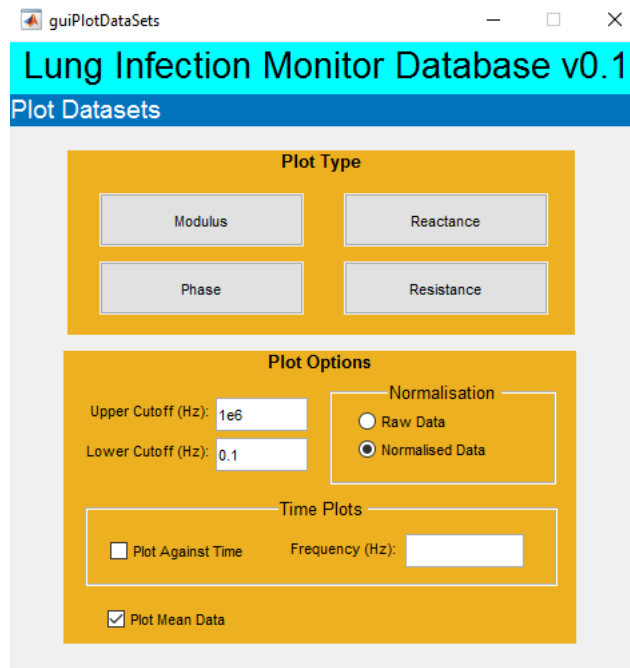


Figure 3.10. GUI plotting options selection.

To determine the significance of any changes in impedance occurring over time, statistical analysis was performed using Minitab 18 Statistical Software (Minitab LLC). Initially, normality testing was performed on data from early experiments using the Anderson-Darling test. This test suggested no significant deviation from normality, therefore the two sample t-test ($\alpha = 0.05$) was adopted for all experiments. It assessed the significance of any changes to normalised impedance by comparing the negative control chambers to the bacterial chambers for example.

3.5 Ag/AgCl Electrode Methods

The first sensor investigated within this study was the Ag/AgCl flexible WoundSense electrode. As will be highlighted in Chapter 4, Ag/AgCl electrodes have desirable electrochemical properties and are currently used in the measurement of various biological signals, including ECGs (225,226).

3.5.1 Ag/AgCl Electrode Experimental Assembly

The Ag/AgCl electrodes were supplied in sterile packaging, ready for use by Ohmedics Ltd. Electrodes were secured between acrylic plates using silicone sealant (Servisol, Farnell code 31665), to create arrays of self-contained wells with the sensors at the bottom of each well (in Figure 3.11 an example set up is shown, with 4 electrodes out of a possible 8 per plate sealed in place). These acrylic plates were manufactured to the same dimensions as standard microplates. The sealant was left to cure at room temperature for at least 16 hours. Initially, different sealant patterns were trialled, and any leaking visualised by filling each chamber with 0.1% CV solution for 24 hours which resulted in an appropriate sealant pattern being selected (Figure 3.12). Prior to experimental use, sensors were rinsed thoroughly in dH₂O to remove any surface residues remaining from the manufacturing process.



Figure 3.11. Ag/AgCl sensor plate assembly. Here 4 sensors have been secured between the acrylic plates, which have the potential to house up to 8 sensors.



Figure 3.12. Image of crystal violet leakage from chamber after 24 hours (during sealant pattern testing).

3.5.2 Ag/AgCl Electrode Characterisation

For an initial characterisation of these electrodes, simple impedance measurements (sweeps) were conducted in 0.9% w/v NaCl (saline solution). After securing 4 electrodes between acrylic plates to form 4 isolated wells as detailed previously, the electrodes were rinsed in dH₂O and 750 µL of saline solution added to each well. The system was then incubated at room temperature for 2 hours to allow any initial background processes to settle (186). Using the PalmSens device, a series of consecutive measurements were made, each using a 200 mV perturbation voltage ($1 - 1 \times 10^6$ Hz). For comparison, consecutive measurements using the lower 10 mV measurement voltage were also performed using new electrodes. Following this, for a further set of new electrodes filled with saline solution, the series of impedance measurements in Table 3.2 was conducted consecutively. Together, these experiments aimed to assess the sensor's impedance response at each different voltage.

Table 3.2. Ag/AgCl electrode characterisation measurement voltages.

Sweep No.	1	2	3	4	5	6	7	8	9	10	11
Measurement Voltage (mV)	1	1	10	10	20	40	60	80	100	200	20

3.5.3 Ag/AgCl Electrode LB Medium Growth Experiments

To investigate the ability of the Ag/AgCl electrodes to detect the growth of bacteria using EIS, initial experiments were conducted using LB medium. For each experiment, 8 electrode/well assemblies were created. Following this, sensors were rinsed in dH₂O and sterilised by submerging in 70% v/v EtOH in dH₂O solution. Each well was then immediately filled with 750 µL of sterile LB medium and left in the microbiology safety cabinet for around 30 minutes to allow for any remaining ethanol to evaporate.

The sensors were next incubated overnight (around 16 hours) at 37 °C, enabling any background processes to settle (186). The media in each well was then replaced with 750 µL of fresh LB medium, and a sterile impedance sweep carried out at 37 °C. Next, four wells were inoculated with 7.5 µL of stock bacterial culture, forming approximately a 1% starting inoculum. An impedance measurement was taken for each sensor, followed by incubating the chambers at 37 °C in a humid environment (created using wet paper towels). After a further 5 hours and 24 hours, more measurements were performed. Additionally, colony counting was carried out at 0 hours and 24 hours. This procedure was followed twice for *P. aeruginosa* (first using a 20 mV and then a 200 mV measurement voltage), and for *S. aureus* using a 20 mV

measurement voltage. The PalmSens 4 device and manual clipping (no multiplexer) were used to perform measurements in each case.

3.5.4 Ag/AgCl Sensor Zone of Inhibition

To visualise any local inhibitory effect of the electrodes upon PA14 growth, the Ag/AgCl electrodes were secured inside 6 cm Petri dishes (using Servisol silicone sealant, $n = 12$). After 70% v/v EtOH sterilisation, 5 mL of hot LB agar was poured into each dish, covering the sensors. After cooling, 0.5 mL of stock culture diluted to 1% of its initial concentration was spread onto 8 plates, and 0.5 mL of sterile LB medium spread onto the remaining 4 plates (Figure 3.13). For the sterile, and half of the bacterial plates, EIS measurements with a 200 mV measurement voltage were performed at 0 Hrs, 5 Hours, 24 Hours and 48 Hours with 37 °C incubation in between. At the end of the experiment, the plates were photographed, and the appearance of the electrodes and surrounding agar visually assessed. This procedure was derived from that carried out during antibiotic susceptibility testing, where a zone of inhibition due to an effective drug can be visualised (227).

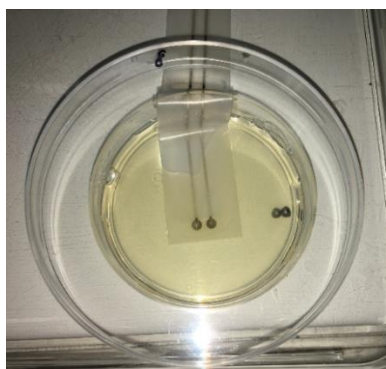


Figure 3.13. Zone of inhibition experimental set up. An electrode was secured to a Petri dish and agar poured on top. Once set, inoculated LB medium was added.

3.5.5 Minimal Inhibitory Concentration of Silver

Further investigating the bactericidal effects of these sensors, the minimal inhibitory concentration (MIC) of silver on *P. aeruginosa* was next determined using silver nitrate (AgNO_3). A 5 mL stock solution of silver nitrate (Sigma-Aldrich, code 204390) in LB medium was created at a concentration of 1 g/L. Via serial dilutions, the following solutions were also obtained: 100 mg/L, 10 mg/L and 1 mg/L, and each of these solutions filter sterilised (0.22 μm , Millex-GP syringe filter unit). One colony of *P. aeruginosa* was added to each of these 5 mL solutions, and to a further blank LB solution. Each sample was incubated at 37 °C for 70 hours, and visible growth assessed. The lowest silver nitrate concentration at which visible growth

was inhibited was determined. Using this silver nitrate result it was possible to extrapolate the MIC of silver alone and, therefore, estimate the quantity of silver hypothesised to have been released by the electrodes during growth experiments.

3.5.6 Ag/AgCl Electrode Wound Bed Model Development

To build upon the preliminary experiments where bacterial growth in LB medium was measured using the Ag/AgCl electrodes, a more accurate simulation of the wound environment was desired.

As an intermediate step, the process described for the LB growth experiments (Section 3.5.3) was first repeated using SWF instead of LB medium. For this experiment, manual on-bench PalmSens measurements were performed at 0 Hours (sterile), 0 Hours (inoculated), 1 Hour, 2 Hours, 5 Hours, 24 Hours and 48 Hours with humid 37 °C incubation in between. A 20 mV perturbation voltage was applied during measurements of *S. aureus* growth, as this experimental combination elicited the greatest normalised impedance response in LB medium (Chapter 4). Whilst an initial sterile impedance sweep was carried out for consistency with the previous experiments, normalisation was performed against the subsequent post-inoculation measurement. By performing data normalisation against this non-sterile starting measurement, the protocol was believed to more accurately reflect a real-life scenario where a sterile initial wound state would not be possible. A number of bacteria will naturally already be present in a wound, even if not clinically infected.

Advancing this, a collagen matrix gel was incorporated into the model. This combination of the collagen matrix and SWF is referred as the wound bed model (WBM) throughout this study. For growth experiments performed in this WBM with the Ag/AgCl sensors, electrodes were rinsed with dH₂O, sterilised by submerging in 70% EtOH and placed face down onto a sterile dish containing LB medium in the microbiology safety cabinet for 2 hours. This enabled ethanol evaporation and electrode surface settlement. Sensor chambers in this instance were created using 24-well plate wells (which required sensor substrate trimming to fit). Onto the base of each well, 200 µL of collagen matrix solution (Section 3.2.2) was spread and the plates incubated at 37 °C for 1 hour. The collagen matrix solution was developed such that complete polymerisation and, therefore, gel formation would occur within this incubation period. After this time, 0.9 mL of SWF was gently added to each well, ensuring not to break up the gel. Bacterial wells were then inoculated with 0.1 mL of stock bacterial culture (~10% inoculation density in an attempt to elicit more pronounced changes) and sterile negative controls had 0.1

mL sterile LB medium added for consistency. A single sterile sensor was then placed face down onto each wound bed model and folded over such that direct contact between the electrodes and the “wound bed” was maintained when the lid was then taped in place (Figure 3.14).

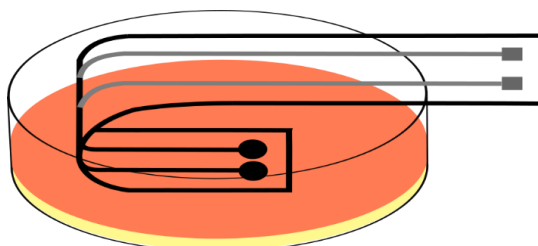


Figure 3.14. Depiction of a Ag/AgCl sensor wound bed model well. Electrodes were folded face down on top of the collagen matrix and SWF wound bed model which was formed within a well of a 24-well plate (not to scale).

The WBM impedance measurements were performed with a 20 mV measurement voltage, using the multiplexer system and Solartron impedance analyser. This enabled sustained chamber incubation at 37 °C as chambers did not need to be removed from the incubator for manual connection and on bench measurement, therefore, bacterial growth was not disturbed (Figure 3.15). Both *S. aureus* and *P. aeruginosa* growth were investigated in the model. Additionally, *P. aeruginosa* growth was studied using a 200 mV measurement voltage and a comparison to the 20 mV result made (as was done in the LB medium experiments). For each of these experiments, numerous measurements were performed over at least a 24-hour period.

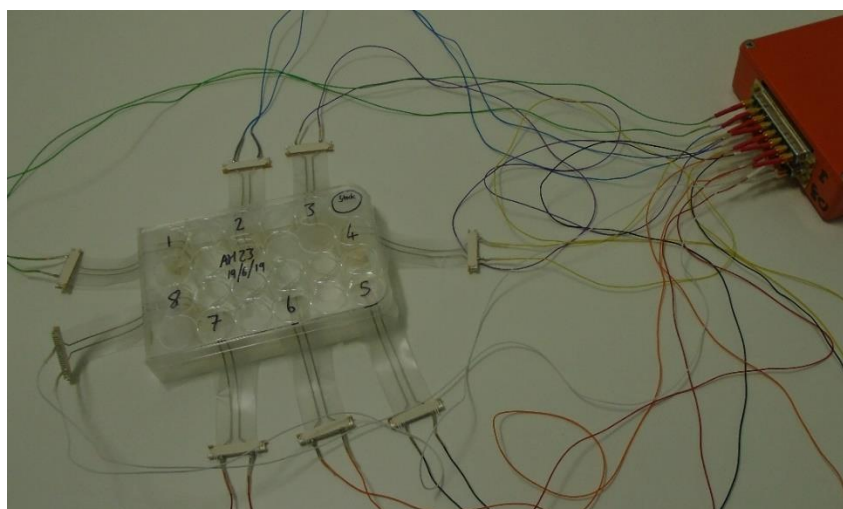


Figure 3.15. Image of the Ag/AgCl sensor automated WBM measurement set-up. Each WBM was formed within a separate well of the 24-well plate and sensors folded on top. Sensors were then connected to the multiplexer relay box (orange). This entire arrangement was placed into the incubator for the duration of the experiment.

3.6 Carbon Electrode Methods

Carbon was the second electrode material investigated in this project. Described in more detail within Chapter 5, the stability and low cost of carbon sensors has made them attractive for biological applications such as blood glucose monitoring (222,228,229).

3.6.1 Carbon Electrode Assembly and Conditioning

The carbon sensors were manufactured as described in Section 3.3. Arrays of multiple electrodes at the bottom of isolated wells were again created by securing sensors between acrylic plates with Servisol silicone adhesive and leaving to cure at room temperature for at least 16 hours (Figure 3.16).



Figure 3.16. Carbon electrodes assembled into an array of 8 sensor wells.

The sensors were then thoroughly rinsed in dH₂O to remove any residues from their surface, and each chamber immediately filled with 750 μ L of 0.9% w/v NaCl in dH₂O. Electrochemical conditioning was performed by applying a +2 V rms (vs OCP) potential for 3 minutes followed by a -2 V rms (vs OCP) potential for 3 minutes (126, 209). Using the Solartron and multiplexer system, an impedance sweep between 0.1 - 1 $\times 10^6$ Hz (200 mV) was performed for each sensor both prior to and following conditioning. This confirmed the desired reduction in baseline impedance and an improvement in sensor consistency (Figure 3.17).

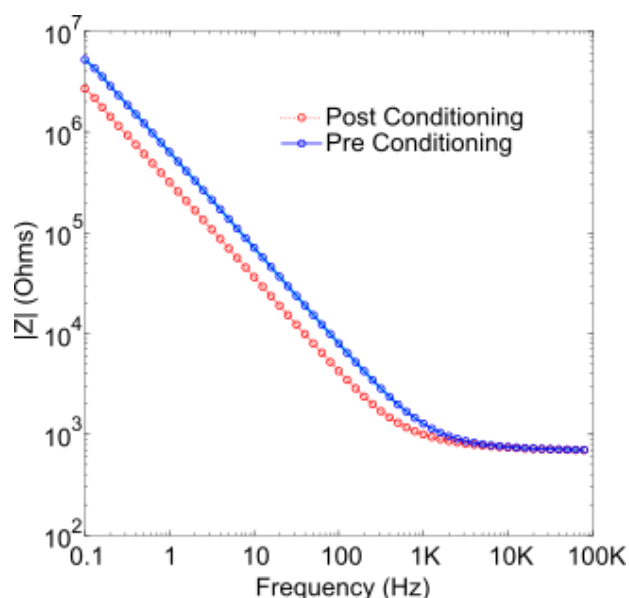


Figure 3.17. Carbon electrode conditioning effects. A clear reduction in impedance modulus is shown here ($n = 4$).

3.6.2 Carbon Electrode LB Medium Growth Experiments

In a similar manner to the bacterial growth experiments performed with the Ag/AgCl sensors, LB medium experiments were conducted using the carbon sensors. Here, a range of different common wound pathogens (namely *S. aureus*, *S. epidermidis* and *P. mirabilis*) were used to investigate the carbon sensors' suitability for wound infection detection. Furthermore, due to availability of the multiplexer system for these experiments, it was possible to conduct impedance sweeps at a far greater frequency than previously reported by Ward et al., who used these sensors for the detection of *P. aeruginosa* after 24 hours (118). Here, it was possible to perform measurements up to once every 30 minutes. This time reflected the fact that a finite time is required to perform an impedance sweep: around 2 minutes for 0.1 – 1 × 10⁶ Hz or 1.25 minutes for 1 Hz - 1 × 10⁶ Hz per sensor. Most commonly 8 sensors were measured over the wider frequency range, however, in some situations it was more suitable to use the smaller frequency range, enabling up to 16 sensors to be measured consecutively at a frequency of 30 minutes. Alternatively, increasing the time between measurements to one hour for example meant that up to 16 sensors could be measured across the full frequency range.

Following conditioning, sensor arrays were sterilised with 70% v/v EtoH in dH₂O and immediately filled with 750 μL of LB media (ensuring the electrode surface did not dry). The sensors were left in the sterile microbiology safety cabinet for 30 minutes to allow for ethanol evaporation, and then incubated for at least 16 hours at 37 °C in a humid environment (created

by wet paper towels). This incubation enabled the settlement of any background processes prior to experimental measurements (186). Each well's contents were then replaced with 750 μL of fresh LB medium, and a sterile impedance sweep carried out using a 200mV measurement voltage. Next, bacterial wells were inoculated with 7.5 μL of stock bacterial culture. All sensors were then connected to the multiplexer cable harness (Figure 3.18) and incubated at 37 °C continuously for the remainder of the experiment. Automated Solartron impedance measurements (200 mV) were performed over 24 hour periods up to every 30 minutes. Colony counting was carried out both initially, and after 24 hours.

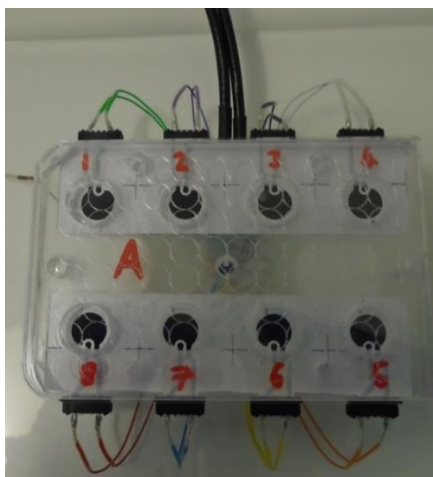


Figure 3.18. Carbon electrode assembly and cable harness connection. Each plate could contain up to 8 electrodes in self-contained wells, and up to 16 electrodes in total could be connected to the multiplexer system for automated measurements.

3.6.3 Carbon Electrode SWF Experiments

After confirming the ability of these sensors to detect a range of wound pathogens in LB medium the methods outlined in Section 3.6.2 were repeated, instead using SWF as the settlement and growth medium. For these experiments, no initial sterile impedance measurement was taken. By omitting this sterile normalisation point for SWF experiments (in the same way as with the previous sensors), a scenario closer to real-life was created since wounds are not sterile initially. Again, automated measurements were performed up to every 30 minutes over at least 24 hour periods, with *S. aureus*, *P. aeruginosa* and *P. mirabilis* investigated in this instance.

3.6.4 Carbon Electrode Wound Bed Model Adaption

For the same reasons outlined previously in Section 3.5.6, experiments were next conducted in the WBM which provided a closer simulation of the wound environment. The WBM experimental set-up used for the Ag/AgCl sensors relied heavily upon the flexibility of those sensors. The substrate used for these carbon sensors was of lower cost for experimental purposes and, consequently, did not incorporate the same flexibility. For this reason, it was necessary to adapt the wound bed model for these sensors.

In this case, the sensors were located at the base of the WBM. Following sensor conditioning and sterilisation, each well was filled with 750 μL SWF. After ethanol evaporation (as previously) sensors were incubated for 16 hours at 37 °C in a humid environment to allow for any background electrode processes to settle. Following this, the SWF was removed and the collagen solution prepared as previously (Section 3.2.2); 100 μL of this was pipetted into each well and the arrangement incubated for 1 hour at 37 °C to fully polymerise the matrix (216). SWF (750 μL) was then gently pipetted on top of each collagen gel. Next, 7.5 μL of bacterial stock culture was added to the bacterial chambers and 7.5 μL of sterile LB medium added to the negative controls for consistency. Plates were then returned to the incubator and multiplexer-controlled impedance measurements (200 mV, 0.1 – 1 x 10⁶ Hz) performed every hour to 5 hours, and then a final measurement performed after 24 hours. This procedure was carried out for both *S. aureus* and *P. aeruginosa* growth and, again, colonies were enumerated at the start and end of each experiment.

3.6.5 Carbon Electrode Saline Experiments

Through performing experiments with washed cells in 0.9% w/v NaCl (saline solution) where no bacterial growth occurred, the impedance changes arising only due to direct interactions between the bacterial cells themselves and the sensor interface were investigated. Again, sensors were first electrochemically conditioned, wells sterilised in 70% EtOH and incubated for at least 16 hours in the experimental medium (0.9% w/v NaCl here). After obtaining washed bacterial cells using the methods detailed in Section 3.2.3, the effects of placing these cells onto the sensors over time were determined via normalised impedance. Measurements were performed at 200 mV using the Solartron and multiplexer assembly. This process was carried out with both *S. aureus* and *P. mirabilis* cells, with the aim of detecting cellular adsorption to the sensors over time.

Further to these experiments, a high concentration of washed *S. aureus* cells was diluted to obtain a range of cell concentrations (around 10^6 – 10^8 CFU/mL). Starting with an impedance sweep of sterile saline and then performing measurements on this range of incrementally increasing bacterial cell concentrations (one after the other on each electrode, 750 μ L each, $n = 3$), the immediate cell concentration dependent effects upon impedance were investigated. For the final measurement, a sterile aliquot of saline solution was measured once more to probe for any lasting cell/sensor interactions such as adsorption.

3.6.6 Equivalent Circuit Modelling

For a sample of the experiments conducted with these carbon sensors, equivalent circuit modelling was performed. This enabled further insight to be gained into the electrochemical mechanisms underlying the observed changes in normalised impedance. The circuit employed was simple, containing only solution resistance (R_s), charge transfer resistance (R_{ct}) and a constant phase element (CPE) (Figure 3.19). This circuit is similar to the Randle's equivalent circuit (Section 2.3.10), however, omits the Warburg impedance element due to the data obtained from these sensors lacking a low frequency tail in the Nyquist plot that is characteristic of Warburg diffusion (231). The Nyquist plots instead appeared to contain only the beginnings of the characteristic semi-circular shape (Figure 3.20).

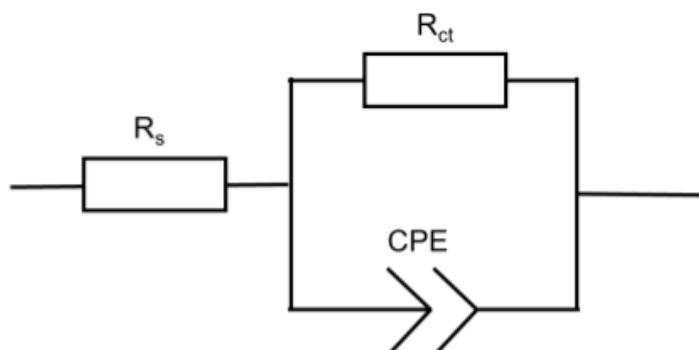


Figure 3.19. The simple equivalent circuit model used to fit carbon sensor data.

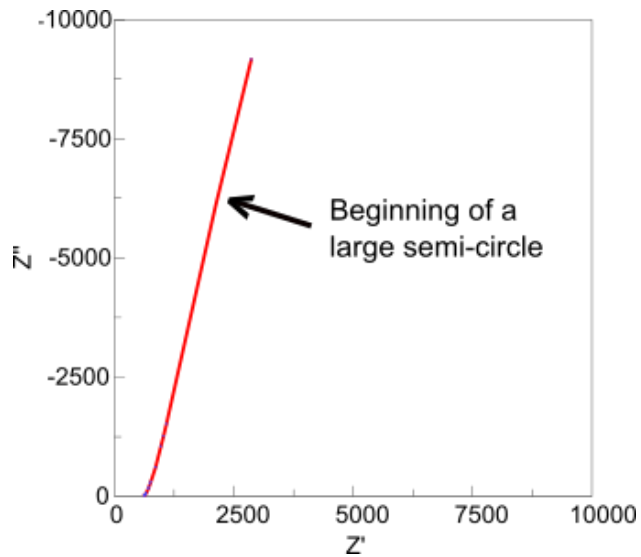


Figure 3.20. Example Nyquist plot obtained using a carbon sensor. In this case, a measurement of *P. aeruginosa* in LB medium was performed. The plot appears to follow the start of a larger semi-circular shape, with no clear Warburg diffusion behaviour evident (Section 2.3.10).

Start (S) and end (E) raw data was fitted for each individual sensor using the Z-View instant fit function (Scribner Associates), and a percentage change value for each circuit element between these times calculated:

$$\text{Change (\%)} = \left(\frac{X_E - X_S}{X_S} \right) * 100 \quad (41)$$

where X_S and X_E are the circuit element values at the start and end of the period being investigated respectively. Either 0-hour and 24-hour data, or sterile and high cell density data were used as these start and end points. Using these points, the full extent of any change could be assessed. Averaging was performed for each sensor condition, and statistical testing carried out (two sample t-test, $\alpha = 0.05$).

3.7 Platinised Carbon Electrode Methods

The final sensor investigated in this project was the Ohmedics Ltd platinised carbon electrode (PCE). Whilst retaining desirable properties of the carbon sensors such as stability, it was hypothesised that these PCE sensors would be more sensitive to small electrochemical changes induced by the bacteria.

3.7.1 PCE Sensor Assembly and Conditioning

Due to the larger geometry of these sensors compared to the previous sensors, a different well assembly was required. For these sensors, rectangular acrylic walls were secured on top of the sensors using silicone adhesive sealant (Servisol) and left to cure for at least 16 hours at room temperature (Figure 3.21).

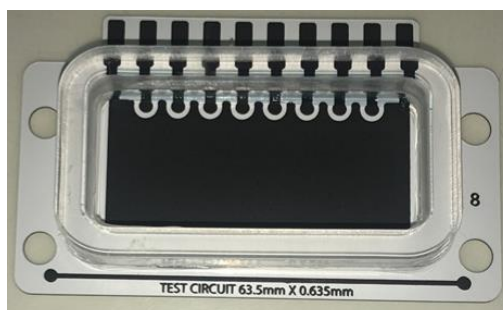


Figure 3.21. Acrylic wall secured onto PCE sensor to create a well.

Prior to use, each sensor was rinsed thoroughly in dH₂O and chemically conditioned by filling the chamber with 3 mL of NaOH solution (proprietary composition, supplied by Ohmedics Ltd) for 1 hour (procedure adapted from Wei et al. 2007 (232)). Sensors were then thoroughly rinsed for a second time and dried in a fan-assisted box oven at 40 °C for 1 hour (Heratherm, Thermo Scientific). The benefit of this process can be seen in Figure 3.22, where a large reduction in impedance magnitude is present across a wide range of frequencies.

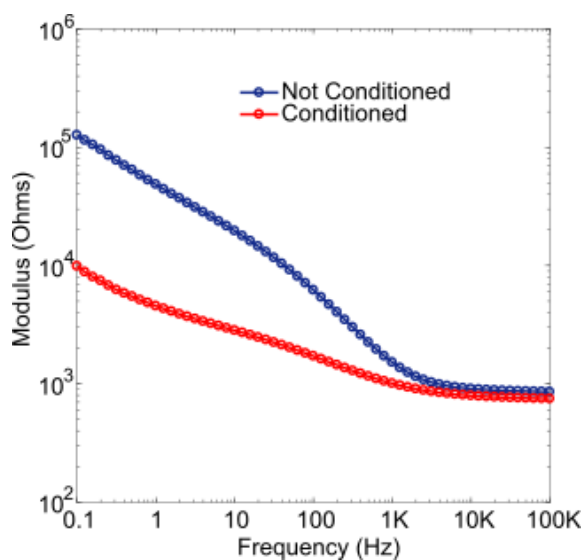


Figure 3.22. Effect of the NaOH chemical conditioning process upon the PCE sensors.

Sensors were then attached to the bases of 96-well plates for support (using double sided tape), with up to three sensors able to be attached to each plate as shown in Figure 3.23. The 96-well plate lids remained sterile and were used as chamber lids after full assembly sterilisation in ethanol (full procedure detailed in Section 3.7.2). Individual sensors could be connected to the multiplexer system for automated measurements, using the central working electrode and counter electrode only (Figure 3.23). In the case of the WBM, manual clipping was used with several working electrodes from each sensor utilised (as will be detailed in the subsequent sections).

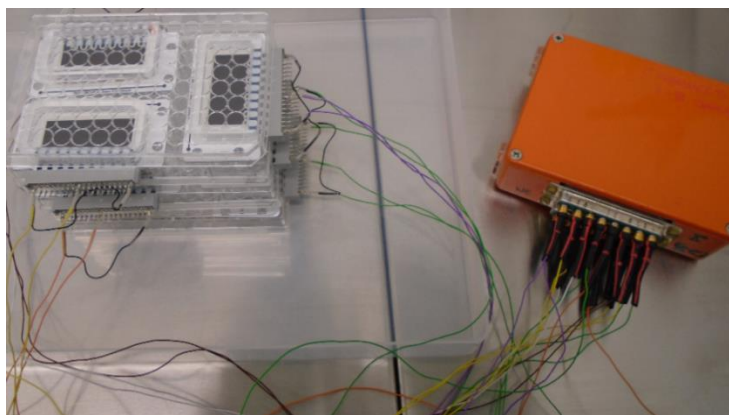


Figure 3.23. Assembly of PCE sensors for automated multiplexer measurements.

3.7.2 PCE LB Medium Growth Experiments

For an initial experiment aiming to detect *S. aureus* growth in LB medium with the PCE sensors, the same measurement process as previously was used. This enabled a direct comparison to be made between sensor types. Namely, the conditioned sensors were sterilised in 70% EtOH and immediately filled with 2 mL of LB medium. It should be noted that the larger volume of medium here is in line with the larger surface area of these sensors. The sensors were then aired in the microbiology containment hood for at least 30 minutes to allow any remaining ethanol to evaporate, before incubating the plates for 16 hours in a humid incubator at 37 °C (allowing background electrode processes to settle (186)). The contents of each well were subsequently replaced with aliquots of fresh LB medium, and an initial sterile impedance sweep carried out between 0.1 - 1×10^6 Hz (200mV). Due to low frequency noise, the minimum frequency was later changed to 1 Hz to improve efficiency. Bacterial wells were then inoculated with 20 μ L of overnight culture media, incubated at 37 °C and automated measurements performed using the Solartron and multiplexer system at regular intervals over 24 hours.

Following this, the initial sterile measurement was removed from the protocol; the non-sterile post inoculation measurement was instead used as the baseline for normalisation. Experiments involving *S. aureus* and *P. aeruginosa* growth in LB medium were carried out and analysed in this way. This normalisation method was used previously in SWF and WBM experiments with the carbon sensors, moving towards a more realistic measurement procedure for wounds.

3.7.3 Dry Sensor Preparation Method

Following this confirmation of the ability of these sensors to rapidly detect bacterial growth, alterations to the electrode preparation process were proposed to make it more practical (with a view to commercialisation). The new preparation method (referred to as “method B”) first involved replacing the 70% EtOH sterilisation step with sterilisation in 100% EtOH. Sensor wells were submerged in the 100% EtOH solution for around 20 seconds, and then immediately fully air dried in the microbiology safety cabinet. It is commonly accepted that diluted ethanol has a higher bactericidal efficacy than pure ethanol (233), with 70% v/v EtOH frequently used laboratories (although lower concentrations have also been shown to be effective (234)). The benefit of moving to the use of 100% EtOH was its faster evaporation, resulting in more rapid sensor drying at room temperature. It would, however, be expected that sensors such as these would be sterilised by other means (using radiation for example) if commercially manufactured for a medical device. Secondly, no overnight incubation (16 hours) in LB medium was carried out prior to measurement. This was expected to have a negative impact upon the initial stability of the sensor response, however, it was deemed a necessary step towards developing a practical device. Instead, a 15-minute settlement step before use was implemented. Overall, these changes resulted in reagent free sensors that could (in theory) be packaged in a dry, sterile state for distribution and immediate placement onto a wound, without any extended incubation time required before use.

To evaluate the effects of these changes to sensor preparation, a series of sensors were prepared as indicated in Table 3.3. Each sensor was filled with 2 mL of sterile LB medium and EIS measurements performed over 5 hours. In this table, Sensor 1 was prepared using the proposed new method (B) and Sensor 5 using the previous method (A). The other sensors were used to provide comparisons for each step of the new process, and further verify the effectiveness of the NaOH conditioning step.

Table 3.3. Electrode preparation methods used to test the new dry sensor preparation technique.

Sensor No.	NaOH Conditioning?	100% EtoH Sterilisation?	Overnight LB Incubation?
1	√	√	X
2	X	√	X
3	√	X (70% EtoH and no dry)	X
4	√	√	√
5	√	X (70% EtoH and no dry)	√

3.7.4 PCE SWF Growth Experiments

A series of experiments were next conducted in SWF, measuring the growths of *S. aureus*, *P. aeruginosa*, *E. coli* and *P. mirabilis*. The new dry sensor preparation method (B) was used: 100% EtOH sterilisation with no extended LB settlement. Otherwise, these experiments followed the methodology of the LB medium experiments described in Section 3.7.2 (but instead using SWF). Again, the initial sterile measurements were omitted, and normalisation was performed against a non-sterile starting state.

3.7.5 Wound Bed Model Adaption and Double Sensor Model Development

The wound bed model was next adapted for use with the PCE sensors. Once more, the electrodes were situated at the base of the model (Figure 3.24) and here, due to the larger surface area of these sensors compared to the previous carbon sensors, the volumes of collagen matrix solution and SWF were increased.

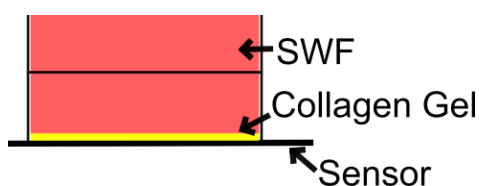


Figure 3.24. Diagram of the PCE WBM configuration (side view).

Following conditioning, sterilisation in ethanol and air drying (preparation method B, Section 3.7.3), the sensors were each rinsed with 2 mL of SWF to wet the surface. Each sensor was then coated in 800 μ L of collagen matrix solution, ensuring to pipette carefully to avoid the formation of bubbles on the surface. Incubation at 37 °C for 1 hour was then carried out to gel the matrix, followed by gently filling each sensor with 2 mL of SWF. With this WBM, *S.*

aureus and *P. aeruginosa* were first grown separately but simultaneously by inoculating the bacterial chambers with 20 μL of the desired stock culture (~1% inoculation density). For consistency, the same volume of sterile LB medium was added to each negative control. In all previous PCE experiments multiple sensors were used for each chamber condition (for example *S. aureus*) and a reading taken from only the central working electrode on each sensor (via the cable harness and multiplexer). For these WBM experiments, however, multiple working electrodes were instead measured on a single sensor to obtain three replicates (Figure 3.25). This was due to the large volume of collagen required to cover the sensor surface and its associated high cost, meaning it was necessary to reduce the number of sensors used in each experiment. Impedance sweeps were, therefore, carried out on bench with incubation at 37 °C in between measurement sets, due to the need for manual connection via crocodile clips to each electrode for these experiments. Measurements were typically performed at 0 Hours, 1 Hours, 2 Hours, 5 Hours and 24 Hours, ensuring sufficient incubation time. A second WBM experiment repeated this protocol, using an increased inoculation volume (1800 μL SWF and 200 μL stock culture, 10% inoculation density). This experiment additionally involved the growths of *S. aureus* and *P. aeruginosa* together in a polymicrobial culture (1800 μL SWF and 200 μL of each stock culture).

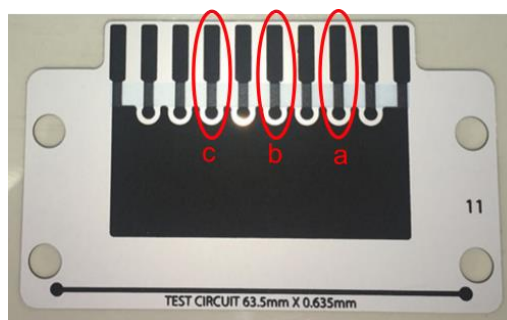


Figure 3.25. Image of a PCE sensor with the individual working electrodes used in the WBM experiments highlighted.

It was later hypothesised that this WBM arrangement (with the collagen gel formed directly on top of a base sensor) may not best simulate the positioning of a sensor in contact with a real wound. The sensor would be unlikely to lie face up, parallel to the ground, and would also have more direct contact with the wound exudate rather than be somewhat shielded from this by the tissue analogue to the collagen matrix. To solve this, a “double sensor” wound bed model (dWMB) model was developed. To create a single chamber, two electrodes were conditioned and dried as previously. The rectangular acrylic chamber wall was then removed from one

sensor, and two 0.5” holes punched into the outer edge of the sensor’s counter electrode. This provided one hole to pipette through, and a second enabling the release of air and minimising bubble formation. Both sensors were then sterilised in 100% EtOH and allowed to dry fully. The sensor with holes was then secured onto the rectangular chamber walls of the other sensor (Servisol sealant) so that both sensors faced each other (Figure 3.26). A further acrylic rectangle was then secured on top of the sensor with holes, resulting in the arrangement shown in Figure 3.26 (left to cure overnight at room temperature for ~16 hours). These arrangements were then taped onto the bases of 96-well plates as previously and sterilised once more with 100% EtOH.

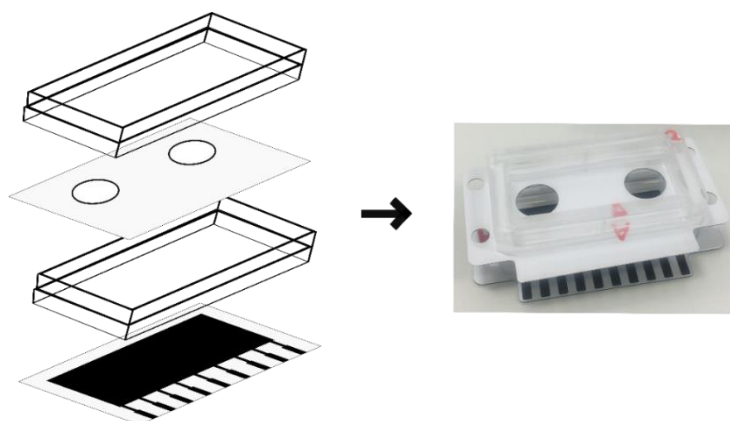


Figure 3.26. Assembly of the double sensor wound bed model (dWBM).

To wet both sensor surfaces the arrangement was rinsed with sterile dH₂O. Through each of the top sensor holes, 400 μ L of collagen matrix solution was next pipetted, resulting in 800 μ L of the solution spread over the base sensor. The system was then incubated for 1 hour at 37 °C to gel the matrix, before filling with 15 mL SWF (Figure 3.27). In this case, pipetting was performed through one hole and the other hole allowed for air outflow. Experiments were then performed with *S. aureus*, *P. aeruginosa* and a polymicrobial culture (as with the WBM experiments), with 150 μ L used for a ~1% inoculation here and 1.5 mL for a 10% inoculation density (adjusted to a total volume of 15 mL using SWF). Again, manual clipping was used for measurements, with 3 working electrodes on each of the top and base sensors used. Incubation at 37 °C was performed in between measurements.

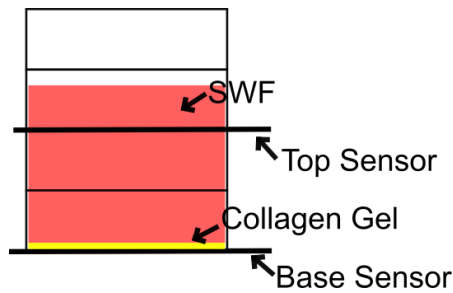


Figure 3.27. Diagram (side view) of the double sensor wound bed model (dWBM).

3.7.6 Incorporating Wound Dressings into the WBM

The protocol outlined for the WBM previously (Section 3.7.5) was repeated for these experiments, with the addition of ~10 cm² sections of wound dressing being added to each sensor chamber following inoculation (Figure 3.28). The dressings investigated are detailed within Table 3.4, and in each instance *S. aureus* (NCTC8325) was the pathogen grown in the WBM at an inoculation concentration of ~1% v/v (as previously). Several impedance measurements were, once more, conducted over 24-hour time periods on-bench using manual clipping, with incubation at 37 °C in between.

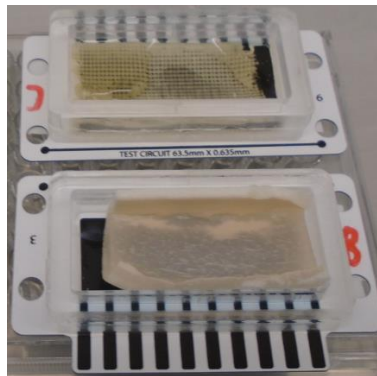


Figure 3.28. Assembly for dressing studies conducted in the WBM.

Table 3.4. Details of the wound dressings studied in the *S. aureus* WBM experiments.

Dressing	Manufacturer	Type
Acticoat absorbent with SILCRYST™	Smith & Nephew	Calcium alginate dressing with nano-crystalline silver
Advazorb	Advancis Medical	Non-adherent foam dressing
N-A® Ultra	Johnson & Johnson	Silicone coated knitted viscose dressing

Activon Tulle	Advancis Medical	Knitted viscose dressing with Manuka honey
Mepitel®	Mölnlycke®	Soft silicone coated atraumatic wound contact layer

3.7.7 PCE Saline Experiments

Once more, experiments were performed using washed bacterial cells in 0.9% w/v NaCl solution to investigate the impedance response caused directly by cellular interactions with the electrode in the absence of growth. Analogous to the experiments performed with the carbon sensors (Section 3.6.5), both the effects of the cells over an extended period and the immediate cell concentration dependent effects were studied. In each case, colony counting was used to verify the lack of bacterial growth during these experiments.

The sensors were again conditioned and prepared using method B, as detailed in Section 3.7.3. Firstly, high concentrations of washed *S. aureus* and *P. aeruginosa* cells were obtained from stock cultures (Section 3.2.3) and 2 mL of either bacteria or sterile saline added to each sensor ($n = 3$ each). The sensors were incubated at 37 °C and automated (multiplexer) measurements were performed every 0.5 Hours until 6 Hours, and every hour thereafter until 24 hours. By performing an initial impedance sweep of sterile saline for all sensors, the immediate effects of introducing either the *S. aureus* or *P. aeruginosa* cells could be assessed. To study the effects upon impedance over time, normalisation was performed against the second measurement (first non-sterile measurement) as was done in the majority of previous experiments.

Next, the impact of an increasing concentration of *S. aureus* cells on the sensor surface was explored. Newly prepared sensors with 2 mL sterile 0.9% NaCl had a sterile sweep carried out. Washed cells were obtained at a range of concentrations (from around 10^6 to 10^8 CFU/mL), and a series of impedance measurements performed at room temperature with an incrementally increasing cell concentration placed onto the sensors for each sweep.

3.7.8 Equivalent Circuit Modelling

Equivalent circuit fitting was performed on a selection of PCE results to assess the electrochemical underpinnings of the impedance changes seen. For these sensors it was necessary to include a Warburg diffusion element in the circuit model, due to the measured low frequency response (an example Nyquist plot is provided in Figure 3.29, full circuit model

theory is provided in Section 2.3.10). The circuit shown in Figure 3.30 was, therefore, used to model the PCE sensor data.

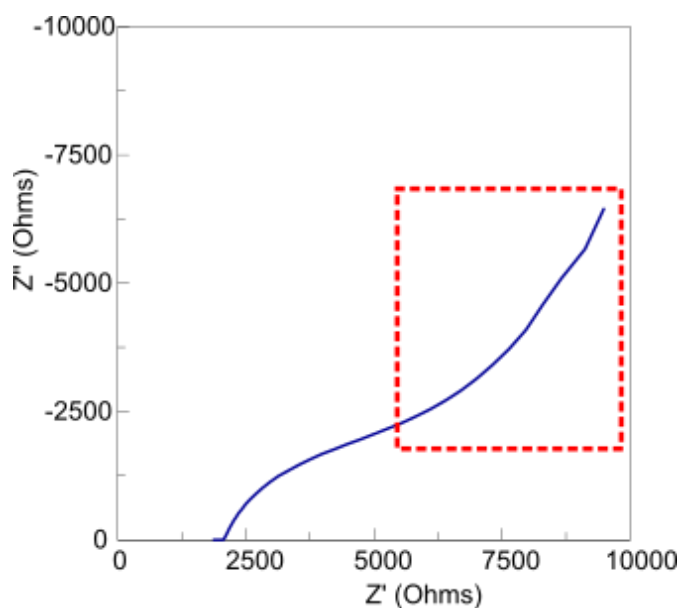


Figure 3.29. Example Nyquist plot for a PCE sensor. High frequency Warburg diffusion behaviour (highlighted in red) is evident, with this taking the form of a finite length reflective (open) element (Section 2.3.10).

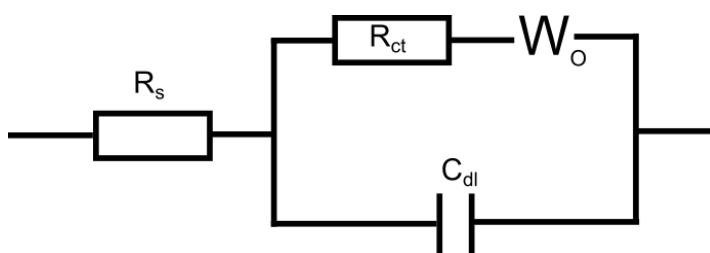


Figure 3.30. Equivalent circuit model used to fit selected PCE sensor data. Based on the Randle's circuit, R_s represents solution resistance, R_{ct} the charge transfer resistance, W_o the finite space (open) Warburg diffusion element and C_{dl} the double layer capacitance. For further details, refer to Section 2.3.10.

To fit the raw impedance data to this model, the following steps were carried out using the Z-View software package (Scribner Associates). For each sensor, the experimental data at frequencies above 100 Hz was first fitted (using the instant fit function) to a simplified version of the circuit in Figure 3.30 which omitted the Warburg diffusion element. This gave approximate values for R_s , R_{ct} and C_{dl} . The remaining low frequency data was then fitted to the circuit shown in Figure 3.31 to obtain approximate values for the Warburg element parameters. These approximate values were then entered into the complete circuit model (Figure 3.30) as starting points, and the data across the full frequency range fitted. The exponential Wo-P

parameter was set constant at 0.5 as indicated in the Z-view manual for Warburg diffusion. Percentage changes for each circuit element were then calculated (as described in Section 3.6.6) and averaging performed.



Figure 3.31. Circuit used to approximate Warburg element values for low frequency data.

3.7.9 Effects of Bacterial Concentration upon Impedance Response During Growth

The impact of bacterial concentration upon the measured normalised impedance response was next further explored through multiple *S. aureus* LB medium growth experiments. To obtain the different starting concentrations, stock bacterial cultures of NCTC8325 were diluted with LB medium such that cell densities of 10^6 , 10^7 and 10^8 CFU/mL were each placed on multiple sensors (prepared as described in Section 3.7.3). In a similar manner to the previous LB growth experiments, automated impedance measurements were performed at 0 hours, 0.5 hours, 1 hour and then every hour (for 24 hours) at 37 °C.

In the resulting data, it was apparent that the signatures for the different concentrations were initially distinct at key regions of impedance change. The normalised values over time for these parameters, namely normalised modulus at 1 Hz and normalised phase at 200 Hz, were therefore focused on. A MATLAB script was created which calculated the rate of change of these parameters at each time point, for each bacterial concentration. The highest rate of change value and the rate of change value at 1 hour for each bacterial concentration were then identified for each parameter, and these values plotted against concentration. Trend lines fitted to the data in these graphs provided approximate relationships between rate of impedance change and the bacterial concentration present in the sample. To verify the accuracy of these relationships, a further *S. aureus* growth experiment was carried out.

3.7.10 Neural Network Development for Bacterial Detection

As large volumes of data were collected throughout this study (through the repetition of experiments multiple times with multiple replicates in each instance), it was believed that machine learning may be a suitable algorithmic approach, with the desired outcomes of applying machine learning being:

- to detect the presence of infection in a sample;

- to identify the pathogen responsible for the infection (or identify the infection as polymicrobial).

For a detailed explanation of ANN and the chosen model (Multi-Layer Perceptron Classifier) please refer to Chapter 2. A popular programming language for machine learning, Python was used to develop the ANN in conjunction with the dedicated machine learning library “Scikit-learn” (235). The Spyder integrated development environment (part of the Anaconda distribution, Anaconda Inc.) was used throughout.

The first step in this model development process was to choose which EIS signature features would be used as input data (“feature selection”). Whilst automated feature selection processes involving statistical methods can be used in machine learning, manual feature selection was deemed most appropriate for this project as prior knowledge of the significance of key EIS signature regions had been gained (236,237). Firstly, the experimental data used was limited to that obtained during growth experiments (namely in LB medium, SWF or the WBM) and data from the 24-hour measurements only. A rationale behind the selection of each feature will be provided within Section 6.10, however, the following features were selected:

- Growth medium
- Normalised Modulus at 1 Hz and 1 kHz
- Normalised (Absolute) Phase at 1 Hz, 100Hz and 1 kHz

When performing feature selection, it is desirable to select the minimum possible number of features which accurately reflects the key information within the dataset. This optimises the accuracy of the model and the computational cost, and minimises the required EIS measurement time in this case (238). Furthermore, a CSV file was created which contained the stated data for each sensor/sample involved in a growth experiment (medium, normalised impedance data) in addition to whether the sample was sterile or infected, and the causative pathogen. It should be noted that the normalised impedance values from individual sensors/samples were used rather than averaged data, as would be the case when obtaining data from a real wound.

The first ANN was developed with the aim of correctly identifying the presence of bacteria within a sample (“ANN1”). To create this predictive algorithm, the steps outlined in Figure 3.32 were followed. The CSV data file was imported, and the growth medium type and 5 key normalised impedance values were assigned to variable “X” (input data). In this case, the presence of bacteria (denoted 0 for sterile or 1 for contaminated) was assigned to the variable

“Y” (true output data). A label encoder was next used to convert the media types to numeric labels. This encoding was saved for use in later neural network testing. The train/test split for the supervised learning was next defined, with 75% of the CSV file data entries being randomly chosen to train the neural network and the remaining 25% reserved for testing the resulting model. Before model training, however, the input data was scaled using the “Standard Scalar” to standardise the input data, such that it had a mean of 0 and unit variance. Feature scaling is commonly recommended in machine learning to optimise model performance and increase the learning rate (239), with this particular method being recommended for feature scaling within scikit-learn. Once more, this transform was saved for consistency in later ANN testing.

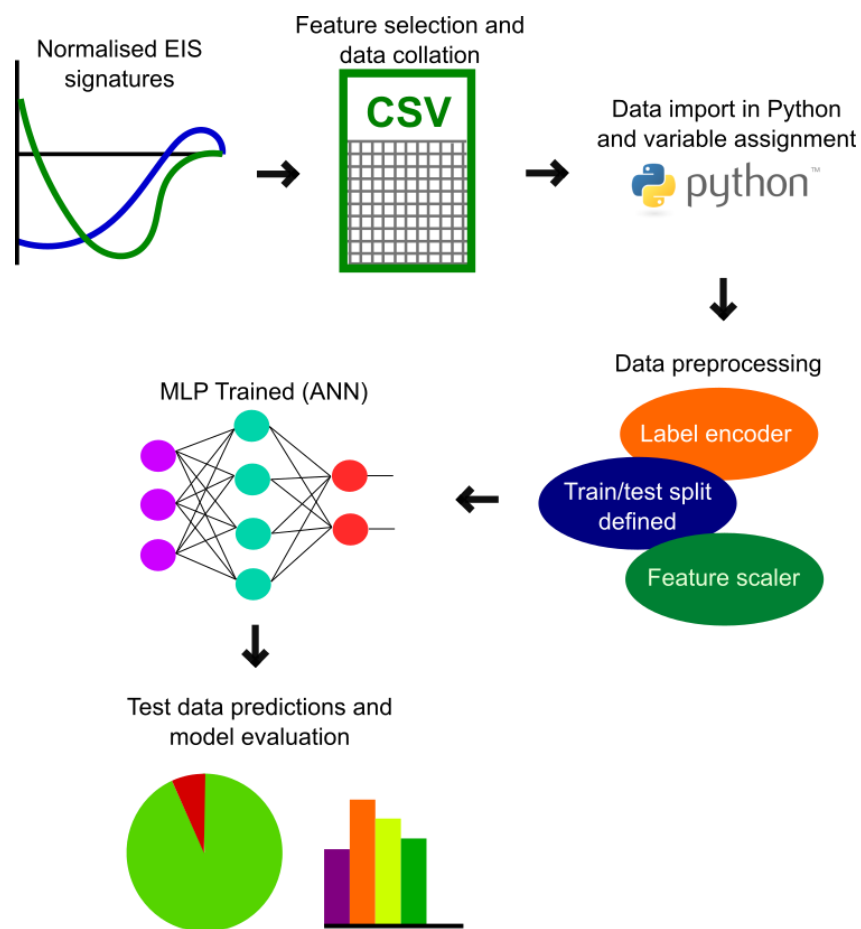


Figure 3.32. Flowchart describing the development of the ANN predictive model.

The training data was next used to build the neural network model. The model chosen was the Multi-Layer Perceptron classifier (MLP classifier), a feed-forward neural network (the key parameters associated with this model were introduced in Chapter 2). Despite being critical in the avoidance of both over- and under-fitting, no definitive guidance exists for selecting the

number of hidden layers and neurons. Most frequently, trial and error methods are used to tune ANN hyperparameters such as these (240,241). For simplicity, therefore, trial and error was used to optimise the ANN1 hyperparameters. As mentioned in Chapter 2, the simplest ANN structure which provides the highest accuracy is desired. Initially selecting just 2 hidden layers, the network was first trained with 4 neurons in each hidden layer and all other parameters as default (Section 2.4.3). This model was trained 3 times, and on each occasion classification predictions for the test data were obtained and compared to their true labels to verify the performance of the obtained model. To aid this, a classification report and confusion matrix were printed. The former presented the “precision” ($t_p/(t_p + f_p)$) where t_p is the number of true positives and f_p false positive), “recall” (or sensitivity, $t_p/(t_p + f_n)$ with f_n being false negatives) and “F₁-score” (harmonic mean of precision and recall (242)) for the predictions. The confusion matrix presented the numbers of t_p, t_n (true negative), f_p and f_n in a single matrix (M) such that element M_{ij} stated the number of samples known to be in category i and predicted to be in category j . In particular, however, the F₁-score was noted for each model. The number of neurons in each hidden layer was then increased methodically, until the average F₁ score over the three training runs for each network structure was optimised. This process was then repeated for the number of hidden layers, the learning type/rate, and the maximum number of iterations. Ultimately, the final network consisted of 4 hidden layers with 8 neurons each, a maximum of 600 iterations and all other parameters were set to their default values (with supporting evidence provided in Section 6.10). The final ANN1 model was saved for later use in the classification of new samples.

This ANN creation process (Figure 3.32) was next repeated, with minor modifications, to obtain a predictive model for the bacterial species present in each sample (“ANN2”). In this case, the name of the bacterial species (or “Sterile”) for each data entry was instead assigned to the variable “Y”. These species labels were converted to numeric labels using a label encoder, which was again saved. A feature scaler was once more applied to the input data and saved. Using the same protocol described above, a network structure and hyperparameter trial and error optimisation process was carried out. In this case, the final ANN2 consisted of 4 hidden layers each containing 12 neurons, the “Invscaling” learning process was selected with an initial rate of 0.01 (Section 2.4.3), and 600 was the maximum number of iterations. The final ANN2 model was also saved for later use in the classification of new samples. From the experimental training data used, this model could predict one of the following bacterial species: *E. coli*, *P. aeruginosa*, *P. mirabilis*, *S. aureus*, Polymicrobial or Sterile.

4. ASSESSING THE SUITABILITY OF Ag/AgCl ELECTRODES FOR THE DETECTION OF WOUND PATHOGENS

4.1 Introduction

This chapter explores the suitability of screen-printed Ag/AgCl electrodes for the detection of wound pathogens via electrochemical impedance spectroscopy (EIS). Ag/AgCl electrodes enable efficient passage of current across their interface, and allow for the detection of electrochemical reactions at their surface (225). Such electrodes are more suitable than their polarisable counterparts for low frequency measurements and those where sensor movement is likely, therefore, they are favoured in biological applications (192). Further, the low noise, low impedance, stability and relatively low cost of Ag/AgCl electrodes makes them attractive for a range of clinical scenarios including ECG measurements (212, 214).

Farrow et al. (2012) have previously investigated the ability of the Ag/AgCl flexible WoundSense electrodes (Ohmedics Ltd) to detect *S. aureus* (129). It was found that, around 4-8 hours after inoculation of media with a cell density of around 1×10^6 CFU/mL, some changes to normalised phase could be seen. Through experiments performed with lower bacterial concentrations, however, the electrodes were found to have an inhibitory effect upon growth. Within this section, the results of all experiments conducted with the Ag/AgCl WoundSense electrodes in this study are presented. These experiments aimed to further the work carried out previously by:

- exploring the antimicrobial properties of the sensors in more depth;
- attempting to reduce this inhibitory effect and obtain clearer normalised impedance signatures;
- investigating Gram-negative *P. aeruginosa* in addition to Gram-positive *S. aureus*;
- using a wider range of growth conditions.

4.2 Ag/AgCl Electrode Voltage-Induced Instability in Saline Solution

The first step to assessing their suitability for rapid bacterial detection (in line with project objective 1, Section 1.8), the Ag/AgCl sensors were first characterised by performing EIS measurements in 0.9% w/v NaCl in dH₂O. This enabled both the baseline impedance of the sensors to be visualised, and the impact of applied perturbation potential magnitude to be assessed. Note that the PalmSens 4 device was used to obtain these results, as described in Section 3.5.2.

Firstly, multiple consecutive impedance sweeps using a 200 mV rms measurement potential were carried out on several Ag/AgCl sensors. When comparing the average impedance spectra obtained with each sweep, stark differences were observed even between the first and second measurements (Figures 4.1A, 4.1B). An immediate, marked reduction in both magnitude (Figure 4.1A) and absolute phase (Figure 4.1B) highlighted a lack of sensor stability at 200 mV. Through repeated measurements with new electrodes at a lower perturbation voltage, a contrasting result was found: using a 10 mV perturbation voltage, the plots in Figures 4.1C and 4.1D were obtained. In this case, no visible changes occurred between measurements and, therefore, the sensor response appeared to be far more stable. The baseline impedance magnitude was, however, higher at low frequencies when using the lower measurement potential ($\sim 10^5 \Omega$ compared to $\sim 10^2 \Omega$ when using 200 mV, Figures 4.1A, 4.1C). This change in impedance magnitude and stability is almost certainly due to voltage effects on the silver chloride/silver oxide layer around the electrode surface. It may be possible to reduce this effect using long periods of electrode wetting or repeated EIS cycles, but for immediate measurements on the Ag/AgCl electrodes it is a significant factor for consideration.

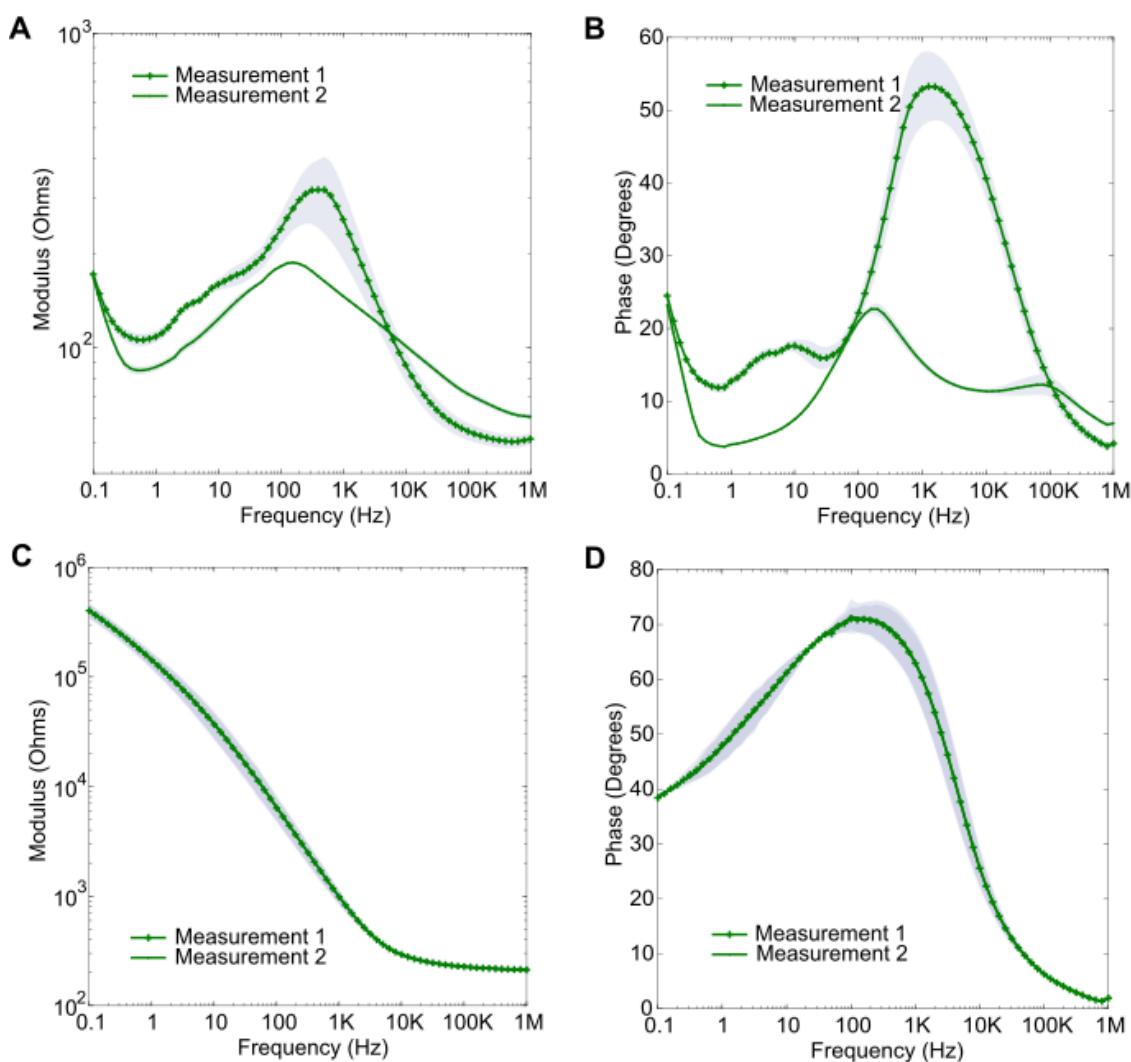


Figure 4.1. Impedance spectra obtained through repeated measurements of 0.9% w/v NaCl in dH₂O with Ag/AgCl electrodes. (A) and (B) are the modulus and absolute phase plots respectively with a 200 mV perturbation voltage used ($n = 4$); (C) and (D) are the modulus and phase plots respectively with a 10 mV perturbation voltage used ($n = 3$), measurements 1 and 2 cannot be visually separated in this case. Average values are shown with shading representing ± 1 standard deviations.

Following this, a range of increasing perturbation voltages were investigated consecutively as outlined in Table 3.2 (Section 3.5.2). For tested voltages of 60 mV and above, a large decrease in impedance modulus in the mid to low frequency range was observed (Figure 4.2A), resulting in the modulus plot losing its expected characteristic high value at low frequencies (Section 2.3). For these voltages, the corresponding Nyquist plots contained high noise levels and showed a “looping” structure (Figure 4.2B). Similar low frequency behaviour is commonly referred to as a “low frequency hook” or “inductive loop” (243). Most commonly this references the case where the loop follows a complete semicircle and is below the x-axis,

having a positive imaginary component. In this case, however, the response remained in the negative complex plane. This is believed to be because a complete semi-circle was not obtained before the phenomena changing the response at lower frequencies began to dominate, however, the underlying reasons for this looping behaviour are thought to be the same as those proposed in the literature. Specifically, processes such as electron transport changes in the silver oxide layer due to Ag^+ ion migration, and electrode surface adsorption processes have been highlighted as likely causes of this low frequency looping (243–245). Conversely, for the tested perturbation voltages of 40 mV and below, a partial semi-circular shape conventional of the Nyquist plot was obtained (Figure 4.2B). Larger noise was, however, present at the lowest voltages (Figure 4.2A) due to operating at the limit of the impedance analyser's range. Using such low voltages likely resulted in currents of a magnitude unable to be reliably resolved by the instrument. Further, after initially applying these increasing voltages up to 200 mV, a final measurement using 20 mV characterised the impedance decrease as partially reversible, despite not refreshing the medium for this measurement (Figure 4.2A).

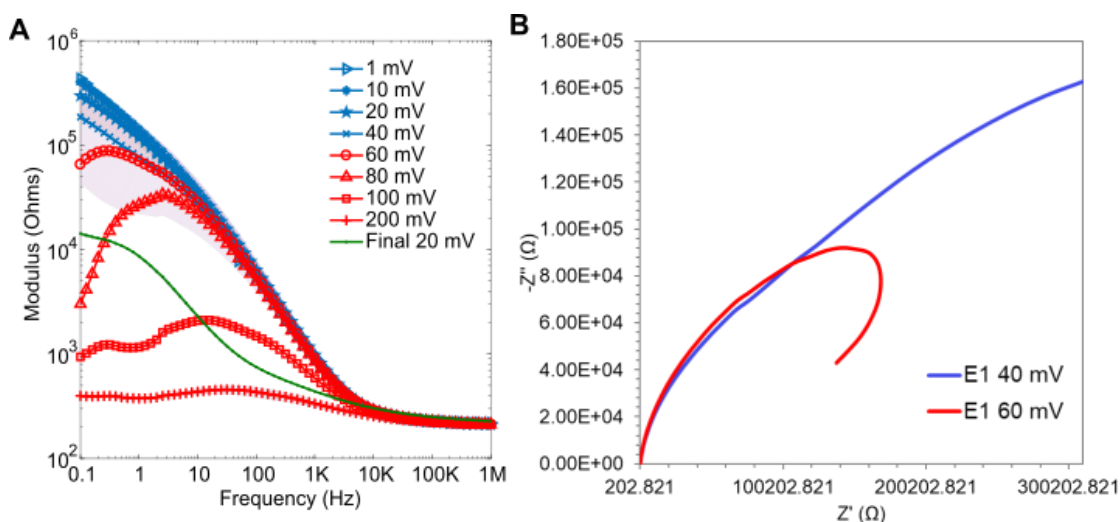


Figure 4.2. The effects of using different perturbation voltages upon impedance: (A) displays the decrease in modulus and change to plot shape as the voltage is increased ($n = 3$, shading depicts ± 1 standard deviation); (B) shows an example from a single electrode (E1) of the “looping” behaviour occurring at higher voltages, but not at lower voltages.

These experiments therefore indicated that, whilst a very low perturbation voltage such as 1mV would not be appropriate for EIS measurements with these sensors due to the level of noise present, lower voltages appear to have a more stable and predictable impedance response at low frequencies. As this is necessary for the intended wound infection monitoring application, at this point using a lower measurement voltage appeared most promising. This result,

associated with the polarisation behaviour of the sensor, will be discussed in more electrochemical detail within Section 7.2.1.

4.3 Ag/AgCl Electrode Detection of Bacteria in LB Medium is Impacted by Applied Measurement Voltage

After this initial Ag/AgCl sensor characterisation, their suitability for rapid bacterial detection and any impedance changes occurring due to bacterial growth were next directly assessed in line with research objectives 1 and 2 (Section 1.8). Experiments were conducted in LB medium, using both a 200 mV measurement voltage (as used previously by Farrow et al. (129)) and a 20 mV measurement voltage. Following the characterisation experiments presented in Section 4.2, 20 mV was expected to result in greater sensor stability without the increased noise that is present when using very low perturbation voltages (such as 1 mV).

4.3.1 200 mV Inhibits Bacterial Growth in LB

Following overnight sensor incubation in LB medium and an impedance measurement of fresh sterile media with all sensors ($n = 8$, 0.1 Hz – 1×10^6 Hz, 200 mV), four Ag/AgCl sensor wells were inoculated with *P. aeruginosa* (PA14) at an average concentration of 1.2×10^7 CFU/mL (range $(0.8 - 1.6) \times 10^7$ CFU/mL). The other chambers remained sterile for comparison, and impedance measurements were carried out after 0 hours, 5 hours and 24 hours of incubation (37 °C) with the PalmSens 4 instrument. After 5 hours, a reduction in viable cell concentration had occurred, with only 6.6×10^5 CFU/mL (range $(3.2 - 9.7) \times 10^5$ CFU/mL) remaining. Similarly, by 24 hours no visible colonies were present during colony counting, indicating a cell density of $< 10^4$ CFU/mL.

Overall, the impedance signatures for the sterile and bacterial wells were very similar: large shifts in impedance were present for both (Figures 4.3A, 4.3B). These changes were similar to those seen previously when a 200 mV perturbation potential was applied in the characterisation experiments (Figure 4.1). Again, repeated EIS measurements in quick succession at 200 mV caused a large reduction in impedance (Figure 4.3, changes between the initial sterile “0 Hrs Sterile” and first post-inoculation measurement “0 Hrs”). When an extended time period elapsed between measurements, however, such as the 0-5 hours or 5-24 hours gaps here, this conditioning effect partially reversed and an increase in impedance was seen. Furthermore, these shifts dominated the normalised impedance plots (Figures 4.3C, 4.3D) and any

differences observed due to the presence of bacteria were far smaller in comparison. Despite this and the observed bactericidal action, a significant difference in normalised modulus at 6 kHz (Figure 4.3C) was observed between the sterile and bacterial chambers after 5 hours ($p < 0.001$) and 24 hours of incubation ($p = 0.003$). A 200 mV perturbation voltage was not, however, believed to be suitable for detecting the growth of bacteria in LB medium: bactericidal action was observed, and sensor instability dominated the impedance response. Whilst the sensor response may eventually settle with a combination of predetermined measurement cycling and pauses between measurements, for the wound infection monitoring application being investigated an immediately stable response is desired.

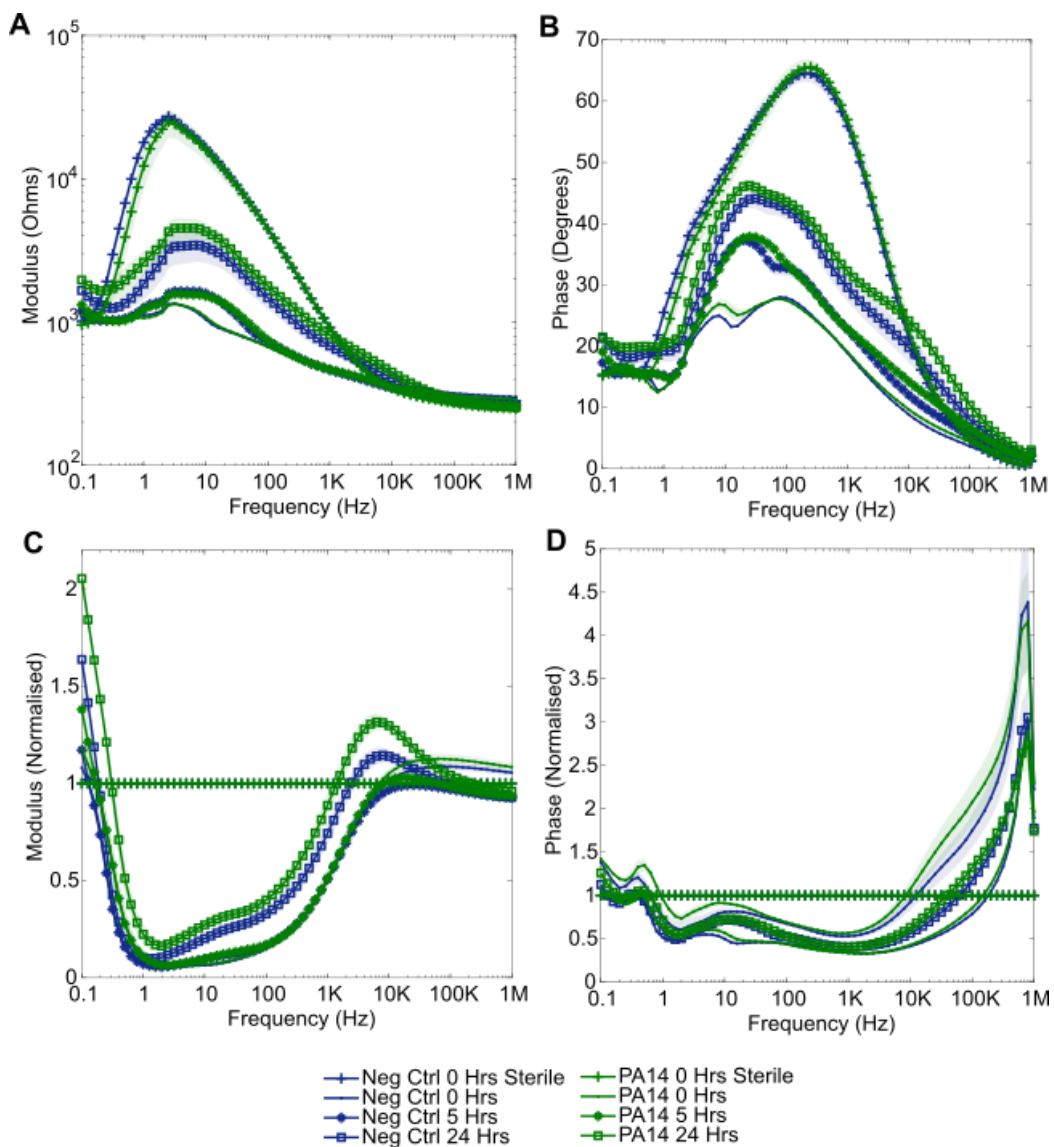


Figure 4.3. Impedance response associated with the inoculation of LB medium with *P. aeruginosa* (PA14) and performing measurements with a 200 mV perturbation voltage over 24 hours. Plots show: (A) modulus; (B) absolute phase; (C) modulus normalised against a sterile initial sweep; (D) phase normalised against a sterile initial sweep ($n = 4$, shading depicts ± 1 standard deviation).

4.3.2 20 mV Permits Bacterial Growth in LB

The previous LB medium experiment protocol was repeated, using a lower perturbation voltage (20 mV rms). These experiments aimed to determine if this voltage was more successful in both enabling and detecting bacterial growth, whilst also immediately providing a more stable sensor response. Firstly, *P. aeruginosa* (PA14) was again studied, with the resulting impedance plots shown in Figure 4.4. In this case, the bacteria successfully grew from an average starting concentration of 1.0×10^7 CFU/mL (range $(1.0 - 1.1) \times 10^7$ CFU/mL) to 1.6×10^9 CFU/mL (range $(0.9 - 2.1) \times 10^9$ CFU/mL) over 24 hours. Again, some changes to impedance over time were common to both the sterile control and bacterial chambers, however, these were of a smaller magnitude than in the previous 200 mV experiments (Figures 4.4A, 4.4B). Furthermore, the normalised impedance changes were more pronounced for the bacterial chambers and, therefore, distinguishable from the sterile signatures (Figures 4.4C, 4.4D). In particular, differences between the bacterial and sterile chambers emerged in the low frequency region after 24 hours. These were significant at both 0.1 Hz in normalised modulus ($p = 0.017$) and 1Hz in normalised (absolute) phase ($p = 0.001$).

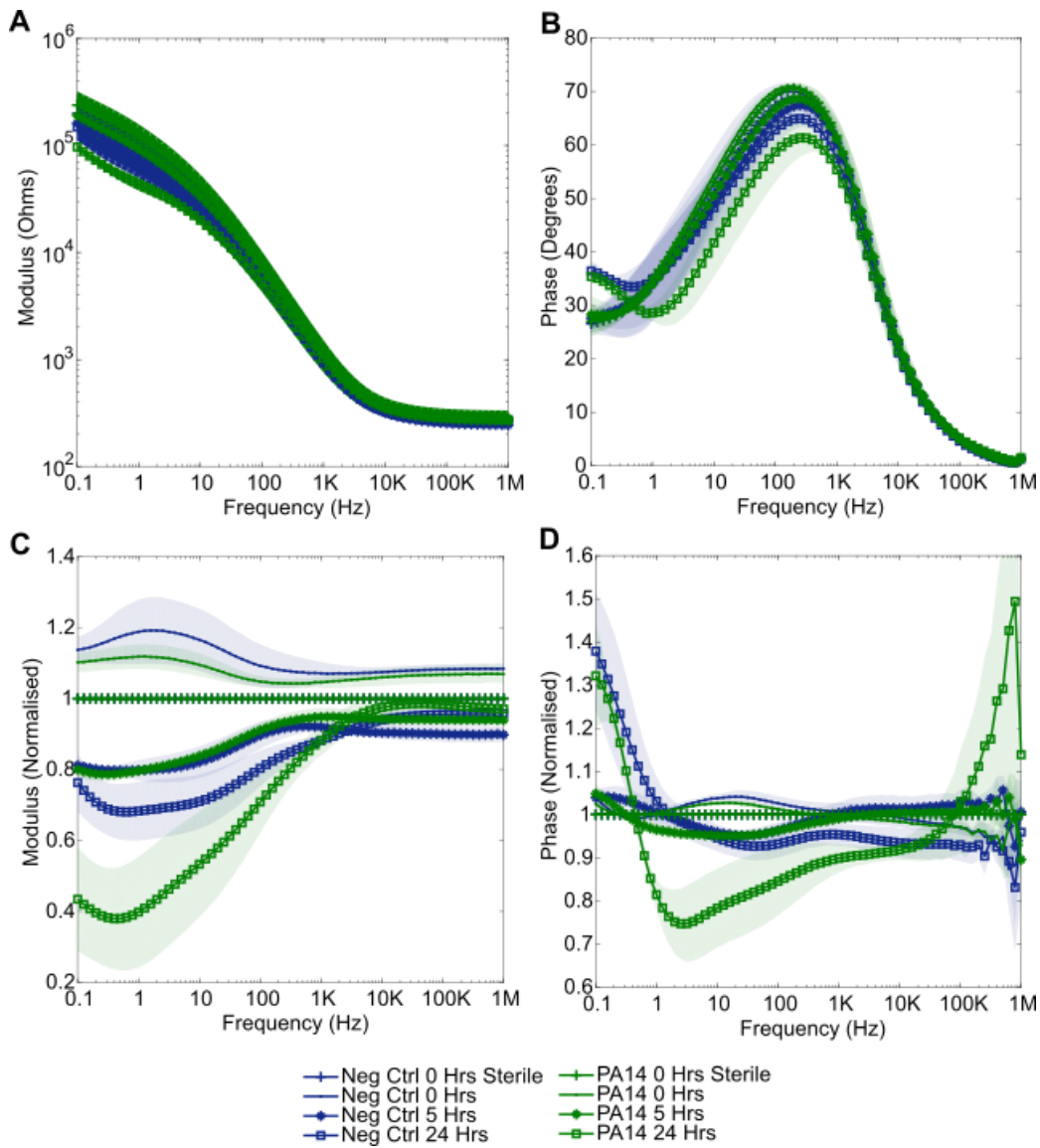


Figure 4.4. Impedance response associated with the inoculation of LB medium with *P. aeruginosa* (PA14) and performing measurements with a 20 mV perturbation voltage over 24 hours. Plots show: (A) modulus; (B) absolute phase; (C) modulus normalised against a sterile initial sweep; (D) phase normalised against a sterile initial sweep ($n = 4$, shading depicts ± 1 standard deviation).

This experiment was next repeated using *S. aureus* NCTC8325, to evaluate if any differences in impedance response could be identified between the pathogens. Once more, growth occurred using this lower perturbation voltage: the starting concentration was 7.4×10^5 CFU/mL (range $4.8 \times 10^5 - 1.2 \times 10^6$ CFU/mL), rising to 7.3×10^7 (range $2.4 \times 10^6 - 1.6 \times 10^8$ CFU/mL) after 24 hours of incubation. The raw impedance plots did not show any clear bacterial signatures (Figures 4.5A, 4.5B), but low frequency normalised impedance changes were evident for the *S. aureus* chambers (Figures 4.5C, 4.5D). These were of larger magnitude than those obtained with *P. aeruginosa* and took the form of increases in normalised modulus and phase, in contrast

to the decreases caused by PA14. The features also emerged earlier, being significant after 5 hours as observed via 0.1 Hz normalised modulus ($p < 0.001$) and 1 Hz normalised phase ($p < 0.001$) for example.

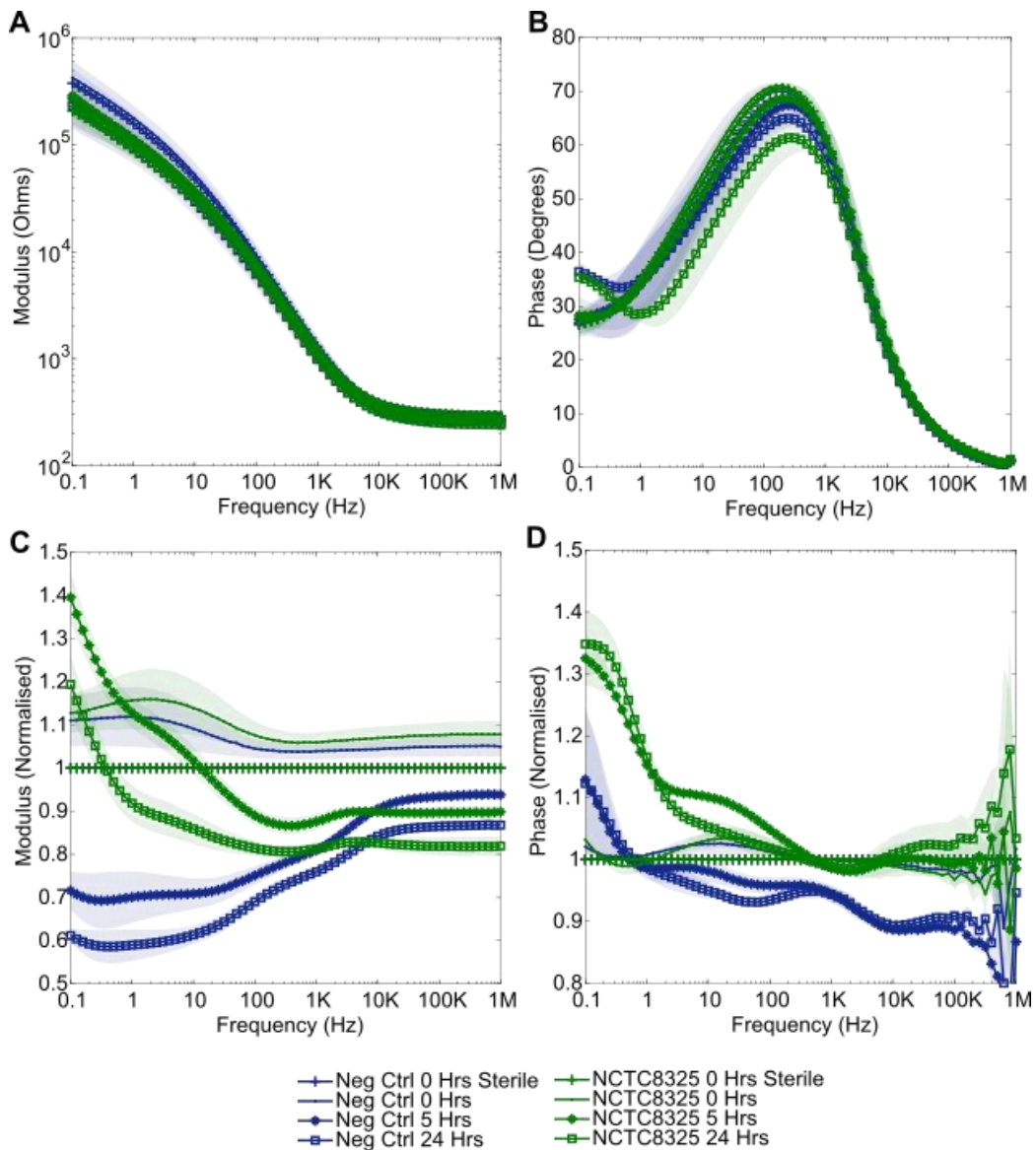


Figure 4.5. Impedance response associated with the inoculation of LB medium with *S. aureus* (NCTC8325) and performing measurements with a 20 mV perturbation voltage over 24 hours. Plots show: (A) modulus; (B) absolute phase; (C) modulus normalised against a sterile initial sweep; (D) phase normalised against a sterile initial sweep ($n = 4$, shading depicts ± 1 standard deviation).

The lower 20 mV perturbation voltage, therefore, appeared more appropriate than 200 mV for the detection of bacteria in LB medium with these Ag/AgCl sensors. At 20 mV, bacterial growth occurred and clearer bacterial signatures emerged.

4.4 The Ag/AgCl Electrode Surface Causes a Zone of Inhibition

The bactericidal action of the Ag/AgCl sensors, witnessed when using a 200 mV voltage during EIS measurements, was further investigated through observing the sensor's zone of inhibition. With sensors secured under LB agar, either sterile ($n = 4$) or PA14 inoculated ($n = 4$) LB medium was pipetted onto the agar and several EIS measurements (200 mV) carried out over 48 hours. For comparison, 4 further sensors had PA14 inoculated media added but no EIS measurements performed. The appearance of each sensor-agar system after 48 hours is displayed in Figure 4.6.

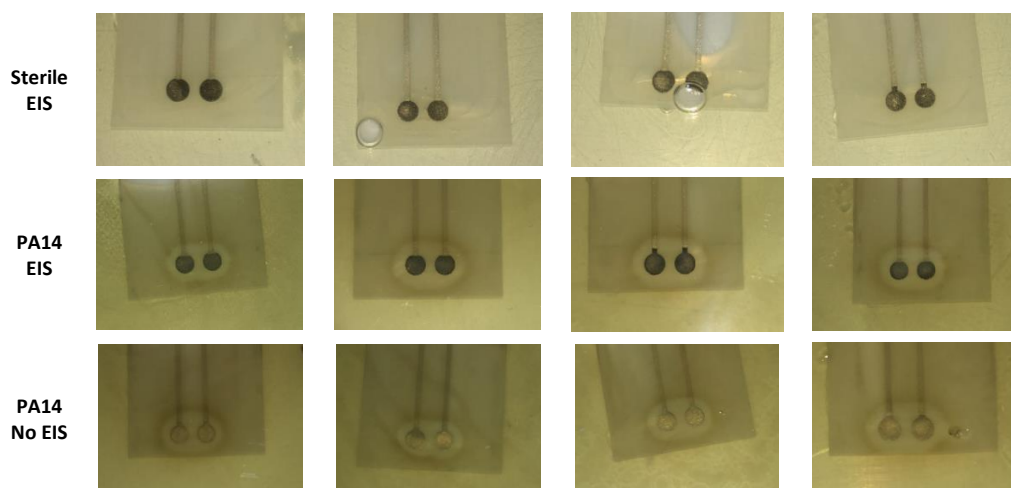


Figure 4.6. Ag/AgCl electrode zone of inhibition experiments performed with *P. aeruginosa* (PA14). Images show results for each condition ($n = 4$) after 48 hours of incubation at 37°C. The bacteria were unable to grow in the vicinity of the electrodes, irrespective of any EIS measurements performed. Additionally, EIS measurements caused darkening of the electrode surfaces.

Two key observations can be made. Firstly, performing the EIS measurements caused the electrodes to become darker in appearance. This is believed to be due to the oxidation of silver from the ink, leading to the formation of a new black AgCl film on the electrode surfaces (246,247). It provides evidence that electrode surface changes occurred during the 200 mV EIS measurements. Secondly, a clear zone of inhibition was present for all bacterial replicates, regardless of whether EIS was performed or not. Bacterial growth was inhibited on and immediately surrounding the sensor; this effect is believed to arise from the antimicrobial action of silver ions originating from the electrode ink. It can be concluded, therefore, that the sensor material would likely inhibit any direct bacterial contact with the electrode surface irrespective of applied measurement voltage, limiting the value of these sensors in infection detection applications.

4.5 Calculation of the Minimal Inhibitory Concentration of Ag⁺

Next, the antimicrobial effects of the Ag/AgCl sensors were further explored by considering the minimal inhibitory concentration (MIC) of silver, where the MIC is the smallest concentration of silver which prevents visible growth of the bacteria occurring (248). During the LB growth experiments, when using a 200 mV perturbation voltage a reduction in viable cell count occurred and no visible growth was observed (Section 4.3.1). This was hypothesised to be due to the release of silver ions into the media and, therefore, by obtaining an estimate of the MIC of silver the minimum concentration of silver released by the sensors could be approximated. Using this effect, various wound care products on the market have incorporated silver to support wound healing. Dressings such as the Acticoat range by Smith and Nephew gradually release silver over several days to help prevent infection within a wound (249,250). Whilst the precise mechanisms underlying the antimicrobial action of silver are still under study and differ between bacterial species, in general it is believed that the silver ions released in solution interact with bacterial cell membranes leading to the damage of vital enzymes (68).

In this study, silver nitrate (AgNO₃) was added to LB medium at various concentrations, and these samples inoculated with a single colony of *P. aeruginosa* (PA14). It has previously been noted that the inoculating cell density has minimal impact upon the MIC result (249). After 70 hours of incubation at 37 °C, the samples appeared as shown in Figure 4.7.

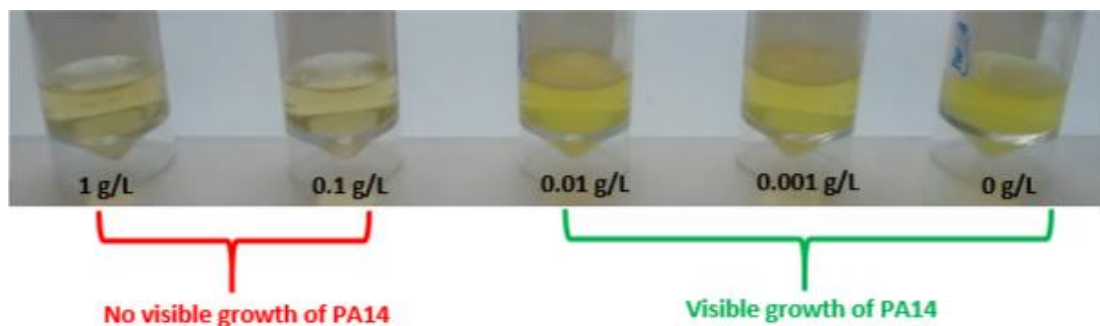


Figure 4.7. Assessing the MIC of AgNO₃. PA14 inoculated samples of LB medium containing various concentrations of AgNO₃ after 70 hours of incubation at 37 °C are shown, with growth only visible for AgNO₃ concentrations of 0.01 g/L and below.

From the appearance of each sample, the emergence of visible growth was assessed. As growth was evident for the 0.01 g/L (10 mg/L) sample but not for the 0.1 g/L (100 mg/L) sample, it was concluded that (for AgNO₃ and PA14 in LB medium) the MIC lay between **10 - 100 mg/L**. Whilst this is not a precise value, due to a lack of MIC experimental consistency a wide range of MIC values for AgNO₃ acting on *P. aeruginosa* were found in other published studies, from

around 8 – 70 mg/L (251). The MIC result obtained here, therefore, appears to be approximately in line with previous observations.

This result must be translated into an assessment of the antimicrobial action of silver alone, not AgNO₃. The following calculation assumes no bacterial growth inhibition by any other component of AgNO₃. Silver nitrate has a molar mass of 169.87 g, of which silver contributes 107.87 g (252), thus silver contributes to the total weight by the fraction: $107.87/169.87 = 0.635$. The corresponding concentration of silver in solution was therefore between 6.35 mg/L and 63.5 mg/L. During the LB experiments in Section 4.3.1 (where the antimicrobial effects of these electrodes were initially observed), each electrode well had a volume of 750 µL. The minimum mass of silver estimated to have been released into solution by each sensor over the course of the described 24-hour experiment was, therefore, estimated by multiplying by this volume. This resulted in an estimated range of **4.76 - 47.6 µg** of released silver ($6.35 \times 750 \times 10^{-6} \text{ mg} - 63.5 \times 750 \times 10^{-6} \text{ mg}$). For comparison, the Acticoat dressing has been estimated to release 2.26 µg/cm² of silver over 24 hours (253). A range of Acticoat dressing sizes are available, however, assuming that the 5 cm x 5 cm (25 cm²) dressing is applied to a wound, approximately 56.5 µg of silver would be released in a day ($2.26 \text{ µg/cm}^2 \times 25 \text{ cm}^2$). The quantity of silver released by this Ag/AgCl sensor to a wound may, therefore, be of the same order of magnitude or slightly lower than that of a common antimicrobial wound dressing if several measurements at 200 mV are conducted (as in Section 4.3.1). These sensors may, therefore, similarly benefit the wound healing process by reducing the occurrence of infection. This finding does, however, reinforce the idea that the sensors may not be appropriate for bacterial detection applications.

4.6 Wound Bed Model Development for the Assessment of Ag/AgCl Sensor Bacterial Detection in a Wound Environment

After obtaining some encouraging results in LB medium (Section 4.3), efforts were next focused upon detecting the growth of bacteria in environments more closely modelling the wound bed, in line with research objective 3 (Section 1.8). Firstly, an experiment was carried out using a simulated wound fluid (SWF). This then led to the development of a wound bed model (WBM) incorporating an additional collagen matrix.

4.6.1 20 mV Detection of Bacteria in SWF

In the previous 20 mV perturbation voltage LB growth experiments, *S. aureus* elicited the clearest EIS bacterial signatures (Section 4.3.2). For this reason, *S. aureus* was selected to trial this growth experiment in SWF, where all experimental methods remained the same except for the substitution of LB medium for SWF. In this case EIS normalisation was performed against the first inoculated measurement, more accurately simulating the measurement process for a real wound that would not have a sterile initial state. Further, measurements were performed over 48 Hrs in this instance (again using the PalmSens4 instrument).

Once more the bacteria proliferated, from an average starting concentration of 7.2×10^5 CFU/mL (range 3.0×10^5 - 1.2×10^6 CFU/mL) to 1.9×10^7 CFU/mL (range 2.8×10^6 - 3.5×10^7 CFU/mL) after 48 hours of incubation at 37 °C. The resulting raw modulus and absolute phase plots (Figures 4.8A and 4.8B respectively) are broadly similar in magnitude to the previous LB medium impedance plots. In the normalised modulus and phase plots, however, key differences can be seen. In normalised modulus (Figure 4.8C), a reduction was observed for the *S. aureus* chambers, in contrast to the increase seen in LB medium (Figure 4.5). Similarly, in normalised phase (Figure 4.8D) a high frequency trough emerged that had not been observed previously. Statistical significance emerged for these changes after 5 hours of growth, for example at 200 Hz for normalised modulus ($p = 0.046$) and at 20 kHz for normalised phase ($p < 0.001$). As there was no significance before this point, and no notable change between the 24 hour and 48 hour signatures, only the 0-, 5- and 24-hour data is presented (in line with previous results). This experiment, therefore, successfully demonstrated the ability of these Ag/AgCl sensors to detect bacteria in a simulated wound fluid.

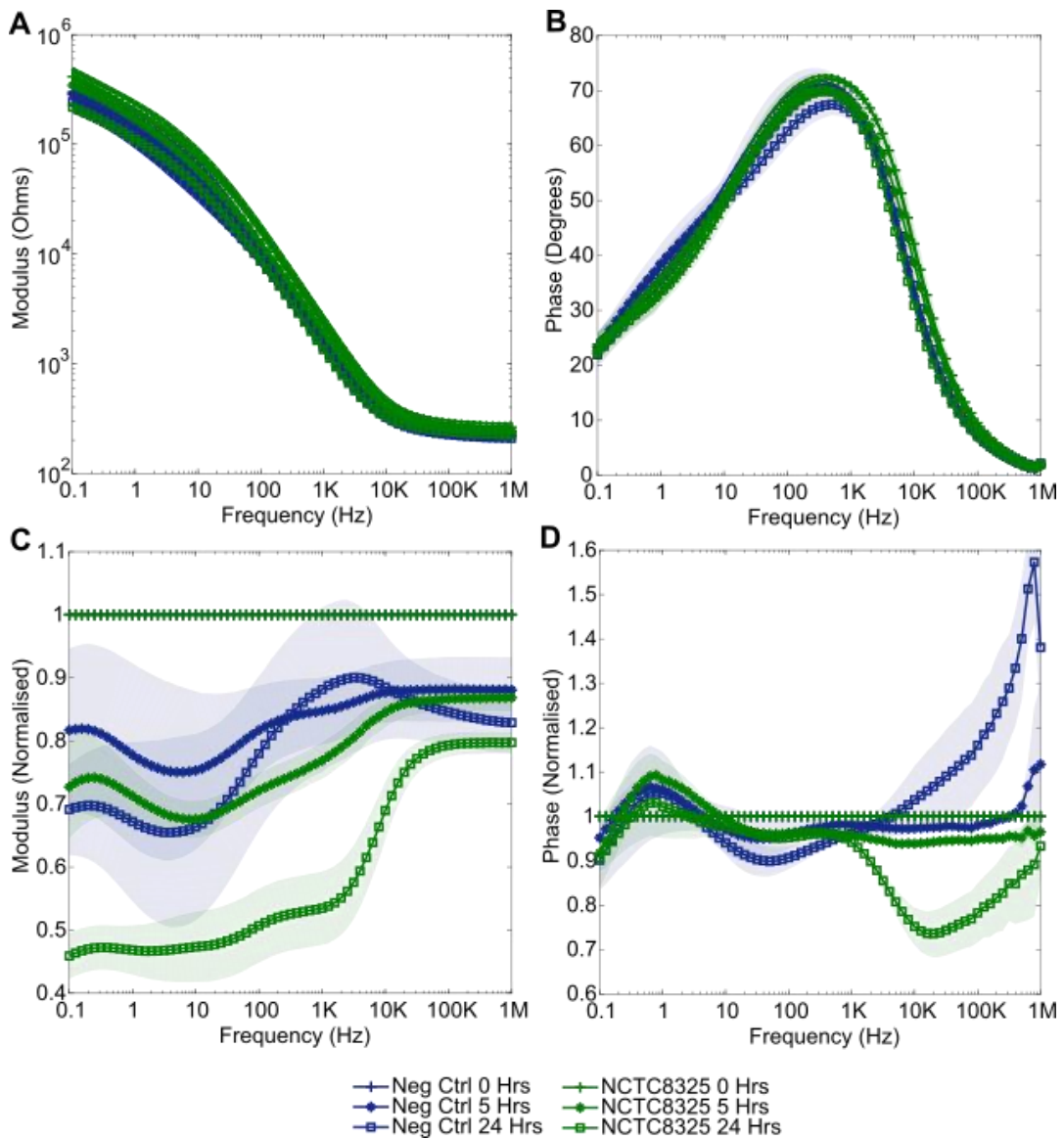


Figure 4.8. Impedance response associated with the inoculation of SWF with *S. aureus* (NCTC8325) and performing measurements with a 20 mV perturbation voltage. Plots show: (A) modulus; (B) absolute phase; (C) modulus normalised against first post-inoculation measurement; (D) phase normalised against first post-inoculation measurement ($n = 4$, shading depicts ± 1 standard deviation).

4.6.2 Collagen Matrix WBM Assessment at 20 mV

A collagen gel matrix was next incorporated into the previous SWF experiment, with the flexible Ag/AgCl electrode placed face down onto this “wound bed” (Figure 4.9). Adapted from the novel model developed by Werthén et al (2010), the 3D collagen gel matrix mimicked the structure of wound tissue, and enabled bacteria to form embedded biofilms akin to those formed in real wounds (216). Abundant in human skin, type I collagen was found by the group to be the most appropriate protein to emulate the dermal layer of the skin in their wound bed

model. Further, they validated that this model accurately simulated the growths of both *S. aureus* and *P. aeruginosa* in wounds.

For the first time, overnight incubation of the electrodes *in situ* (to allow background currents to settle) was not practical due to the model's assembly process. Instead, this step was replaced by an initial 2-hour sensor settlement in LB medium before assembly. This reduced settlement time had the benefit of moving towards a more realistic device, where overnight settlement in the wound environment before measurement would negate the rapid detection aim. Similarly, it was not practical to perform an initial sterile impedance sweep, therefore this was omitted. For these experiments, the models were incubated continuously for 48 hours and the Solartron multiplexer system used to perform automated EIS measurements with a 20 mV perturbation voltage.

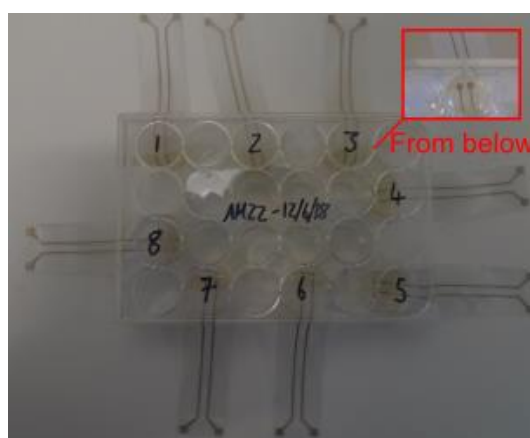


Figure 4.9. Image of the Ag/AgCl sensor WBM from above and below.

Firstly, *S. aureus* (NCTC8325) was grown in the WBM from a starting concentration of 4.5×10^7 CFU/mL (range $(2.3 - 6.2) \times 10^7$ CFU/mL) to 3.1×10^8 CFU/mL (range $(2.1 - 4.1) \times 10^8$ CFU/mL) after 48 hours. The errors in the impedance plots here (showing the inter-sensor variability) were larger than previously seen, in particular at frequencies above 10 Hz (Figure 4.10). Variability in sensor contact with the collagen gel is the most likely cause of this, as a delicate folding procedure was required to place the sensors onto the WBM. Inevitably, contact was not uniform across all sensors. Impedance modulus retained the same shape as before (Figure 4.10A), however, the WBM resulted in the measurement of higher absolute phase angles at low frequencies than in the previous experiments (Figure 4.10B). Again, some normalised modulus and phase variations occurred for the sterile models, with only slightly more pronounced changes occurring in the *S. aureus* models (Figures 4.10C, 4.10D). Due to

the high levels of error, no significant differences emerged until the 48-hours measurement point (seen via normalised phase at 1 Hz, $p = 0.002$).

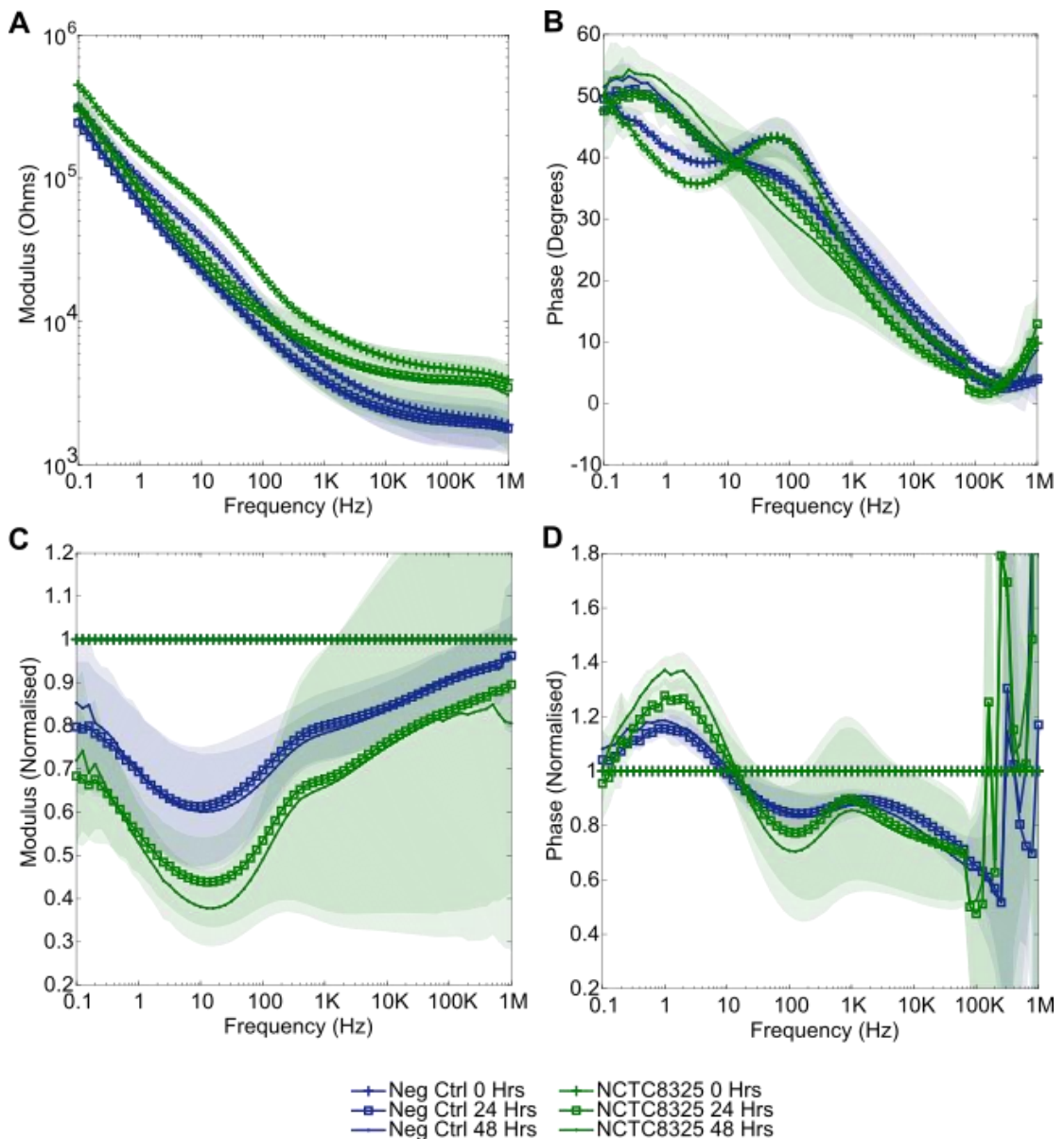


Figure 4.10. Impedance response associated with the inoculation of the WBM with *S. aureus* (NCTC8325) and performing measurements with a 20 mV perturbation voltage over 24 hours. Plots show: (A) modulus; (B) absolute phase; (C) modulus normalised against the first (post-inoculation) measurement; (D) phase normalised against the first (post-inoculation) measurement ($n = 4$, shading depicts ± 1 standard deviation).

Similarly, the growth of *P. aeruginosa* (PA14) in the wound bed model was measured (average starting concentration 9.1×10^7 CFU/mL, range $4.0 \times 10^7 - 1.4 \times 10^8$ CFU/mL). In Figure 4.11 an image of the experimental assembly at 72 hours is provided; bacterial chambers appear green in colour due to the production of pyocyanin by PA14 in this experiment. This experiment was carried out over 72 hours, aiming to determine if larger differences in normalised impedance

could be observed than previously. The normalised impedance spectra (Figure 4.12) appeared very similar to those obtained with *S. aureus*, yet significant changes emerged earlier at 24 hours here (normalised modulus 0.1Hz, $p = 0.004$). Again, the standard deviations from inter-sensor variability limited the significance of the observed differences between the sterile and bacterial chambers.

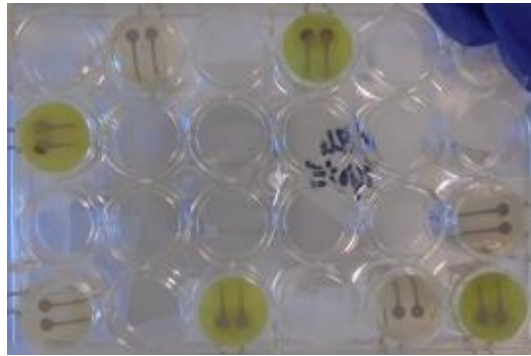


Figure 4.11. Image from below of the WoundSense assembly after 72 hours of PA14 growth in the WBM (20 mV voltage used for measurements). Chambers with green pigmentation contained bacteria, whereas clear chambers were sterile controls.

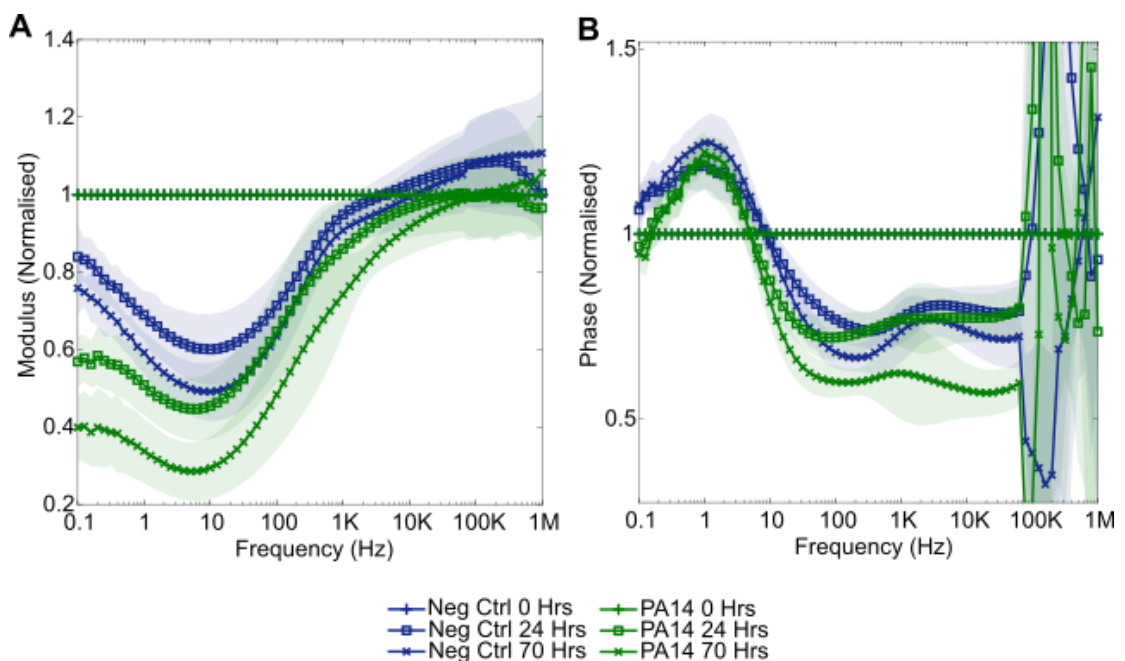


Figure 4.12. Impedance response associated with the inoculation of the WBM with *P. aeruginosa* (PA14) and performing measurements with a 20 mV perturbation voltage over 72 hours. Plots show: (A) modulus normalised against first (post-inoculation) measurement; (B) phase normalised against first (post-inoculation) measurement ($n = 4$, shading depicts ± 1 standard deviation).

Therefore, through performing experiments in the wound bed model at 20 mV, some significant differences in normalised impedance emerged. There did not, however, emerge any clear bacterial “signatures” that could be reliably used for the identification of bacterial infection,

and high errors were present throughout. It is believed that lowering the measurement voltage made the diffusion profile less sharp, and decreased the quantity of chemical reactions occurring (186). This is further discussed within Chapter 7.

4.6.3 The Presence of a Collagen Matrix Enables Bacterial Growth at 200 mV

It was hypothesised that using the 200 mV (higher) perturbation potential may be necessary to drive electrochemical reactions that can be detected as bacteria grow (Section 3.4.1). Further, it was believed that the WBM may provide a more protective environment for the bacteria, thus growth may not be inhibited (as was the case previously in LB medium at 200 mV). To test these ideas, a *P. aeruginosa* WBM experiment using a 200 mV perturbation potential was performed.

Whereas previously bactericidal effects were observed, in the WBM *P. aeruginosa* grew from an average starting concentration of 8.6×10^7 CFU/mL (range 4.8×10^7 - 1.3×10^8 CFU/mL) to 5.3×10^9 CFU/mL (range $(3.5 - 7.3) \times 10^9$ CFU/mL) after 24 hours of incubation at 37 °C. This supported the idea that the collagen gel provides a more defensive environment for the bacteria. Protective biofilm formation in the matrix is supported and additionally, as the type of growth medium influences the antimicrobial power of silver, this result suggests that the collagen matrix may decrease silver's toxicity (216,249). Figure 4.13 shows that visible growth occurred, with bacterial chambers possessing the characteristic green pigmentation of the metabolite pyocyanin.

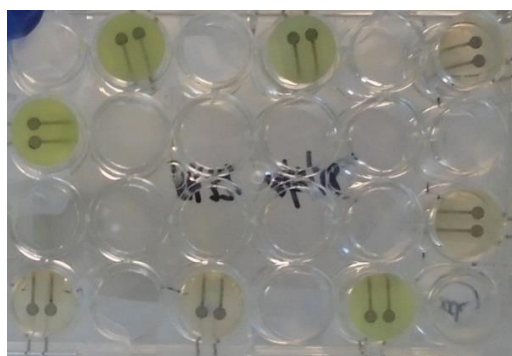


Figure 4.13. Image from below of the WoundSense assembly after 24 hours of PA14 growth in the WBM with a 200 mV voltage used for measurements. Chambers with green pigmentation contained bacteria, whereas clear chambers were sterile controls.

Despite this growth, no statistically significant changes between the negative control and bacterial chambers had emerged in the EIS signatures by the end of the 24-hour experiment.

This indicated that the 200 mV voltage provided no benefits over the 20 mV method for bacterial detection, where significance occurred after 24 hours with PA14. Within Figure 4.14 the normalised modulus and phase plots are shown, and it is clear that the detection of *P. aeruginosa* in the WBM via significant changes in impedance was not possible in this experiment.

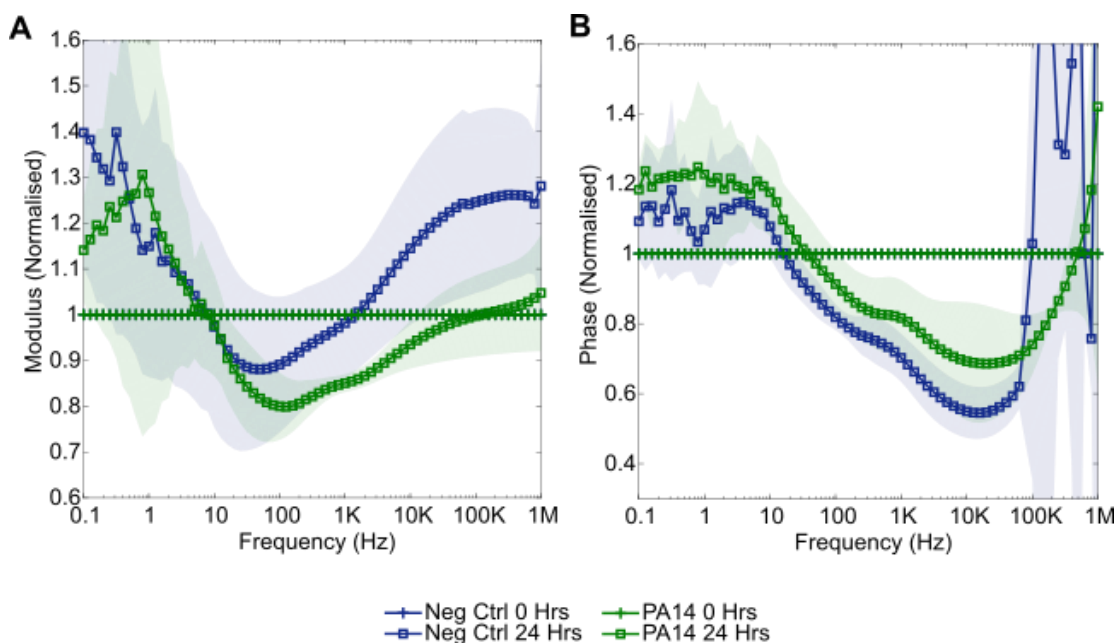


Figure 4.14. Impedance response associated with the inoculation of the WBM with *P. aeruginosa* (PA14) and performing measurements with a 200 mV perturbation voltage over 24 hours. Plots show: (A) modulus normalised against the first (post-inoculation) measurement; (B) phase normalised against the first (post-inoculation) measurement ($n = 4$, shading depicts ± 1 standard deviation).

4.7 Discussion and Summary

Within this chapter, the flexible Ag/AgCl WoundSense electrodes were employed in a variety of experiments to assess their suitability for the detection of common wound bacteria *S. aureus* and *P. aeruginosa*. By first performing EIS characterisation measurements in saline solution, it was found that the applied measurement voltage had a considerable impact upon the sensor stability. Using a measurement voltage below 60 mV resulted in a stable impedance response. Conversely, measurements using higher voltages resulted in a more unpredictable and unstable sensor impedance profile, with various interfacial phenomena being influential in this result.

Following this, bacterial growth experiments were conducted in different growth media. A comparison was made between the impedance spectra obtained using a 20 mV and a 200mV measurement voltage. By using these two voltages, the importance of sensor stability compared

to the electrochemical benefits of creating a higher electric field at the interface for probing the changes induced by the bacteria was assessed. Ultimately, clear advantages to the use of the 20 mV measurement voltage were observed. In LB medium it was possible to detect the presence of bacteria after 5 hours at both voltages, however, clearer EIS signatures emerged when using 20 mV due to the increased sensor stability at this voltage. Further, when using 200 mV bacterial growth inhibition was observed. Interestingly, this antimicrobial effect was reduced by the introduction of the collagen matrix in the WBM, however, clear bacterial signatures still did not emerge.

Furthermore, despite successfully detecting two key wound pathogens with these Ag/AgCl sensors, a number of negative indications to their use in bacterial detection were found:

- a lack of sensor consistency resulting in larger than desired errors throughout;
- sensor instability causing dominating negative control EIS signature variation;
- bacterial growth inhibition and an antimicrobial sensor surface;
- no rapid bacterial detection or clear EIS signature formation in the WBM.

Whilst some of these effects were minimised by using a lower measurement voltage, they could not be eliminated. Thus, the use of other electrode materials for an EIS based bacterial sensor merited consideration.

5. ASSESSING THE SUITABILITY OF CARBON ELECTRODES FOR THE DETECTION OF WOUND PATHOGENS

5.1 Introduction

Aiming to address the first project objective (Section 1.8) and improve upon the Ag/AgCl electrode results, a carbon electrode was next assessed for rapid bacterial detection.

Carbon electrodes possess many beneficial properties that make them suitable for electrochemical applications. Crucially, carbon electrodes are stable, inexpensive and provide an inert surface (229). These features in particular indicate a potential advantage over the Ag/AgCl electrodes previously investigated in this study; in Chapter 4 it was concluded that a more stable and inert sensor able to be operated over a wider potential range was desired. Carbon was, therefore, considered worthy of investigation. Whilst available in different forms such as carbon nanotube and graphene, screen-printed carbon sensors have the additional benefit of being disposable and, therefore, have already been utilised in many medical and biosensing applications. Examples include devices such as blood glucose monitors and DNA sensors (222,228,229). Furthermore, screen-printed carbon sensors able to detect bacteria within 24 hours via changes in normalised impedance were developed previously within the research group (118,223). These earlier studies focused upon the detection of common respiratory tract pathogens in sputum, in particular *P. aeruginosa*, with applications in cystic fibrosis patient infection monitoring. The carbon sensors were re-assessed in this project to determine their suitability for wound infection detection. The sensors were, therefore, reproduced for this study and investigated with a number of key aims, including:

- to obtain impedance signatures for bacteria clinically important to wound infection;
- to identify and perform experiments using a range of relevant growth conditions (such as the wound bed model);
- to minimise the time to detection by increasing measurement frequency via the multiplexer system.

5.2 Carbon Electrode Detection of Bacteria in LB Medium

Aiming to identify characteristic changes to impedance that occur due to bacterial growth (objective 2, Section 1.8), LB medium experiments were conducted. Firstly, the growth of *S. aureus* strain NCTC8325 in LB medium was studied. Following an initial measurement of sterile LB medium, measurements of *S. aureus* growth were performed every 30 minutes for 6 hours, and then every subsequent 2 hours until the final measurement after 24 hours. From an average starting cell density of 1.8×10^6 CFU/mL (range $(1.3 - 2.3) \times 10^6$ CFU/mL, $n = 3$), the

concentration increased to 3.6×10^8 CFU/mL (range $(2.9 - 4.6) \times 10^8$ CFU/mL) after 24 hours. There was, therefore, no indication of growth inhibition. This was an immediate advantage over the Ag/AgCl electrodes studied in Chapter 4, which displayed bacterial growth inhibition (particularly when a 200 mV measurement voltage was used).

Due to the high baseline impedance of the carbon sensors (a magnitude of over $10^6 \Omega$ at 0.1 Hz) compared to the magnitude of any changes occurring, it was evident that the raw modulus and phase plots were not appropriate for highlighting any differences between the sterile and bacterial wells (Figure 5.1). Promisingly, in these plots a high sensor consistency was indicated via the minimal error shading visible. The data shown is limited to that below 1×10^5 Hz due to no changes of interest occurring above this frequency throughout the project.

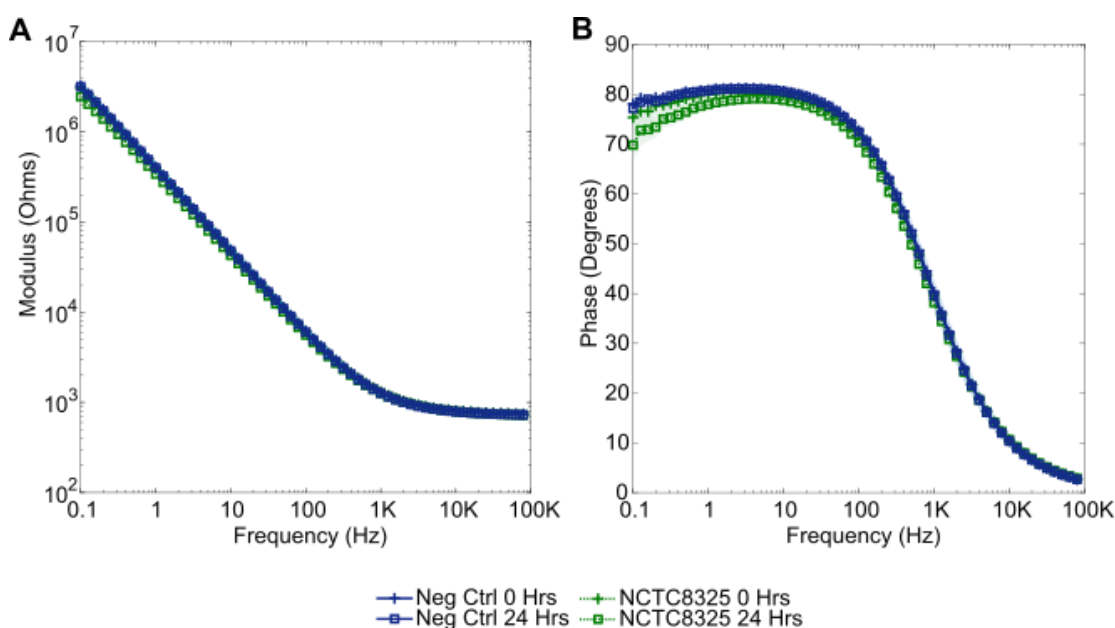


Figure 5.1. Raw impedance plots associated with the inoculation of LB medium with *S. aureus* (NCTC8325) and performing measurements over 24 hours with carbon sensors. Plots show (A) modulus and (B) absolute phase ($n = 3$, shading depicts ± 1 standard deviation).

In contrast, the normalised impedance plots displayed clear differences between the *S. aureus* and the sterile wells, which could be used to detect bacterial growth. Whereas minimal changes to normalised impedance occurred over the 24-hour period for the sterile controls, for the bacterial wells clear signatures emerged. In normalised modulus, a reduction in the normalised value occurred at frequencies below 1 kHz (Figure 5.2A); in normalised phase a 1 kHz trough and a high frequency shoulder emerged by 24 hours (Figure 5.2B); in normalised reactance a decreasing trend was seen across the full frequency range (Figure 5.2C); finally, normalised resistance presented varying low frequency changes during bacterial growth (Figure 5.2D). For normalised resistance in particular, a high level of noise was observed below 1 Hz as diffusion

limitation conditions were approached. A common area of electrochemical noise as a system approaches DC, some studies employ stirring or the use of micro electrodes to limit the diffusion layer thickness and minimise the impact of these processes (Sections 1.6 and 2.3). At low frequencies the system's impedance is also at its highest (Figure 5.1), therefore, such low frequency noise is also likely to be a consequence of approaching the instrumentation's low current limit. In general, however, the standard deviation shading present in these normalised plots is minimal, indicating a consistent and stable sensor response.

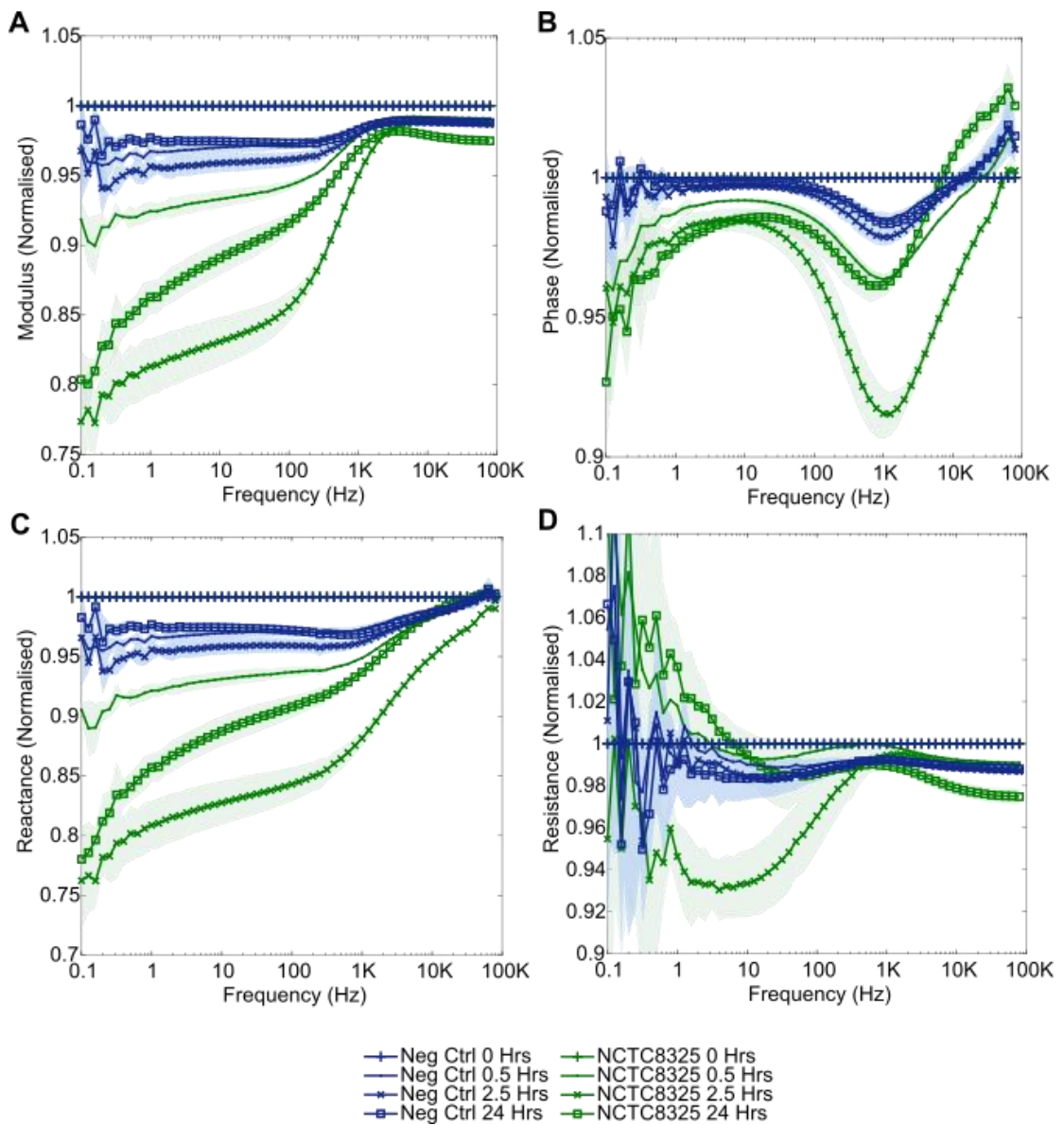


Figure 5.2. Normalised impedance signatures obtained following the inoculation of LB medium with *S. aureus* (NCTC8325) and performing 200 mV measurements with the carbon sensors over 24 hours. Plots show: (A) normalised modulus; (B) normalised (absolute) phase; (C) normalised reactance; (D) normalised resistance. Normalisation was performed against a sterile initial state ($n = 3$, shading depicts ± 1 standard deviation).

By focussing on key frequencies where the normalised impedance changes during *S. aureus* growth were largest, the time-based plots shown in Figure 5.3 were created. It was calculated that after only 30 minutes of growth, the *S. aureus* normalised impedance response was significantly different to the sterile response (two sample t-test, $\alpha = 0.05$). Rapid detection of *S. aureus* was, therefore, achieved. For example, detection was possible via normalised phase at 1 kHz ($p = 0.007$ after 30 minutes ($n = 3$)). Interestingly, for each key feature the changes were most pronounced after around 2.5 hours; normalised values had changed by up to 20% at this time. For normalised modulus, phase, and reactance (Figures 5.3A, 5.3B and 5.3C) the change's magnitude increased before later reducing to an intermediate but significant value ($p < 0.05$). The 5 Hz normalised resistance behaviour was slightly different: initially a trough formed (significant from 2 to 6 hours, p-value range 0.004 – 0.028), which then developed into a shoulder (significant between 16 and 20 hours, p-value range 0.024 – 0.045). These continuous changes were believed to result from the combination of various processes occurring over different timescales, including initial bacterial metabolism, cell settlement and later biofilm formation (143,165,254).

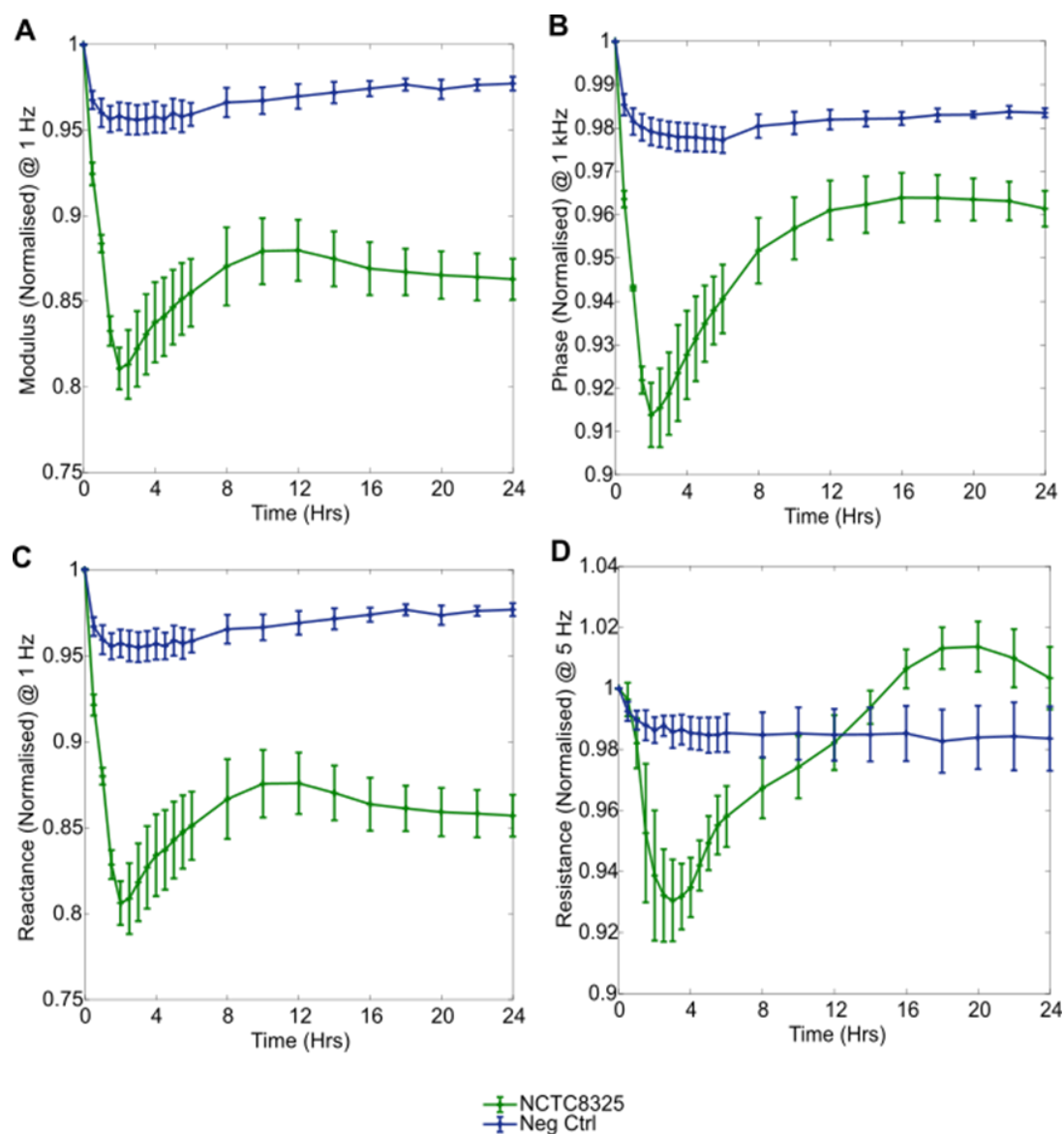


Figure 5.3. *S. aureus* (NCTC8325) growth in LB medium time-based plots. Plots were obtained by concentrating on the changes to normalised impedance at specific frequencies over time. Plots show: (A) normalised modulus at 1 Hz; (B) normalised (absolute) phase at 1 kHz; (C) normalised reactance at 1 Hz; (D) normalised resistance at 5 Hz ($n = 3$, error bars depict ± 1 standard deviation).

Next, *S. epidermidis* (NCTC11964) growth in LB medium was investigated. The obtained normalised impedance signatures contained very similar features to those observed during *S. aureus* growth, indicating common underlying electrochemical mechanisms. Notably, a reduction in the normalised modulus value below 1 kHz (Figure 5.4A) and a 1kHz normalised phase trough (Figure 5.4B) were observed. Again, these features maximised at around 2.5 hours, with normalised value changes of up to 15% observed in this case. The plots shown omit data below 1 Hz due to high noise levels (as was seen in Figure 5.2). For normalised modulus at 1 Hz, the impedance changes were significantly different vs the negative controls from 1.5 hours ($p = 0.020$) and remained significant at 24 hours ($p = 0.013$), despite later increases in

normalised modulus (Figure 5.4C). For normalised phase at 1 kHz (Figure 5.4D) changes were significant after 30 minutes ($p = 0.006$), however, only remained significant until 12 hours ($p = 0.037$). After this time, the trough was no longer present, however, again a high frequency normalised phase shoulder began to emerge. As a delayed effect, this was hypothesised to be due a later process such as the settlement of a high concentration of cells on the electrode or biofilm formation, ideas which are further investigated within Section 5.5.

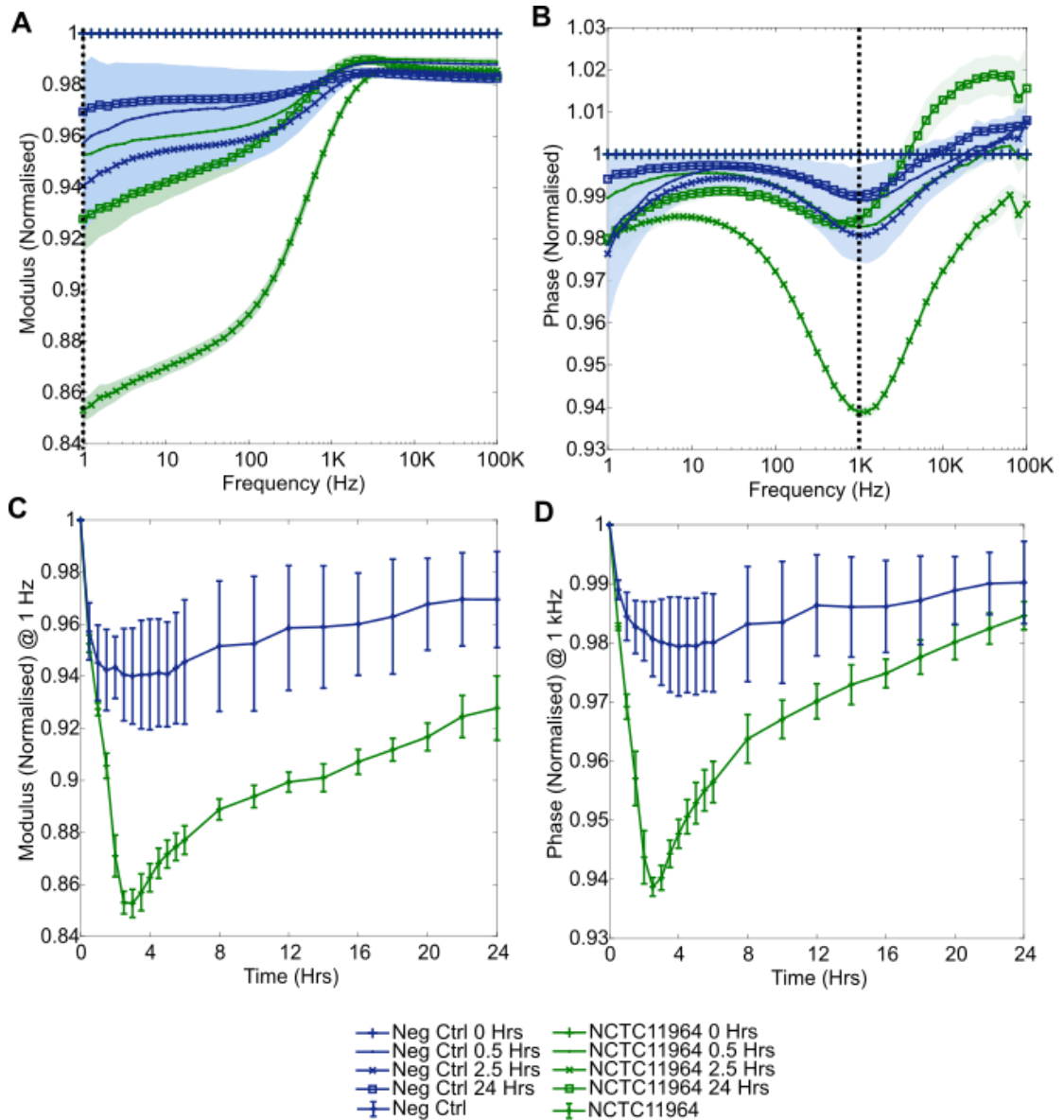


Figure 5.4. Impedance response associated with the growth of *S. epidermidis* (NCTC11964) in LB medium to an average concentration of 3.8×10^7 CFU/mL after 24 hours. Plots show: (A) normalised modulus; (B) normalised (absolute) phase; (C) 1 Hz normalised modulus over time; (D) 1kHz normalised phase over time ($n = 4$, errors depict ± 1 standard deviation).

Finally, *P. mirabilis* (DSM4479) growth in LB medium was also measured over 24 hours, with a starting cell density of 7.4×10^6 CFU/mL (range $(6.9 - 8.9) \times 10^6$ CFU/mL) rising to 4.6×10^9 CFU/mL (range $(3.7 - 5.3) \times 10^9$ CFU/mL). Once more, normalised impedance signatures emerged during bacterial growth which contained similar features to those seen with the other bacteria under study. These included a reduction in normalised modulus value (Figure 5.5A) and a 1 kHz normalised phase trough (Figure 5.5B). During this experiment the level of noise was again high at low frequencies, resulting in the earliest significance in normalised modulus at 1 Hz emerging after 2 hours ($p = 0.025$, Figure 5.5C). Once more, differences were observed more rapidly through normalised phase at 1 kHz, after 1 hour of growth ($p = 0.001$, Figure 5.5D). Here, the impedance responses were sustained. Normalised value changes of up to 25% were observed, with only a minimal reduction in the signature features between 2.5-24 hours. Whilst this maximum magnitude of change varied between species, the magnitude of sterile control changes also varied and so this is not believed to be a reliable species differentiator. Further, negative control changes in normalised phase at high frequencies resulted in no clear feature for the bacterial sensors here.

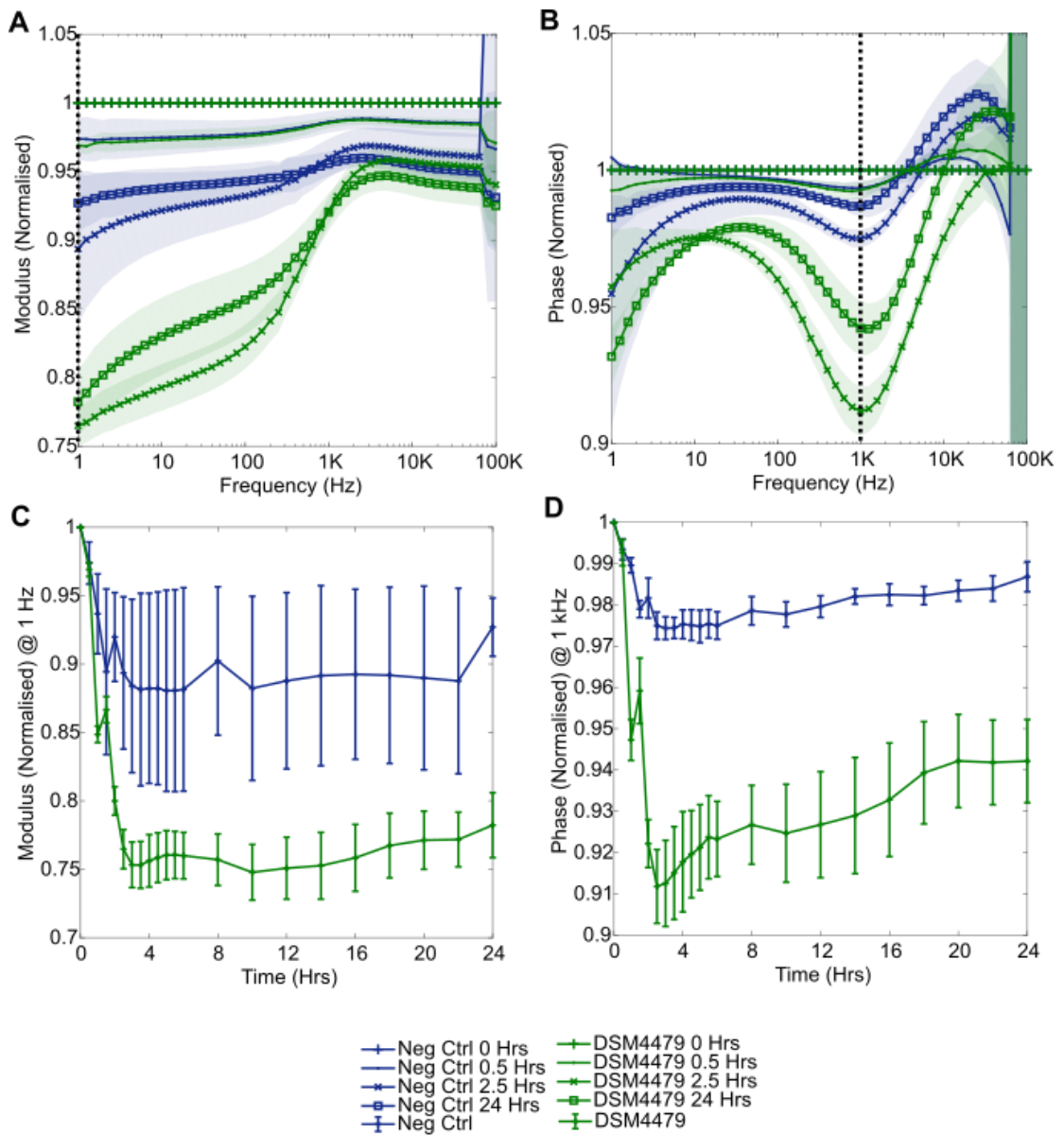


Figure 5.5. Impedance response associated with the growth of *P. mirabilis* (DSM4479) in LB medium over 24 hours. Plots show: (A) normalised modulus; (B) normalised (absolute) phase; (C) 1 Hz normalised modulus over time; (D) 1kHz normalised phase over time ($n = 4$ for *P. mirabilis* chambers, $n = 3$ for sterile controls, errors depict ± 1 standard deviation).

Furthermore, a range of wound bacteria were successfully detected in LB medium within 1 hour using these carbon sensors. Largely similar normalised impedance signatures were obtained for each, with these discussed in more detail within Chapter 7. A difference in the timing of EIS signature features, and the changes occurring at high frequency phase in particular emerged from these experiments as areas which may have some level of species dependence. A number of notable differences between *P. mirabilis* and the staphylococci studied exist, in particular morphological differences (such as the presence of flagella in *P. mirabilis*), the resulting differences in motility, and metabolic differences (Section 2.2.5). It is,

therefore, likely that a combination of such differences influences the impedance at the sensor interface. In addition, the sensors had no detrimental effect upon bacterial growth during the impedance measurements, with clear biofilm formation evident both visibly and via crystal violet staining (Figure 5.6).

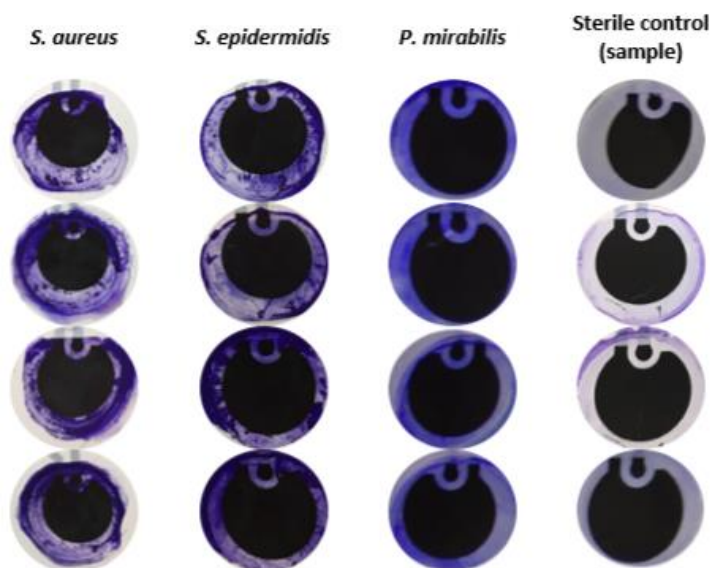


Figure 5.6. CV staining images resulting from bacterial growth experiments performed in LB medium. Areas of violet dye indicate organism DNA and biofilm matrix protein staining. A lack of staining for negative control chambers indicated no bacterial attachment, whereas staining for the *S. aureus*, *S. epidermidis* and *P. mirabilis* growth chambers indicated attachment.

5.3 Carbon Electrode Detection of Bacteria in SWF

Following the successful detection of bacteria in LB medium, the growths of common wound pathogens in SWF were next investigated using the carbon sensors (objective 3, Section 1.8). The SWF, containing a mixture of physiological salt solution and foetal bovine serum (Section 3.2.2), mimicked the protein content, ionic content and viscosity of real wound exudate (215,216). As bacterial growth is dependent upon numerous media specific factors (including nutrient availability (255)), investigating the detection of bacteria in SWF via EIS was an important experimental progression. Again, several impedance sweeps were performed over at least 24-hour periods. Only starting cell densities will be stated as experiments were performed over varying lengths of time. For consistency, and as no results of interest were obtained beyond 24 hours, no data outside this time is reported. Whereas in LB medium the impedance signature features often varied significantly over time, the features seen in SWF generally only increased in magnitude with time. For this reason, and to increase clarity in the figures, only the 0-hour and 24-hour data is shown in the subsequent normalised impedance plots. Time-

based plots at key frequencies are provided to illustrate the evolution of these features over time. Further, the data shown here has been normalised against an inoculated starting state (as was done with the SWF and WBM Ag/AgCl electrode experiments).

Firstly, baseline raw modulus and phase plots obtained from measurements of sterile SWF are shown in Figure 5.7. Very high consistency between the sensors was again found, as evidenced by a lack of standard deviation shading, supporting measurement reliability. The SWF had a lower baseline impedance modulus at low frequencies by around a factor of 10 compared to that seen in LB medium (Figure 5.1), however, otherwise the modulus and phase plots had a very similar appearance to the LB medium plots. Compositional differences between the SWF and LB medium are believed to underlie this small difference in baseline impedance, which further supports the need to conduct these SWF experiments.

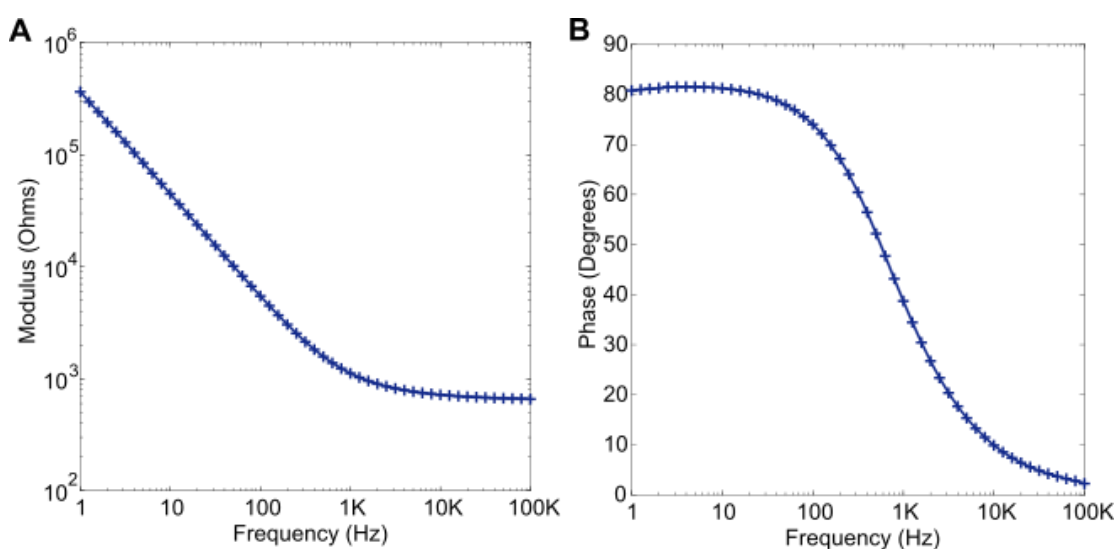


Figure 5.7. The baseline (A) modulus and (B) absolute phase plots obtained using the carbon sensors in sterile SWF ($n = 4$, shading depicts ± 1 standard deviation). A lack of visible shading indicates high sensor consistency in the SWF.

The growth of *S. aureus* (NCTC8325) in the SWF was next studied, with wells inoculated to an average starting cell density of 3.3×10^6 CFU/mL (range $(1.8 - 4.6) \times 10^6$ CFU/mL). Clear normalised impedance signatures emerged over the course of the experiment (Figure 5.8). In normalised modulus (Figure 5.8A), a reduction in normalised value was seen below 1 kHz; in normalised phase (Figure 5.8B), both a mid-frequency trough and a high frequency shoulder were observed. Statistically significant features had emerged by the 5-hour measurement point: at 5 hours, $p = 0.022$ for normalised modulus at 1 Hz and $p = 0.001$ for normalised phase at 630 Hz for example. It should be noted that the measurement frequency in this particular experiment was lower than in a number of other cases (as can be seen in Figures 5.8C, 5.8D);

with more frequent measurements between 2 and 5 hours a faster detection time may have been achieved. Each key feature of the normalised signatures obtained here was also observed during the *S. aureus* LB medium study (Section 5.2), however, the frequencies, magnitudes and timings of the normalised phase characteristics in particular were different. The influence of growth medium upon the impedance profiles was, therefore, highlighted (and is discussed in more detail in Chapter 7). Key factors such as bacterial adaptation and growth rates within the different media, and the availability of different nutrients (leading to different metabolic products) are likely to be influential in the impedance response (255).

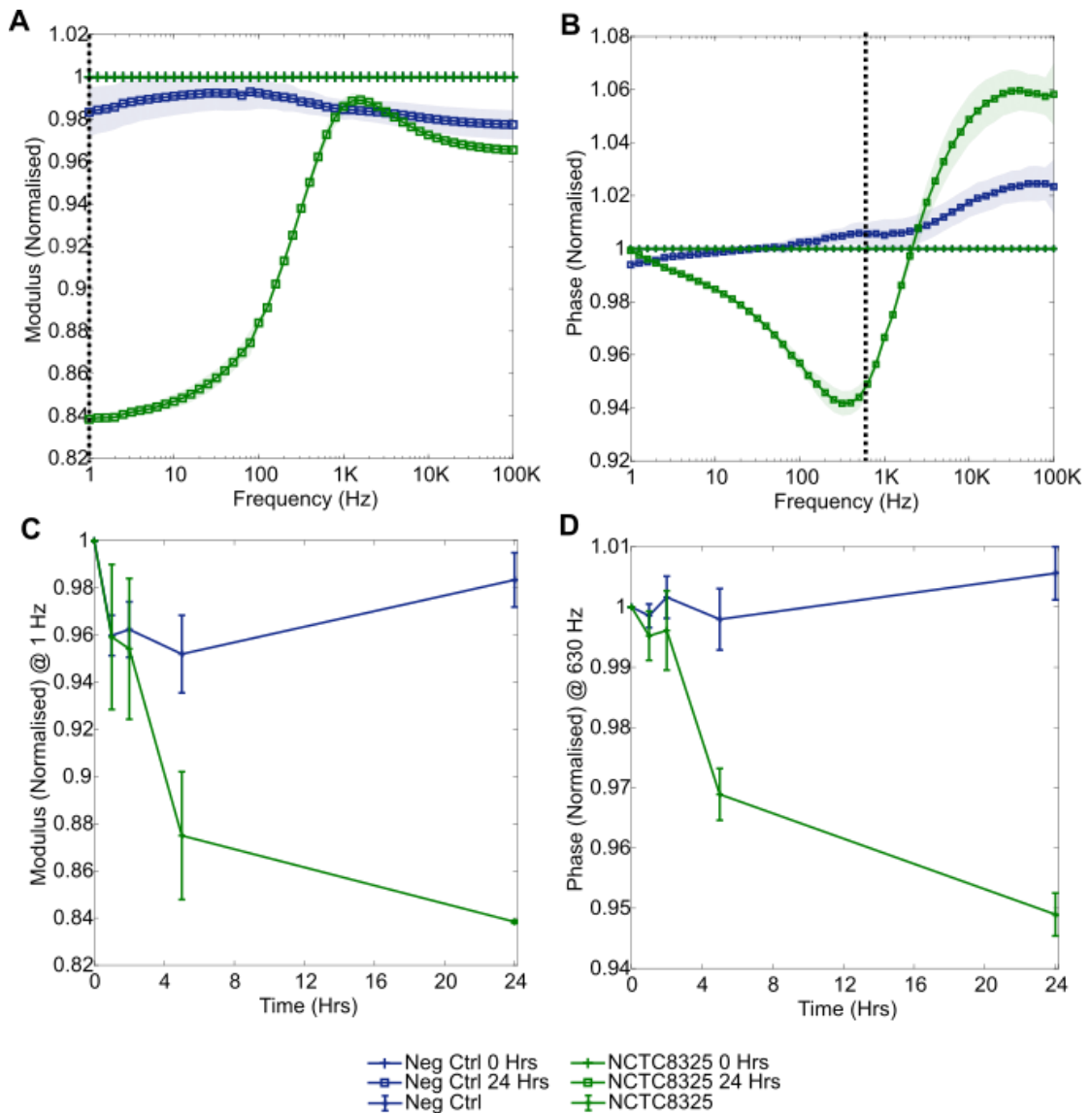


Figure 5.8. Impedance response associated with the growth of *S. aureus* (NCTC8325) in SWF. Plots show: (A) normalised modulus; (B) normalised (absolute) phase; (C) 1 Hz normalised modulus over time; (D) 630 Hz normalised phase over time, which provided a region of low standard deviation close to the turning point of the normalised trough. ($n = 3$ for *S. aureus*, $n = 4$ for negative controls, errors depict ± 1 standard deviation).

Similarly, during *P. aeruginosa* (PA14) growth in SWF from an average starting cell density of 9.3×10^6 CFU/mL (range 4.4×10^6 - 1.3×10^7 CFU/mL), normalised impedance signatures emerged (Figure 5.9). These were, however, influenced by decreases in impedance below 50 Hz which occurred for both the negative control and bacterial chambers (Figures 5.9A, 5.9B). Further, in these low frequency regions large error was observed. As stated previously, diffusion processes and system limitations result in this being a common area of electrochemical noise. In addition, the impedance of the electrode itself contributes most at low frequencies, therefore, this effect may also be due to moisture settling on the electrode connectors over time in the incubator for example (256). Whereas *S. aureus* growth resulted in a high frequency normalised phase shoulder (Figure 5.8B), this did not emerge during *P. aeruginosa* growth (Figure 5.9B). The mid-frequency normalised phase trough and reduction in normalised modulus were, however, present once more. Due to high errors at 1 Hz, the normalised modulus values at 10 Hz are instead plotted against time (Figure 5.9C). Normalised phase is again plotted at 630 Hz, as this provided the region of lowest error close to the trough turning point (Figure 5.9D). For *P. aeruginosa*, statistical significance emerged after 2 hours of growth in SWF, as observed via 630 Hz normalised phase ($p = 0.017$).

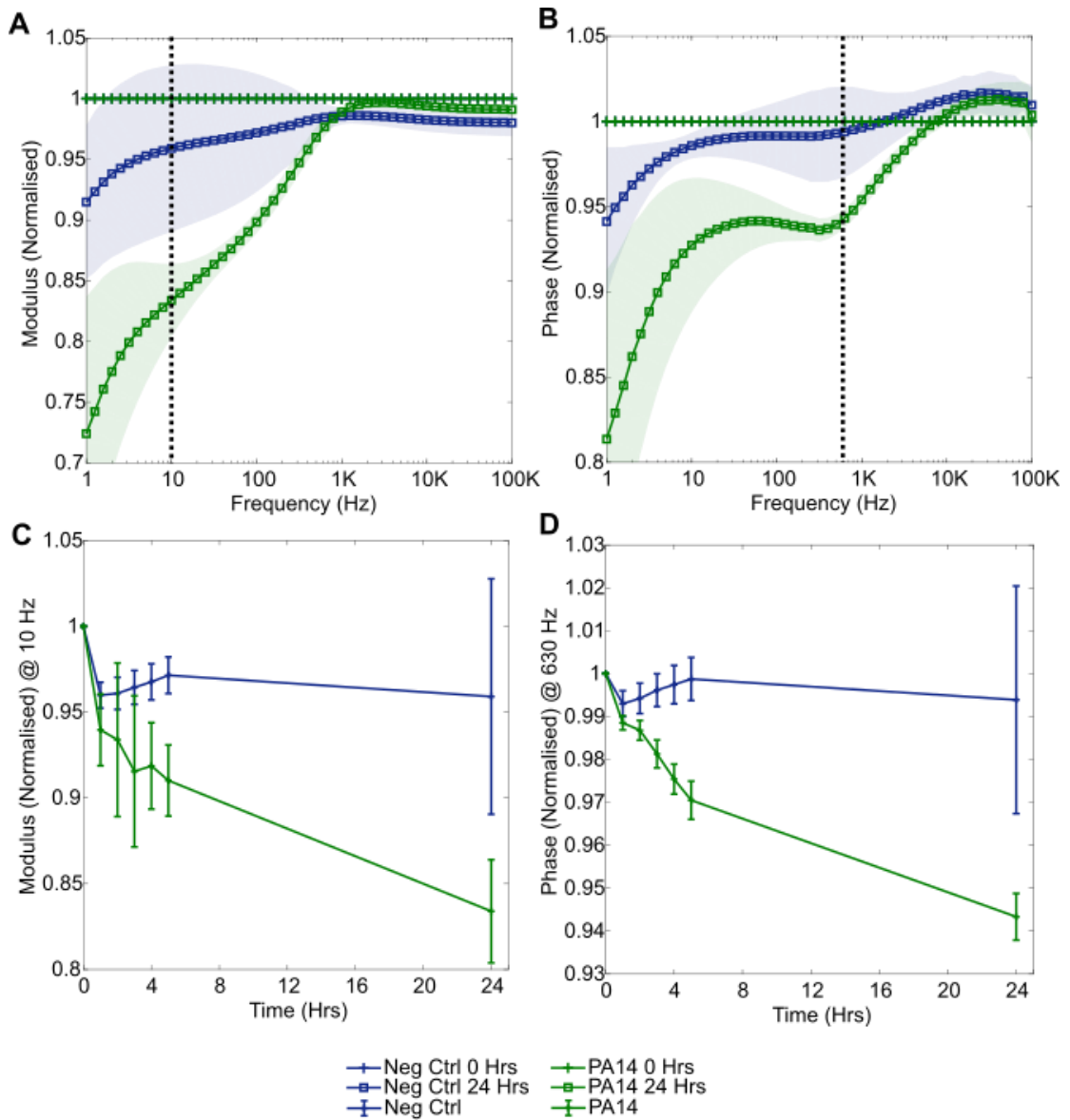


Figure 5.9. Impedance response associated with the growth of *P. aeruginosa* (PA14) in SWF. Plots show: (A) normalised modulus; (B) normalised (absolute) phase; (C) 10 Hz normalised modulus over time; (D) 630 Hz normalised phase over time ($n = 4$, errors depict ± 1 standard deviation).

Finally, normalised impedance signatures were obtained for *P. mirabilis* (DSM4479) growth in the SWF from an average starting cell density of 6.3×10^6 CFU/mL (range $(5.9 - 6.8) \times 10^6$ CFU/mL). Like the other species studied, a reduction in normalised modulus value was observed in the mid to low frequency area (Figure 5.10A), and a normalised phase trough was present (Figure 5.10B). There were again large low frequency errors, therefore, the frequency at which normalised modulus changes were most distinct was 10 Hz (Figure 5.10C, significant from 2.5 hours with $p = 0.007$). For normalised phase the key frequency was again 630 Hz (Figure 5.10D), with significance from 2.5 hours ($p = 0.010$). In this instance a large change occurred for both the negative control and bacterial chambers at high frequencies in normalised

phase. This feature was, therefore, believed to be unrelated to the presence of *P. mirabilis*, unlike when it was observed for *S. aureus*. High frequency EIS noise such as this is commonly believed to derive from instrumentation limitations, including the negative influence of cables (257).

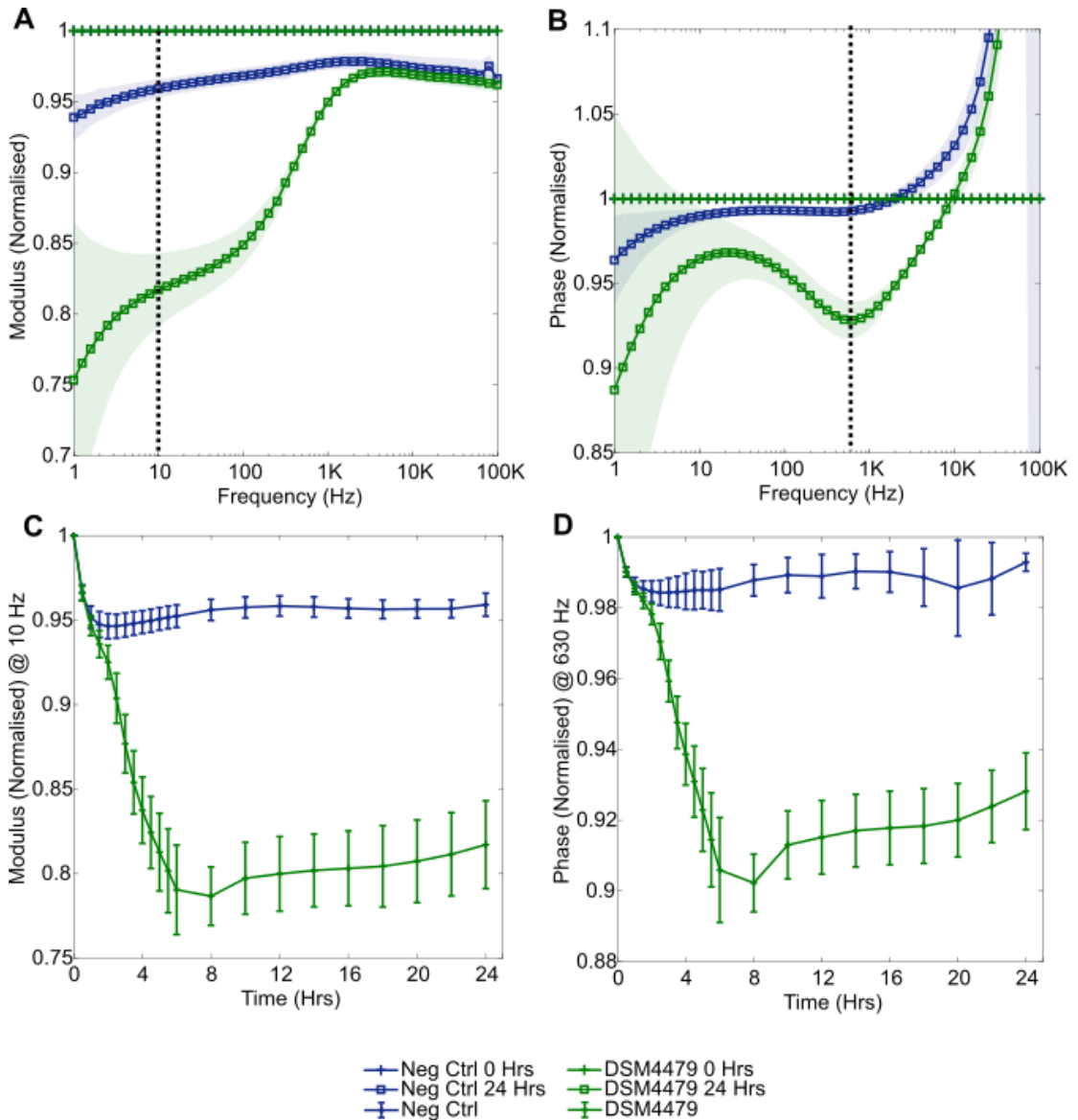


Figure 5.10. Impedance response associated with the growth of *P. mirabilis* (DSM4479) in SWF. Plots show: (A) normalised modulus; (B) normalised (absolute) phase; (C) 10 Hz normalised modulus over time; (D) 630 Hz normalised phase over time ($n = 4$, errors depict ± 1 standard deviation).

This series of experiments, therefore, demonstrated the ability of these carbon sensors to detect a range of wound pathogens in a simulated wound fluid. As in LB medium, many prominent signature features were common to each pathogen. Some additional subtle differences were present that will be highlighted in further detail within Chapter 7 (Discussion); these may have

been influenced by cell concentration and motility for example. As a result of this success, it was deemed appropriate to progress to measurements in the more advanced wound bed model.

5.4 Carbon Electrode Detection of Bacteria in the Wound Bed Model

The growths of two key wound pathogens, *S. aureus* and *P. aeruginosa*, in the wound bed model were next explored using the carbon sensors (objective 3, Section 1.8). Briefly, this physical model consisted of a collagen gel formed on the electrode surface to mimic wound tissue, and simulated wound fluid pipetted above (Section 3.6.4) (216). Figure 5.11 provides the baseline impedance plots for the sterile wound bed model. When compared to the baseline SWF plots (Figure 5.7), the only notable difference is a lower phase angle at frequencies below 30 Hz, surrounded by a larger error than previously. This is believed to arise from inhomogeneous distribution of the collagen gel on the sensor, an anticipated consequence of the solution pipetting process. Noise due to the collagen matrix is further discussed within Chapter 7.

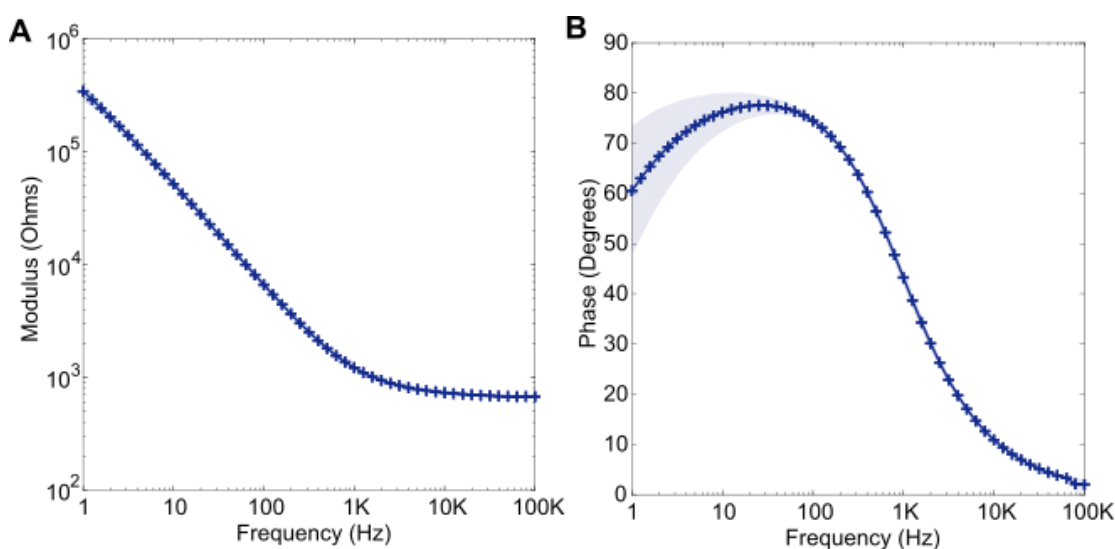


Figure 5.11. The baseline (A) modulus and (B) absolute phase plots obtained using the carbon sensors in a sterile WBM ($n = 4$, shading depicts ± 1 standard deviation).

As previously, normalisation was carried out against the first impedance measurement, performed immediately following inoculation. The normalised impedance plots resulting from *S. aureus* growth in the WBM from 2.8×10^6 CFU/mL (range $(2.6 - 2.9) \times 10^6$ CFU/mL) to 3.0×10^8 CFU/mL (range $(0.7 - 8.0) \times 10^8$ CFU/mL) over 24 hours are displayed within Figure 5.12. Despite some large standard deviations and negative control variation at frequencies

below 100 Hz in both normalised modulus (Figure 5.12A) and normalised phase (Figure 5.12B), significant differences between the sterile controls and the *S. aureus* wells emerged. For normalised modulus the changes at 100 Hz were key, due to the balance between magnitude and error at this frequency; for normalised phase 630 Hz was the key location for impedance change. In both regions, significant changes were visible after 4 hours of growth (with $p = 0.015$ in each case, Figures 5.12C and 5.12D). Interestingly, the high frequency normalised phase shoulder seen previously for *S. aureus* in both LB medium and SWF was again present in the WBM (Figure 5.12B).

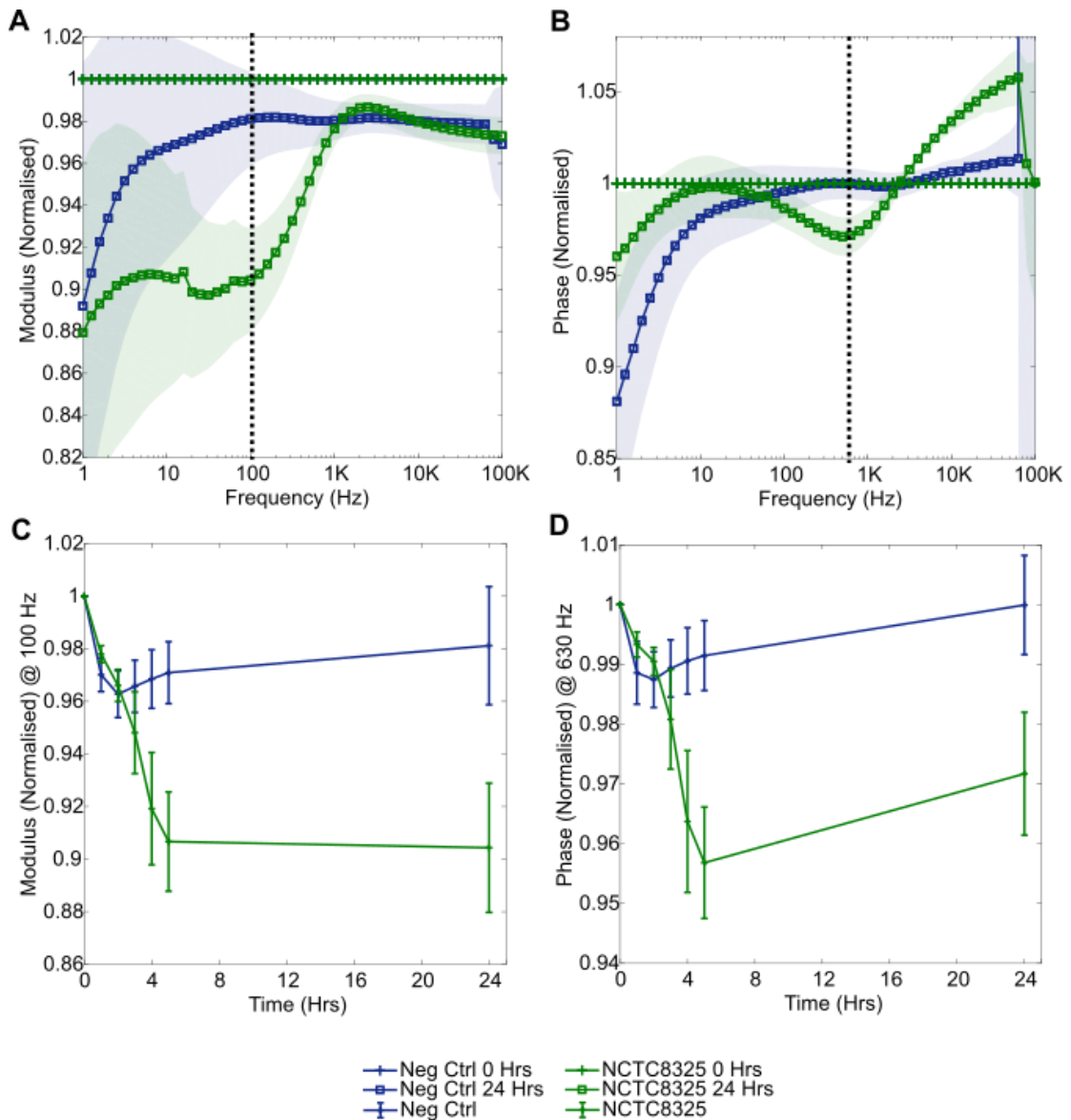


Figure 5.12. Impedance response associated with the growth of *S. aureus* (NCTC8325) in the WBM. Plots show: (A) normalised modulus; (B) normalised (absolute) phase; (C) 100 Hz normalised modulus over time; (D) 630 Hz normalised phase over time ($n = 4$, errors depict ± 1 standard deviation).

Likewise, Figure 5.13 displays the normalised impedance plots resulting from *P. aeruginosa* growth in the WBM. From an initial concentration of 3.1×10^7 CFU/mL (range $(1.5 - 3.9) \times 10^7$ CFU/mL), the PA14 concentration increased to 3.2×10^9 CFU/mL (range $(1.5 - 4.3) \times 10^9$ CFU/mL). The obtained normalised modulus profile (Figure 5.13A) was similar in shape to the *S. aureus* profile (Figure 5.12A), however, in this case statistical significance was observed at the slightly earlier time of 3 hours (1Hz, $p = 0.015$). In contrast, the normalised phase signatures for the two bacteria were different in both the high and low frequency areas (Figure 5.13B vs Figure 5.12B). At 1 Hz, a significant difference between PA14 and the negative controls was present by 24 hours ($p = 0.012$). As this has previously been an area of high noise, it may not be an accurate indicator of infection. Changes in this frequency region have, however, previously been associated with pyocyanin production by this species (118). Further, the high frequency shoulder seen with *S. aureus* was again not present for *P. aeruginosa*. This may be a more reliable feature that enables differentiation between these two bacterial species. Furthermore, it was possible to detect both pathogens in the WBM far more rapidly using these carbon electrodes than was possible with the Ag/AgCl electrodes in Chapter 4. Significant EIS signature changes were observed after 3-4 hours here, compared to the previous electrodes where a minimum of 24 hours was required.

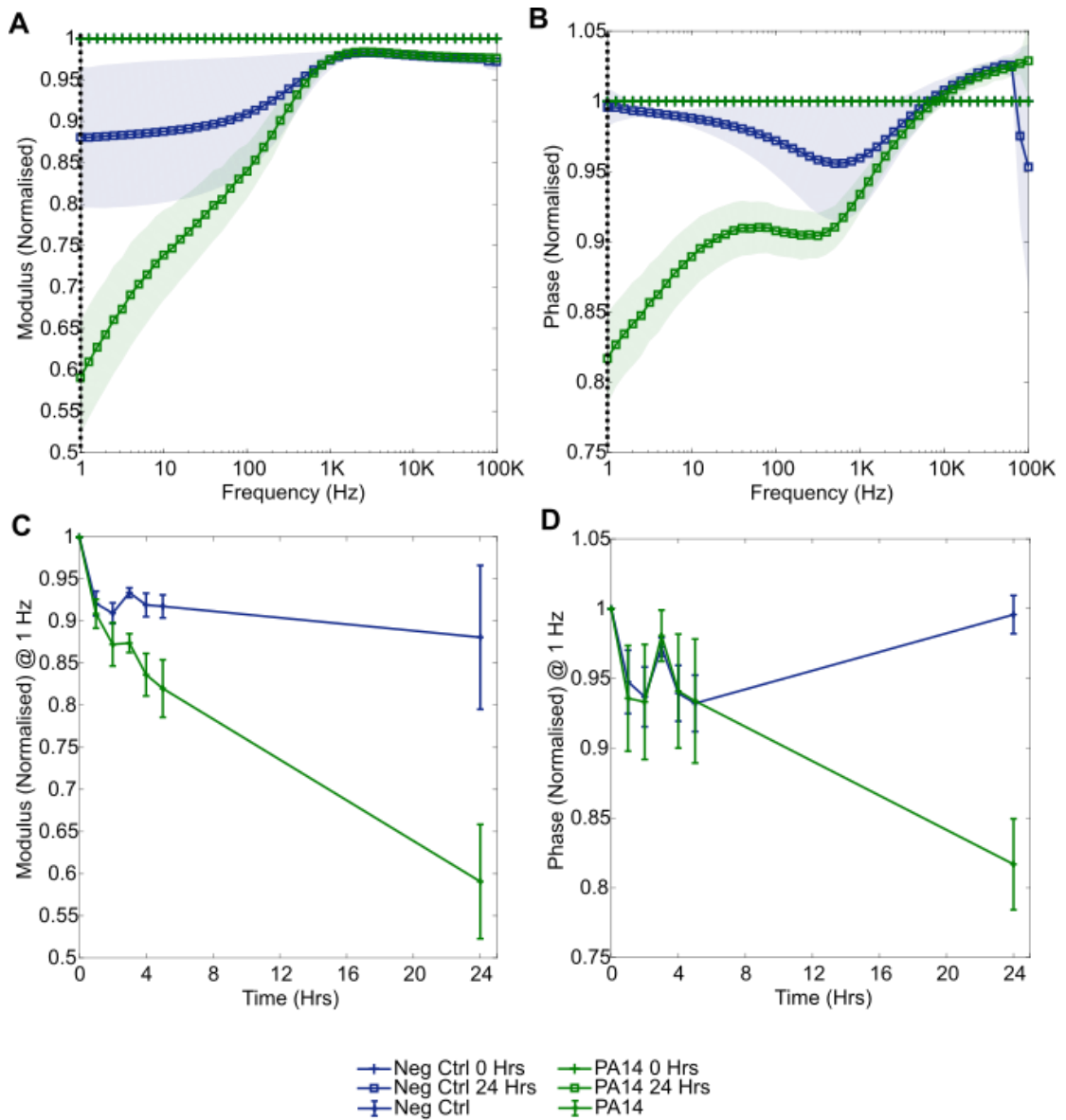


Figure 5.13. Impedance response associated with the growth of *P. aeruginosa* (PA14) in the WBM. Plots show: (A) normalised modulus; (B) normalised (absolute) phase; (C) 1 Hz normalised modulus over time; (D) 1 Hz normalised phase over time ($n = 4$ negative control, $n = 3$ PA14, errors depict ± 1 standard deviation).

5.5 The Influence of Direct Cell/Electrode Processes Upon the Measured Carbon Electrode Impedance Signatures

After obtaining normalised impedance signatures for a number of wound pathogens during their growth in nutrient rich media, experiments were next conducted in 0.9% w/v NaCl where the bacteria lacked the nutrients for growth. These experiments provided insight into the impedance response induced only by the cells in isolation, without metabolic processes influencing the signatures.

5.5.1 Effects of Washed Cells in Saline Over Time Upon Impedance

Firstly, a high concentration of *P. mirabilis* (DSM4479) washed cells were placed onto sensors and measured over 24 hours. At 0 hours, the average cell density was 5.0×10^8 CFU/mL (range $(4.3 - 5.9) \times 10^8$ CFU/mL). Through colony counting it was confirmed that, as intended, no increase in bacterial concentration had occurred during the 24 hours (3.0×10^8 CFU/mL at 24 hours, range $(2.7 - 3.3) \times 10^8$ CFU/mL).

The results show changes in normalised impedance which were smaller in magnitude than those observed in experiments previously, where active growth of *P. mirabilis* was possible (Figure 5.14A, 5.14B). This is well illustrated in normalised modulus at 10 Hz, where a maximum change of around 0.04 normalised units occurred in 0.9% w/v NaCl, in contrast to LB medium for example where the change was around 0.22 normalised units (Figure 5.5). This indicates that *P. mirabilis* cell behaviour promoted by the metabolism of nutrients dominated the larger impedance response seen in nutrient rich media. Despite observing smaller changes in saline solution, the impedance response was statistically significant immediately after inoculation of the electrodes with *P. mirabilis*, observed as a normalised resistance peak at 30 Hz ($n = 4$, $p = 0.012$). Furthermore, it was apparent that cellular settlement and adsorption to the carbon surfaces occurred over time. A progressively increasing change as a function of time was seen in both normalised modulus and normalised phase, despite a lack of cell growth. These features became significantly different to the negative controls 30 minutes after inoculation and reached minima after 6 hours (Figure 5.14C, 5.14D; $p = 0.009$ for normalised modulus at 10 Hz, $p = 0.001$ for normalised phase at 200 Hz). This suggests that *P. mirabilis* cells adhered to the carbon electrodes over this 6-hour period. Within Chapter 7 the impact of this result upon our understanding of bacterial impedance signatures will be discussed in the context of wider literature.

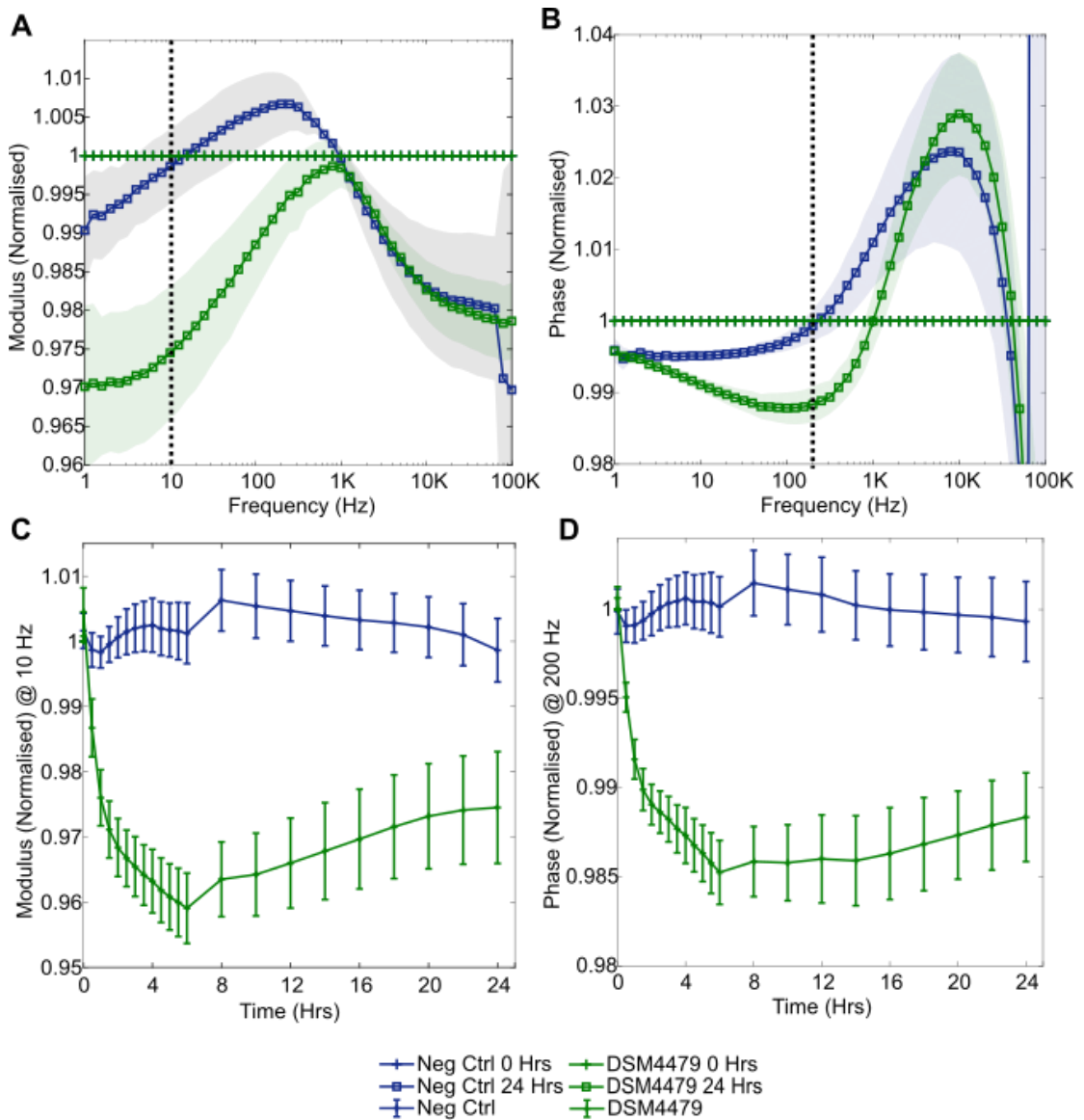


Figure 5.14. Impedance response associated with measurements of *P. mirabilis* (DSM4479) in 0.9% v/w NaCl over 24 hours. Plots show: (A) normalised modulus; (B) normalised (absolute) phase; (C) 10 Hz normalised modulus over time; (D) 200 Hz normalised phase over time ($n = 4$, errors depict ± 1 standard deviation).

A similar experiment was conducted using *S. aureus*, in this case with measurements performed over just 2.5 hours, using the lower average initial concentration of 7.7×10^5 CFU/mL (range $3.6 \times 10^5 - 1.8 \times 10^6$ CFU/mL). Again, a lack of growth was confirmed via colony counting after the final measurement (6.0×10^5 CFU/mL at 2.5 hours, range $4.1 \times 10^5 - 1.2 \times 10^6$ CFU/mL). For both normalised modulus and phase there were no clear differences between the sterile control and bacterial signatures (Figure 5.15A, 5.15B). There were slightly more pronounced changes for *S. aureus* observed in normalised resistance in the form of a low frequency peak (Figure 5.15C), however, this feature was not statistically significant during the measured period (Figure 5.15D). No direct cellular interactions with the sensor could

therefore be detected in this experiment. The difference between this result and that obtained with *P. mirabilis* in saline is believed to be due to the lower concentration of *S. aureus* cells, and differences in the motility and morphology of the two species.

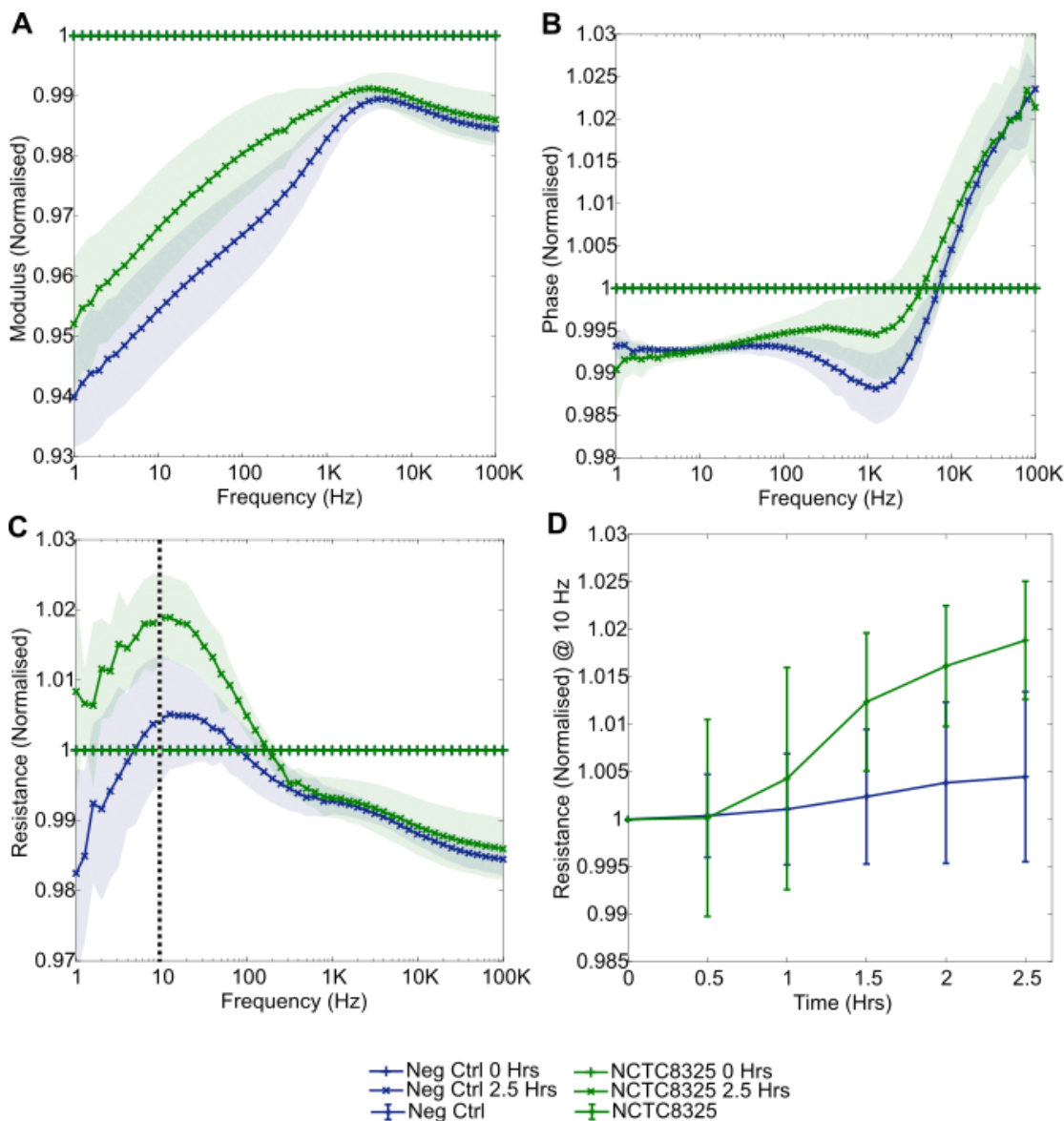


Figure 5.15. Impedance response associated with measurements of *S. aureus* (NCTC8325) in 0.9% v/w NaCl over 2.5 hours. Plots show: (A) normalised modulus; (B) normalised (absolute) phase; (C) normalised resistance; (D) 10 Hz normalised resistance over time ($n = 4$, errors depict ± 1 standard deviation).

5.5.2 *S. aureus* Cell Concentration Dependent Effects Upon Impedance

As a concentration of *S. aureus* cells in the order of 10^5 CFU/mL did not cause any significant changes in the experiment presented above, next multiple *S. aureus* concentrations were investigated. The immediate cell concentration dependent effects upon impedance were studied

by measuring the impedance of a range of washed cell concentrations, from 1.8×10^6 CFU/mL (denoted with a multiplication factor (MF) of “1” in subsequent plots) and doubling incrementally (denoted “2”, “4” etc) to a MF of 128. In theory the “128” concentration corresponded to 2.3×10^8 CFU/mL, however, colony counting indicated that the actual cell density was slightly lower at 5.9×10^7 CFU/mL. As previously in Figure 5.15, the effects upon impedance were most prominent for normalised resistance (Figure 5.16A). Here, a significant concentration dependant peak was observed at 10 Hz for concentrations above approximately 3.6×10^6 CFU/mL (MF 2), with $p = 0.02$ (Figure 5.16C). Furthermore, the impedance signature did not return to its baseline value when the final aliquots of washed cells were removed from the electrode surfaces and replaced with sterile aliquots. This suggests that *S. aureus* had a persisting effect upon the electrode surface, unrelated to the breakdown of metabolites within the media. A likely cause of this is the adsorption of bacterial cells onto the electrode surface, as was also believed to be the case with *P. mirabilis*. Additionally, a similar concentration dependent peak was visible in normalised phase at high frequencies (Figure 5.16B) for cell densities above around 5.8×10^7 CFU/mL (MF = 32, $p = 0.029$). Previously seen for staphylococci in nutrient rich media, this peak is not believed to originate from metabolic processes (as discussed within Chapter 7). Further, the effects of bacterial cell concentration upon impedance response are additionally explored using the PCE sensors in Chapter 6, where added LB medium cell density experiments are described.

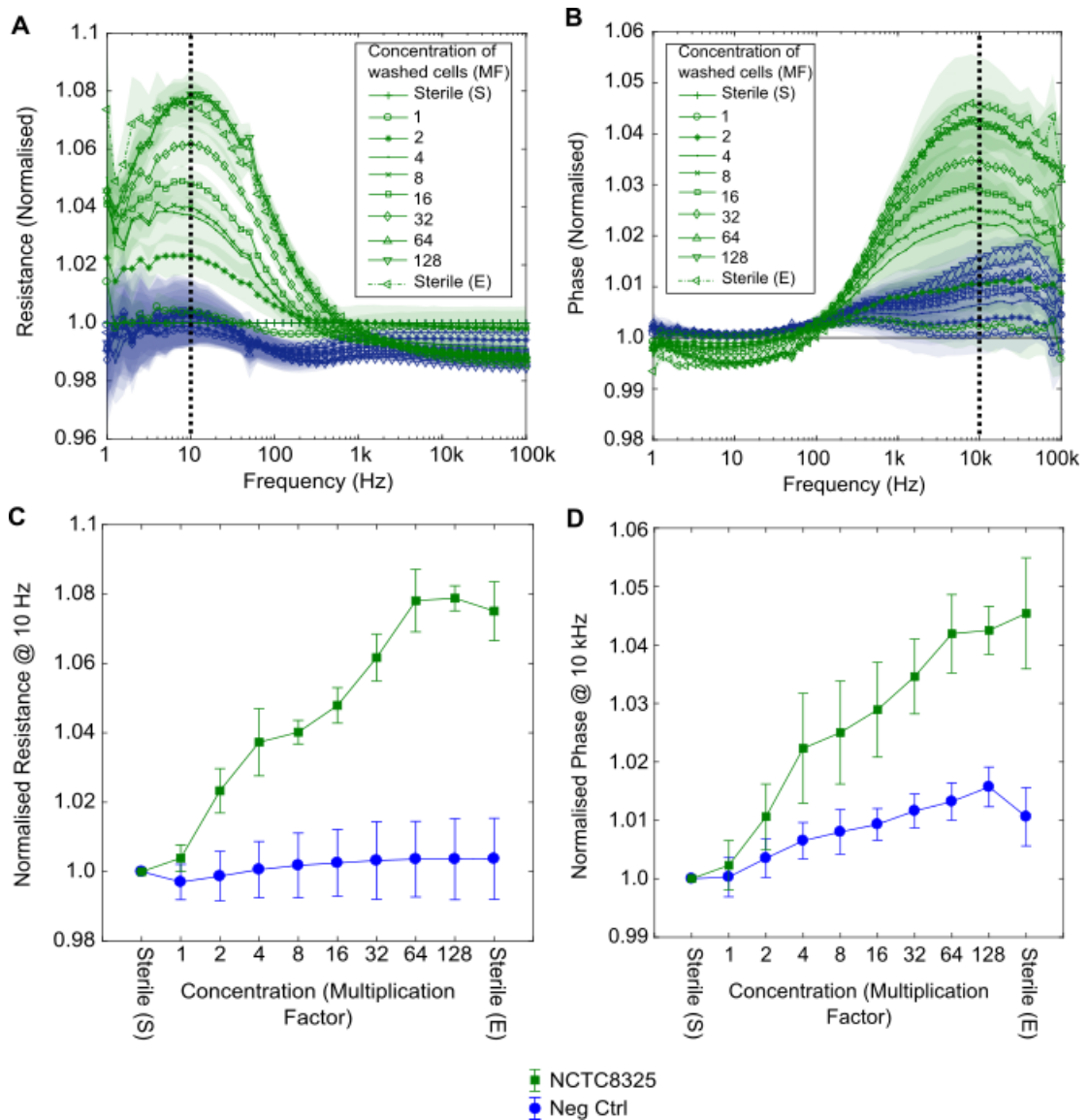


Figure 5.16. Measurements of *S. aureus* (NCTC8325) at increasing concentrations (denoted as multiplication factors, MF) in 0.9% w/v NaCl: (A) an increasing normalised resistance peak is visible in the chambers containing NCTC8325, which appears to be concentration dependent. Replacement of the 0.9% NaCl at the end of the experiment with a sterile aliquot “(sterile (E))” has little impact upon this peak; (B) normalised phase showing a similar concentration dependent peak at high frequencies; (C) normalised resistance data at 10 Hz and (D) normalised (absolute) phase data at 10 kHz showing the increases as functions of concentration (error bars represent ± 1 standard deviation, $n = 3$).

5.6 Exploration of the Mechanisms Underpinning the Bacterial Impedance Signatures via Equivalent Circuit Modelling

Equivalent circuit fitting analysis was next performed on a sample of experiments carried out using the carbon sensors to further explore the electrochemical processes underlying some key changes to impedance observed. Circuits with few elements such as the simple circuit selected (Figure 3.19) are often applied to biological EIS studies due to their simplicity (196).

5.6.1 *P. mirabilis* Circuit Modelling Results

The results obtained from *P. mirabilis* growth in LB medium and *P. mirabilis* settlement in saline were first chosen for this modelling, as these growth conditions provided great contrast. Further, this species caused significant changes to normalised impedance in each case, and measurements were performed over an identical time period.

Firstly, in Figure 5.17 the circuit fitting results for the LB medium growth experiment are shown. The average percentage change for each modelled circuit element at 24 hours are compared in Figure 5.18, with the only clear change occurring for charge transfer resistance. A significant reduction in charge transfer resistance was present for the bacterial chambers (average change $-91\% \pm 3.5\%$ ($n = 4$) vs a negative control average change of $-45.9\% \pm 6.6\%$ ($n = 3$), $p = 0.009$). A reduction in R_{ct} such as this has previously been associated with the growth of microorganisms on carbon-based electrodes, supporting the earlier conclusion that these EIS changes were dominated by growth-related processes (258–260).

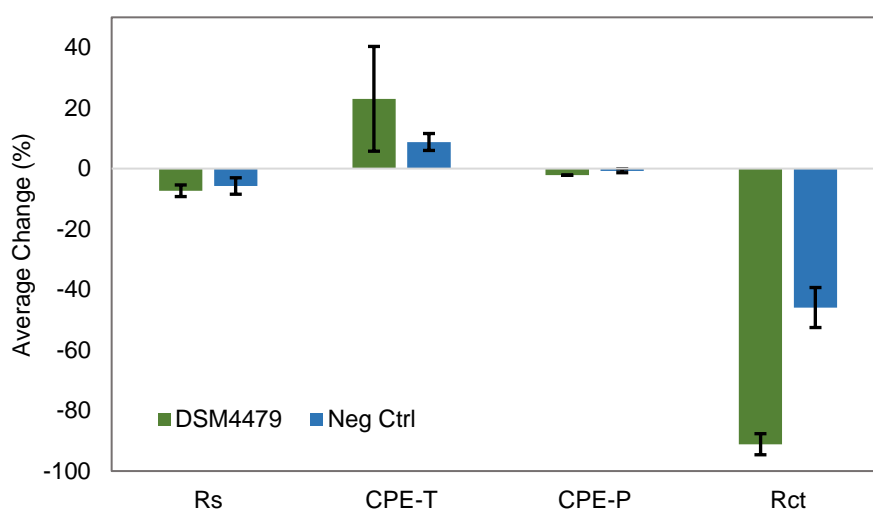


Figure 5.17. *P. mirabilis* (DSM4479) growth in LB medium circuit fitting results, with: R_s representing solution resistance (Ohms); CPE-T the constant phase element's capacitive magnitude (Farads); CPE-P the constant phase element index which indicates the component's likeness to a true capacitor (for an ideal capacitor CPE-P = 1); R_{ct} representing the charge transfer resistance (Ohms). Data was modelled to the equivalent circuit shown in Figure 3.19, and average percentage changes at the 24-hour measurement point calculated for each component and compared. R_{ct} values are provided in Appendix A, as this proved to be a consistent indicator of bacterial growth with the PCE sensors in Chapter 6.

In contrast, when modelling the *P. mirabilis* 0.9% w/v NaCl results, at the 24-hour measurement point no significant changes had occurred for any circuit element (Figure 5.18).

Larger errors were present for Rct, however, these remained smaller in magnitude than the *P. mirabilis* percentage changes observed in LB medium. This analysis further supports the hypothesis that, for *P. mirabilis*, the impedance changes observed in nutrient rich media such as LB medium (and thus the changes to charge transfer resistance) were driven by growth related metabolic processes and not cell-electrode interactions such as adsorption.

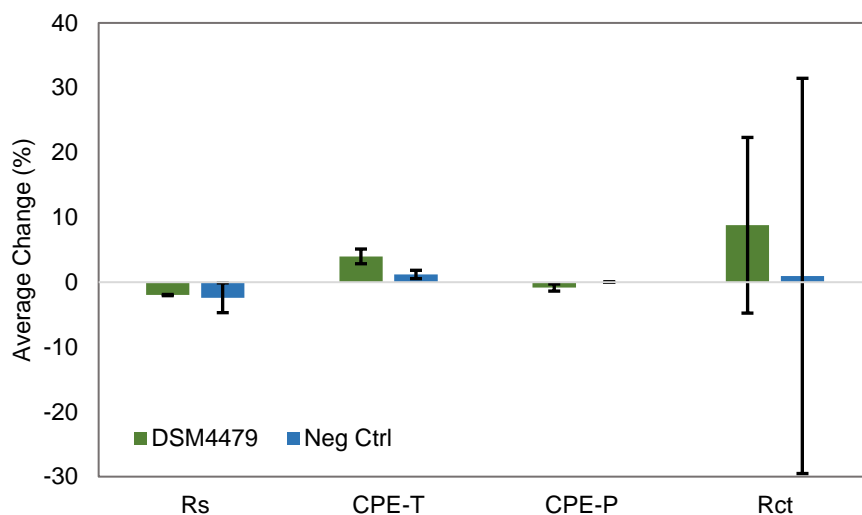


Figure 5.18. *P. mirabilis* (DSM4479) in 0.9% w/v NaCl circuit fitting results, with: *Rs* representing solution resistance (Ohms); *CPE-T* the constant phase element's capacitive magnitude (Farads); *CPE-P* the constant phase element index which indicates the component's likeness to a true capacitor (for an ideal capacitor $CPE-P = 1$); *Rct* representing the charge transfer resistance (Ohms). Data was modelled to the equivalent circuit shown in Figure 3.19, and average percentage changes at the 24-hour measurement point calculated for each component and compared. *Rct* values are provided in Appendix A.

5.6.2 *S. aureus* Circuit Modelling Results

The LB medium and saline results for *S. aureus* were next modelled using the basic equivalent circuit in Figure 3.19. Again, these growth conditions were studied as they were the most contrasting. Firstly, at the 24-hour LB medium measurement point, a significant increase in *CPE-T* (the constant phase element magnitude) was present for the bacterial sensors when compared to the sterile controls (Figure 5.20). For *S. aureus*, an average increase of $19.5\% \pm 2.1\%$ was present, vs an increase of $2.4\% \pm 0.2\%$ for the controls ($n = 3$, $p = 0.005$). Again, a greater decrease in *Rct* was seen for the bacterial sensors than the sterile sensors, however, for this experiment no statistical significance was found for this component (Figure 5.19, $p = 0.062$).

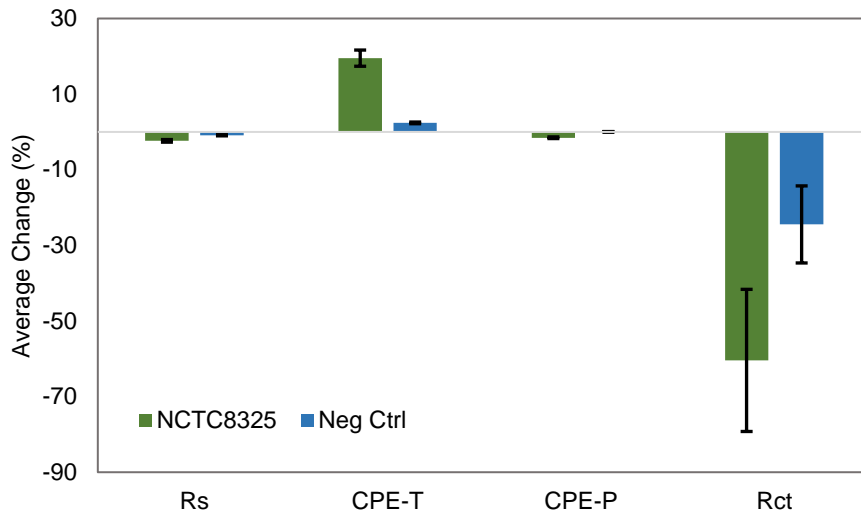


Figure 5.19. *S. aureus* (NCTC8325) growth in LB medium circuit fitting results. Data was modelled to the equivalent circuit shown in Figure 5.17, and average percentage changes at the 24-hour measurement point calculated for each component and compared. Rct values are provided in Appendix A.

Figure 5.20 was produced using data from the *S. aureus* cell concentration experiments (performed in 0.9% w/v NaCl), with percentage changes calculated at the largest cell density (5.9×10^7 CFU/mL (MF = 128)). In this case no significant differences emerged between the bacterial and sterile sensors for any circuit element, despite clear features being visible in the normalised spectra (Figure 5.16).

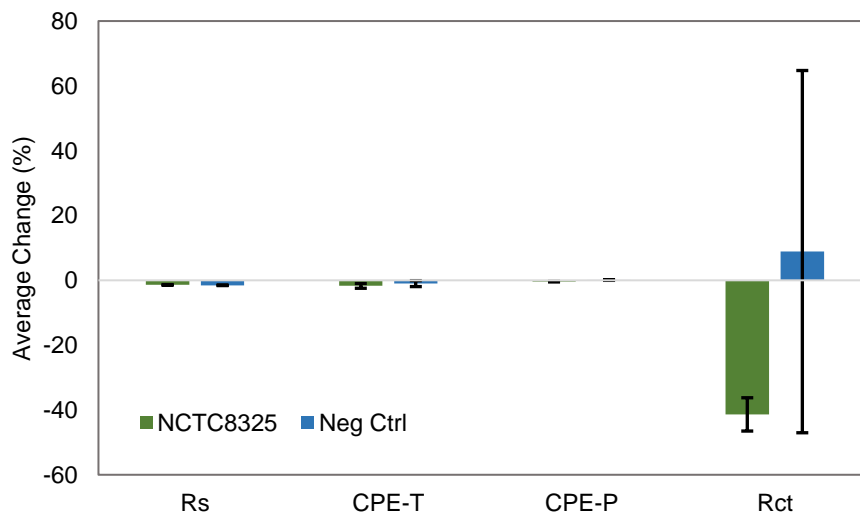


Figure 5.20. *S. aureus* (NCTC8325) in 0.9% w/v NaCl circuit fitting results. Data was modelled to the equivalent circuit shown in Figure 5.17, and average component percentage at the cell density of 5.9×10^7 CFU/mL calculated. Rct values are provided in Appendix A.

Due to a lack of consistency in circuit component changes between these bacterial species, circuit modelling does not appear to offer a clear indication of the presence of infection in general. Instead, the normalised impedance spectra present a more reliable approach to bacterial detection. Changes to specific circuit components such as CPE-T and Rct could, however, aid in the differentiation between species. From this analysis, it is suggested that during bacterial growth both capacitance and charge transfer can be influenced. Processes such as bacterial cell polarisation and nutrient breakdown into smaller ionic components will likely be influential in this result (148,150).

5.7 Discussion and Summary

Within this chapter, simple screen-printed carbon electrodes were investigated for their suitability in wound infection monitoring applications. Firstly, normalised impedance signatures for a number of key wound pathogens were obtained in LB medium. Importantly, significant features were detected within only 30 minutes - 1 hour for each species. Similar growth signatures were then obtained for bacteria in a simulated wound fluid, and finally a wound bed model. By using these different growth conditions, it became evident that the media impacted both the locations and timings of signature features. This highlighted the importance of attempting to model the wound environment to gain appropriate insight into the potential of these sensors for use in an *in situ* wound monitoring device. In general, however, key changes such as a mid-frequency normalised phase trough were common throughout.

Notably, through measurements of washed bacterial cells which lacked the conditions for growth, it was indicated that early adsorption of both *P. mirabilis* and *S. aureus* to the sensors could be inferred. Further, the common key bacterial signature features in nutrient rich media were found to be dominated by growth-related processes such as metabolism. Additionally, cell concentration dependant *S. aureus* signature features were identified which could be detected immediately above a threshold cell concentration and were similar to those observed late in the Staphylococcal growth signatures alone. A summary of these bacterial processes influencing impedance during growth is provided in Figure 5.21 (refer to Section 1.6.2). In particular, the association between bacterial concentration and time to detection is further explored with the PCE sensors in Section 6.9. Finally, basic equivalent circuit modelling indicated that both changes to charge transfer and capacitance may arise from bacterial growth.

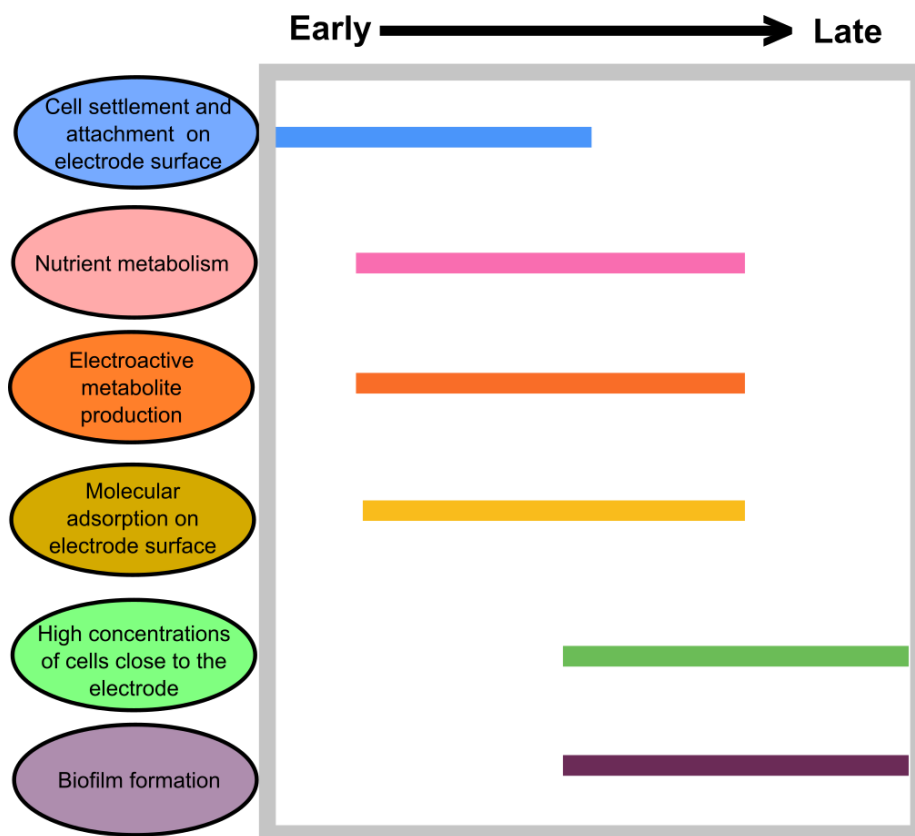


Figure 5.21. Timeline of influence for bacterial mechanisms impacting impedance signatures.

Ultimately, these carbon sensors appeared more suitable than the Ag/AgCl sensors for bacterial detection. No growth inhibition or stability issues were observed, and rapid bacterial detection was possible via the emergence of clear impedance signature features. A key area for improvement, however, is the high baseline impedance of these carbon sensors. In the experiments conducted, this meant that the observed normalised changes were of a small magnitude. It was hypothesised that, by using electrodes with a lower baseline impedance, the magnitude of normalised impedance changes detected during bacterial growth would increase. It was proposed that altering the electrode material could improve their sensitivity and allow more detailed EIS signatures, characteristic of each bacterial species to be obtained. Consequently, a more sophisticated carbon-based electrode is investigated in the subsequent chapter.

6. ASSESSING THE SUITABILITY OF PLATINISED CARBON ELECTRODES FOR THE DETECTION OF WOUND PATHOGENS

6.1 Introduction

So far within this thesis, the results of assessing the suitability of both Ag/AgCl and carbon screen-printed sensors for wound infection detection have been presented. Of these two materials carbon was the most suitable, demonstrating superior bacterial interaction, stability and detectable changes in normalised impedance during bacterial growth. Further addressing objective 1 (Section 1.8), the final sensor investigated was a screen-printed Platinised Carbon Electrode (PCE). Whilst retaining the desirable properties of the previous carbon sensors, it was hypothesised that the platinum on carbon additive may enhance the observed impedance responses. With cited applications in glucose detection for example, carbon electrodes modified with platinum have electro-catalytic properties that promote the detection of small organic molecules (261,262). Any superiority of this sensor over the previously studied electrodes for bacterial detection was assessed. Due to the promising results obtained, more elaborate wound models and experimental conditions were explored than previously.

6.2 PCE Detection of Bacteria in LB Medium

Culture medium growth experiments were once more used to first indicate the suitability of the electrodes for bacterial detection and determine any characteristic impedance signatures (project objectives 1 and 2, Section 1.8).

6.2.1 Using a Sterile Normalisation Point

S. aureus (NCTC8325) growth in LB medium was first studied using the PCE sensors, with the resulting raw modulus and absolute phase plots shown in Figure 6.1. The baseline impedance of these sensors in LB medium, as seen via the “0 Hrs” data, is over two orders of magnitude lower than with the simple carbon sensors (around $10^4 \Omega$ vs $10^6 \Omega$ at 0.1 Hz, Figures 5.1A, 6.1A). It was (correctly) hypothesised that this reduction in baseline impedance would result in more pronounced changes in normalised impedance occurring because of bacterial growth. Further, absolute phase has a lower value over a wider frequency range (PCE in Figure 6.1B vs simple carbon in Figure 5.1B). Over the 24 hour period of incubation at 37 °C, the *S. aureus* cell density increased from 3.6×10^6 CFU/mL (range $(2.3 - 5.2) \times 10^6$ CFU/mL) to 3.6×10^8 CFU/mL (range $(2.7 - 4.9) \times 10^8$ CFU/mL). During this time, decreases in both modulus (Figure 6.1A) and absolute phase (Figure 6.1B) occurred.

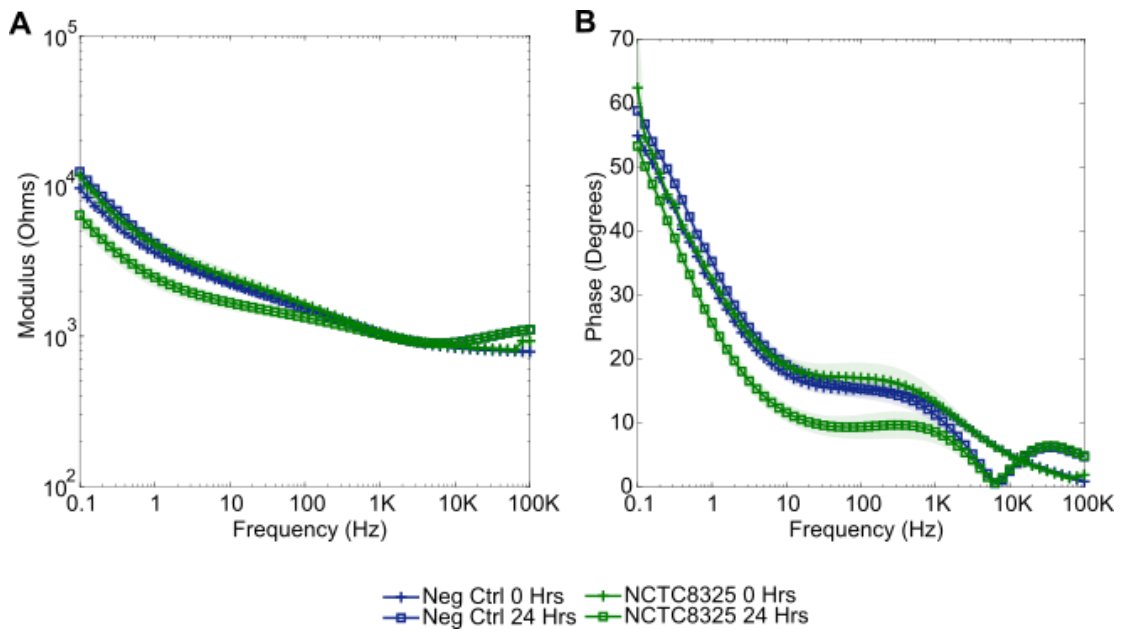


Figure 6.1. Impedance response associated with the growth of *S. aureus* (NCTC8325) in LB medium, measured using platinised carbon electrodes. Plots show: (A) modulus; (B) absolute phase ($n = 4$, errors depict ± 1 standard deviation).

Again, these impedance changes were emphasised using normalisation. By normalising against a sterile first impedance sweep, the plots in Figure 6.2 were created. Within each of the normalised modulus (Figure 6.2A), phase (Figure 6.2B), reactance (Figure 6.2C) and resistance (Figure 6.2D) plots, a decrease in magnitude at frequencies below around 1 kHz was observed for the bacterial sensors alone. There were, however, some additional undesirable changes to impedance for all chambers: noise was present in the spectra (visible at 10 kHz normalised phase and 0.1 Hz normalised resistance for example), and further changes unrelated to bacterial growth at low frequencies were seen via negative control peak formation at frequencies below around 10 Hz.

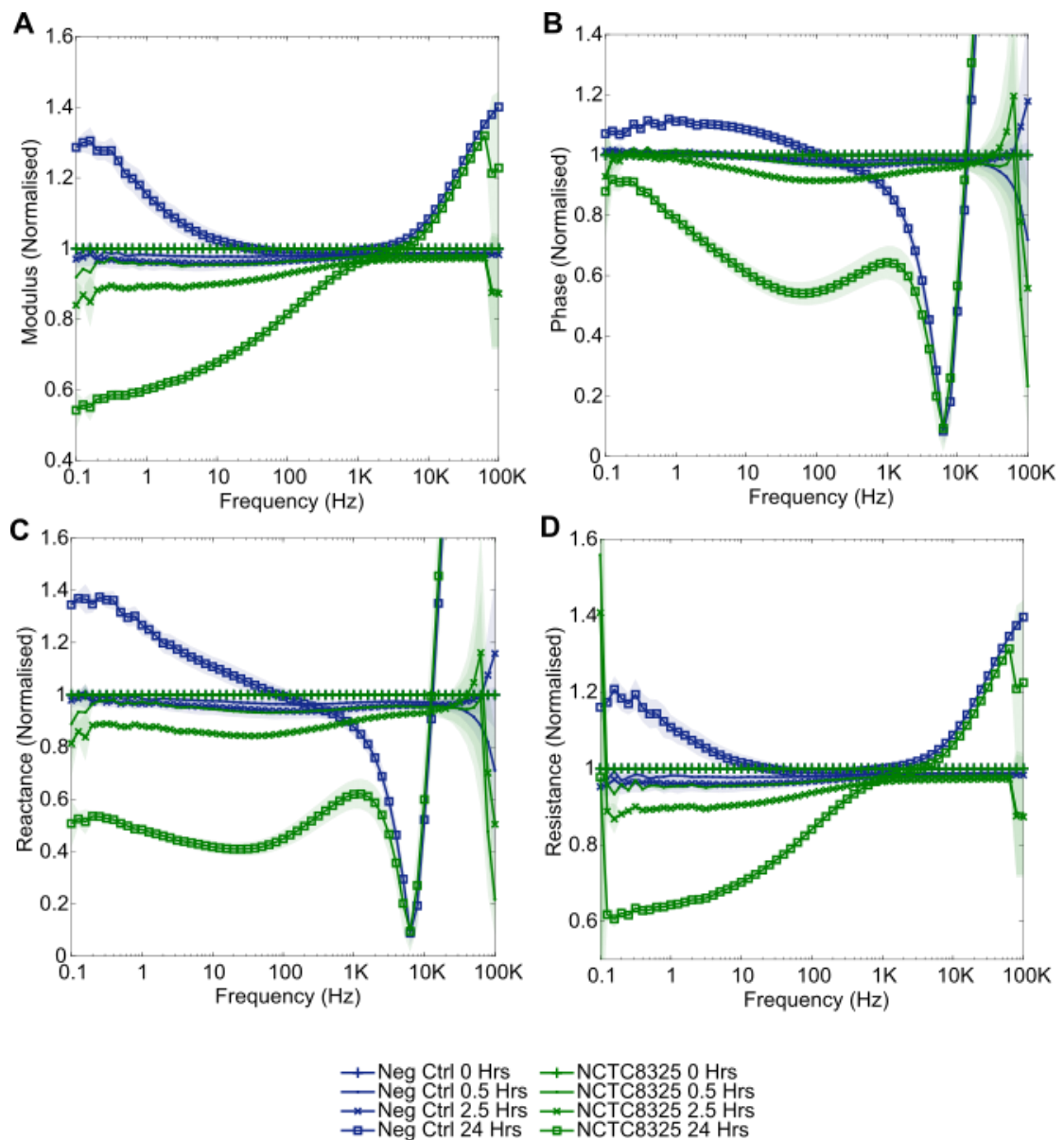


Figure 6.2. Normalised impedance response associated with the growth of *S. aureus* (NCTC8325) in LB medium. Normalisation was performed against a sterile starting point. Plots show: (A) normalised modulus; (B) normalised (absolute) phase; (C) normalised reactance; (D) normalised resistance ($n = 4$, errors depict ± 1 standard deviation).

By focusing upon the changes in normalised modulus at 1 Hz and normalised phase at 60 Hz, where in both cases notable bacterial signature features emerged, their full extent could be visualised (Figure 6.3). For normalised phase at 60 Hz in particular changes were detected rapidly, significant after only 30 minutes ($p = 0.029$). Using the same method for *S. aureus* detection with the previous basic carbon sensors, detection after 30 minutes was also possible. With these PCE sensors however, the magnitudes of change were larger at around 0.4 and 0.45 normalised units for normalised modulus and phase respectively, compared to around 0.2 and 0.1 normalised units respectively when the basic carbon sensors were used (Figure 6.3 vs

Figure 5.3). This is believed to be a result of the far lower baseline impedance of the PCE sensors, with any changes to impedance consequently being a larger fraction of this baseline. Further, for *S. aureus* detection in LB medium with the basic carbon sensors, the changes to normalised impedance maximised at around 2.5 hours before reducing in size. Conversely, with these PCE sensors a sustained response was observed. Normalised impedance changes maximised by around 10 – 16 hours and remained at those levels until the final 24-hours measurement.

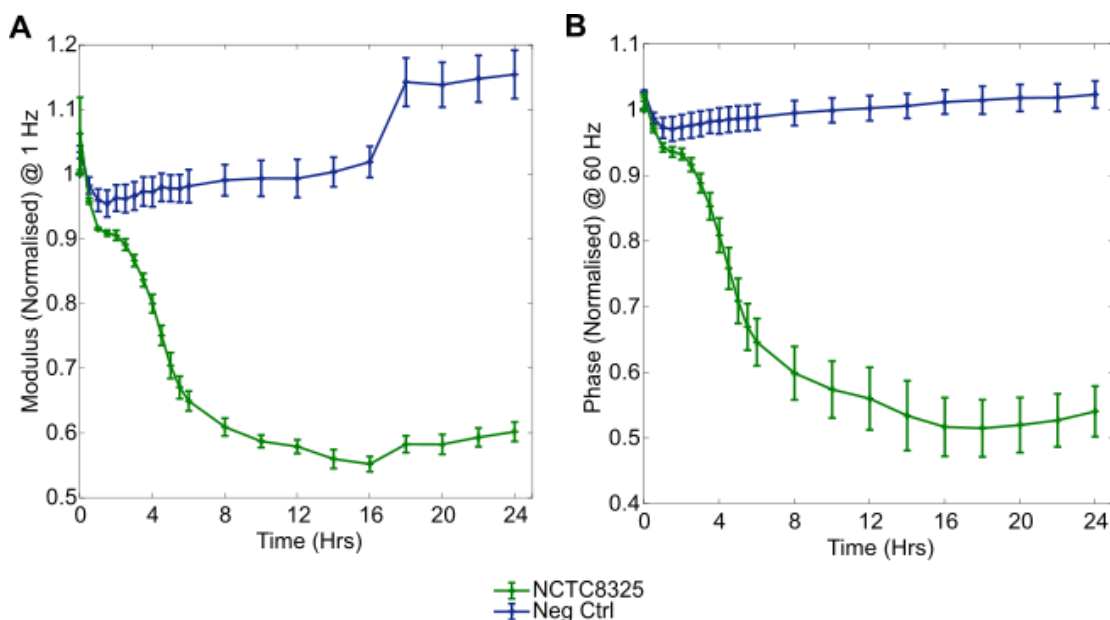


Figure 6.3. *S. aureus* (NCTC8325) growth in LB medium over 24 hours, time-based plots. Plots show: (A) normalised modulus at 1 Hz; (B) normalised (absolute) phase at 60 Hz ($n = 4$, error bars depict ± 1 standard deviation).

6.2.2 Using a Non-Sterile Normalisation Point

The *S. aureus* LB growth experiment was next repeated, but instead with the first measurement being performed after bacterial inoculation and normalisation carried out against this non-sterile point. This reflected a move towards a more practical measurement process. In this case, the characteristic reductions in normalised modulus (Figure 6.4A) and normalised absolute phase values (Figure 6.4B) were again observed. No large areas of noise were present here, and negative control variation was of a smaller magnitude than in the previous experiment. Further, as 0.1 Hz noise was present previously and these low frequency measurements were time consuming, 1 Hz was chosen as the measurement cut-off frequency here. Overall, the *S. aureus* signature was very similar to that obtained in Section 6.2.1, demonstrating the reproducibility of these results. With normalisation performed against a non-sterile state, any immediate effects of bacterial inoculation could not be studied here. An initial settlement time of around 3 hours was evident in the time-based plots (Figures 6.4C, 6.4D), where the bacterial and sterile

responses both decreased. After this time, the sterile response remained at a constant level, with the bacterial sensors' impedance decreasing. The earliest time to observe a significant impedance decrease was greater than when normalisation was performed against a sterile point, at 3.5 hours here (normalised phase at 100Hz, $p = 0.033$). More frequent measurements were performed in this experiment (every 0.5 hours rather than every 2 hours after 6 hours) to determine if any additional insight could be gained, however, no added benefit was noted.

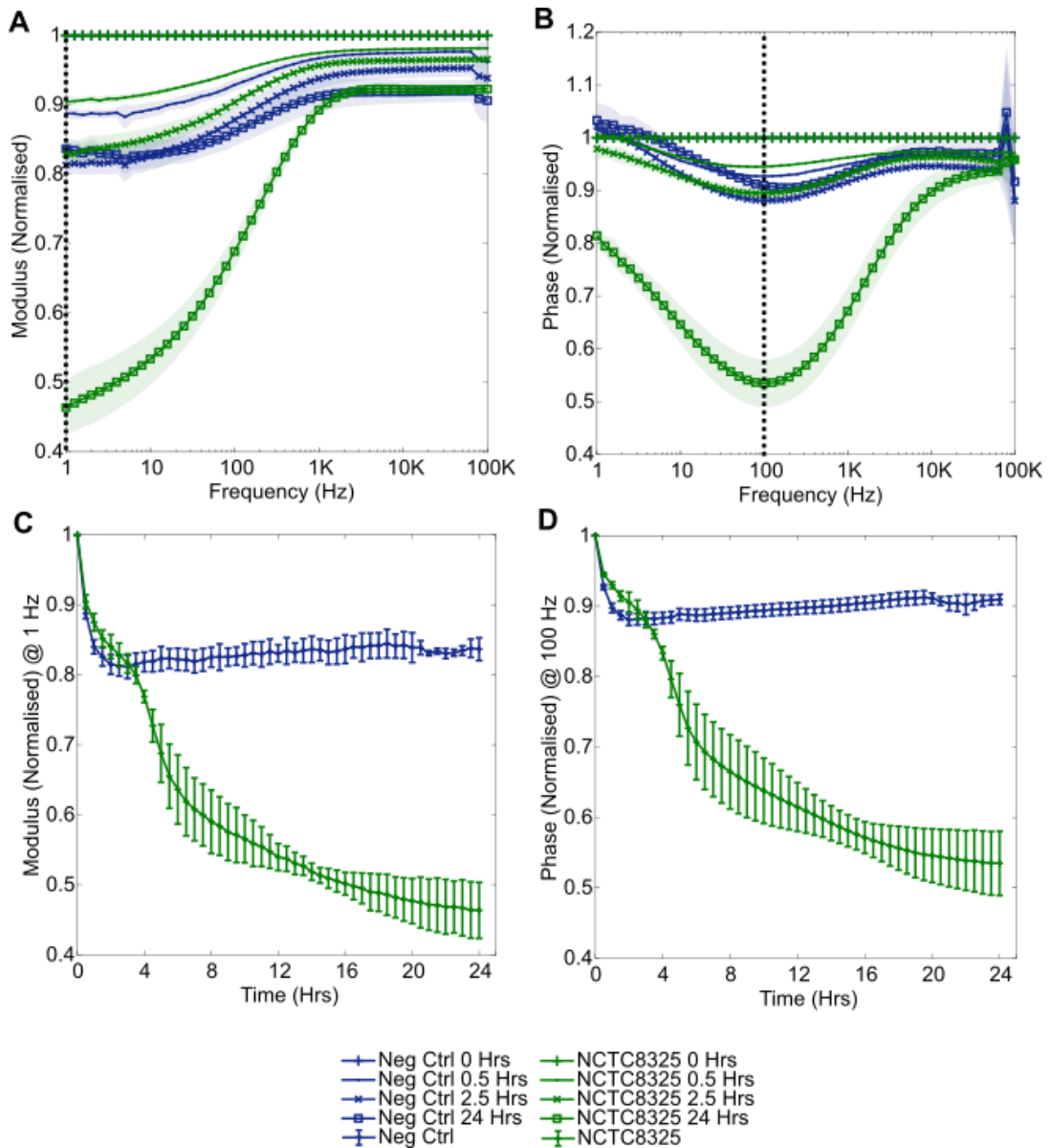


Figure 6.4. Normalised impedance response associated with the growth of *S. aureus* (NCTC8325) in LB medium. Normalisation was performed against a non-sterile starting point. Plots show: (A) normalised modulus; (B) normalised (absolute) phase; (C) normalised modulus time-based plot at 1 Hz; (D) normalised phase time-based plot at 100 Hz ($n = 4$, errors depict ± 1 standard deviation).

Next, *P. aeruginosa* was grown in LB medium over 24 hours from an initial concentration of 4.6×10^6 CFU/mL (range $(2.8 - 6.6) \times 10^6$ CFU/mL) up to 9.0×10^9 CFU/mL (range $3.7 \times 10^9 - 1.6 \times 10^{10}$ CFU/mL). Normalised impedance signatures were obtained with similar features to *S. aureus*, namely a reduction in modulus value below 1 kHz (Figure 6.5A) and normalised phase trough formation around 100 Hz (Figure 6.5B). As these features were again sustained over time, only the 0-hours and 24-hours signatures are shown for clarity. In the time-based plots (Figures 6.5C, 6.5D), an initial lag phase of limited response lasting around 2 hours is seen, followed by more rapid change up to around 10 hours, and then a levelling-off of the response. Again, frequent measurements were performed here (every 0.5 hours) to probe the full extent of these changes at regular intervals over 24 hours. In both normalised modulus at 1 Hz and normalised phase at 100 Hz, significant changes were detected after 1.5 hours of growth ($p = 0.009$ and $p = 0.008$ respectively).

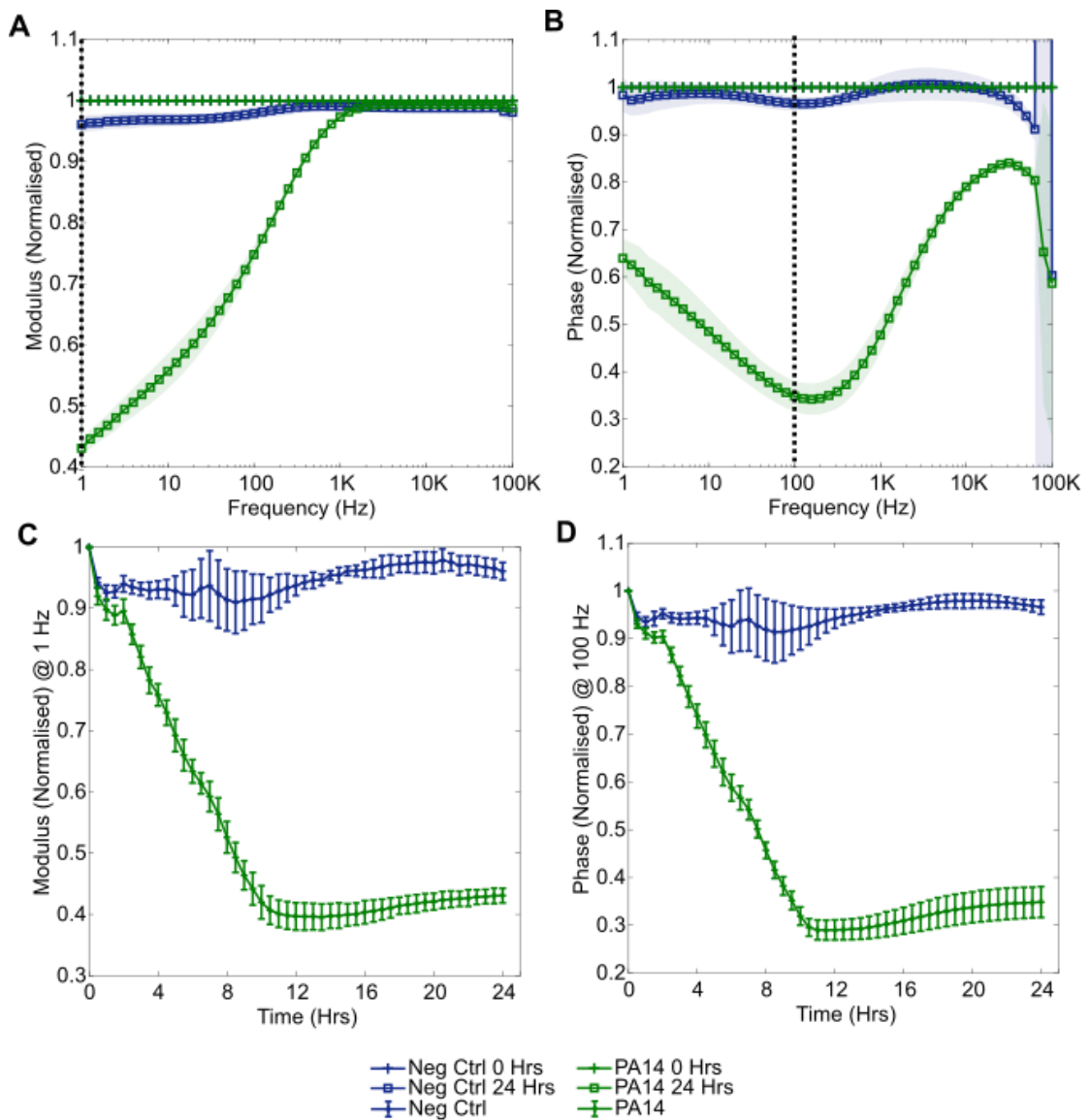


Figure 6.5. Normalised impedance response associated with the growth of *P. aeruginosa* (PA14) in LB medium. Normalisation was performed against a non-sterile starting point. Plots show: (A) normalised modulus; (B) normalised (absolute) phase; (C) normalised modulus time-based plot at 1 Hz; (D) normalised phase time based plot at 100 Hz ($n = 4$, errors depict ± 1 standard deviation).

For both pathogens, clear bacterial signatures emerged. These spectra broadly had very similar appearances, with differences in time-based plots likely to be influenced by a range of factors including differences in the motility of the two bacteria for example. These results will be further discussed in Chapter 7. Overall, the PCE sensors' ability to detect bacteria in LB medium was demonstrated via large, sustained changes to normalised impedance. Bacterial growth on each PCE sensor was observed via CV staining at the end of each experiment, as shown in Figure 6.6.

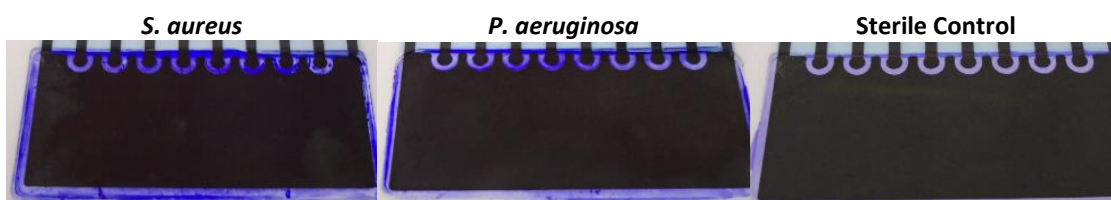


Figure 6.6. A sample of CV staining images resulting from PCE bacterial growth experiments performed in LB medium. Limited staining was present for the sterile control, with any colour here likely due to insufficient chamber rinsing. Extensive, dark staining for the *S. aureus* and *P. aeruginosa* growth chambers indicated bacterial attachment to the sensors.

6.3 Evaluation of a Dry PCE Sensor Preparation Method

It was hypothesised that the existing sensor preparation method, which required a series of steps that ultimately required sensors to remain wet and be used immediately, would not be practical for clinical use. With a view to potential commercialisation in future, a simplification of the electrode preparation process was desired. The proposed new method involved carrying out sterilisation using 100% EtOH (instead of 70%), meaning that sensors could easily air dry immediately after sterilisation and, in theory, could be packaged and used at a later date. Additionally, the overnight settlement in media step was removed, as this would not be practical to perform at the point of care for a real-life wound monitoring device. The effects of this change in electrode preparation are explored in this section, with the old (method A) vs new (method B) preparation processes summarised in Figure 6.7. Electrodes were set up using the conditions reproduced in Table 6.1, and impedance measurements of 2 mL sterile LB medium performed over 5 hours.

Table 6.1. Sensor preparation parameters, reproduced from Table 3.3.

Sensor No.	1 Hour NaOH Conditioning?	100% EtoH Sterilisation?	Overnight LB Incubation?
1	✓	✓	X
2	X	✓	X
3	✓	X (70% EtoH and no dry)	X
4	✓	✓	✓
5	✓	X (70% EtoH and no dry)	✓

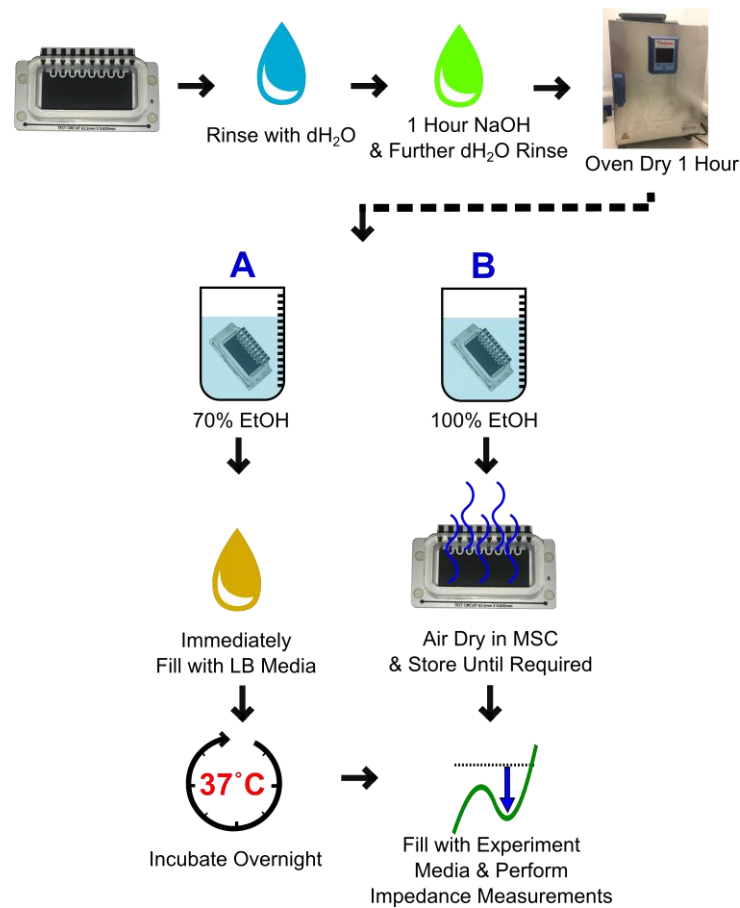


Figure 6.7. Flow diagram outlining PCE preparation methods A and B. Excluding the NaOH conditioning step, method A is in line with the process used in previous chapters and was used during the PCE LB experiments. Method B is the proposed new method, enabling sensor drying and storage for later use (MSC = microbiology safety cabinet).

Sensor 1 (highlighted in red) was prepared using method B and sensor 5 was prepared using method A. Normalised modulus (Figure 6.8A) and normalised phase (Figure 6.8B) showed a range of changes after 5 hours in sterile LB, in particular in normalised modulus at 1 Hz and normalised phase at 10 Hz (with time-based plots shown in Figures 6.8C and 6.8D respectively). The normalised impedance variation over time was minimal for both sensors 4 and 5 (highlighted in green), the only sensors which had been incubated overnight in LB medium prior to measurement. Despite this yielding the most desirable response, performing this incubation process immediately prior use would not be practical for *in situ* wound monitoring and, therefore, an alternative electrode preparation process was desired. The proposed alternative (sensor 1) had some impedance variation over time, however, it varied less than sensors 2 and 3 which were not conditioned in NaOH and sterilised in 70% EtOH respectively. This, therefore, indicated both that the NaOH had a positive impact upon sensor stability, and that the 100% EtOH sterilisation was preferable to 70% usage. Further, for sensor 2 large decreases in normalised modulus and phase in areas previously seen to indicate bacterial

growth were observed, strongly indicating against the use of its preparation method. Overall, if not wishing to use an overnight incubation step, the proposed sensor 1 preparation method had the most stable response in this experiment. Sterile instability at key bacterial frequencies (normalised modulus at 1 Hz for example) was minimal, therefore, method B was considered appropriate to adopt for future experiments.

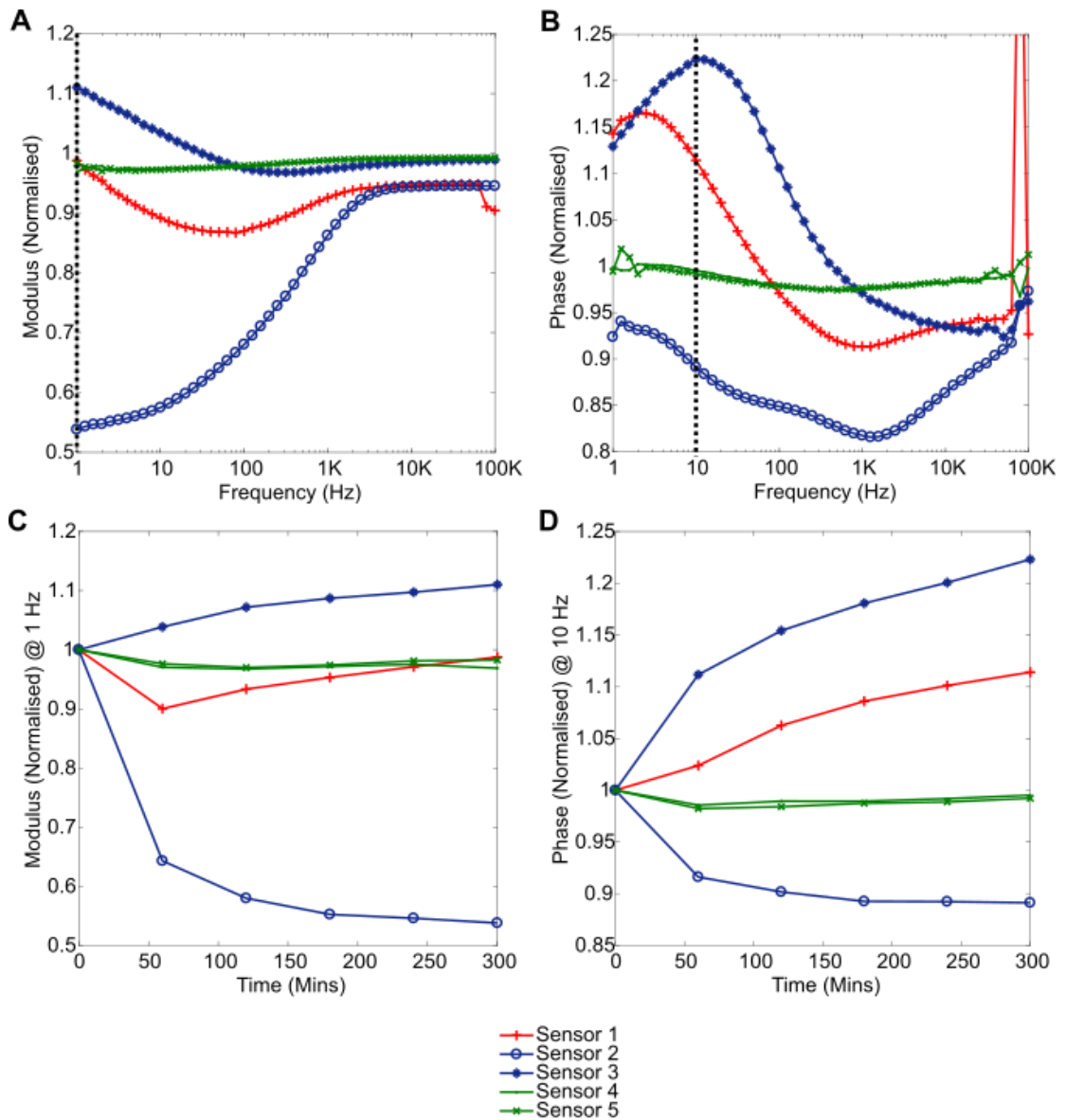


Figure 6.8. Characterisation of the PCE response associated with the preparation method A vs proposed new method B. Sensor numbers refer to those detailed in Table 6.1. Plots show: (A) normalised modulus after 5 hours of sterile LB measurements; (B) normalised (absolute) phase after 5 hours; (C) normalised modulus at 1 Hz; (D) normalised (absolute) phase at 10 Hz.

6.4 PCE Detection of Bacteria in SWF

In line with project objective 3 (Section 1.8), the PCE sensors were next assessed in models more closely simulating the wound environment. After preparing electrodes using the new method (B), growth experiments were next conducted using SWF (Section 3.2.2). Firstly, baseline modulus and absolute phase plots were obtained from measurements of sterile SWF aliquots with the PCEs. As seen in Figure 6.9, the impedance of these sensors was again far lower than the previous carbon sensor. Impedance modulus values were slightly higher in the SWF than in LB medium at 0.1 Hz (around $1.1 \times 10^4 \Omega$ vs $1.0 \times 10^4 \Omega$, Figure 6.9A vs Figure 6.1A), whereas absolute phase was slightly lower at 50° for SWF at 0.1 Hz (compared to 60° in LB medium, Figure 6.9B vs 6.1B). Good sensor consistency was again evident through minimal standard deviation shading.

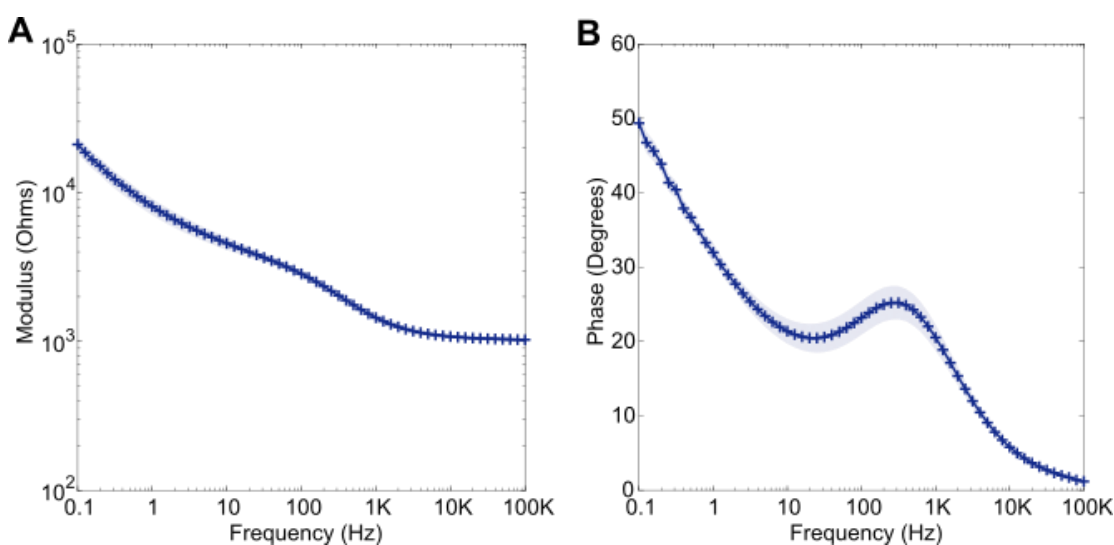


Figure 6.9. The baseline (A) modulus and (B) absolute phase plots obtained using the PCE sensors in sterile SWF ($n = 4$, shading depicts ± 1 standard deviation).

S. aureus and *P. aeruginosa* were next grown separately but simultaneously in SWF over 24 hours, on 4 sensors each. The signatures obtained for each bacterium during this experiment could, therefore, be directly compared. Measurements were performed less frequently in this experiment as it was conducted without the multiplexer, accommodating for the fact that it was carried out at the same time as a comparable WBM experiment (see Section 6.5.1 for more details). In normalised modulus (Figure 6.10A) a reduction in value occurred for both bacteria below 1 kHz, as was also observed in LB medium. Similarly, again a normalised absolute phase trough which minimised in the mid-frequency region emerged for each pathogen (Figure 6.10B). These features were common to both *S. aureus* and *P. aeruginosa*, however their

magnitudes differed. For both normalised modulus at 1 Hz (Figure 6.10C) and normalised phase at 200 Hz (Figure 6.10D), this difference is highlighted via time-based plots. The *S. aureus* normalised impedance changes were statistically different to the negative controls from 2 hours ($p = 0.024$, normalised phase at 200 Hz), however, significance was achieved more rapidly for *P. aeruginosa* after 1 hour ($p = 0.032$). Further, differences between the two bacterial signatures were significant from 1 hour ($p = 0.012$, normalised phase at 1 kHz), and remained significant for all key normalised impedance changes at 24 hours (p-value range 0.002 – 0.009).

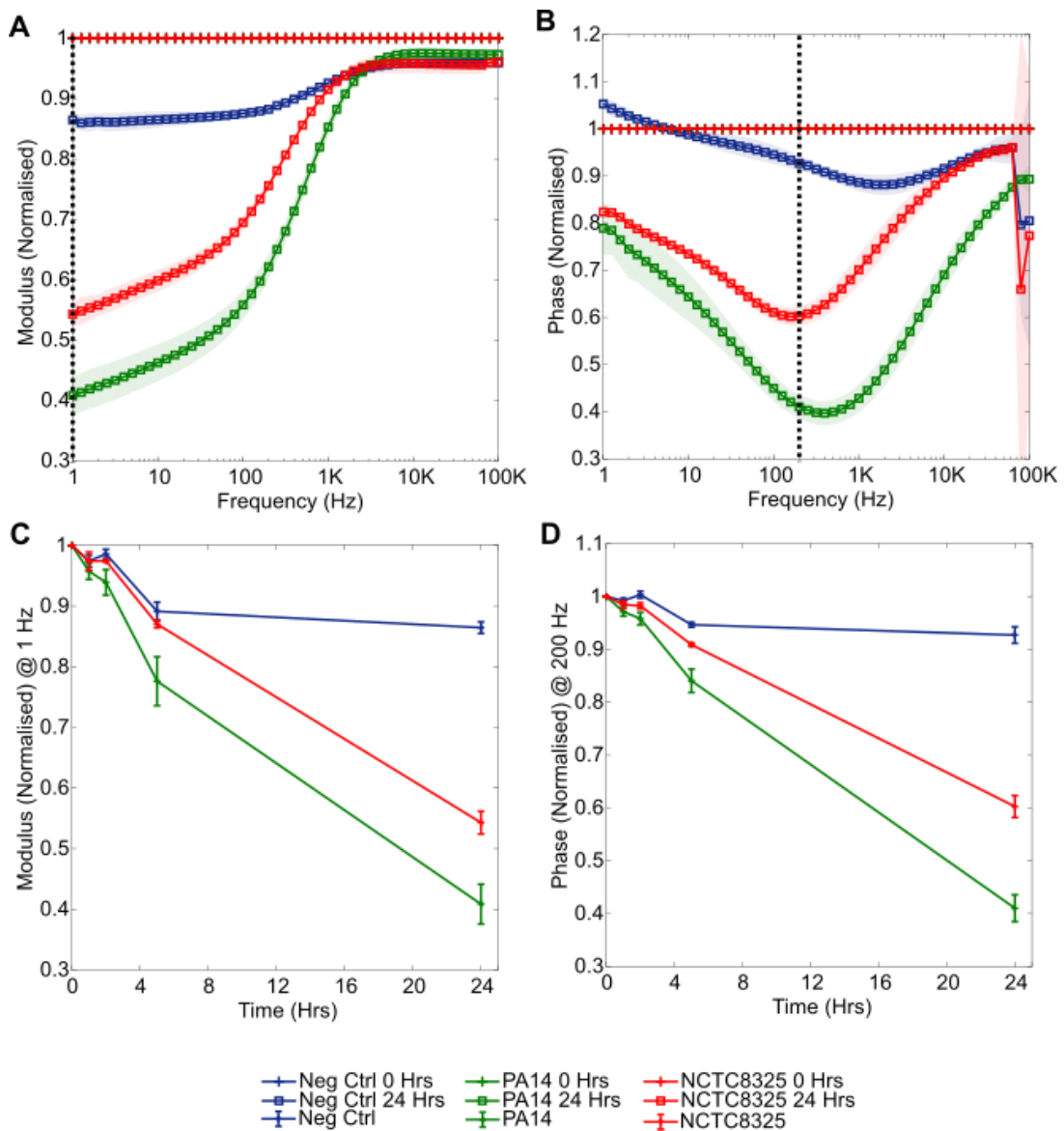


Figure 6.10. Impedance response associated with the growth of *S. aureus* (NCTC8325) and *P. aeruginosa* (PA14) separately but simultaneously in SWF. Plots show: (A) normalised modulus; (B) normalised (absolute) phase; (C) 1 Hz normalised modulus over time; (D) 200 Hz normalised phase over time. ($n = 4$ each, errors depict ± 1 standard deviation).

Initial and final cell densities are provided in Table 6.2; it is apparent that *P. aeruginosa* proliferated more during the experiment, despite sharing the same initial concentration as *S. aureus*. This variance in bacterial growth is likely to be a key influencing factor in the magnitude differences observed between the impedance signatures.

Table 6.2. Cell densities for *S. aureus* and *P. aeruginosa* over the simultaneous SWF growth experiment.

Species	0 Hrs Cell Density (CFU/mL)	24 Hrs Cell Density (CFU/mL)
<i>S. aureus</i>	3.2×10^6	1.7×10^8
<i>P. aeruginosa</i>	3.2×10^6	3.2×10^9

Subsequently, *E. coli* (DSM30083) was grown in SWF (Figure 6.11). In this case, measurements were performed every hour as the bacteria grew from an average concentration of 4.3×10^6 CFU/mL (range $(1.3 - 6.4) \times 10^6$ CFU/mL), to 1.2×10^9 CFU/mL (range $9.8 \times 10^8 - 1.3 \times 10^9$ CFU/mL). Once more, the modulus and absolute phase reductions characteristic of bacterial growth were observed (Figures 6.11A and 6.11B respectively). The standard deviations surrounding the negative control sensors in this experiment were slightly larger than observed previously, indicating lower sensor consistency in this case (Figures 6.11C, 6.11D). This may have been a result of insufficient sensor rinsing during the conditioning process, or manufacturing inconsistencies for example. Consequently, statistical significance was detected at the slightly later time of 3 hours via normalised phase at 200 Hz for example ($p = 0.011$).

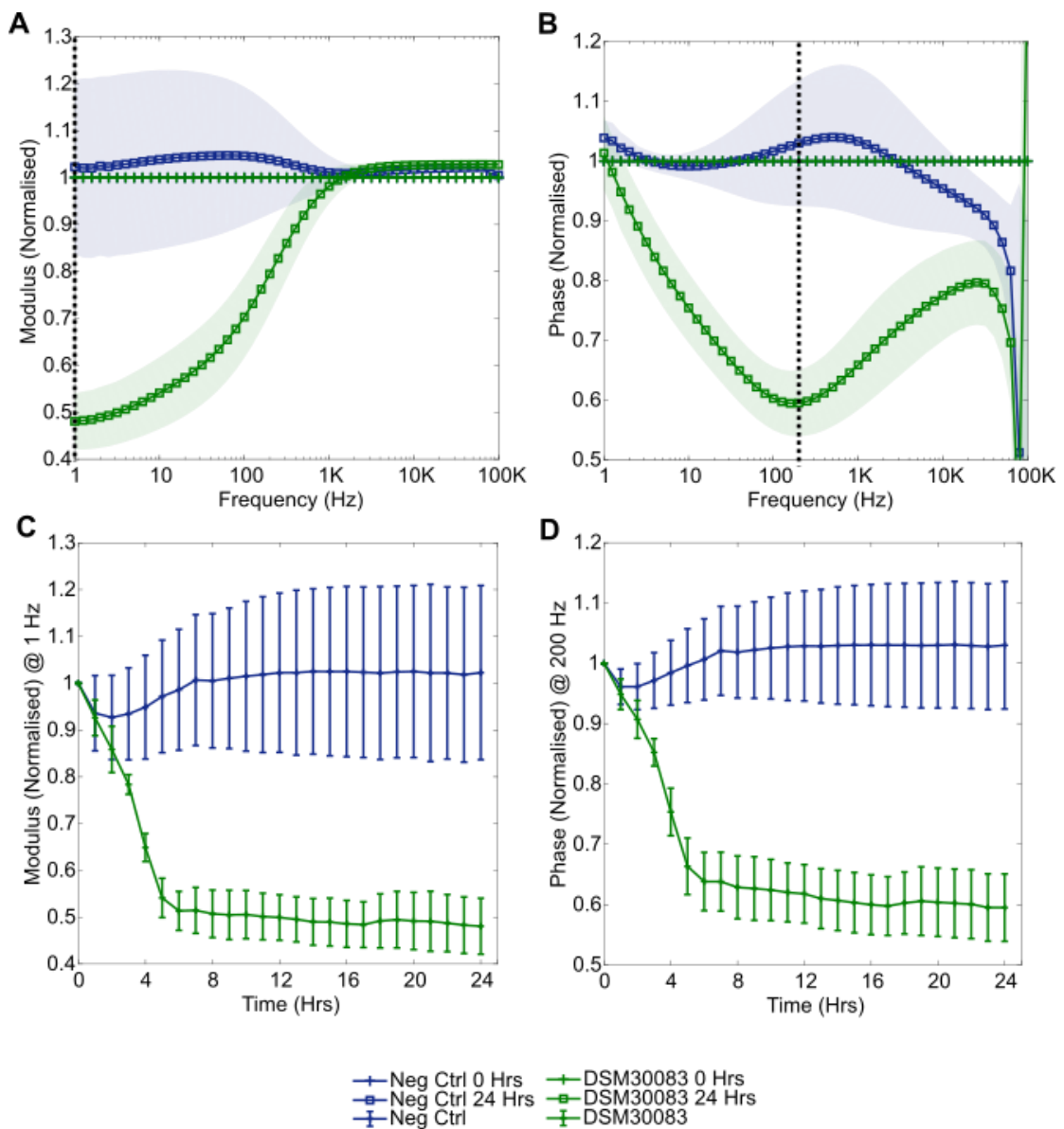


Figure 6.11. Impedance response associated with the growth of *E. coli* (DSM30083) in SWF. Plots show: (A) normalised modulus; (B) normalised (absolute) phase; (C) 1 Hz normalised modulus over time; (D) 200 Hz normalised phase over time. ($n = 3$ for *E. coli* due to broken connection, $n = 4$ negative controls, errors depict ± 1 standard deviation).

Finally, *P. mirabilis* growth in SWF was studied over 24 hours, with an initial cell concentration of 5.8×10^6 CFU/mL (range $(4.3 - 7.5) \times 10^6$ CFU/mL) rising to 2.2×10^9 CFU/mL (range $(1.0 - 3.2) \times 10^9$ CFU/mL). The bacterial sensors again produced the characteristic reduction in normalised modulus and normalised phase trough formation (Figures 6.12A and 6.12B respectively).

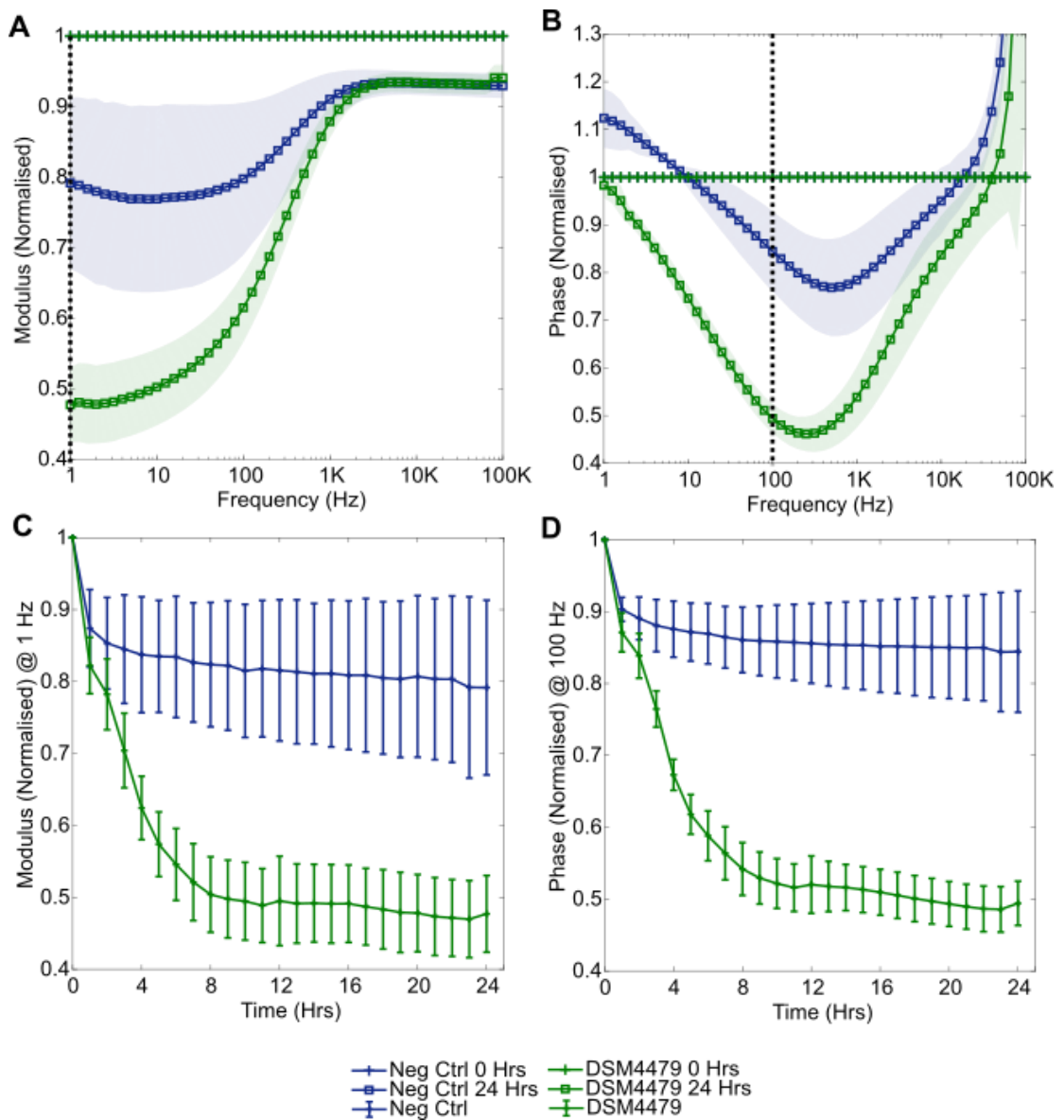


Figure 6.12. Impedance response associated with the growth of *P. mirabilis* (DSM4479) in SWF. Plots show: (A) normalised modulus; (B) normalised (absolute) phase; (C) 1 Hz normalised modulus over time; (D) 100 Hz normalised phase over time. ($n = 4$ for *P. mirabilis*, $n = 2$ for negative controls due to contamination of $n = 2$ wells, errors depict ± 1 standard deviation).

6.5 PCE Detection of Bacteria in Model Wound Environments

The WBM was next adapted for use with the PCE sensors, further addressing project objective 3 (Section 1.8). Initially, the WBM used previously with the simple carbon sensors was revised for these larger sensors, the wound bed model was then modified into a so called “double wound bed model” (dWBM) which incorporated sensors at both the base and top of the model. This second arrangement enabled bacterial detection in the absence of gravity-mediated settlement to additionally be explored (Section 6.5.2).

6.5.1 Detection of Bacteria in the WBM

Initially for the WBM, the average baseline impedance responses of sterile models were obtained. Coating the electrode with a collagen gel, processes such as charge transfer, diffusion, and the structure of the double layer (Chapter 2) are likely to have been affected by the introduction of this fibrous protein. An understanding of the impact of this gel upon the overall interface impedance was, therefore, desired. In the WBM, impedance modulus ranged from around $10^3 \Omega$ at 10^5 Hz to $1.1 \times 10^4 \Omega$ at 0.1 Hz (Figure 6.13A); absolute phase was maximal at 0.1 Hz, with a value of around 50° (Figure 6.13B). This is very similar to the baseline magnitudes in SWF (Figure 6.9), and it can therefore be concluded that the additional collagen matrix did not notably influence the baseline impedance values of the system. It is believed that the SWF content of the collagen gel, in addition to imperfect adhesion of the gel to the electrode surface and the small volume of gel used (compared to bulk SWF) were key factors in this finding. A difference in sensor consistency was evident between these and the SWF results, however, with larger error shading at frequencies below 1 kHz evident here indicating a decreased consistency (Figure 6.13 vs Figure 6.9). Discussed in Chapter 7, this is expected to have originated from inhomogeneous gel formation across the sensor surface, a likely consequence of the manual pipetting process used when creating the WBM. This gel detachment can be seen in the WBM image within Figure 6.14.

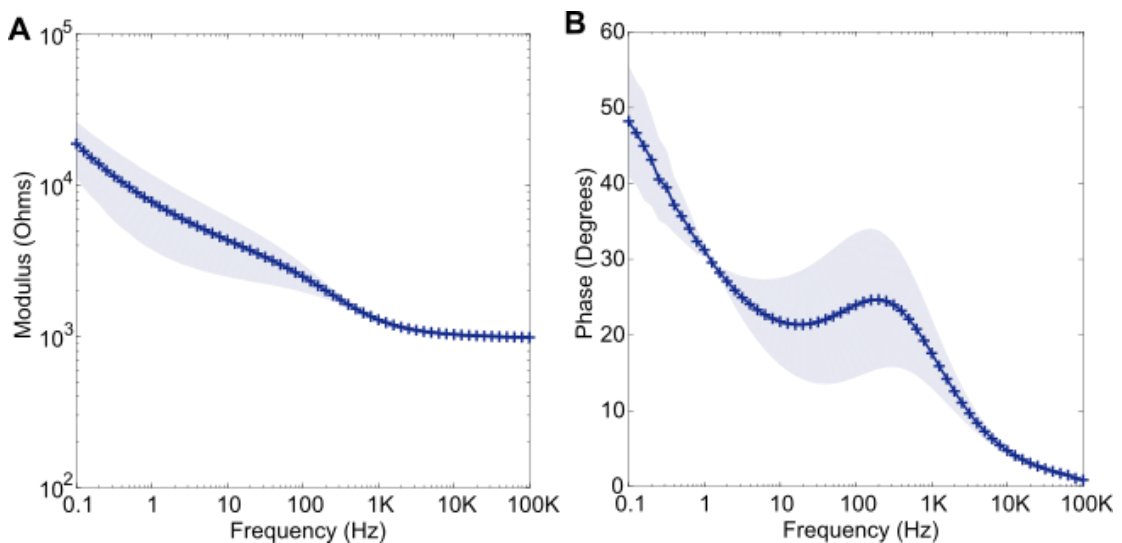


Figure 6.13. The baseline (A) modulus and (B) absolute phase plots obtained using the PCE sensors in sterile WBM ($n = 3$, shading depicts ± 1 standard deviation).



Figure 6.14. Image of a WBM chamber. Some central gel detachment is visible as lighter colouring.

The growths of *P. aeruginosa* (PA14) and *S. aureus* (NCTC8325) were next measured over a 24-hour period in the WBM. These bacteria were grown separately but simultaneously, with cell concentrations provided in Table 6.3. Despite *P. aeruginosa* growing to a higher cell density, after 24 hours the normalised impedance signatures for both bacteria were very similar (Figure 6.13). In each case, a reduction in normalised modulus value below 1 kHz (Figure 6.15A) and a normalised phase trough around 200 Hz developed (Figure 6.15B).

Table 6.3. Cell densities for the *S. aureus* and *P. aeruginosa* simultaneous WBM experiment.

Species	0 Hrs Cell Density (CFU/mL)	24 Hrs Cell Density (CFU/mL)
<i>S. aureus</i>	3.6×10^6	5.6×10^8
<i>P. aeruginosa</i>	3.7×10^6	3.9×10^9

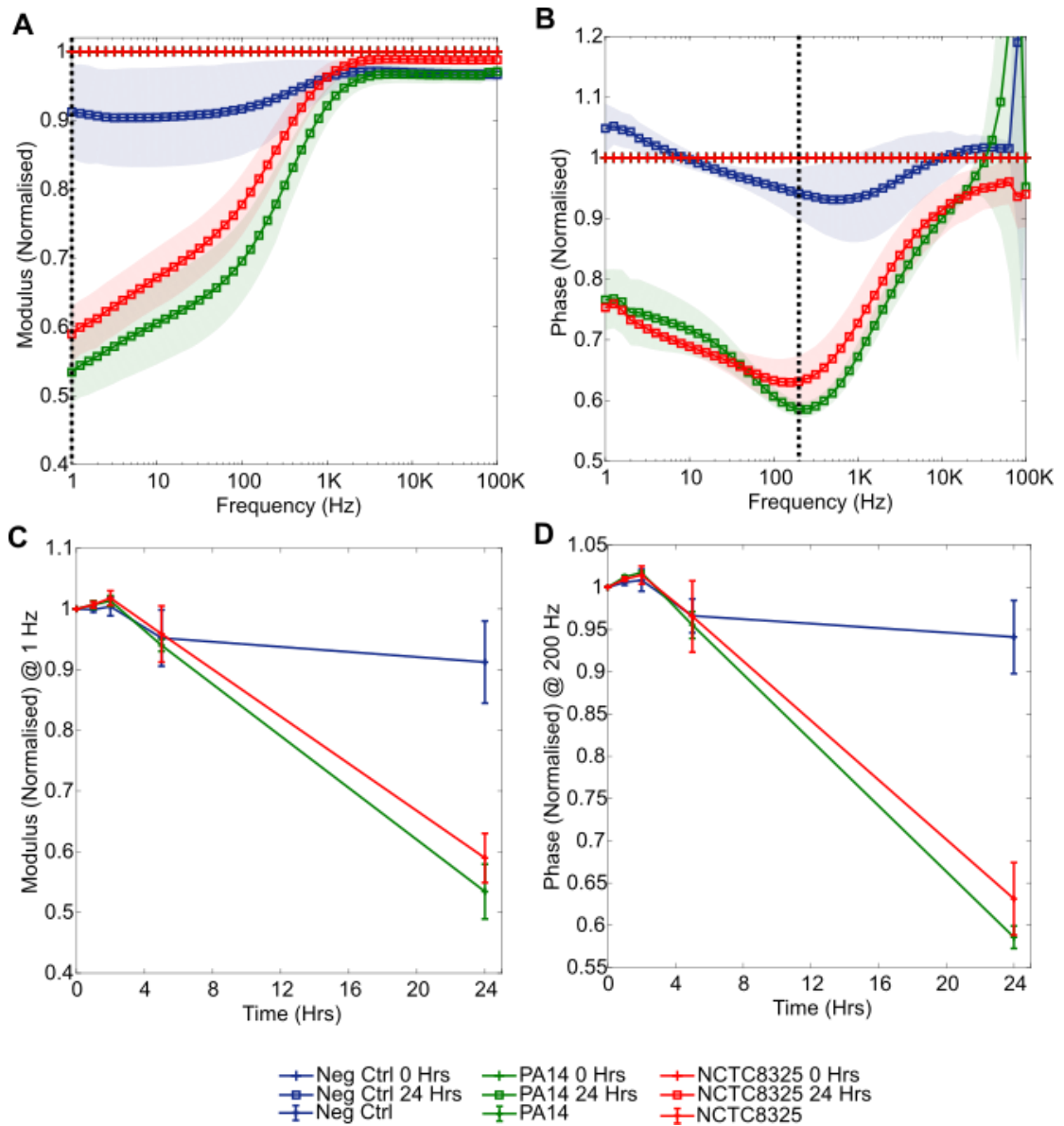


Figure 6.15. Impedance response associated with the growth of *S. aureus* (NCTC8325) and *P. aeruginosa* (PA14) separately but simultaneously in the PCE WBM. Plots show: (A) normalised modulus; (B) normalised (absolute) phase; (C) 1 Hz normalised modulus over time; (D) 200 Hz normalised phase over time. ($n = 3$ each, errors depict ± 1 standard deviation).

In SWF significant differences between these two species were detected, whereas in the WBM this was not the case. As these SWF and WBM experiments were conducted simultaneously and, therefore, under identical conditions, a reasonable comparison can be made. The only identifiable difference between models- the collagen gel covering the sensor surface- is believed to be responsible. In SWF, the signature differences were believed to be due to the greater *P. aeruginosa* proliferation and metabolism, yet despite greater *P. aeruginosa* proliferation again in the WBM, no differences in signature were visible. It is believed that the

collagen gel limited direct bacterial interactions with the electrodes, by covering the electrode surface and providing preferential conditions for biofilm formation. As depicted in Figure 6.16, the additional motile *P. aeruginosa* cells may not have directly interacted with the electrode surface in this WBM experiment, resulting in no clear impedance signature differences emerging here. As manual clipping without use of the multiplexer was required for these WBM measurements (detailed in Section 3.7.5), the number of measurements performed was minimised to minimise disturbances to sensor incubation and, therefore, bacterial growth. This is believed to be responsible for a lack of significant impedance changes before 24 hours (observed, for example, via normalised modulus at 1 Hz and normalised phase at 200 Hz (Figures 6.15C, 6.15D), p-value range 0.003 – 0.006). With more frequent measurements and sustained incubation, significant impedance changes may have been detected earlier.

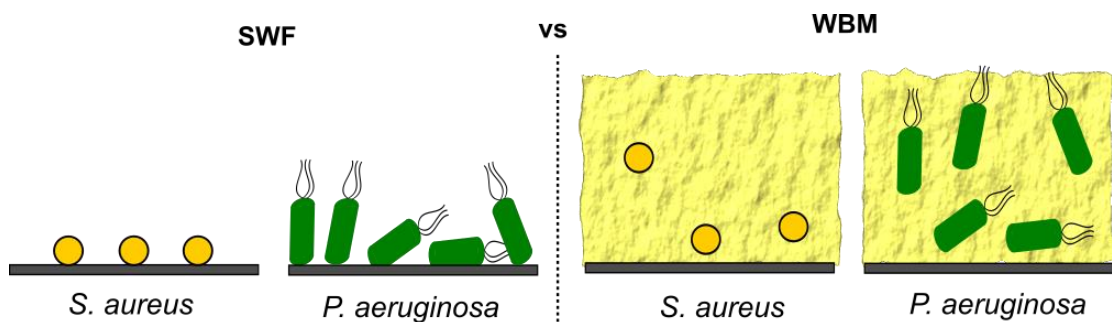


Figure 6.16. Comparison of SWF and WBM experiment bacterial/surface arrangements

P. aeruginosa and *S. aureus* were next grown together in a polymicrobial culture over 24 hours (in addition to individual growth for comparison), with the average cell densities provided in Table 6.4. When grown individually, both bacteria increased in concentration by around a factor of 100 over the course of the experiment. When together in a co-culture *P. aeruginosa* had this same 100-fold concentration increase, however, for *S. aureus* a reduction in viable cell count was observed. *P. aeruginosa* growth was, therefore, seen to out-compete *S. aureus*. In normalised modulus (Figure 6.17A) no clear differences emerged between the three conditions, yet, interestingly, the normalised phase signatures (Figure 6.17B) appeared to reflect this growth pattern. The polymicrobial signature more closely followed the *Pseudomonas* signature, reflective of the growth dominance of this species. This experiment was carried out in isolation, in contrast to the previous WBM experiment which was carried out simultaneously to the SWF for comparison. As a result, there were fewer electrodes to measure, and the models were removed from incubation for shorter time periods. This is likely why significant changes vs the negative controls were detected earlier for all chambers here, from 5 hours in each case. This was observed via normalised phase at 200 Hz for example ($p = 0.014$ for *P. aeruginosa*,

$p = 0.013$ for *S. aureus* and $p = 0.004$ for polymicrobial). As in SWF (Section 6.4), significant differences emerged between the *P. aeruginosa* and *S. aureus* signatures. Here, these were most visible via normalised phase at 1 Hz and 200 Hz, with early significance at 1 hour ($p = 0.006$, normalised phase 200 Hz for example) and 2 hours ($p < 0.001$) and then later significant differences re-emerging at 24hours ($p = 0.027$). A difference in the lag phase of the bacteria may have influenced early differences, with later processes such as biofilm formation instead responsible for the signature differences at 24 hours. The polymicrobial signature was significantly different to the *S. aureus* response only at the 24-hour measurement ($p = 0.001$, normalised phase at 200 Hz). In contrast, the polymicrobial signature was not significantly different to *P. aeruginosa* at any time. This analysis further highlights the dominance of *P. aeruginosa* over *S. aureus* in the polymicrobial WBM.

Table 6.4. Cell densities for *S. aureus* and *P. aeruginosa* in the polymicrobial WBM experiment.

Culture	0 Hrs Cell Density (CFU/mL)	24 Hrs Cell Density (CFU/mL)
<i>S. aureus</i>	7.5×10^6	8.8×10^8
<i>P. aeruginosa</i>	4.4×10^7	3.5×10^9
Polymicrobial – <i>S. aureus</i>	1.3×10^7	9.0×10^6
Polymicrobial – <i>P. aeruginosa</i>	2.0×10^7	3.5×10^9

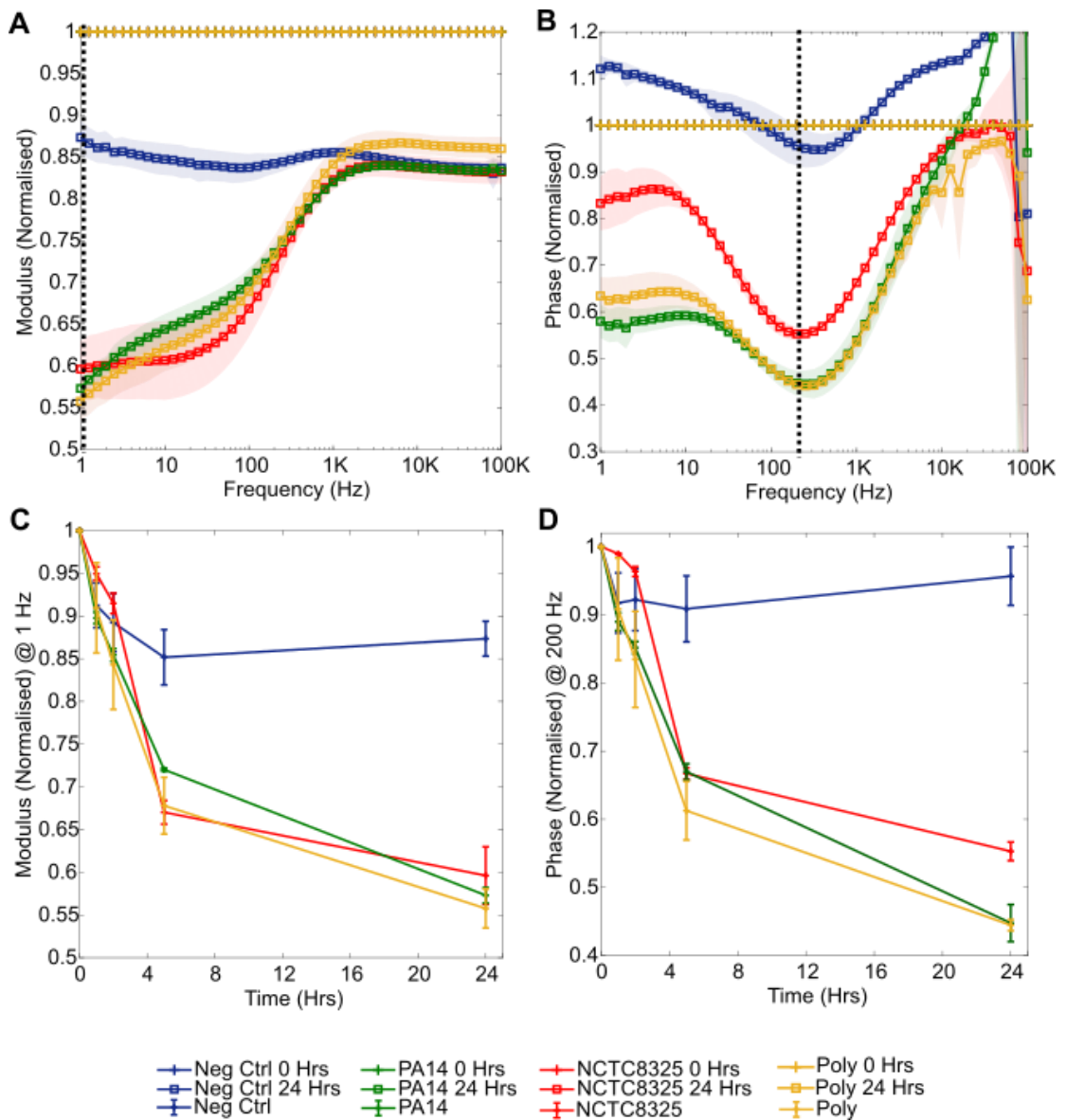


Figure 6.17. Impedance response associated with the growth of *S. aureus* (NCTC8325) and *P. aeruginosa* (PA14) and a polymicrobial NCTC8325 and PA14 culture in the PCE WBM. Plots show: (A) normalised modulus; (B) normalised (absolute) phase; (C) 1 Hz normalised modulus over time; (D) 200 Hz normalised phase over time. ($n = 3$ each, errors depict ± 1 standard deviation).

Within Figure 6.18, photographs of the polymicrobial experiment WBM chambers are provided. The collagen matrix is visible in each chamber as white material, which often appears to have partially detached from the counter electrode in certain areas. Likely a result of the pipetting of media on top of the gel, this reinforces the idea that collagen gel inhomogeneity may impact sensor consistency. Further, both the *P. aeruginosa* and polymicrobial chambers have a green pigmentation characteristic of *Pseudomonas* growth, highlighting the strong presence of this species in the polymicrobial WBM.

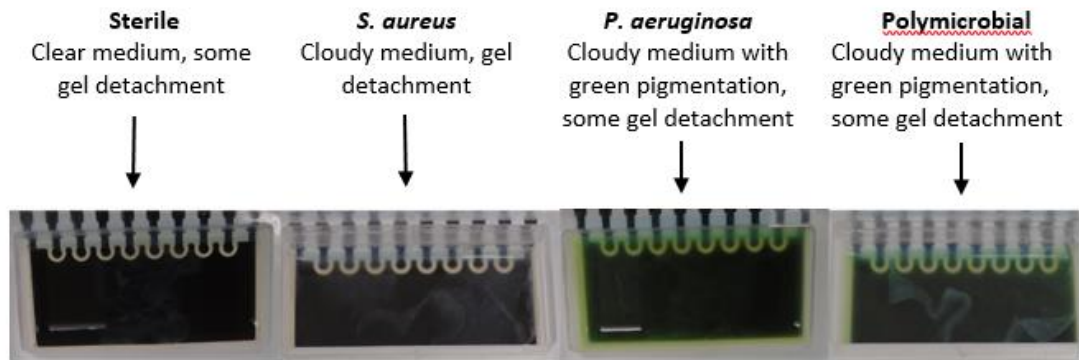


Figure 6.18. Images of the WBM chambers following the PCE polymicrobial experiment.

6.5.2 Detection of Bacteria in the dWBM

Through the series of steps outlined in Section 3.7.5, the double sensor WBM (dWBM) which contained both a base and a top sensor in each model was developed. For each figure within this section, the base sensor results are shown in the left column of the figure and the top sensor results in the right.

The baseline impedance of this set up was again first measured using sterile models, with the results presented in Figure 6.19. Both the base and top sensor impedance moduli (Figures 6.19A and 6.19B respectively) ranged from around $10^3 \Omega$ at 10^5 Hz to around $10^4 \Omega$ at 0.1 Hz, despite the presence of the collagen gel on the base sensor. These values are consistent with those obtained for the WBM (Section 6.5.1). There was, however, lower measurement consistency for the top sensors compared to the base sensors, visible as larger standard deviation shading below 1 kHz. Similarly, for absolute phase (Figures 6.19C, 6.19D) the impedance spectra values were comparable but larger errors were present for the top sensors (in this case around the 1 kHz region). There are multiple possible reasons for this, including the presence of air bubbles on the sensors which could not be seen and irregular sensor connection during measurement (due to the manual connection process and less accessible top sensor connectors). Such factors are further discussed and illustrated within Chapter 7. Additionally, as referred to previously in Chapter 5, electrochemical noise is commonly present at low frequencies due to the impact of diffusion processes.

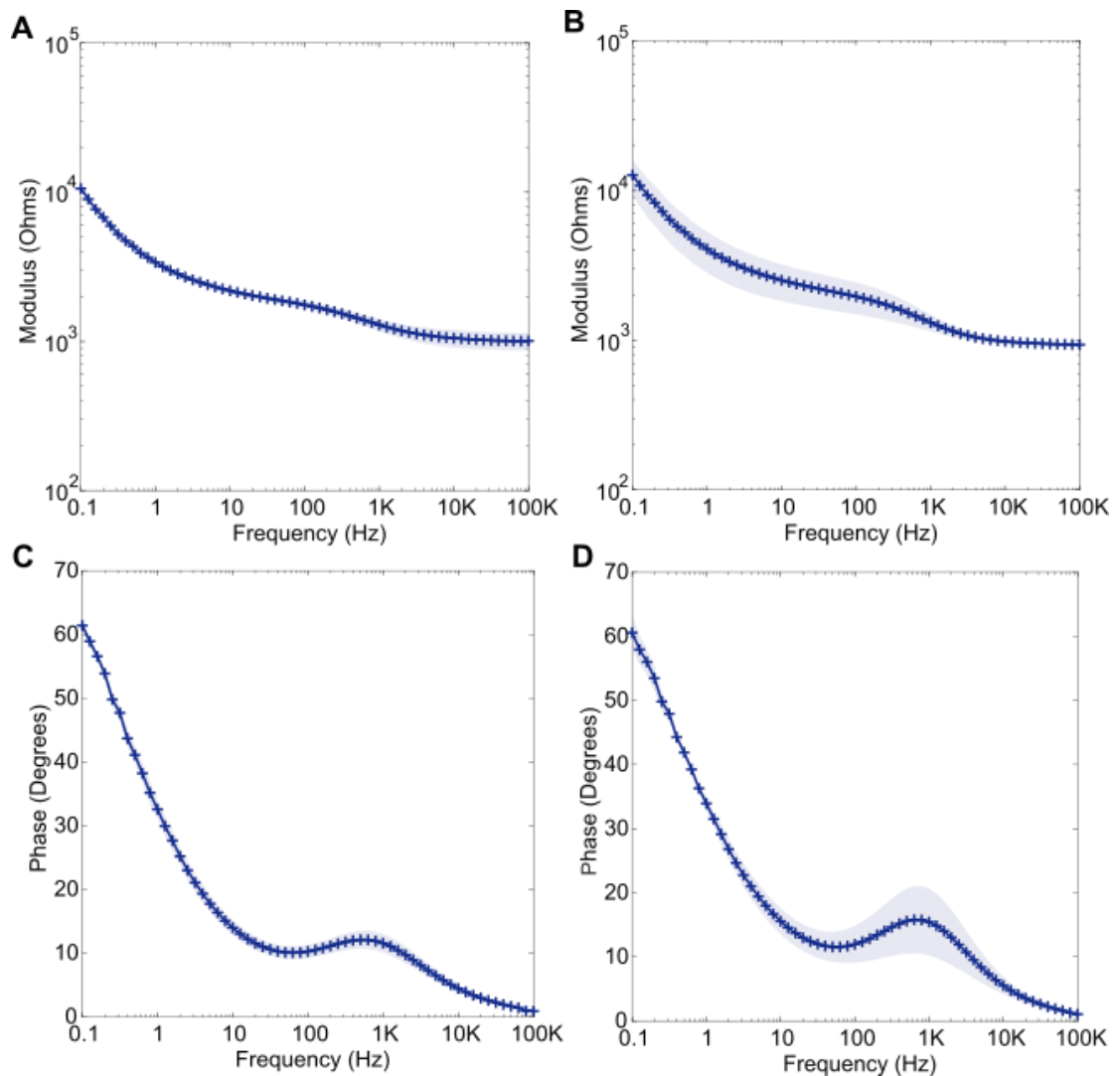


Figure 6.19. The baseline impedance plots obtained for the dWBM, with: (A) modulus for the base sensor; (B) modulus for the top sensor; (C) absolute phase for the base sensor; (D) absolute phase for the top sensor ($n = 3$, shading depicts ± 1 standard deviation).

In line with the WBM experiments, *P. aeruginosa* and *S. aureus* were first grown separately but simultaneously in the dWBM. Table 6.5 reveals that less bacterial growth occurred in this experiment than in the comparable WBM experiment. This is believed to result from incomplete ethanol evaporation after sterilisation, due to the enclosed dWBM configuration. Previously, normalised results below 1 Hz have been omitted due to no further changes of interest being present and the inherent noise associated with these low frequencies. In this experiment, however, the normalised impedance between 0.1 - 1 Hz provided crucial insight. Firstly, the base sensor detected a decrease in normalised modulus below 1 kHz for *P. aeruginosa* in the same manner as previously but detected a sharper decrease for *S. aureus* below 10 Hz only (Figure 6.20A). Caution must be exercised when assessing the changes

within this (previously noisy) diffusion limited region, however, the effects of key metabolites such as pyocyanin may play an important role here. Comparing these signatures to the top sensor's response in Figure 6.20B, large errors at all frequencies above 1 Hz were present in this instance. This prevented differentiation at all but the lowest frequencies, where again each of the three conditions could be visibly separated and *S. aureus* had the largest change. For normalised phase, the both the base and top sensors detected differences between the bacterial signatures for each species (Figures 6.20C and 6.20D respectively). In each case, *S. aureus* growth caused a 1 Hz trough and a smaller mid frequency peak to emerge in a different manner to what has been observed in other experiments for this bacterium. As will be discussed within Chapter 7, this is hypothesised to be a result of the residual ethanol in the WBM, and its interactions with this bacteria's metabolic products. Larger top sensor errors again were present in addition to more pronounced negative control variation, particularly at high frequencies. This phase response differed from *P. aeruginosa*, which caused a broad trough to form, minimising at between 1 Hz and 100 Hz. When comparing between the base and top sensor results, the largest disparity was observed around 100 Hz: the normalised absolute phase values for *S. aureus* in particular differed substantially. Interestingly, in general the *S. aureus* signature was more pronounced than the *P. aeruginosa* signature in this experiment, despite having both lower starting and final concentrations. Again, these findings will be further explored within Chapter 7's discussion in the context of earlier WBM results.

Table 6.5. Cell densities for the *S. aureus* and *P. aeruginosa* simultaneous dWBM experiment.

Species	0 Hrs Cell Density (CFU/mL)	24 Hrs Cell Density (CFU/mL)
<i>S. aureus</i>	2.7×10^6	5.5×10^7
<i>P. aeruginosa</i>	1.5×10^7	5.6×10^8

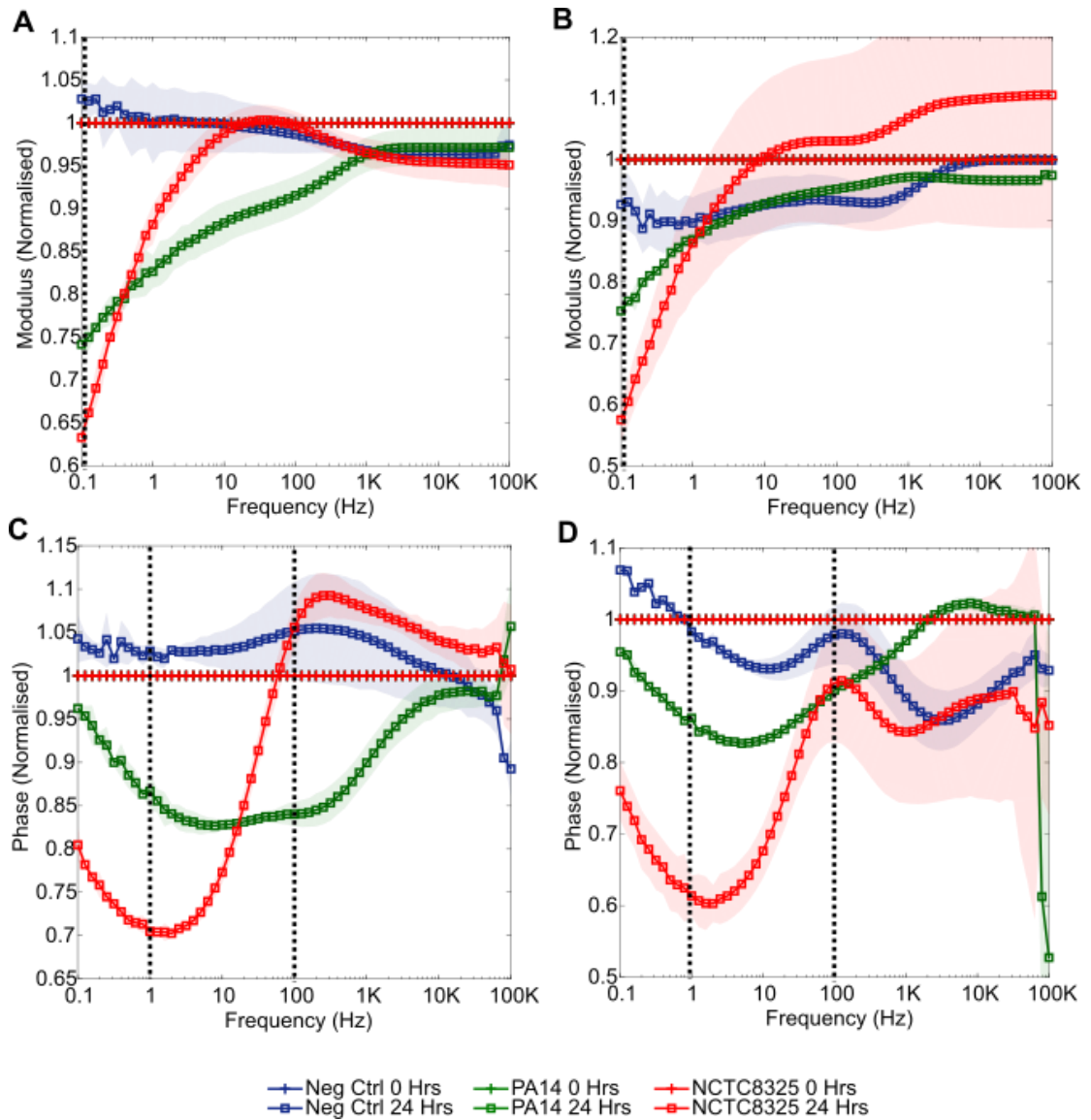


Figure 6.20. Impedance response associated with the growth of *S. aureus* (NCTC8325) and *P. aeruginosa* (PA14) separately but simultaneously in the PCE dWBM. Plots show: (A) normalised modulus for the base sensor; (B) normalised modulus for the top sensor; (C) normalised (absolute) phase for the base sensor; (D) normalised (absolute) phase for the top sensor ($n = 2$ each due to sensor damage in the manual connection process, errors depict ± 1 standard deviation). Dotted lines indicate key frequencies investigated further in time-based plots.

These differences were further explored using time-based plots at the key frequencies indicated by dotted lines in Figure 6.20 (Figure 6.21). As only $n = 2$ replicates were included in these results (due to the exclusion of sensors which displayed a vastly greater impedance because of suspected contact damage during the manual connection process), the statistical significance of the results is often limited. Normalised modulus at 0.1 Hz displayed clear impedance changes for both the base and top sensors (Figures 6.21A and 6.21B respectively), with significant differences observed between the two species at 24 hours in each case (p -value

range 0.001 – 0.014). Similarly, for normalised (absolute) phase at 1 Hz, significant differences again emerged between the bacterial species at 24 hours (p -value range 0.005 – 0.006). For both key locations, the changes were very similar between the top and base sensors; for normalised phase at 100 Hz, however, sensor signature differences were noted (Figures 6.21E and 6.21F). The characteristic decrease at mid-frequencies often seen during bacterial growth may be influenced by gravitational settlement, as this feature (present here only for *P. aeruginosa*) was diminished for the top sensors. Whilst no significant differences could be detected for this feature due to the small replicate number ($p > 0.05$), this remains a potential area of differentiation between species using the base sensors. As was introduced in Chapter 1, there are multiple mechanisms via which bacteria can influence impedance including metabolism of nutrients and membrane contact with the electrode surface. Further, at the low frequencies of interest here (below 100 Hz) the biological tissue α -dispersion is at play, with dipolar interactions at membrane surfaces being influential. Whilst *S. aureus* and *P. aeruginosa* exhibit various differences (Chapter 2), it is residual ethanol within the model that is believed to be most influential in this particular result, as will be discussed within Chapter 7.

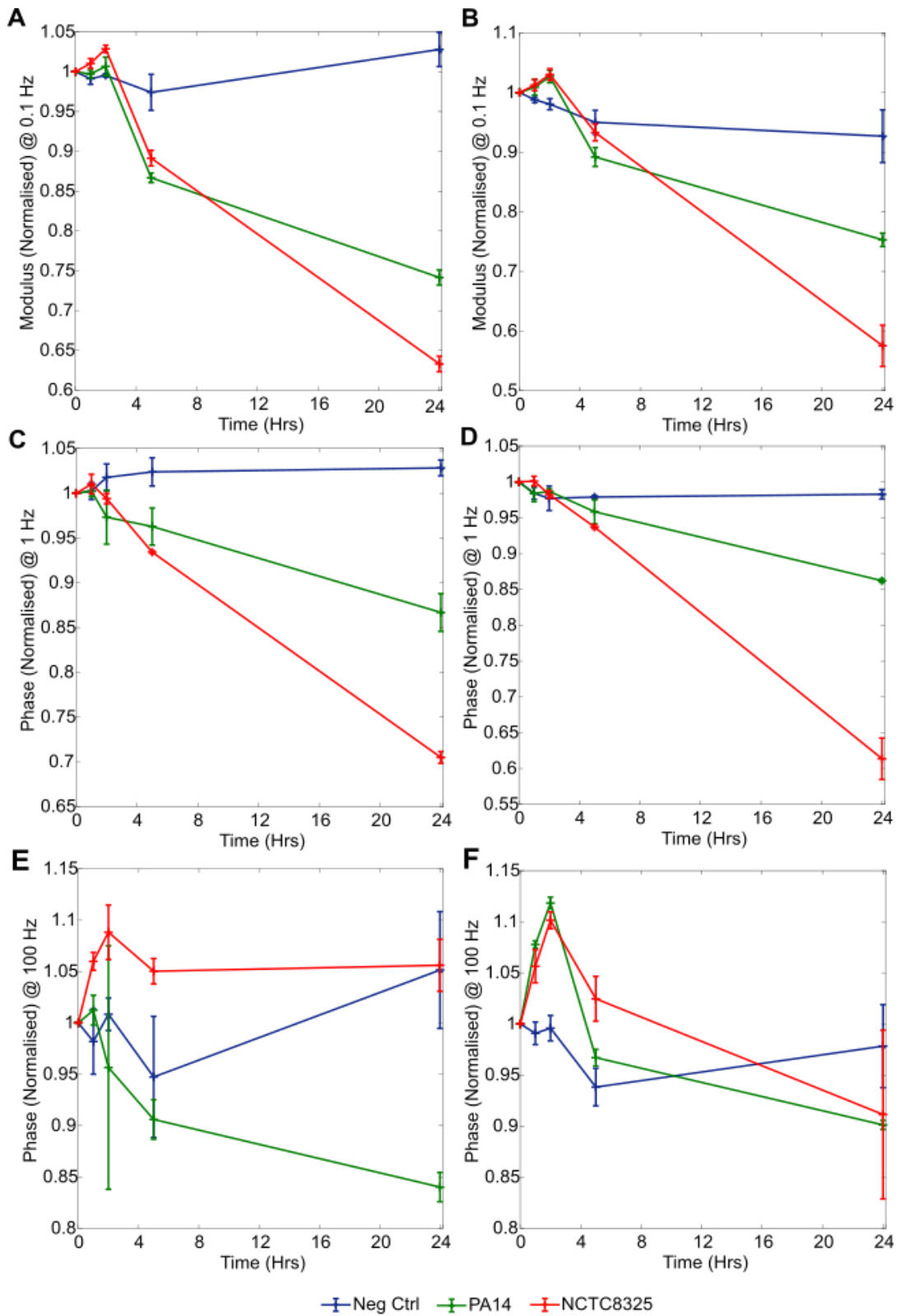


Figure 6.21. *S. aureus* (NCTC8325) and *P. aeruginosa* separate growth in the dWBM over 24 hours time-based plots. Plots show: (A) base sensor normalised modulus at 1 Hz; (B) top sensor normalised modulus at 1 Hz; (C) base sensor normalised phase at 1 Hz; (D) top sensor normalised phase at 1 Hz; (E) base sensor normalised phase at 100 Hz; (F) top sensor normalised phase at 100 Hz ($n = 2$, error bars depict ± 1 standard deviation).

This experiment was next repeated with the addition of a polymicrobial dWBM, containing a co-culture of *P. aeruginosa* (PA14) and *S. aureus* (NCTC8325). Due to the increased number of electrodes being measured in this experiment (24 in total as $n = 3$ replicates for each of the 4 top and 4 base sensors) and resulting increased measurement duration, it was not practical to measure down to 0.1 Hz. Instead, measurements were cut off at 1 Hz as in many previous experiments. Fortunately, this decreased range still enabled several interesting observations to be made. In the same way as the polymicrobial WBM study (Section 6.5.1), when grown separately both the *P. aeruginosa* and *S. aureus* cell densities increased (Table 6.6). Again, when co-cultured *P. aeruginosa* proliferated but *S. aureus* saw a slight decrease in viable cell count after 24 hours of incubation. PA14, therefore, outcompeted its rival in the dWBM, in the same way as in the simpler WBM.

Table 6.6. Cell densities for *S. aureus* and *P. aeruginosa* in the polymicrobial dWBM experiment.

Culture	0 Hrs Cell Density (CFU/mL)	24 Hrs Cell Density (CFU/mL)
<i>S. aureus</i>	2.9×10^7	2.3×10^8
<i>P. aeruginosa</i>	3.4×10^7	5.9×10^8
Polymicrobial – <i>S. aureus</i>	3.0×10^7	2.9×10^7
Polymicrobial – <i>P. aeruginosa</i>	2.8×10^7	6.2×10^8

This growth pattern was once more reflected in the normalised impedance plots (Figure 6.22). For both the base (Figure 6.22A) and top sensors (Figure 6.22B), the familiar decreases in normalised modulus occurred for both pathogens and the polymicrobial culture at frequencies below 1 kHz. The signatures could not be distinguished for the base sensor; however, the top sensor recorded a larger decrease for *S. aureus* while the polymicrobial signature remained close to *P. aeruginosa*. Differences between the *S. aureus* magnitude of change here and in the previous dWBM study may be linked to the larger starting concentration in this experiment, however, interestingly a more pronounced change was recorded for the lower concentration previously despite a 10-fold increase occurring over the course of both studies. Moving on to the normalised phase plots, clear differences between the *S. aureus* and *P. aeruginosa* signatures were again visible (as in the previous dWBM experiment). For both the base and top sensors (Figures 6.22C and 6.22D respectively), PA14 caused a broad phase trough that minimised between 1 Hz and 10 Hz. At frequencies below around 50 Hz the base sensor signatures diverged, with the *S. aureus* and polymicrobial signatures declining more sharply than the *Pseudomonas* signature. Despite PA14 growth dominating in the polymicrobial model, its signature followed that of NCTC8325 for this sensor. It is believed that the influence of

gravitational effects may be responsible, with gravitational effects particularly important for the non-motile *S. aureus*. Contrastingly, the top sensor *S. aureus* signature was distinct from the *P. aeruginosa* spectrum at all frequencies below 10 kHz. Here, the polymicrobial signature lay in an intermediate position, compromising between the two bacterial responses (Figure 6.22D). This would indicate that, whilst *P. aeruginosa* growth dominated, the *S. aureus* cells were still influential in the obtained impedance response.

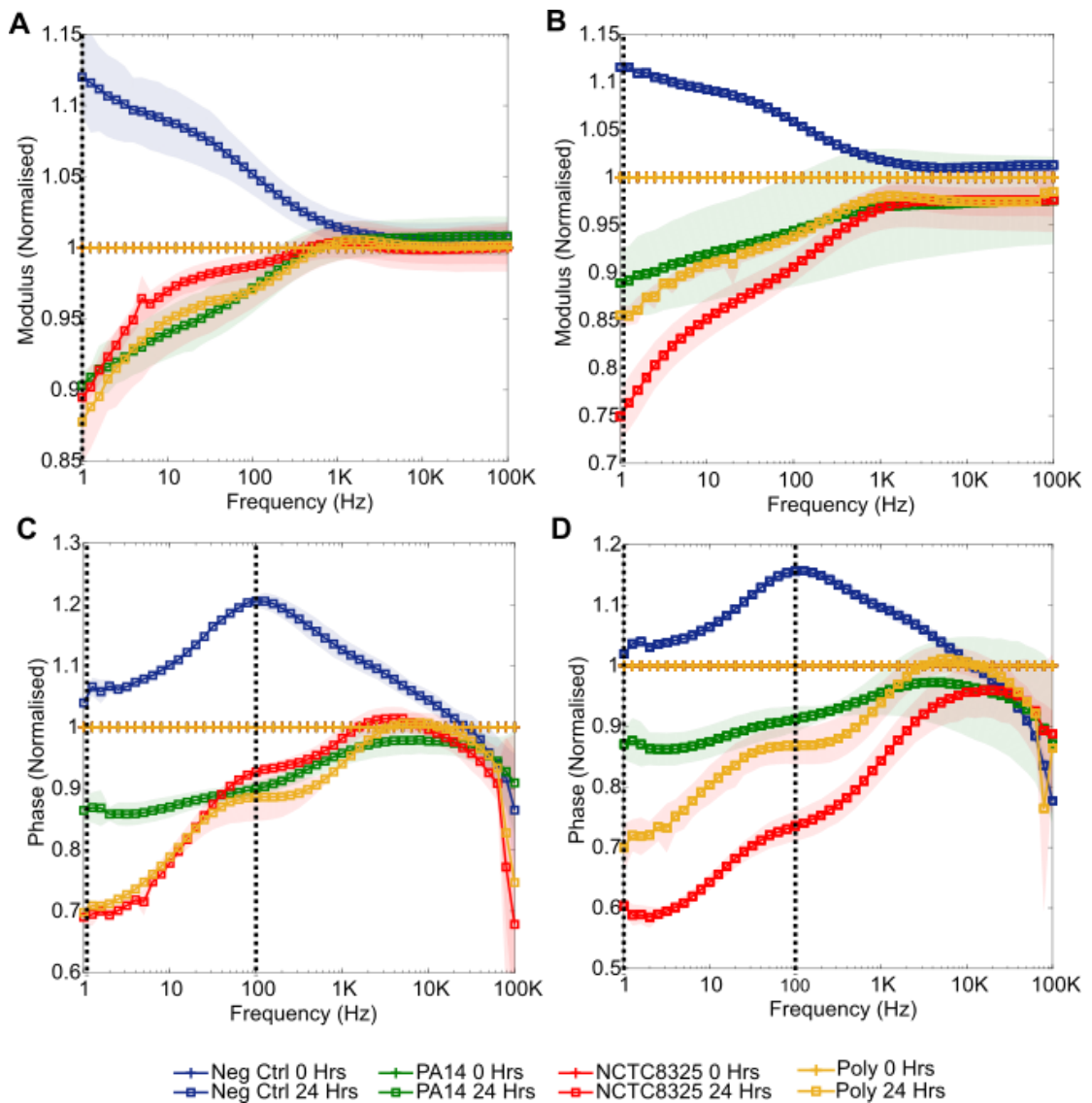


Figure 6.22. Impedance response associated with the growth of *S. aureus* (NCTC8325), *P. aeruginosa* (PA14) and a co-culture of these species (Poly) in the PCE dWBM. Plots show: (A) normalised modulus for the base sensor; (B) normalised modulus for the top sensor; (C) normalised phase for the base sensor; (D) normalised phase for the top sensor ($n = 3$ each, errors depict ± 1 standard deviation). Dotted lines indicate key frequencies investigated further in time-based plots.

Once more concentrating on the key areas of normalised impedance change, the time-based plots in Figure 6.23 were created. For the base sensors the only feature at which the different cultures could be distinguished was normalised phase at 1Hz (Figure 6.23C), with *S. aureus* and the polymicrobial culture showing a similar larger decrease. Conversely, for each key impedance feature measured by the top sensors the different cultures were separable, with *S. aureus* the most pronounced and the polymicrobial culture lying between the two species. The intermediate position of the top sensor polymicrobial signature varied with frequency, more closely matching *S. aureus* at 1 Hz in normalised phase whilst more closely matching *P. aeruginosa* at 100 Hz. For the dWBM therefore, the normalised phase results in particular provided an interesting indication that the mid- to low-frequency spectral regions could enable species and polymicrobial culture component differentiation.

Ultimately, bacteria were still able to be detected by the dWBM top sensors despite a lack of gravitational assistance supporting the contact between the bacterial cells and the sensors. This is a promising result that indicates this sensor could work well when used at different orientations, as required by the location of the wound and positioning of the patient.

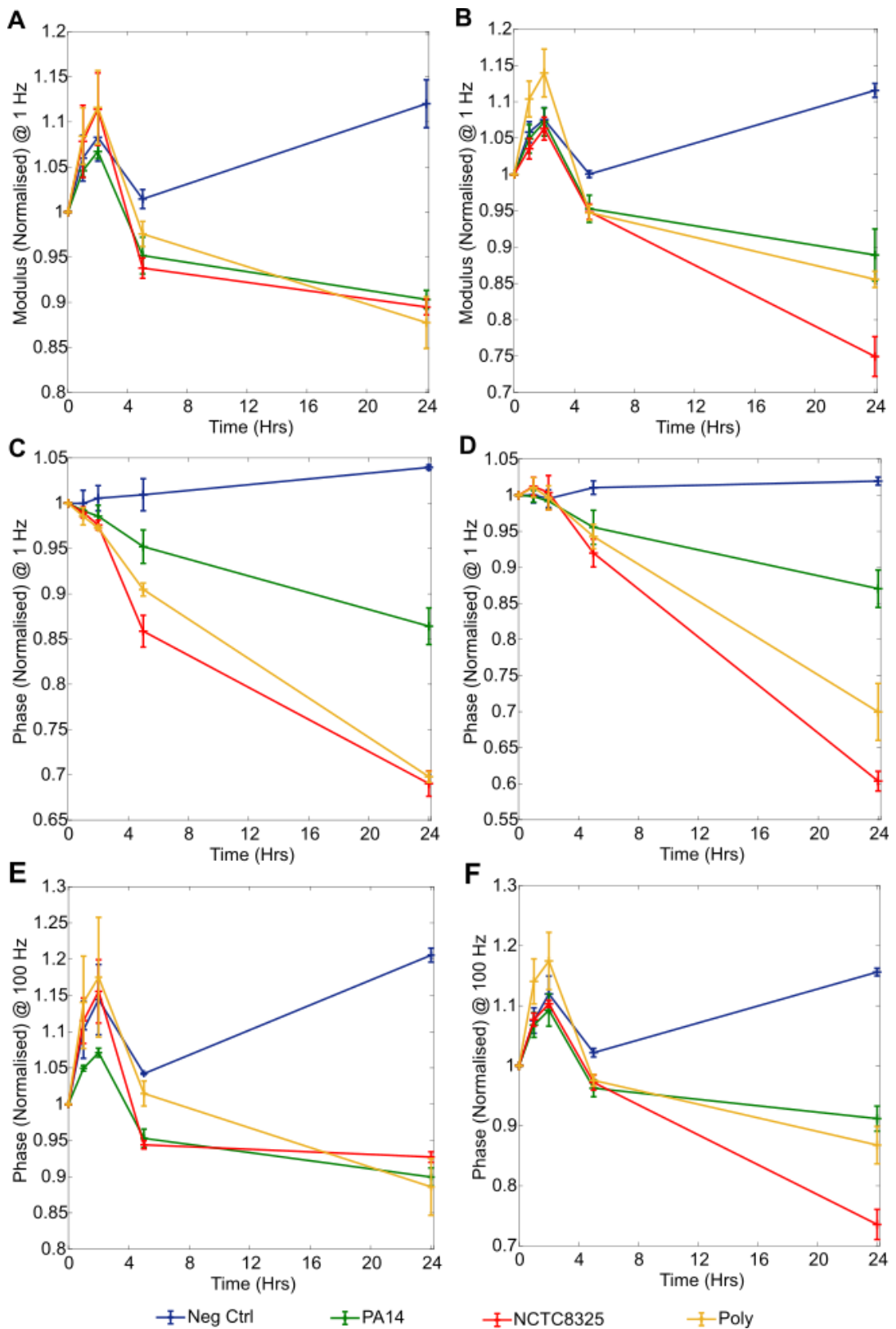


Figure 6.23. *S. aureus* (NCTC8325), *P. aeruginosa* and co-culture of these bacteria (Poly) grown in the dWBM time-based plots. Plots show: (A) base sensor normalised modulus at 1 Hz; (B) top sensor normalised modulus at 1 Hz; (C) base sensor normalised (absolute) phase at 1 Hz; (D) top sensor normalised (absolute) phase at 1 Hz; (E) base sensor normalised (absolute) phase at 100 Hz; (F) top sensor normalised (absolute) phase at 100 Hz ($n = 3$, error bars depict ± 1 standard deviation).

6.6 The Impact of Wound Dressings Upon Impedance and Bacterial Growth

The effects of several common wound dressings upon the wound bed model were next explored, assessing both the impact of the dressings upon impedance and their impact upon the growth of bacteria and, therefore, bacterial signature formation (objective 3, Section 1.8). *S. aureus* strain NCTC8325 was used in each of the following experiments, as this is widely regarded as the most common wound pathogen (26,27).

6.6.1 Acticoat Dressing

Firstly, the “Acticoat absorbent with SILCRYST™” dressing by Smith & Nephew was studied in the WBM (Figure 6.24). No initial significant differences in baseline impedance were observed due to the presence of this dressing in the WBM ($p > 0.05$ at all frequencies), although slight magnitude increases were visible (Figure 6.25).

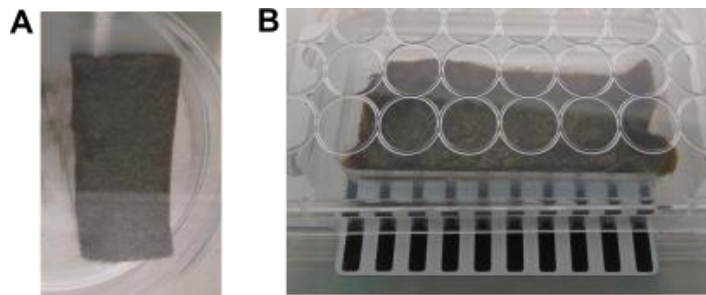


Figure 6.24. Acticoat absorbent dressing images: (A) a section of dressing cut into small sample for experiment; (B) sample of dressing contained in a WBM.

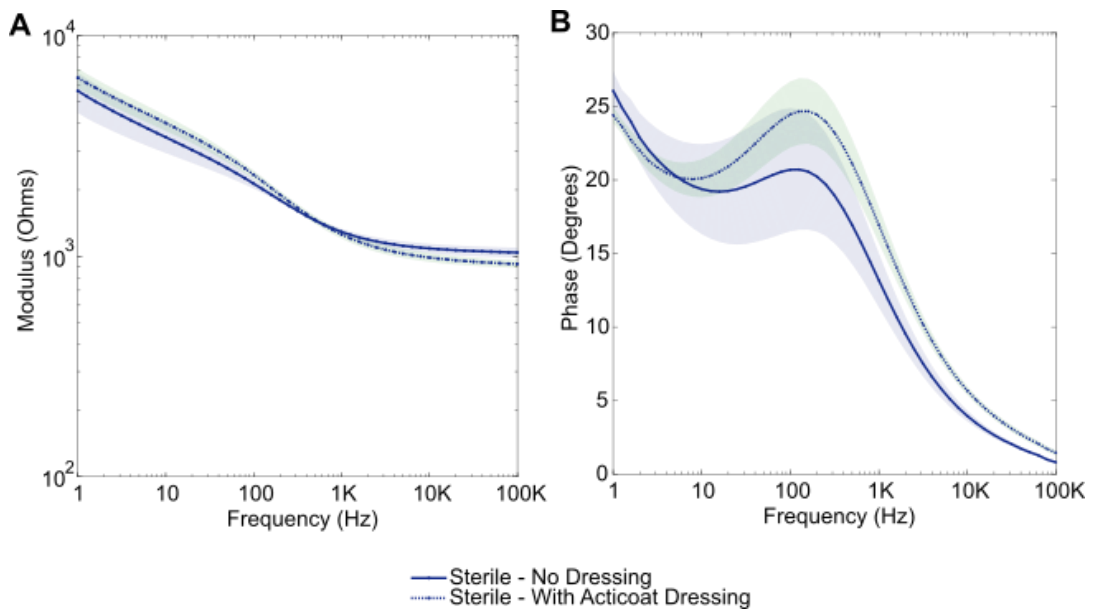


Figure 6.25. The baseline (A) modulus and (B) absolute phase plots observing the initial impact of the Acticoat absorbent with SILCRYST™ dressing upon the WBM ($n = 3$, error bars depict ± 1 standard deviation).

Over the 24-hour experiment period, the antimicrobial properties of this dressing were confirmed via colony counting of bacterial model aliquots. The concentration of *S. aureus* cells increased from 2.5×10^6 CFU/mL to 2.5×10^8 CFU/mL over 24 hours in the basic WBM containing no dressing, whereas the model containing the Acticoat dressing saw a decrease in cell density from 3.7×10^6 CFU/mL to 2.6×10^4 CFU/mL over 24 hours. Supporting the claim that these dressings prevent bacterial growth, the normalised impedance responses also reflected this. Figures 6.26A and 6.26B show the normalised modulus and absolute phase plots respectively, where both sterile and bacterial models containing the dressing had very similar changes in impedance. Specifically, an increase in normalised modulus at low frequencies and normalised phase peak formation at 10 Hz were observed for both dressing models, despite one being sterile and the other containing *S. aureus*. For comparison, the models without dressings followed the results obtained previously, with a clear bacterial signature emerging for *S. aureus* and no notable changes for the negative control. Through exploring the time-based plots in Figures 6.26C and 6.26D, a lack of statistically significant difference between the sterile and bacterial Acticoat models across all measured frequencies was confirmed ($p > 0.05$). Alternatively, without the dressing present significant changes were detected for *S. aureus* growth from 5 hours ($p = 0.007$ at 1 Hz normalised modulus for example).

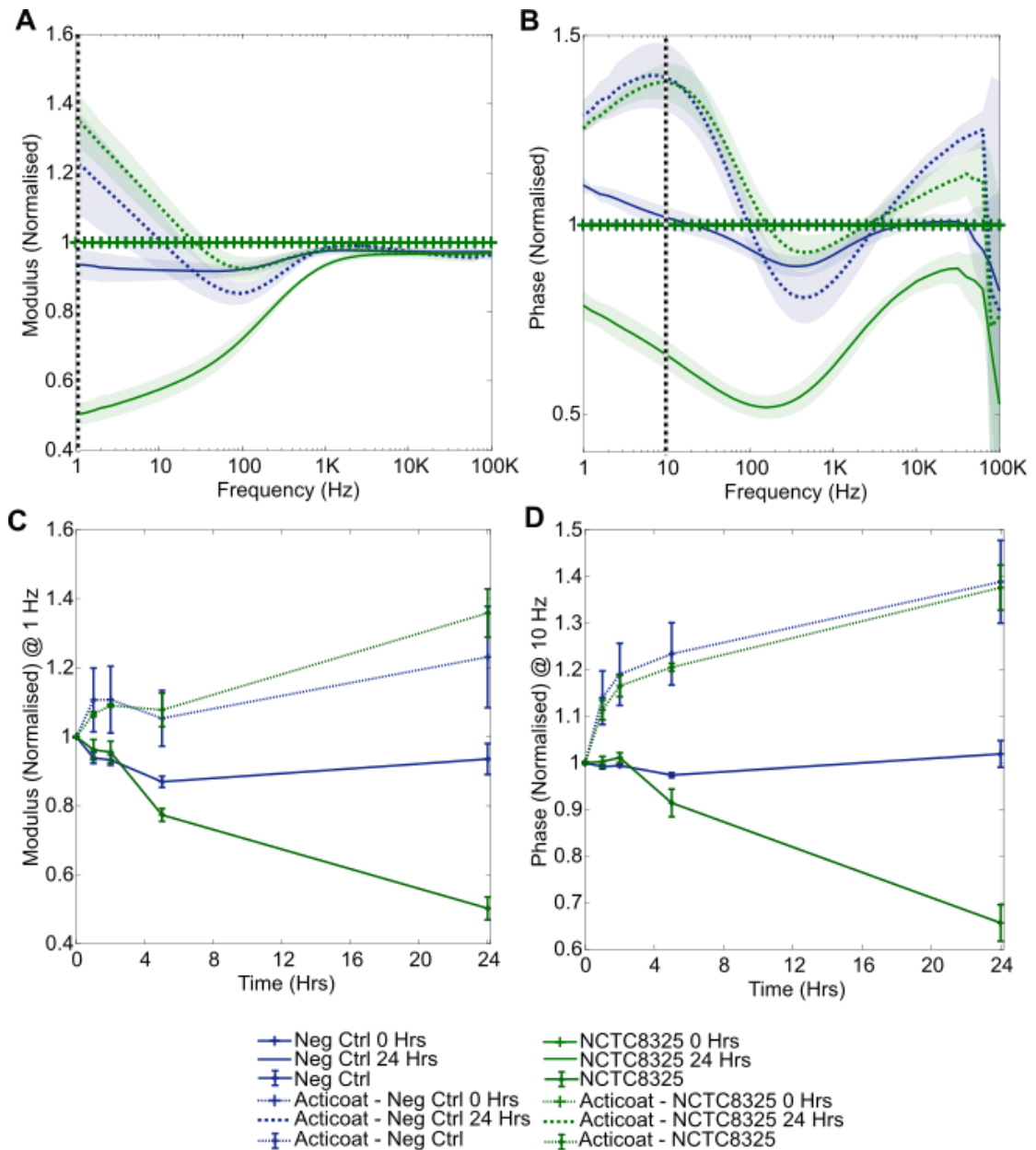


Figure 6.26. Impedance response associated with the growth of *S. aureus* (NCTC8325) in the PCE WBM. Dotted lines are used to represent models where the Acticoat dressing was present, and solid lines where no dressing was present. Plots show: (A) normalised modulus; (B) normalised (absolute) phase; (C) 1 Hz normalised modulus over time; (D) 10 Hz normalised phase over time. ($n = 3$ each, errors depict ± 1 standard deviation).

6.6.2 Advazorb Dressing

The next dressing studied was the “Advazorb” foam dressing by Advancis Medical (Figure 6.27). Due to its absorbent nature, the presence of the dressing immediately increased the baseline impedance modulus of the WBM by around a factor of 10 across all frequencies (Figure 6.28A). By absorbing the majority of the SWF within the model and greatly decreasing

the availability of SWF on the electrode surface, the dressing reduced ion-transport between the sensor electrodes and increased the overall resistivity. Despite this, the baseline modulus error remained comparatively low. For baseline phase (Figure 6.28B), however, the dressing's SWF absorption resulted in large sensor inconsistency, evident via prominent error shading.

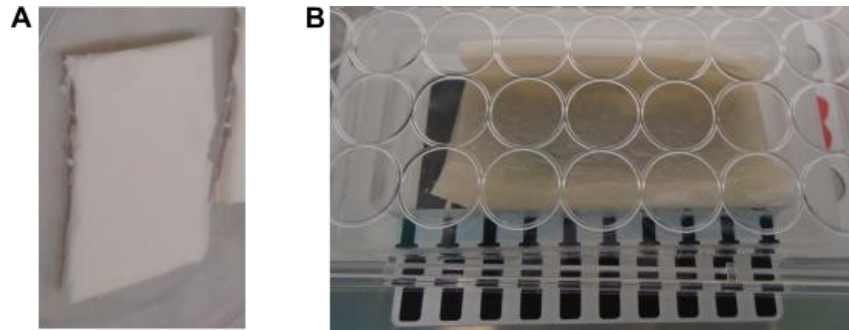


Figure 6.27. Advazorb foam dressing images: (A) a section of dressing cut into small sample for experiment; (B) sample of dressing contained in a WBM.

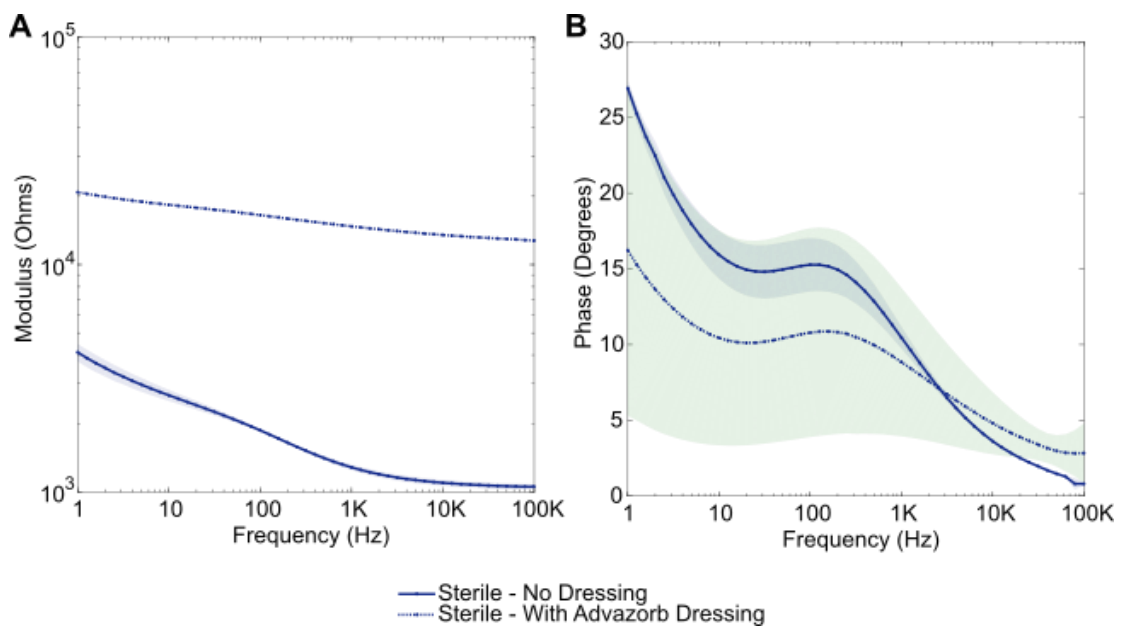


Figure 6.28. The baseline (A) modulus and (B) phase plots observing the initial impact of the Advazorb foam dressing upon the WBM ($n = 3$, error bars depict ± 1 standard deviation).

Ultimately, these large errors and further adsorption of the model's SWF over the course of the experiment resulted in no significant findings emerging for this dressing. Despite an apparently larger normalised modulus increase for the sterile Advazorb dressing model compared to the *S. aureus* Advazorb dressing model, within Figure 6.29A large errors dominated the response. Similarly, in Figure 6.29B some differences are apparent in the normalised phase trends,

however, these are not statistically significant due to the large errors. The adsorption resulted in the model drying to such an extent that colony counting could not accurately be performed at 24 hours. Additional SWF was not added to the model throughout the experiment to maintain consistency between each of the dressing experiments, however this is a potential avenue for future exploration. For comparison, models without the dressing were measured simultaneously and again the characteristic decreases in both normalised modulus and phase were recorded (Figure 6.29). For these basic models, significant impedance changes emerged from 5 hours ($p = 0.002$ for normalised phase at 100 Hz for example).

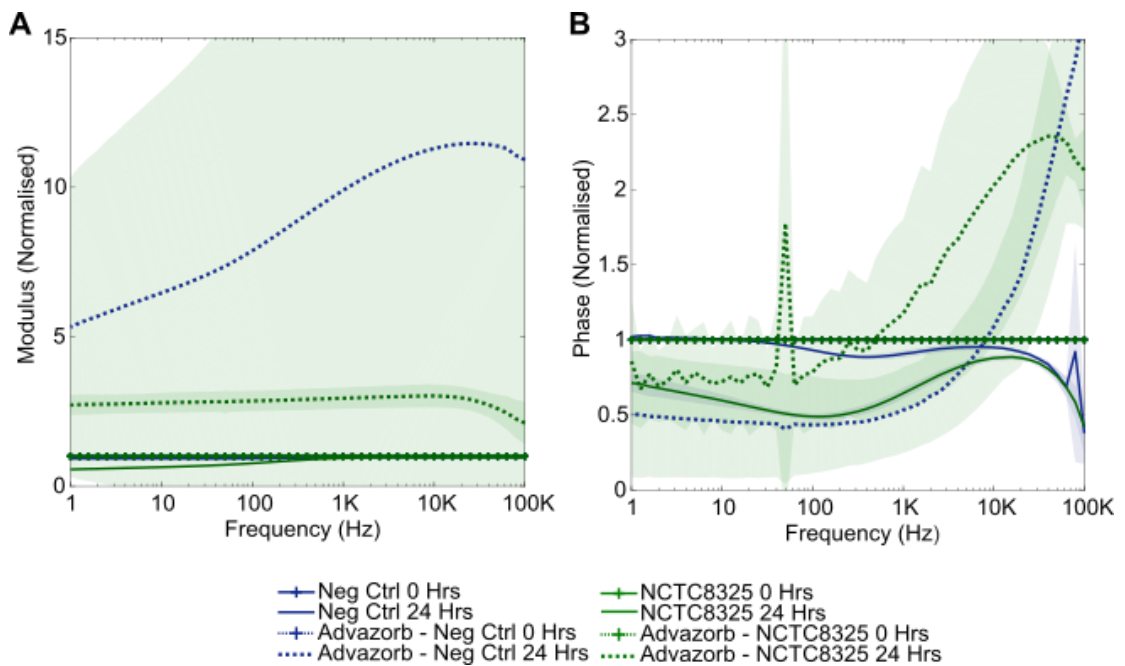


Figure 6.29. Impedance response associated with the growth of *S. aureus* (NCTC8325) in the PCE WBM. Dotted lines are used to represent models where the Advazorb dressing was present, and solid lines where no dressing was present. Plots show: (A) normalised modulus; (B) normalised (absolute) phase ($n = 3$ each, errors depict ± 1 standard deviation). Due to the large errors present, time-based plots are not provided as these were similarly dominated by errors.

6.6.3 N-A[®] Ultra Dressing

The N-A[®] Ultra Dressing by Johnson & Johnson, a silicone knitted wound contact layer, was next studied (Figure 6.30). The introduction of this dressing into the WBM resulted in a slight rise in both the baseline modulus and phase (Figure 6.31), possibly due to sensor coverage, however, values remained of the same order of magnitude. Further, the sensor consistency was slightly decreased by the introduction of the dressing, but in a much smaller way than with the Advazorb dressing for example where large errors were observed. This is due to the non-absorbent nature of this silicone dressing.

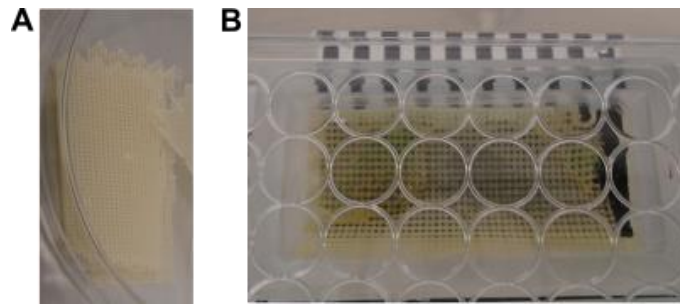


Figure 6.30. N-A Ultra silicone coated knitted dressing images: (A) a section of dressing cut into small sample for experiment; (B) sample of dressing contained in a WBM.

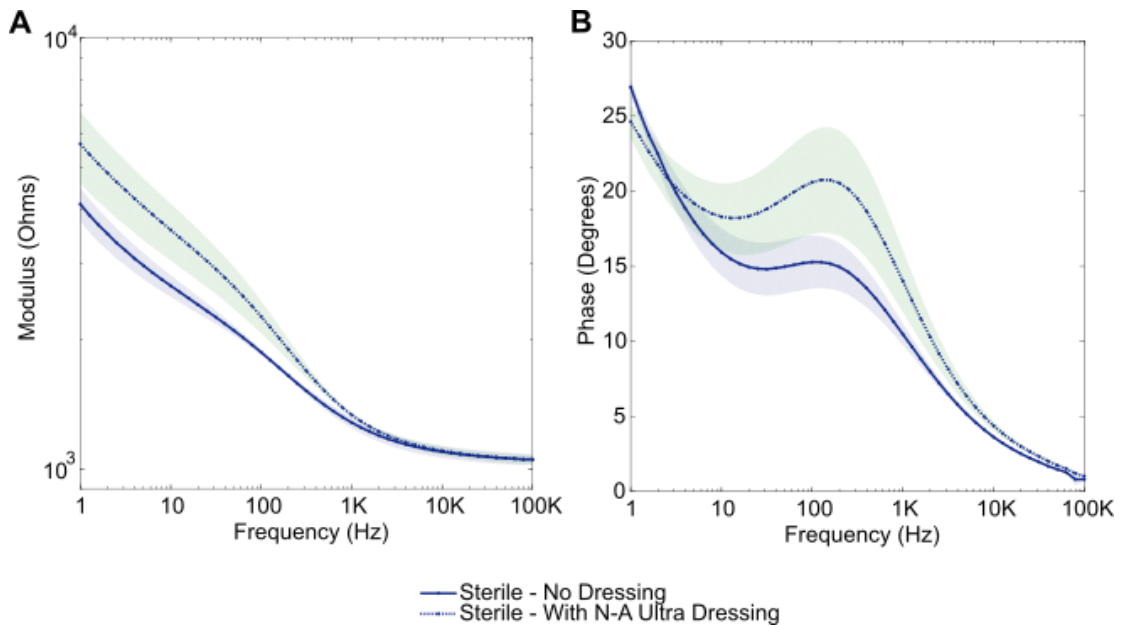


Figure 6.31. The baseline (A) modulus and (B) absolute phase plots observing the initial impact of the N-A Ultra dressing upon the WBM ($n = 3$, error bars depict ± 1 standard deviation).

As might be expected from this silicone dressing (used to prevent tissue adhering to an absorbent dressing used above it), this dressing did not appear to have any impact upon bacterial growth. An increase in *S. aureus* cell density from 2.6×10^7 CFU/mL to 6.9×10^8 CFU/mL for the dressing model occurring over the 24 hours, compared to an increase from 3.9×10^7 CFU/mL to 7.9×10^8 CFU/mL for the non-dressing model. This bacterial growth was reflected in the normalised impedance signatures for both the N-A Ultra dressing model and the control model without the dressing. In normalised modulus (Figure 6.32A) again a decrease below 1 kHz was observed and in normalised phase (Figure 6.32B) trough formation at around 100 Hz occurred. Visualised in the time-based plots provided in Figures 6.32C and 6.32D, these impedance changes due to bacterial growth were statistically significant from 5 hours, with $p = 0.010$ and $p = 0.002$ for the N-A Ultra containing model and its dressing free counterpart respectively (for normalised phase at 100 Hz when compared to their respective

sterile controls). This dressing was, therefore, seen to have minimal impact upon the measured impedance response.

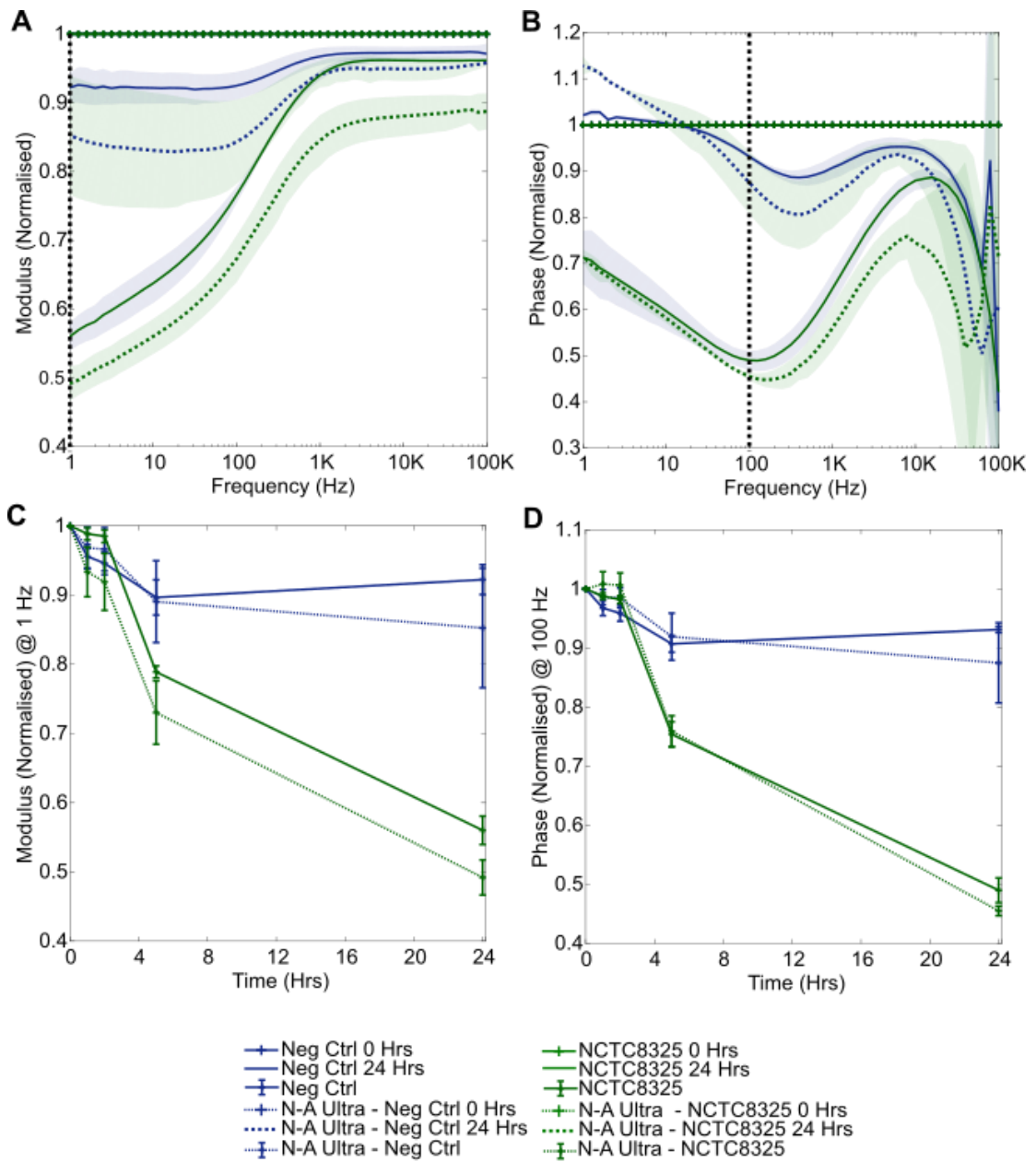


Figure 6.32. Impedance response associated with the growth of *S. aureus* (NCTC8325) in the PCE WBM. Dotted lines are used to represent models where the N-A Ultra dressing was present, and solid lines where no dressing was present. Plots show: (A) normalised modulus; (B) normalised (absolute) phase; (C) 1 Hz normalised modulus over time; (D) 100 Hz normalised phase over time. ($n = 3$ each, errors depict ± 1 standard deviation).

6.6.4 Activon Tulle Dressing

Advancis Medical's Manuka honey impregnated "Activon Tulle" dressing, used to reduce wound bioburden and help prevent infection, was subsequently studied (Figure 6.33). This

dressing resulted in an initial increase in both the baseline impedance modulus and absolute phase (Figure 6.34). In modulus a factor of 5 increase from around $4 \times 10^3 \Omega$ to $2 \times 10^4 \Omega$ at 1 Hz was caused (Figure 6.34A); in absolute phase the increase was most prominent around 10 Hz, moving from 15° to around 38° (Figure 6.34B). These changes are believed to be due to both sensor coverage and the introduction of new ions from the Manuka honey coating. The presence of the dressing did not appear to impact sensor consistency, however, as no change to error shading was evident. Note that for this experiment the dressing-free data was not obtained simultaneously to the dressing data as previously, but nonetheless was obtained using identical experimental conditions.

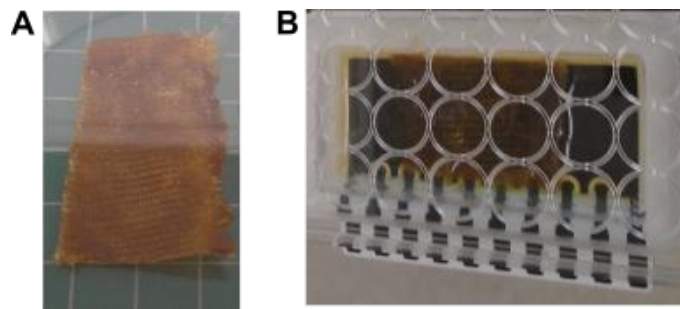


Figure 6.33. Activon Tulle Manuka honey dressing images: (A) a section of dressing cut into small sample for experiment; (B) sample of dressing contained in a WBM.

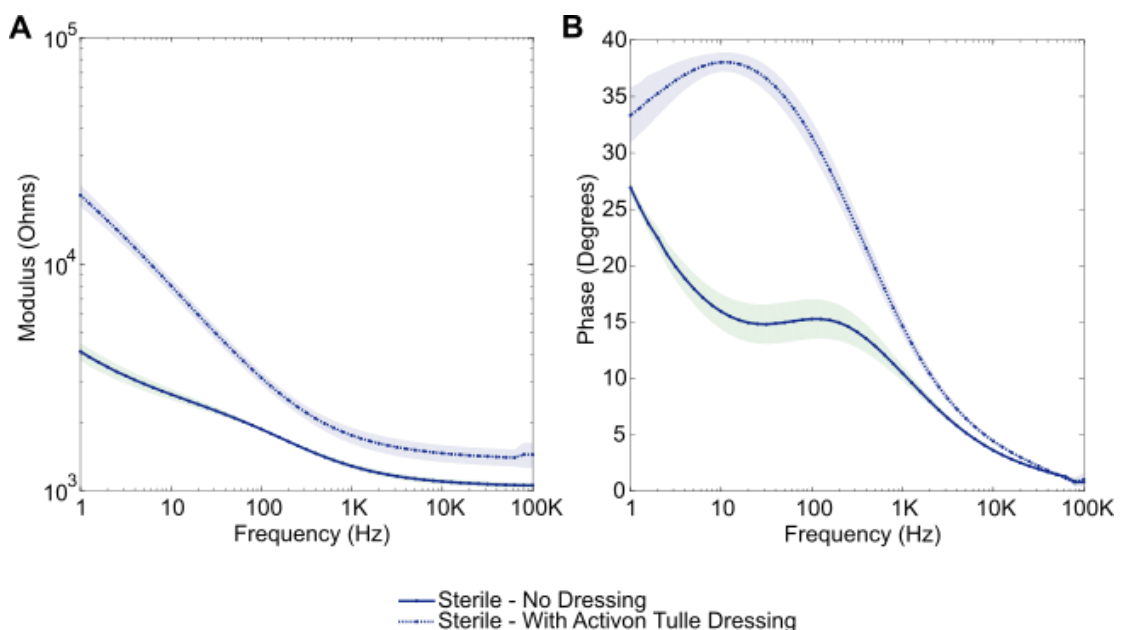


Figure 6.34. The (A) modulus and (B) absolute phase plots assessing the initial impact of the Activon Tulle dressing upon the WBM baseline impedance ($n = 3$, error bars depict ± 1 standard deviation).

This dressing is marketed as having antimicrobial properties and reduces the pH of the wound environment (215). These antimicrobial claims were again verified via colony counting: the initial *S. aureus* concentration was calculated to be 4.3×10^6 CFU/mL, however, after 24 hours <100 CFU/mL remained. In line with this, no clear bacterial impedance signatures emerged over the 24-hour period for the dressing models, in contrast to the dressing-free models (Figures 6.35A, 6.35B). At 1 Hz the normalised modulus changes were of most interest (Figure 6.35C), with a significant difference detected between the bacterial and sterile dressing models at 5 hours alone ($p = 0.032$). This is perhaps indicative of an intermediate stage where some detectable bacterial processes occurred before subsequent cell death. For normalised phase at 100 Hz, the characteristic trough did not emerge for the bacterial chamber containing the Activon Tulle dressing. Instead, the response closely followed that of the sterile dressing model with no significant differences detected ($p > 0.05$). These results, therefore, again indicate that the bactericidal action of the dressing is evident through normalised impedance signature analysis.

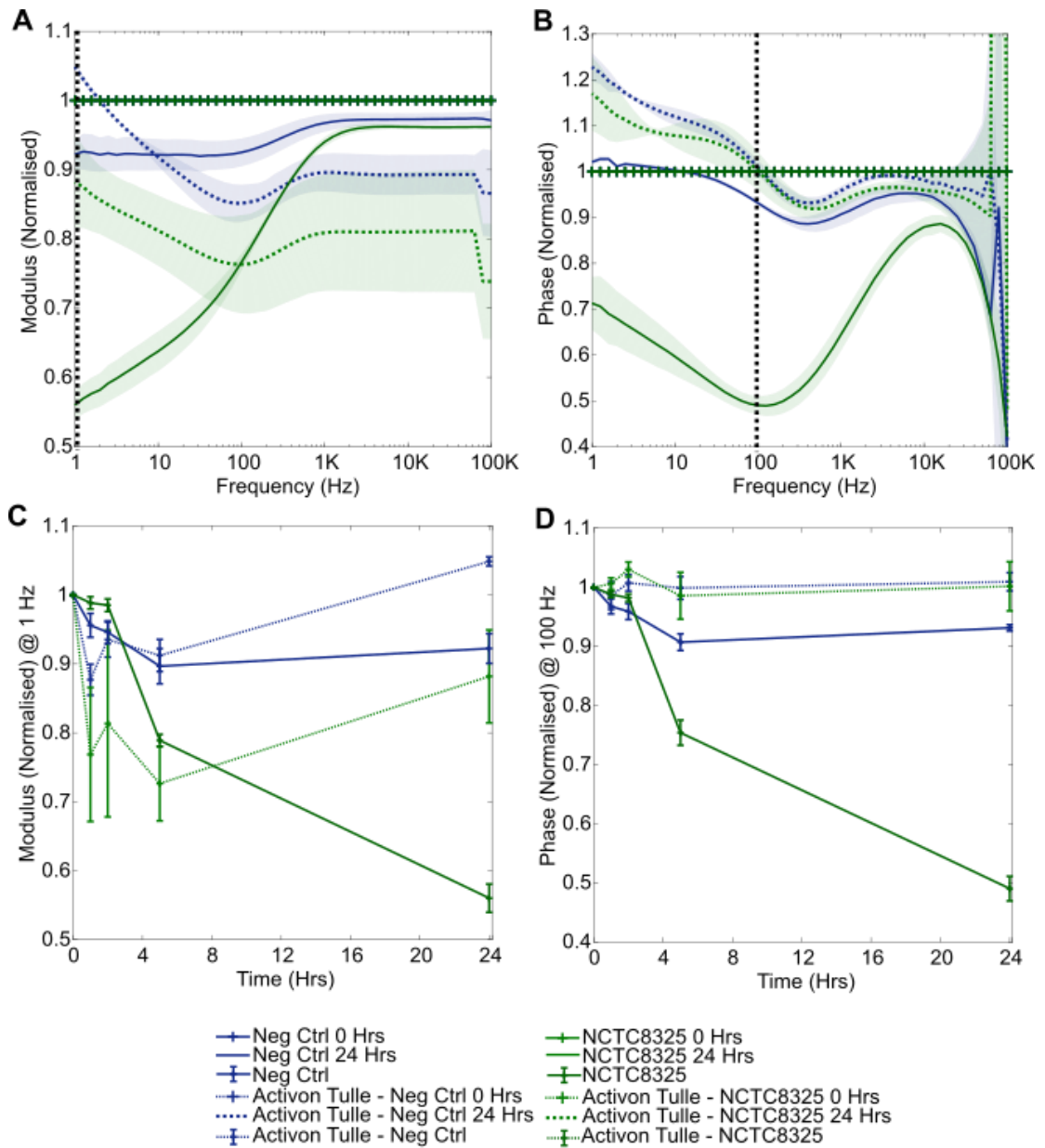


Figure 6.35. Impedance response associated with the growth of *S. aureus* (NCTC8325) in the PCE WBM. Dotted lines are used to represent models where the Activon Tulle dressing was present, and solid lines where no dressing was present. Plots show: (A) normalised modulus; (B) normalised (absolute) phase; (C) 1 Hz normalised modulus over time; (D) 100 Hz normalised phase over time. ($n = 3$ each, errors depict ± 1 standard deviation).

6.6.5 Mepitel® Dressing

Finally, the Mepitel wound contact layer by Mölnlycke was investigated. This soft silicone dressing, with similar properties and applications to the N-A Ultra dressing, is shown in Figure 6.36. In a similar manner to many of the previous dressings Mepitel caused an increase in baseline impedance (Figure 6.37), again believed to be a result of electrode coverage. This

increase was from around 4000 Ω to 9000 Ω in modulus at 1 Hz, and from around 15 $^\circ$ to 27 $^\circ$ for absolute phase at 10 Hz. Slightly larger baseline errors can also be seen for the dressing model's phase in particular. It must again be taken into consideration the fact that the dressing-free model results were not obtained simultaneously to the Mepitel results, however, a comparison may still be made as identical experimental procedures were adopted.

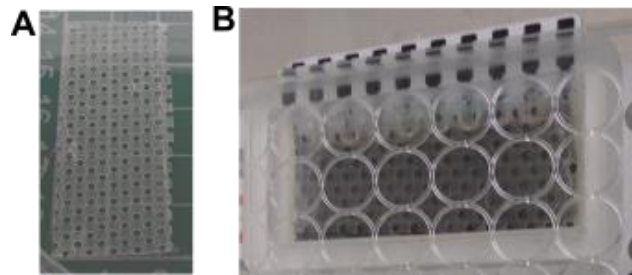


Figure 6.36. Mepitel soft silicone dressing images: (A) a section of dressing cut into small sample for experiment; (B) sample of dressing contained in a WBM.

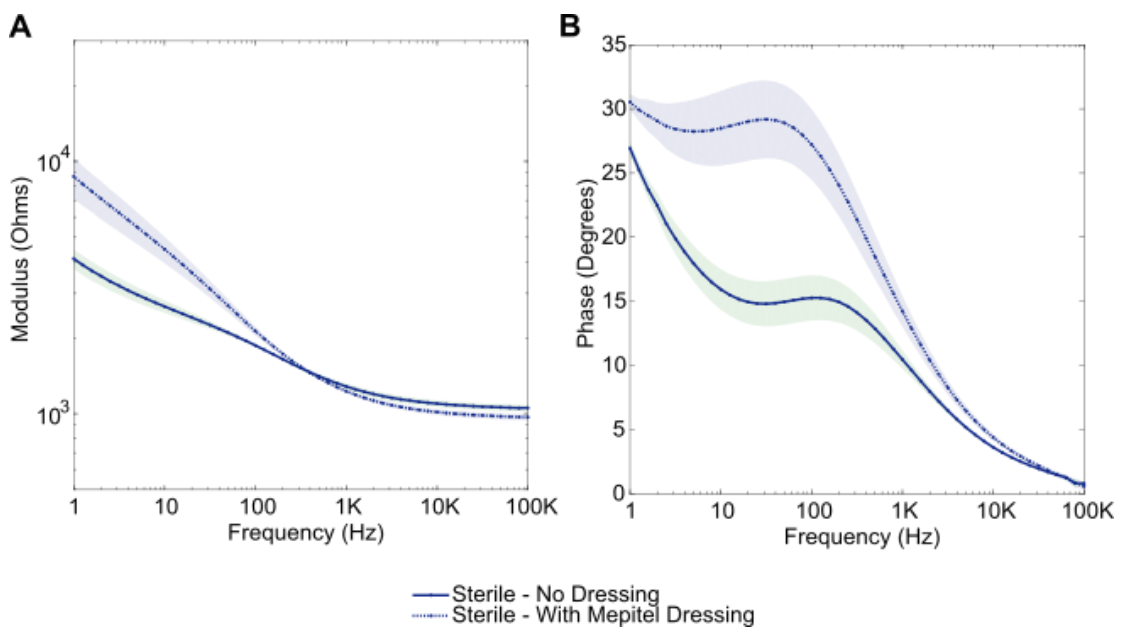


Figure 6.37. The (A) modulus and (B) phase plots assessing the initial impact of the Mepitel dressing upon the WBM baseline impedance ($n = 3$, error bars depict ± 1 standard deviation).

As expected from this inert silicone material, the Mepitel dressing did not appear to influence the bacterial growth rate: an increase from 3.7×10^6 CFU/mL to 1.6×10^8 CFU/mL occurred over 24 hours. This is comparable to a simultaneous negative control growth from 3.2×10^6 CFU/mL to 1.5×10^8 CFU/mL. Further, the expected normalised impedance signatures previously attributed to *S. aureus* growth were observed (Figure 6.38). Specifically, a reduction

in normalised modulus below 1 kHz (Figure 6.38A) and a negative phase trough at 100 Hz (Figure 6.38B) were observed. Focussing upon the changes at key frequencies over time (Figures 6.38C, 6.38D), statistical significance was found for the Mepitel containing *S. aureus* WBM from 5 hours of growth ($p = 0.023$, normalised phase at 100 Hz). This is comparable to the dressing free models, also demonstrating significant changes from 5 hours ($p = 0.002$, normalised phase at 100 Hz).

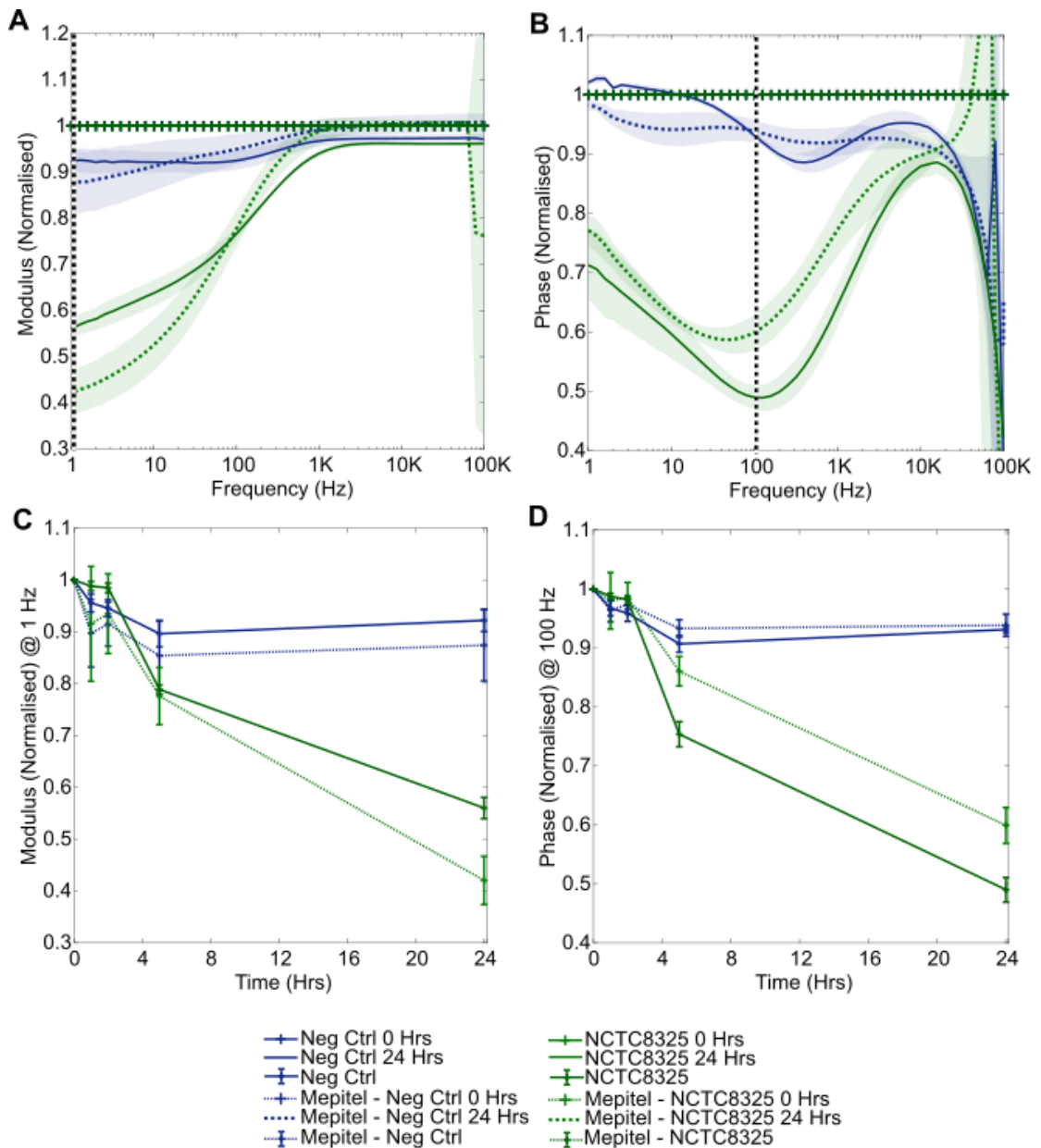


Figure 6.38. Impedance response associated with the growth of *S. aureus* (NCTC8325) in the PCE WBM. Dotted lines are used to represent models where the Mepitel dressing was present, and solid lines where no dressing was present. Plots show: (A) normalised modulus; (B) normalised (absolute) phase; (C) 1 Hz normalised modulus over time; (D) 100 Hz normalised phase over time. ($n = 3$ each, errors depict ± 1 standard deviation).

6.7 The Influence of Direct Cell/Electrode Processes Upon the Measured PCE Impedance Signature

Experiments were next conducted in 0.9% w/v NaCl solution, aiming to assess the extent to which the bacterial cells influence impedance in the absence of growth.

6.7.1 Effects of Washed Cells in Saline Over Time

Washed *S. aureus* and *P. aeruginosa* cells were obtained at cell densities of 7.9×10^7 CFU/mL (range $5.1 \times 10^6 - 1.2 \times 10^8$ CFU/mL) and 5.9×10^7 CFU/mL (range $(4.2 - 7.1) \times 10^7$ CFU/mL) respectively. Via further colony counting after 24 hours of continuous incubation, a lack of growth for both species was confirmed: the *S. aureus* concentration decreased to 1.9×10^4 CFU/mL (range $(1.6-2.4) \times 10^4$ CFU/mL); the *P. aeruginosa* concentration remained of the same order of magnitude at 2.6×10^7 CFU/mL (range $(2.3 - 2.9) \times 10^7$ CFU/mL). The immediate effect of introducing these cells into the electrode wells is evident in Figure 6.39. The sterile controls measured a decrease in normalised modulus upon measurement of fresh saline, in contrast to both the *S. aureus* and *P. aeruginosa* cell measurements when compared to initial measurements of sterile saline solution (Figure 6.39A). For normalised (absolute phase) a reduction also occurred for the controls, compared to a slight increase around 500 Hz for the bacterial sensors (Figure 6.39B). Upon the introduction of the bacteria, significant differences between both *S. aureus* and *P. aeruginosa* and the negative controls were evident immediately, with $p = 0.034$ and $p = 0.041$ respectively (normalised modulus at 1 Hz). The cell concentration dependence of these immediate impedance changes is explored further in Section 6.7.2.

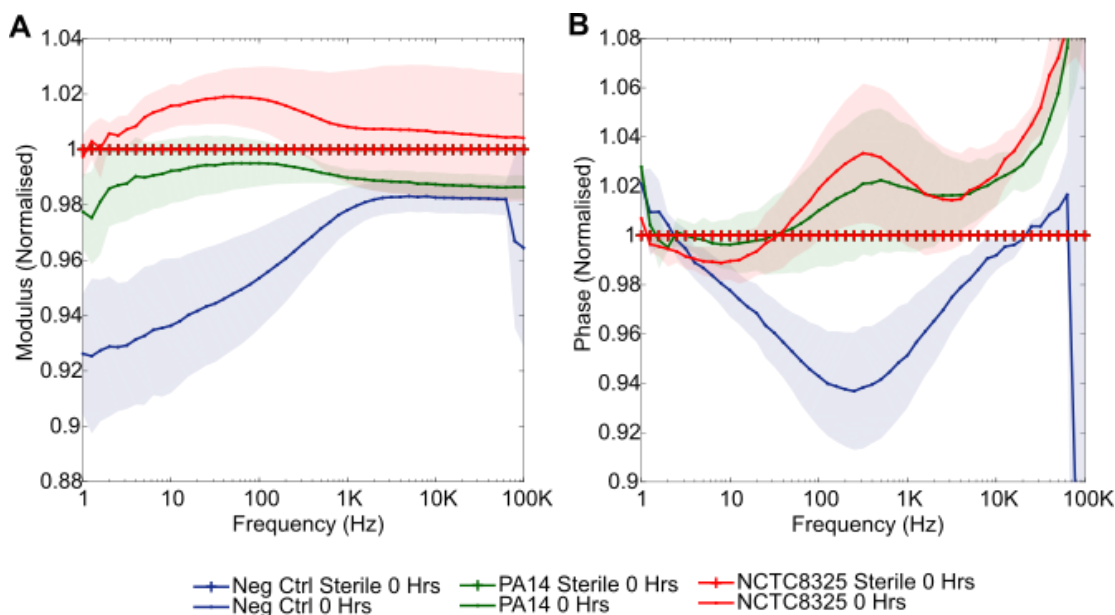


Figure 6.39. Impedance response associated with the introduction of washed *S. aureus* and *P. aeruginosa* cells into 0.9% w/v NaCl. Normalisation was performed against a sterile initial measurement (“Sterile 0 Hrs”), with plots showing: (A) normalised modulus; (B) normalised (absolute) phase ($n = 3$ each, errors depict ± 1 standard deviation).

Beyond this initial response, these washed cells were left on the sensors for 24 hours and the subsequent normalised impedance response obtained. For the results in Figure 6.40, normalisation was carried out against the non-sterile starting point (“0 Hrs”) to allow for a fair comparison with the previous PCE growth experiments. The washed bacterial cells resulted in an increase in normalised modulus at frequencies below around 1 kHz for both bacteria (Figure 6.40A). Further, both bacteria caused normalised (absolute) phase peak formation (Figure 6.40B). This increase in absolute phase corresponded to increasingly negative phase values, indicating that the response was becoming more capacitive. The initial modulus and phase decreases for the controls are shown to quickly plateau over the course of the experiment, with bacterial changes instead growing steadily over time (Figures 6.40C, 6.40D). Due to the lack of bacterial growth throughout this experiment, these changes are believed to arise from cell settlement on and adsorption to the sensors over time. The significance of this result upon our understanding of the bacterial growth signatures is discussed within Chapter 7.

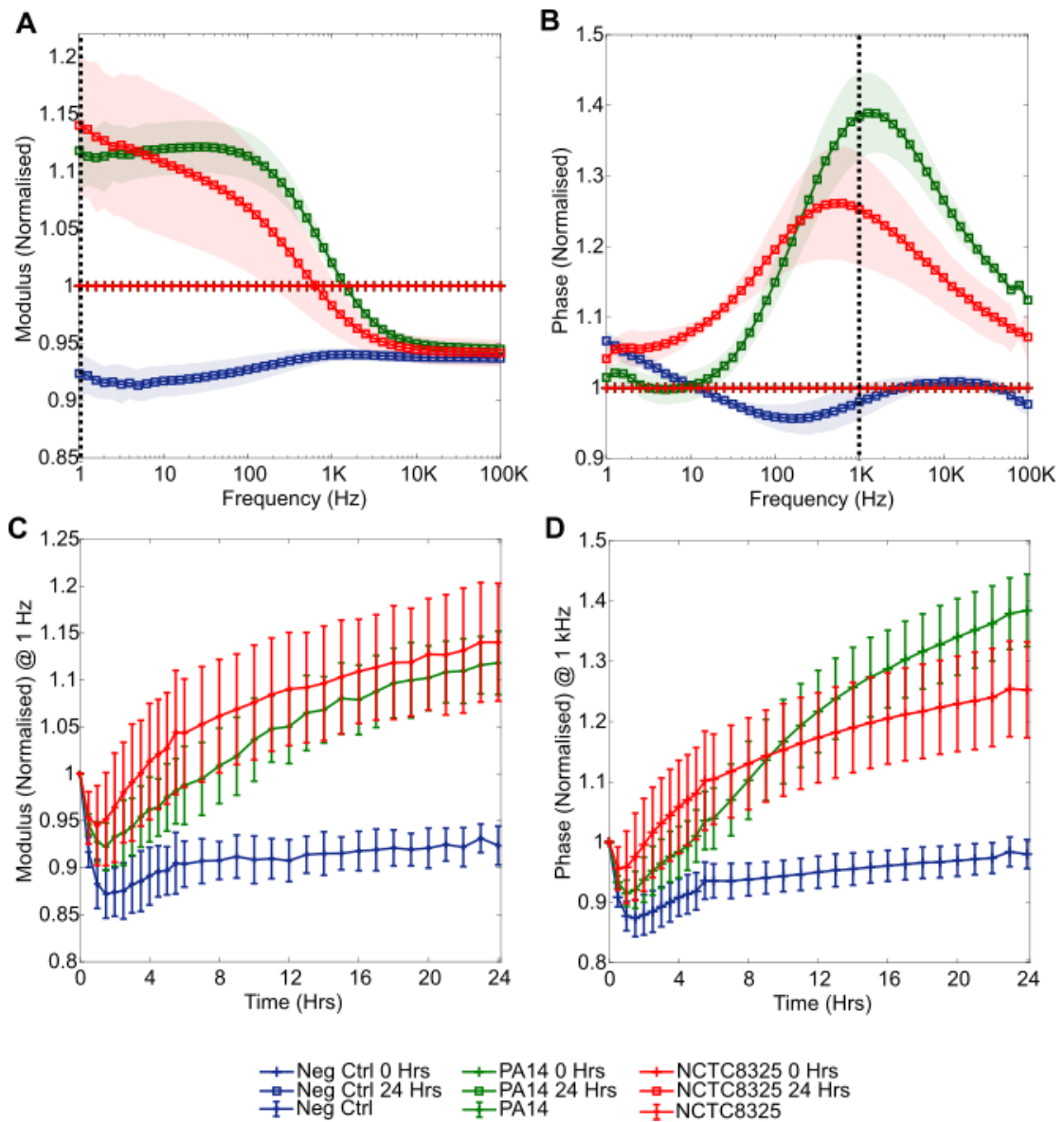


Figure 6.40. Impedance response associated with measurements of *S. aureus* (NCTC8325) and *P. aeruginosa* (PA14) in 0.9% v/w NaCl over 24 hours. Plots show: (A) normalised modulus; (B) normalised (absolute) phase; (C) 1 Hz normalised modulus over time; (D) 1 kHz normalised phase over time ($n = 3$, errors depict ± 1 standard deviation).

Although the impedance changes detected here due to cell settlement on and attachment to the sensors are of a smaller magnitude than those observed during the growth experiments, the changes observed in the mid-frequency phase region are of particular interest. Recall that during the PCE dWBM experiments (Section 6.5.2) peak formation in this region was similarly observed, in particular for *S. aureus*. This feature of the dWBM signature may therefore be linked to cellular attachment to the electrodes. Further, the visible differences in impedance signatures between the species here after 24 hours may be a result of their different concentrations or structural differences. This variance may also be due to differences in the

motilities of these two species. These contributions may similarly be influential in the dWBM signature differences that were observed (Section 6.5.2). Discussed in detail within Chapter 7, this saline result further highlights the importance of the mid-frequency normalised phase region for species signature differentiation.

6.7.2 *S. aureus* Cell Concentration Dependent Effects

The immediate effects of placing an increasing concentration of *S. aureus* cells upon the sensors were next explored, replicating the experiment performed with the simple carbon sensors in Section 5.5.2. Following an initial measurement of sterile 0.9% w/v NaCl which provided a sterile normalisation point, sweeps of washed cells at incrementally increasing concentrations from a multiplication factor (MF) of 1 (representing an average of 3.3×10^6 CFU/mL) to a MF of 64 (representing 2.1×10^8 CFU/mL) were performed. The results of colony counting performed on the MF 1 and MF 64 solutions were averaged to obtain these results. As introduced in Chapter 1 and discussed in Section 7, the CFU/mL concentration of bacteria present in a wound infection is not well defined. With estimates suggesting an infection is present for bacterial loads greater than 10^5 - 10^6 CFU/mL, the concentrations used in this experiment are believed to be conceivable for established wound infections (7).

Both the normalised modulus (Figure 6.41A) and normalised phase (Figure 6.41B) increases that emerged due to the settlement of washed cells over time in Section 6.7.1 were again observed here. Further, the magnitude of these features appeared to be dependent upon the concentration of washed cells (Figures 6.41C, 6.41D). The lowest concentration of cells resulting in immediate significant changes was MF 4 (1.3×10^7 CFU/mL), seen via normalised phase at 1 kHz ($p = 0.005$). In the previous section, immediate significant impedance effects were observed for washed *S. aureus* cells at a concentration of 7.9×10^7 CFU/mL, as would be expected from the findings of this experiment. Despite these changes appearing to be proportional to the cell concentration, caution must be exercised as gradual cell adsorption to the sensors over time was also occurring (as observed in Section 6.7.1). This was evident through the sustained impedance response when performing a final measurement of sterile saline solution and, therefore, this is likely to have resulted in higher concentrations of cells than intended during the EIS measurements.

Furthermore, the changes to normalised impedance observed due to washed cells were different to those observed during bacterial growth. As will be discussed in Chapter 7, these saline experiments again verify that the contribution of the cells themselves to the impedance

signatures during growth is minimal (as was also the case with the simple carbon sensors (Section 5.5)). Cell growth and biofilm formation are, therefore, the important mechanisms being detected in normal growth conditions with this technique.

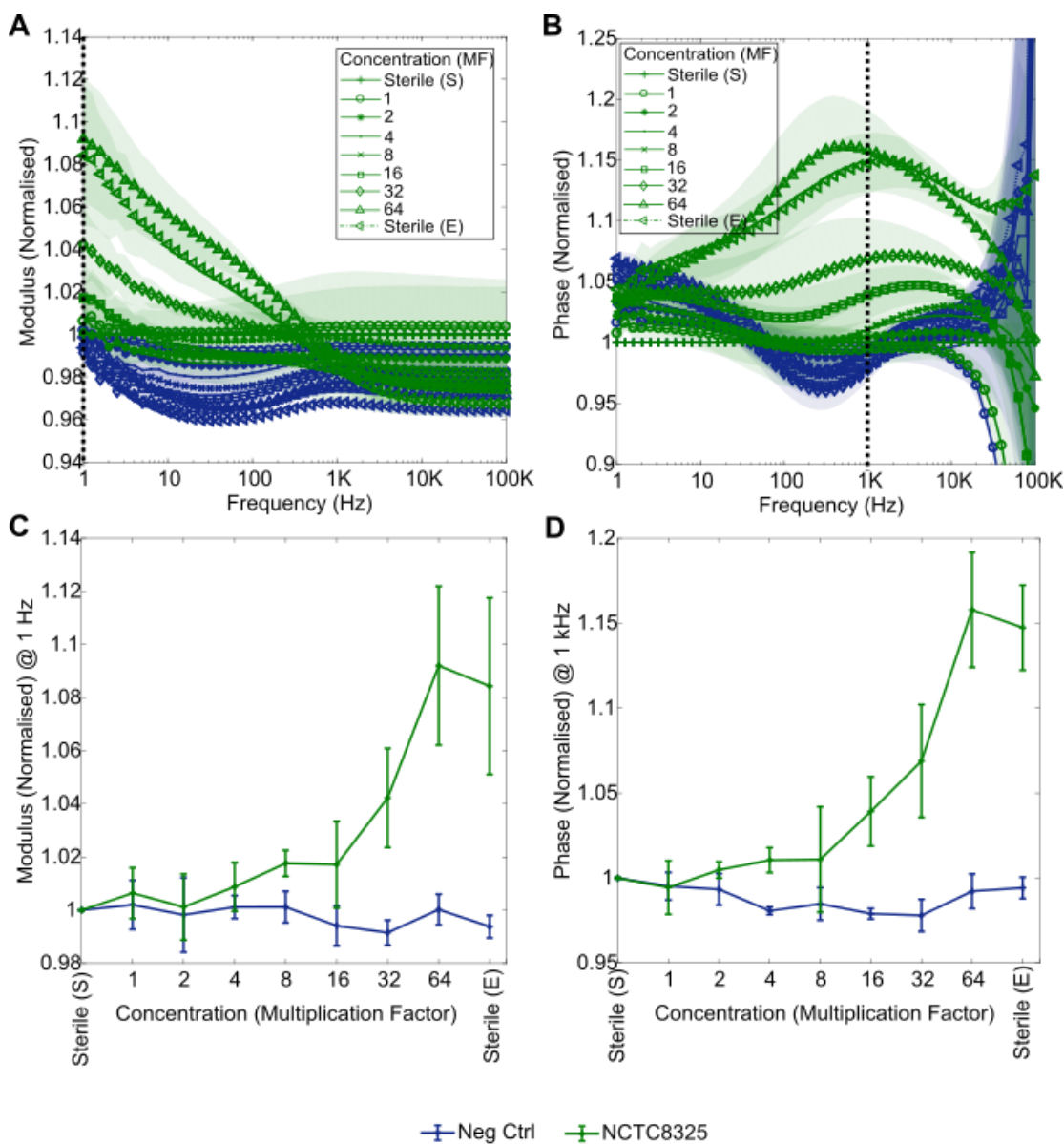


Figure 6.41. Measurements of *S. aureus* (NCTC8325) at increasing concentrations (denoted as multiplication factors, MF) in 0.9% w/v NaCl: (A) an increase in normalised modulus is visible in the chambers containing NCTC8325, which appears to be concentration dependent. Replacement of the 0.9% NaCl at the end of the experiment with a sterile aliquot “(sterile (E))” causes only a slight reduction in the magnitude of this feature; (B) normalised (absolute) phase shows the emergence of a mid-frequency peak, similarly increasing in magnitude in line with an increasing cell concentration; (C) normalised modulus data at 1 Hz and (D) normalised phase data at 1 kHz showing these increases as functions of concentration (error bars represent ± 1 standard deviation, $n = 3$ negative controls and $n = 4$ NCTC8325).

6.8 Exploration of the Mechanisms Underpinning the Bacterial Impedance Signatures via Equivalent Circuit Modelling

In Chapter 5, a decrease in charge transfer resistance was linked to bacterial growth in nutrient rich media. Unlike the basic carbon sensors, for these PCE sensors the equivalent circuit adopted included a Warburg diffusion element because a low frequency tail characteristic of diffusion behaviour was present in the data (as described in Section 3.7.8). This circuit was consistent with the standard Randle's circuit (231), containing elements representing the solution resistance (R_s), charge transfer resistance (R_{ct}), double layer capacitance (C_{dl}) and finite space (open) Warburg diffusion element W_o (Figure 3.30). A Warburg element representing a finite diffusion layer was selected as the EIS response did not display a constant 45° phase angle at low frequencies (as would be expected from semi-infinite diffusion, refer to Chapter 2). Instead, the curve shifted towards a more capacitive response at lower frequencies, as is the case in thin layer electrochemistry where small volumes of electrolytes are typically used (263–265). In this study, only 2 mL of media was spread over an approximate surface area of 10 cm^2 , therefore the low volume thin layer approximation was considered appropriate. Further, considering the characteristic finite space Warburg behaviour described in Section 2.3.10, the reflective finite space Warburg element (W_o) was believed to be the most suitable variation to include in this equivalent circuit model. In line with the carbon electrode circuit modelling in Chapter 5, impedance data obtained in both LB medium and 0.9 % w/v NaCl was modelled to provide the greatest contrast.

6.8.1 Modelling the LB Medium Data

Firstly, circuit fitting was performed with the results obtained during the LB medium growth experiments (Section 6.2). In Figure 6.42, the average percentage change for each circuit component occurring after 24 hours of *S. aureus* growth is shown. For both charge transfer resistance (R_{ct}) and the impedance coefficient of the Warburg diffusion element (W_o -R) a significant reduction occurred during growth, compared to a smaller negative control decrease ($p = 0.001$ and $p < 0.001$ respectively, $n = 4$). Average circuit values for each of these components are provided in Appendix A.

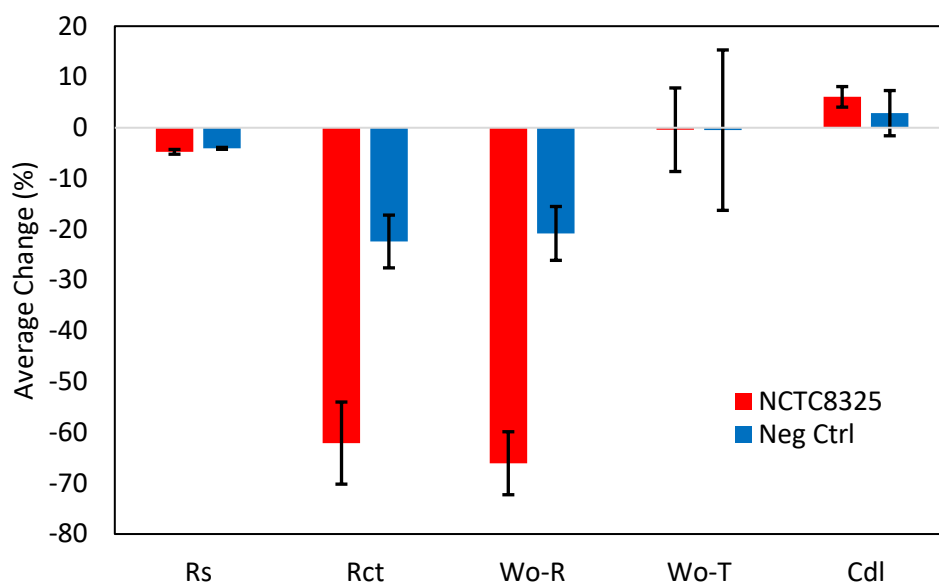


Figure 6.42. Circuit fitting results for *S. aureus* (NCTC8325) growth in LB medium over 24 hours. EIS signatures were obtained using the PCE sensors and modelled using a Randle's circuit, with the percentage changes in the value of each element calculated and plotted ($n = 4$, error bars represent ± 1 standard deviation).

In the same manner, significant reductions also occurred for *P. aeruginosa* during growth in LB medium (Figure 6.43), with $p = 0.001$ for R_{ct} and $p < 0.001$ for Wo-R ($n = 4$). Previously with the carbon sensors a reduction in charge transfer resistance was also linked to bacterial growth (Section 5.6), with the increased number of replicating bacterial cells present facilitating greater charge transfer across the interface. Emerging as a consistent indicator of bacterial growth on carbon-based sensors, these changes will be further discussed within Chapter 7.

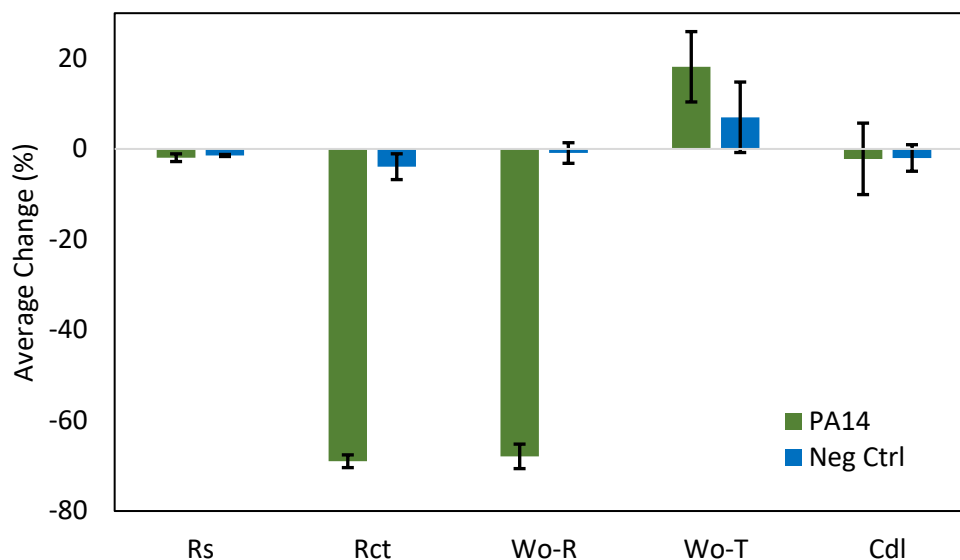


Figure 6.43. Circuit fitting results for *P. aeruginosa* (PA14) growth in LB medium over 24 hours. EIS signatures were obtained using the PCE sensors and modelled using a Randle's circuit, with the percentage changes in the value of each element calculated and plotted ($n = 4$, error bars represent ± 1 standard deviation).

6.8.2 Modelling the 0.9% w/v NaCl Data

The saline experiment data (where washed *S. aureus* and *P. aeruginosa* cells were placed onto the electrodes over an extended time (Section 6.7.1)) was next modelled using the PCE equivalent circuit. Notably, the decreases in R_{ct} and W_o-R which were detected for the bacterial cultures in growth media were not detected here, where growth was inhibited (Figure 6.44). Instead, for R_{ct} a significant increase occurred for both species when compared to the negative control ($p = 0.032$ for *S. aureus* and $p = 0.019$ for *P. aeruginosa*). In conjunction with Section 6.7.1, this result suggests that bacterial cell settlement and adsorption to the sensor surface over time resulted in an increase in charge transfer resistance. In LB medium, this increase in R_{ct} is believed to have been concealed by a dominating reduction in R_{ct} caused by bacterial cell growth and metabolism. Circuit element values are provided in Appendix A.

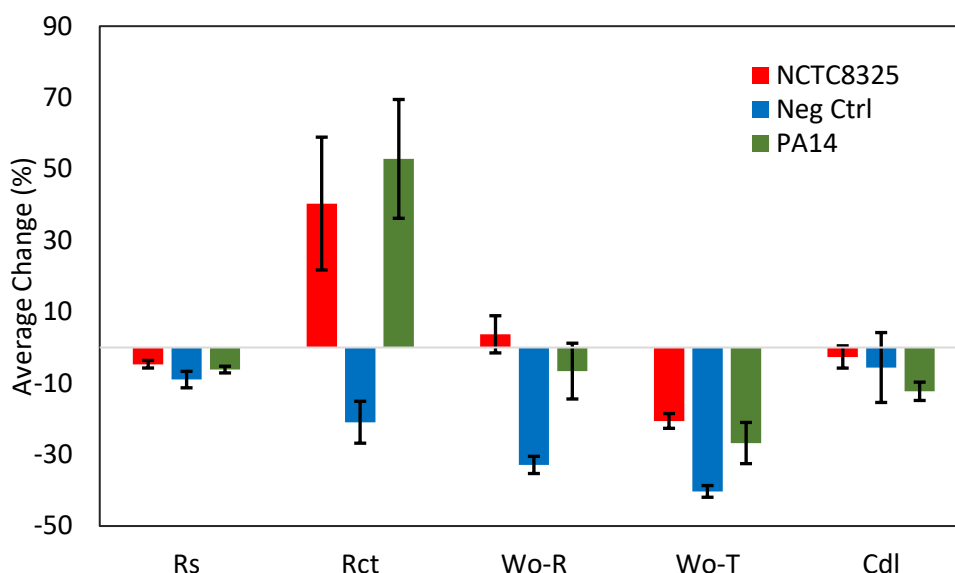


Figure 6.44. Circuit fitting results for washed *S. aureus* (NCTC8325) and *P. aeruginosa* (PA14) cell settlement in 0.9% w/v NaCl over 24 hours. EIS signatures were obtained using the PCE sensors and modelled using a Randle's circuit, with the percentage changes in the value of each element calculated and plotted ($n = 4$, error bars represent ± 1 standard deviation).

6.9 Bacterial Concentration Estimation via Rate of Normalised Impedance Change

Throughout this chapter so far, it has become apparent that these platinised carbon electrodes allow for the rapid detection of bacteria through significant changes to normalised impedance. It has been shown that the magnitude of these normalised impedance shifts increases over time to a sustained maximum during bacterial growth. It has also been found that the immediate magnitude of impedance changes due to washed cells on the sensors is cell concentration dependent. This has, therefore, suggested that the time to detect significant impedance changes has been dependent upon concentration. Aiming to explore if this dependence could be exploited to extrapolate bacterial cell density from early changes to normalised impedance and address the final project objective (Section 1.8), EIS measurements of bacterial suspensions were carried out at different concentrations in LB medium.

A representative wound pathogen with much previous data obtained in both LB medium and a range of other growth conditions, *S. aureus* was selected for these experiments. In the same manner as previously, NCTC8325 growth in LB medium over 24 hours was measured using EIS. The inoculation volumes were adjusted to obtain initial concentrations of approximately 10^6 CFU/mL, 10^7 CFU/mL, and 10^8 CFU/mL ($n = 4$ each). This is in line with the cell densities used in the previous saline experiments (Section 6.7.2), each above the approximate base threshold for wound infection of around 10^5 - 10^6 CFU/mL (Section 1.3). These concentrations were verified via colony counting, with an average stock culture concentration of 1.3×10^8

CFU/mL (range $(1.1- 1.4) \times 10^8$ CFU/mL). The resulting impedance data, normalised against the initial (post-inoculation) measurement, is presented in Figure 6.45. The expected characteristic changes to normalised modulus (Figure 6.45A) and normalised phase (Figure 6.45B) were, once more, observed. After 24 hours, for each key feature the changes were most pronounced for the 10^6 CFU/mL concentration, followed by 10^7 CFU/mL and finally a slightly lower change for 10^8 CFU/mL. Whilst no statistically significant differences between the concentrations were identified, this ordering is believed to reflect the nutrient availability and therefore volume of growth in each culture. Whereas the 10^8 CFU/mL culture was obtained from undiluted overnight stock culture and its nutrient stock depleted, the 10^6 CFU/mL culture consisted of 99% fresh, nutrient rich LB medium and was more supportive of an exponential growth phase. Evidencing this theory, colony counting performed after 24 hours of incubation found that the 10^6 CFU/mL sensors had the largest average increase in cell density (4.6×10^8 CFU/mL at 24 hours) and the 10^8 CFU/mL sensors the smallest increase (7.8×10^8 CFU/mL). Despite this minimal cell density increase for the 10^8 CFU/mL sensors, the emergence of the EIS growth signature verified that this technique could be appropriately applied to the detection of infection in wounds at various stages of infection development.

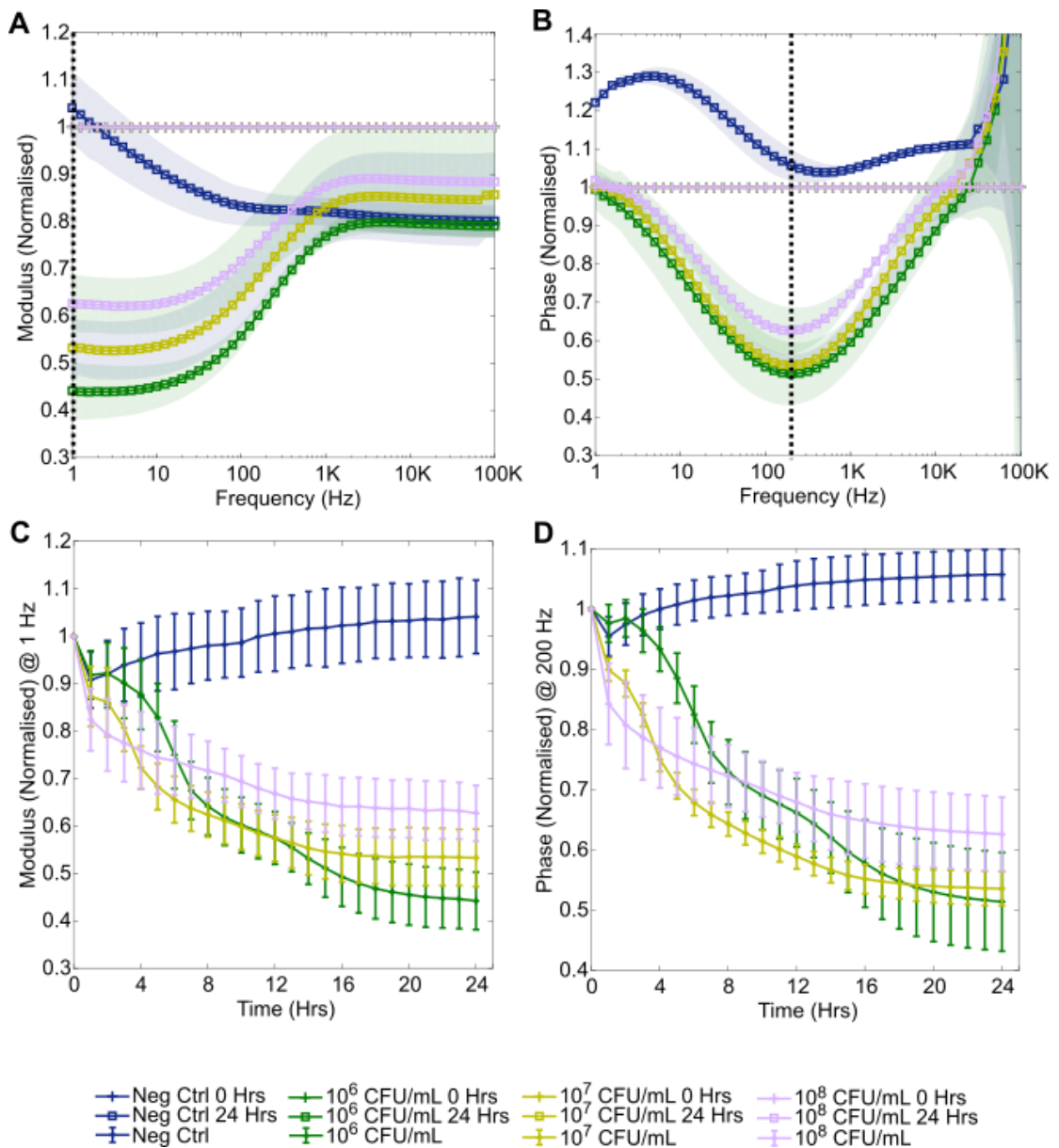


Figure 6.45. Normalised impedance response associated with the growth of different concentrations of *S. aureus* (NCTC8325) in LB medium. Normalisation was performed against a non-sterile starting point. Plots show: (A) normalised modulus; (B) normalised (absolute) phase; (C) normalised modulus time-based plot at 1 Hz; (D) normalised phase time-based plot at 200 Hz ($n = 4$, errors depict ± 1 standard deviation).

By focusing on the earliest normalised impedance changes, it was uncovered that the initial rate of normalised impedance change appeared to have a positive correlation to bacterial cell density (Figures 6.45C, 6.45D). The sensors measuring the highest concentration of cells had the most rapid initial change in normalised impedance; the lowest concentration of cells resulted in the slowest initial change (visualised via time-based plot gradients). This potential distinction between different cell densities occurred in the initial measurement period up to around 4 hours and, therefore, could be a useful parameter in a rapid diagnostic device.

Furthermore, this is in line with the previous finding that larger concentrations could be more rapidly detected. Consequently, a MATLAB script was created to calculate the average instantaneous rate of change for a given normalised impedance feature and cell density at each measurement time. Using the impedance data from the key features selected in Figure 6.45, namely normalised modulus at 1 Hz and normalised phase at 200 Hz, Figure 6.46 was created. Notably, these plots clearly present the fact that the rates of change were largest within the first 500 minutes of measurement.

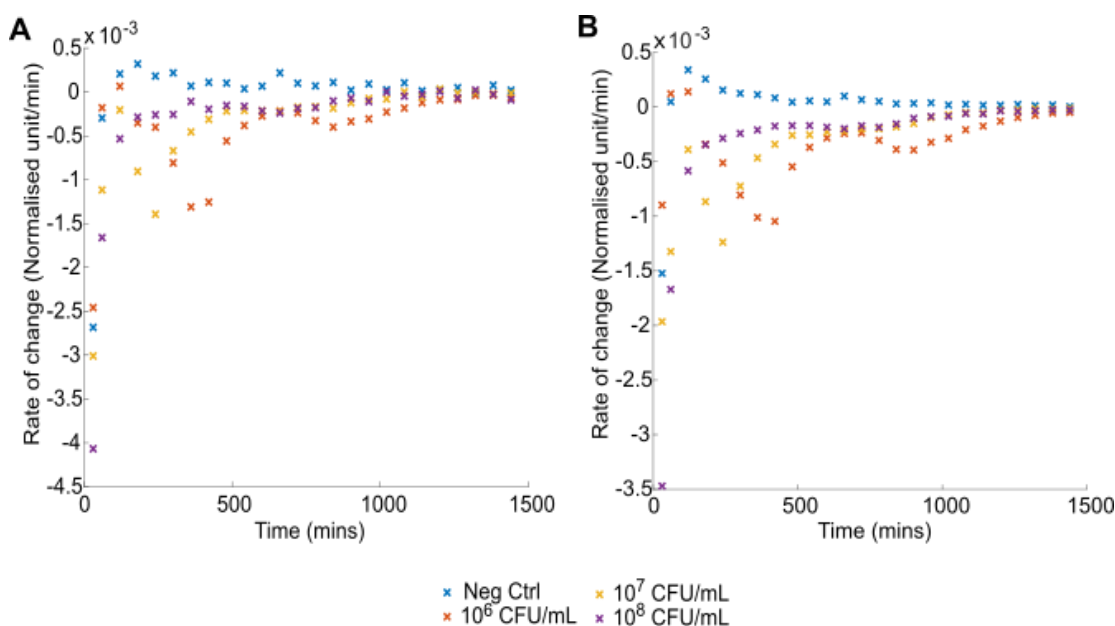


Figure 6.46. Mean rate of change as a function of time for (A) normalised modulus at 1 Hz and (B) normalised (absolute) phase at 200Hz. Data was obtained from the growth of different concentrations of *S. aureus* (NCTC8325) in LB medium over 24 hours ($n=4$).

Using the data presented in these plots, it was first hypothesised that the maximum rate of change for each cell density could produce a curve enabling the determination of unknown cell densities in future. Further, in a bid to make the method more practical for a rapid *in situ* device, the rate of change values after 1 hour of incubation were similarly plotted as a function of concentration. These plots are presented in Figure 6.47 and, for both normalised modulus at 1 Hz and normalised (absolute) phase at 200 Hz, linear relationships between the rates of change (absolute value) and the logarithm of bacterial concentration were found. This, therefore, appears promising as a method of concentration estimation for an unknown sample. The non-zero rate of change values associated with the sterile negative controls must also be considered, however. These indicate that rates of change of a similar magnitude to the negative controls or below cannot be reliably attributed to a bacterial concentration. Furthermore, using 1-hour rate

of change data for normalised phase at 200 Hz (Figure 6.47D) may be most suitable as the negative control rate of change lies below the calibration curve in this instance. Returning to the 200 Hz normalised phase values themselves presented in Figure 6.45D, the values at 1 hour themselves are not separated from the sterile control in the same manner. This highlights the potential superiority of this ROC method.

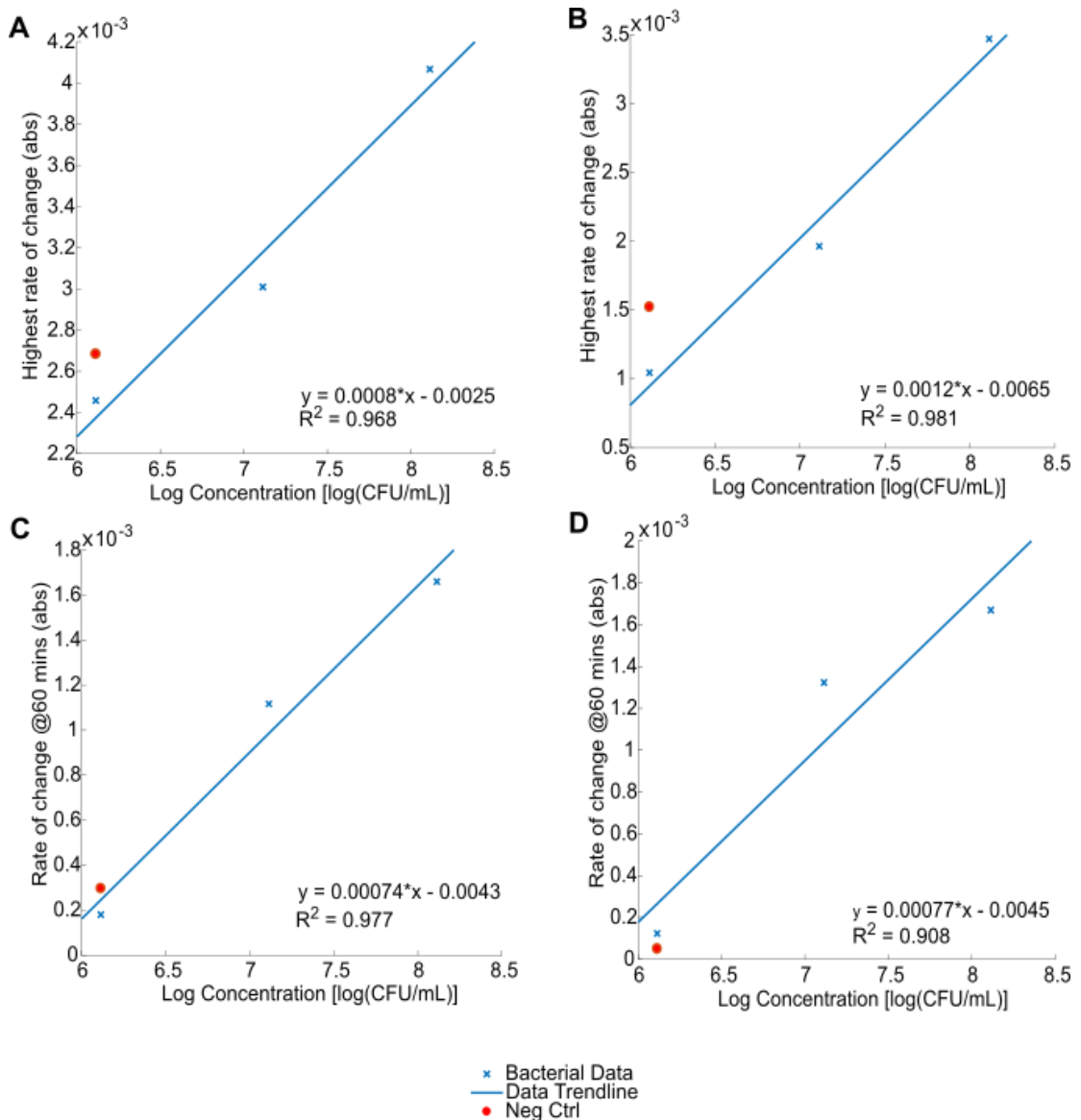


Figure 6.47. Calibration curves obtained for absolute rate of change as a function of concentration, where: (A) plots the highest rate of change of normalised modulus at 1 Hz for each concentration; (B) plots the highest rate of change of normalised (absolute) phase at 200 Hz for each concentration; (C) plots the rates of change at 1 hour for normalised modulus at 1 Hz; (D) plots the rates of change at 1 hour for normalised (absolute) phase at 200 Hz. Average values are shown ($n = 4$). MATLAB was used to obtain the linear fits, corresponding equations and R^2 values.

To test the effectiveness of each of these proposed concentration curves (Figure 6.47), data from an experiment involving the growth of *S. aureus* in LB medium at cell densities either end of the calibrated range was used. For this new experimental data, the rates of change as a function of time were again first obtained using the MATLAB script (Figure 6.48). Once more, the rates of change were largest early in the experiment and were larger for the higher cell density.

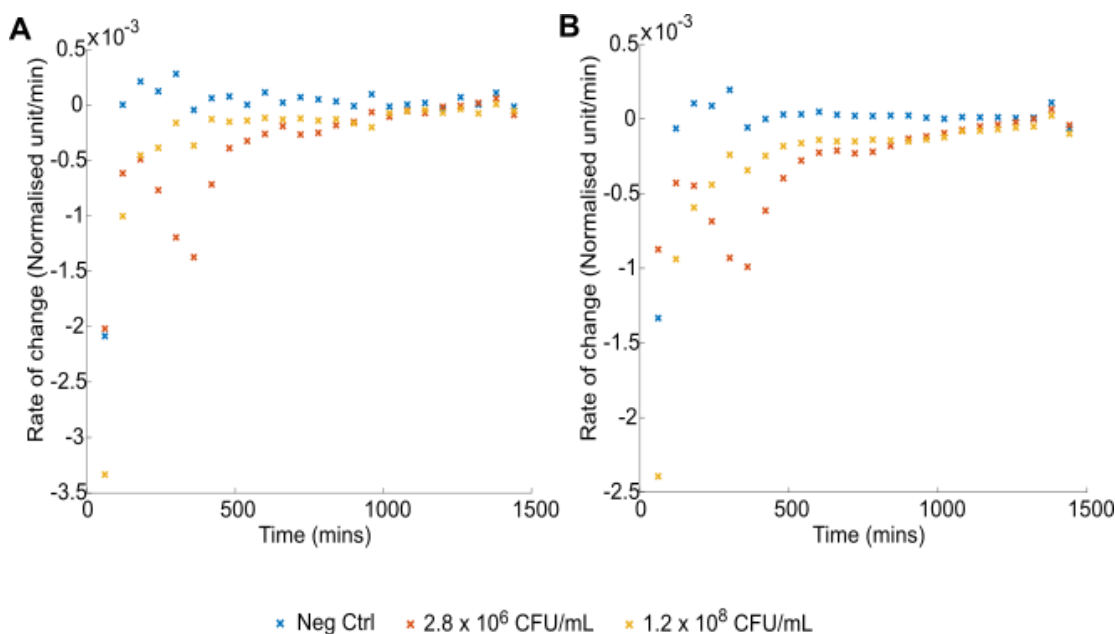


Figure 6.48. Mean rate of change as a function of time for the test data, where: (A) is the normalised modulus at 1 Hz and (B) the normalised (absolute) phase at 200Hz data. Data was obtained from the growth of two different concentrations of *S. aureus* (NCTC8325) in LB medium over 24 hours ($n=4$).

The rate of change values for each parameter were next inserted into the corresponding linear equations obtained in Figure 6.47 and estimates of bacterial concentration obtained (Table 6.10). Firstly, the concentration estimates obtained using the 1 Hz normalised modulus maximum and 1-hour rates of change equations were inaccurate, contra-indicating the use of these. Conversely, the estimates obtained using the normalised phase at 200 Hz equations provided values closer to the true concentrations (calculated via colony counting). Furthermore, the calculation involving the rates of change at 1 hour appeared to give a more consistent approximation of concentration, close to the true values for both the high and low concentration test data (Figure 6.47D, Table 6.7). This experiment, therefore, indicated that using the rate of change of normalised phase at 200 Hz after 1 hour of incubation may give an approximation of cell density within the same order of magnitude.

Table 6.7. Estimates of the average *S. aureus* cell density present in test samples, obtained using the rate of change method ($n = 4$, ROC = rate of change).

Parameter	Absolute ROC Value	log(Estimated Concentration)	Estimated Concentration [CFU/mL]	Actual Concentration (via Colony Counting) [CFU/mL]
Normalised modulus 1 Hz – Maximum ROC	0.002018	5.65	4.4×10^5	2.8×10^6
Normalised modulus 1 Hz – 1 hour ROC	0.002018	8.54	3.5×10^8	2.8×10^6
Normalised phase 200 Hz – Maximum ROC	0.00099	6.24	1.7×10^6	2.8×10^6
Normalised phase 200 Hz – 1 hour ROC	0.0008733	6.98	9.5×10^6	2.8×10^6
Normalised modulus 1 Hz – Maximum ROC	0.003335	7.29	2.0×10^7	1.2×10^8
Normalised modulus 1 Hz – 1 hour ROC	0.003335	10.3	2.1×10^{10}	1.2×10^8
Normalised phase 200 Hz – Maximum ROC	0.002393	7.41	2.6×10^7	1.2×10^8
Normalised phase 200 Hz – 1 hour ROC	0.002393	8.95	9.0×10^8	1.2×10^8

Whilst this new method for bacterial cell density estimation using the rate of change of normalised impedance appears promising from these initial experiments, it is clear that far larger volumes of data are required to truly assess the accuracy of this method. Further, a wide range of bacterial species and concentrations must be involved in the development of the calibration plots and equations. In general, however, this method has been shown to have the potential to enable rapid bacterial concentration estimation via EIS data analysis.

6.10 Development of Neural Networks for the Detection and Identification of Bacteria

Over the course of this chapter, it has become evident that bacteria can be detected via characteristic changes occurring in normalised impedance. It has also, however, become clear that the negative control changes to impedance can be variable in magnitude and frequency (see Figures 6.4A and 6.5A for example). Defining a normalised impedance cut-off point for rapid bacterial detection in the absence of a sterile control may, therefore, be problematic. Further, any differences between the signatures of different species are very subtle and, except

for the WBM results in Section 6.5, cannot be identified by eye unless perhaps grown simultaneously. Since small differences in bacterial signature for the same pathogen have also emerged between experiments and between measurement medium (see Figures 6.10B and 6.15B), it has not been possible to identify bacterial species from visual or simple computational inspection of the impedance signatures. Throughout the course of this project, a large volume of impedance data has been obtained. It was, therefore, hypothesised that artificial neural networks (ANN) could be developed to assist in the detection of bacteria and identification of species from the normalised impedance signatures, in line with the final project objective outlined in Section 1.8.

6.10.1 Training Dataset Overview

The impedance signatures obtained from all experiments conducted in LB medium, SWF, the WBM and the dWBM were included in the neural network training dataset. For each of these growth media, signatures from a range of bacteria were available. Often the experiments reported in this thesis were carried out multiple times to build upon this database of signatures. Within Figure 6.49, a summary of the dataset content is provided. Certain pathogens are more heavily represented in the data than others, with a total of 60 signatures for *S. aureus* compared to just 3 for *E. coli* for example. It was anticipated, therefore, that the resulting ANNs would have a higher accuracy when presented with a new signature from a species well supported by training data such as *S. aureus*. Building upon this dataset in future will greatly strengthen the ANNs, however, this dataset of 175 individual signatures provided a solid foundation for this proof-of-concept work. Each of these signatures contained 142 complex impedance data points across the frequency spectrum, resulting in a total of 24,850 data points.

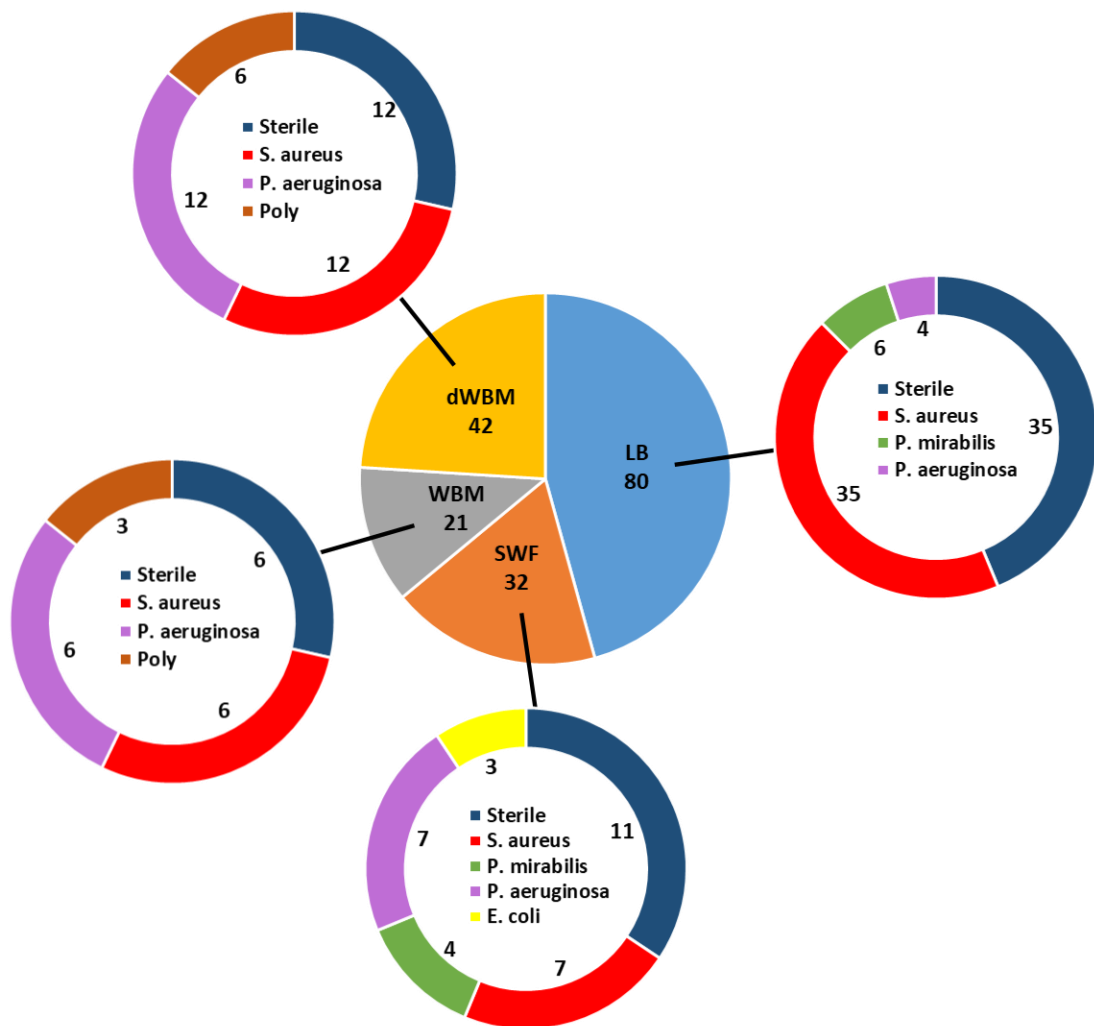


Figure 6.49. Summary of the dataset collated for ANN training.

6.10.2 Model Feature Selection and Rationale

Despite the large number of data points within each signature, it was necessary to select the data points most relevant to the detection and identification of bacteria from the signature. As described in Section 2.4, the simplest ANN structure possible is desired to optimize performance. Throughout this chapter so far, much knowledge has been gained as to where characteristic elements of the bacterial impedance signatures arise and areas of the spectra which have a higher likelihood of containing noise. Using this knowledge, the following features were manually selected from 24-hours data (this time point was chosen for this proof-of-concept work because signature magnitude plateaus had been reached by this time for every growth condition):

- **Growth Medium**

The bacterial impedance signatures have a dependence upon the medium or model that they were obtained in. Each of the different growth conditions, namely LB medium, SWF, the WBM or the dWBM were, therefore, converted into a numeric label and provided as an input feature.

- **Normalised Modulus at 1 Hz and 1 kHz**

A normalised modulus reduction in the mid to low frequency range has emerged as a consistent bacterial growth signature characteristic, regardless of species or medium. In particular, the data at 1 Hz for normalised modulus has consistently shown a reduction over the 24 hours of growth (Figure 6.50). As a baseline point to compare the extent of this change to, the 1 kHz normalised modulus point was also selected. Highlighted in Figure 6.50, the values at this frequency were reflective of any non-specific negative control variations not linked to the presence of bacteria.

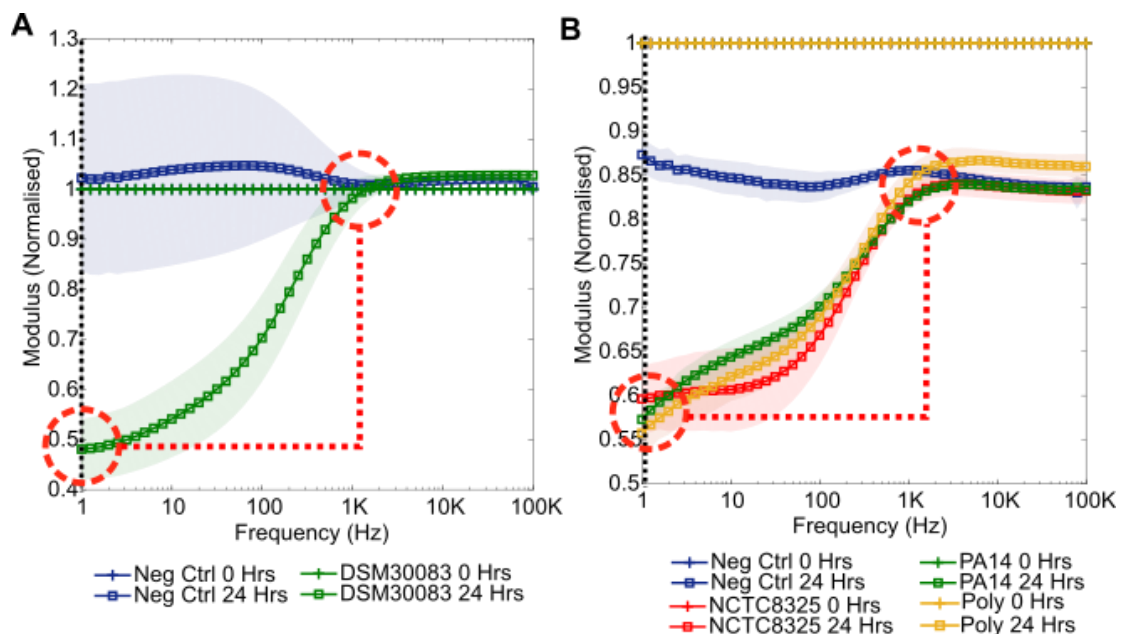


Figure 6.50. Justification of normalised modulus 1 Hz and 1 kHz feature selection. In (A) the reduction at 1 Hz for *E. coli* growth in SWF (originally Figure 6.11) is relative to an unaltered baseline of 1 at 1 kHz. In (B) the *S. aureus*, *P. aeruginosa* and polymicrobial signatures in the WBM (originally Figure 6.17) have their reductions at 1 Hz compared to a shifted baseline at 1 kHz.

- **Normalised (Absolute) Phase at 1 Hz, 100Hz and 1 kHz**

Similarly, the key features of normalised (absolute) phase were selected by considering the bacterial growth signatures obtained within this chapter. The characteristic signatures resulting from bacterial growth each contained mid-frequency normalised phase troughs. Typical examples of this can be seen for *S.*

aureus and *P. aeruginosa* growth in SWF within Figure 6.51A. Slight variations in the frequency of this trough emerged, however, by selecting normalised phase values at both 100 Hz and 1 kHz this trough was consistently captured (Figure 6.51A). Some clear variation in this characteristic signature was evident when using the dWBM (Figure 6.51B), however, the 100 Hz and 1 kHz features were still found to encapsulate a key region of normalised phase change. Additionally, around 1 Hz emerged as a region of interest due to the large inter-species variation observed there. For these reasons, normalised phase at 1 Hz, 100 Hz and 1 kHz were selected as the final features for input into the ANN.

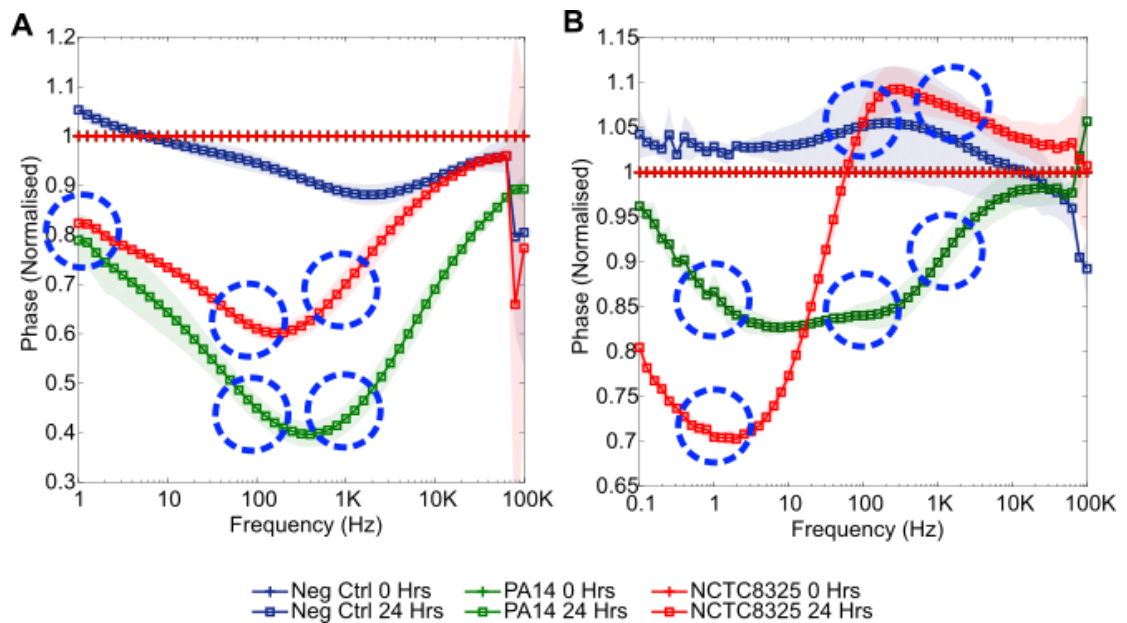


Figure 6.51. Justification of normalised (absolute) phase 1 Hz, 100 Hz and 1 kHz feature selection. In (A) phase signatures characteristic of bacterial growth in rich media are illustrated using *S. aureus* and *P. aeruginosa* growth in SWF (originally Figure 6.10) and in (B) the slightly different signatures of *S. aureus* and *P. aeruginosa* growth in the base dWBM are shown (originally Figure 6.20). In each case the selected features are highlighted in blue.

6.10.3 ANN1 Model Creation for Detecting Infection

Using the 6 features identified above (extracted from each of the 175 dataset signatures), and the paired outputs of sterile (0) or contaminated (1), the first artificial neural network (ANN1) was trained to detect the presence of infection in a sample using the scikit-learn MLP Classifier. As described in Section 3.7.10, the structure and key parameters of the network were optimised using trial and error methods. Starting from a simple network and gradually altering the structure, the average F₁-scores were evaluated at each step change and the model parameters

with the best performance found. Unless otherwise stated, it can be assumed that the default model parameters detailed in Section 2.4.3 were used. To begin, 2 hidden layers were used and only the number of neurons in these hidden layers was altered. From Table 6.8, it can be seen that the smallest number of neurons where the average F₁-score was maximised (and therefore the network performance was optimised) was when 9 neurons per layer were present.

Table 6.8. ANNI number of neurons optimisation for a 2 hidden layer network.

Neurons per Layer	Run 1 F ₁ -score	Run 2 F ₁ -score	Run 3 F ₁ -score	Average F ₁ -Score
4	0.95	0.91	0.82	0.89
5	0.98	0.86	0.95	0.93
6	0.96	0.98	0.98	0.97
7	0.98	0.93	1	0.97
8	0.98	0.98	0.98	0.98
9	0.98	1	1	0.99
10	1	1	0.98	0.99
11	0.98	0.98	1	0.99
12	1	0.98	0.98	0.99

The number of hidden layers was next optimised in a similar manner (Table 6.9). Using 4 hidden layers with the 9 neurons per layer initially provided the optimum result. The number of neurons per layer was then decreased to obtain the simplest structure with the highest F₁-score, which was found to be 8 neurons in each of the 4 hidden layers.

Table 6.9. ANNI number of hidden layers optimisation.

Hidden Layers	Neurons per Layer	Run 1 F ₁ -score	Run 2 F ₁ -score	Run 3 F ₁ -score	Average F ₁ -Score
2	9	1	1	0.98	0.99
3	9	1	0.98	1	0.99
4	9	1	1	1	1
4	8	1	1	1	1
4	7	0.98	1	0.98	0.99

The learning type and rate were next explored. It is evident from Table 6.10 that the default constant learning rate of 0.001 was optimal for this network and, with an F₁-score of 0.99, more minor changes to this learning rate were not explored.

Table 6.10. ANNI learning type and rate exploration.

Learning Type	Initial Rate	Run 1 F ₁ -score	Run 2 F ₁ -score	Run 3 F ₁ -score	Average F ₁ -Score
Constant	0.001	1	0.98	1	0.99
Adaptive	0.001	1	1	0.93	0.98

Invsaling	0.001	0.95	0.98	1	0.98
Constant	0.0001	0.22	0.8	0.49	0.50

Finally, the maximum number of iterations performed was altered as the current network was providing a warning of the fact that it was not converging within the default 200 iterations. The minimum number of iterations for which the F₁-score was maximal and no convergence warning given was 600 (Table 6.11).

Table 6.11. Optimising the maximum number of iterations for ANN1.

Maximum Iterations	Run 1 F ₁ -score	Run 2 F ₁ -score	Run 3 F ₁ -score	Average F ₁ -Score	Convergence warning?
200	1	1	1	1	Yes
500	1	1	0.98	0.99	No
1000	0.98	0.98	0.98	0.98	No
2000	1	1	0.98	0.99	No
600	1	1	1	1	No

The final ANN1, therefore, was chosen to contain 4 hidden layers, each with 8 neurons and the maximum number of iterations set to 600. All other parameters remained at their default setting (Section 2.4.3). Using these hyper-parameters, the final saved ANN1 algorithm was trained (as previously) using a randomly allocated 75% of the training dataset and its performance validated using the remaining 25% of data. The below confusion matrix (Section 3.7.10) resulted:

$$\begin{bmatrix} 21 & 0 \\ 0 & 23 \end{bmatrix}$$

This indicated that (using the remaining test data) 21/21 sterile samples were correctly identified as such and 23/23 contaminated samples correctly identified as such. Further, the classification report is provided in Table 6.12. Notably, this output states that the saved ANN1 had both a precision and recall of 100% for the test data. This neural network was, therefore, shown to be very powerful for the detection of bacteria within samples using the selected 24 hours normalised impedance features.

Table 6.12. ANN1 final algorithm classification report.

	Precision	Recall	F ₁ -Score	Support
Sterile	1.00	1.00	1.00	21
Infected	1.00	1.00	1.00	23
Weighted Average	1.00	1.00	1.00	44

6.10.4 ANN2 Model Creation for Bacterial Species Identification

In the same manner, a neural network for the identification of bacterial species was developed (ANN2). The same training dataset and 6 key features were used once more, with the paired output data in this case being one of the following: *E. coli*, *P. aeruginosa*, *P. mirabilis*, polymicrobial, *S. aureus* or sterile. Again, the network was first trained using all default network parameters (Section 2.4.3) and a simple structure of 2 hidden layers with 4 neurons each. The number of neurons per layer was again first optimised (Table 6.13). The optimum number of neurons per layer for this network was 10, determined via obtaining the highest average F_1 -Score for this structure.

Table 6.13. ANN2 number of neurons optimisation for a 2 hidden layer network.

Neurons per Layer	Run 1 F_1 -score	Run 2 F_1 -score	Run 3 F_1 -score	Average F_1 -Score
4	0.33	0.54	0.42	0.43
6	0.53	0.39	0.55	0.49
8	0.55	0.6	0.69	0.61
9	0.67	0.71	0.72	0.70
10	0.79	0.81	0.53	0.71
11	0.73	0.46	0.82	0.67
12	0.68	0.72	0.71	0.70

The number of hidden layers was next optimised (Table 6.14). The highest F_1 -Score was once more achieved for 4 hidden layers (Table 6.14). The number of neurons per layer was then adjusted until optimal, with 12 neurons per hidden layer providing the best F_1 -Score at 0.73.

Table 6.14. Optimisation of the number of hidden layers for ANN2.

Hidden Layers	Neurons per Layer	Run 1 F_1 -score	Run 2 F_1 -score	Run 3 F_1 -score	Average F_1 -Score
2	10	0.76	0.51	0.55	0.61
3	10	0.6	0.68	0.71	0.66
4	10	0.62	0.70	0.74	0.69
5	10	0.69	0.54	0.69	0.64
4	12	0.81	0.65	0.73	0.73
4	11	0.69	0.69	0.61	0.66
4	9	0.74	0.62	0.74	0.70

Using this structure, the learning type and rate were next explored (Table 6.15). The “invscaling” type provided the highest performing network (refer to Section 2.4.3 for details) with a higher initial rate of 0.01 preferable to the default of 0.001.

Table 6.15. Exploration of learning type and rate for ANN2.

Learning Type	Initial Rate	Run 1 F ₁ -score	Run 2 F ₁ -score	Run 3 F ₁ -score	Average F ₁ -Score
Constant	0.001	0.75	0.64	0.72	0.70
Invscaling	0.001	0.70	0.61	0.66	0.66
Adaptive	0.001	0.69	0.61	0.68	0.66
Constant	0.0001	0.49	0.24	0.24	0.32
Constant	0.01	0.84	0.77	0.78	0.80
Adaptive	0.01	0.79	0.78	0.82	0.80
Invscaling	0.01	0.91	0.90	0.88	0.90

Finally, due to a lack of model convergence during training (as in ANN1), the maximum number of iterations was altered. Once more, it was found that 600 iterations allowed for model convergence and the optimum F₁-Score (Table 6.16).

Table 6.16. Results of altering the maximum number of iterations for ANN2.

Maximum Iterations	Run 1 F ₁ -score	Run 2 F ₁ -score	Run 3 F ₁ -score	Average F ₁ -Score	Convergence warning?
200	0.84	0.89	0.88	0.87	Yes
500	0.7	0.75	0.74	0.73	No
1000	0.81	0.89	0.93	0.88	No
2000	0.72	0.81	0.72	0.75	No
600	0.83	0.87	0.96	0.89	No
700	0.87	0.86	0.83	0.85	No
800	0.91	0.89	0.83	0.88	No
900	0.86	0.81	0.77	0.81	No

The final ANN2 algorithm was, therefore, trained using: 4 hidden layers of 12 neurons each; the “invscaling” learning type with an initial rate of 0.01; 600 maximum iterations; all other parameters at their default setting. The saved model resulted in the below confusion matrix, which breaks down the model predictions compared to the true results:

$$\begin{bmatrix} 1 & 0 & 0 & 0 & 0 & 0 \\ 0 & 5 & 0 & 0 & 1 & 0 \\ 0 & 0 & 3 & 0 & 0 & 0 \\ 0 & 0 & 0 & 3 & 0 & 0 \\ 0 & 0 & 0 & 2 & 11 & 0 \\ 0 & 0 & 0 & 0 & 0 & 18 \end{bmatrix}$$

The first row corresponds to the classification of *E. coli*, with 1/1 samples correctly classified as such. In the next row we see that 5/6 *P. aeruginosa* samples were correctly classified, and 1/6 incorrectly classified as *S. aureus*. In rows 3 and 4 we see that all 3 samples for each of *P. mirabilis* and the polymicrobial cultures respectively were correctly classified. Next, 11/13 *S. aureus* were correctly classified, with 2 misclassified as polymicrobial. Finally, 18/18 sterile samples were correctly classified as such. The corresponding classification report is provided

in Table 6.17. Notably, this states that the overall precision of the model was 95%, with a recall of 93%. Whilst the performance of this network is lower than ANN1, considering the complexity of the task performed by ANN2 this result is exceptionally promising. Furthermore, it is anticipated that as the volume of training data is increased in future, these validation scores will improve.

Table 6.17. Classification report for the final ANN2 algorithm.

	Precision	Recall	F₁-Score	Support
<i>E. coli</i>	1.00	1.00	1.00	1
<i>P. aeruginosa</i>	1.00	0.83	0.91	6
<i>P. mirabilis</i>	1.00	1.00	1.00	3
Polymicrobial	0.60	1.00	0.75	3
<i>S. aureus</i>	0.92	0.85	0.88	13
Sterile	1.00	1.00	1.00	18
Weighted Average	0.95	0.93	0.94	44

6.11 Discussion and Summary

Throughout this chapter, the use of platinised carbon electrodes for the rapid detection of wound bacteria has been explored. Ultimately, through carrying out various bacterial growth experiments, the superior performance of these sensors over the simple carbon sensors was verified. Notably, the lower baseline impedance of these sensors and their sustained consistency resulted in more pronounced normalised impedance signatures being observed during bacterial growth. When using the same electrode settlement steps as previously, it was once more possible to detect bacterial growth within 30 minutes. Due to the success of these experiments, a more practical electrode conditioning process was adopted which created dry sensors that could be stored before use. Whilst this resulted in some initial sensor instability and a consequential increase in time to bacterial detection, with further process refinements in future it is believed possible to decrease the time to detection once more.

With these sensors, explorations of sensor performance in the wound environment were taken further than previously. Firstly, a double sensor WBM which accounted for gravitational settlement effects was created and the influence of these effects assessed. Secondly, various wound dressings were incorporated into the WBM, and their effects studied. Except for a highly absorbent dressing which would require additional medium to be added in future, these experiments confirmed the sensors' ability to detect the growth (or lack of) bacteria in the presence of various common dressings.

Crucially, a variety of impedance data analysis techniques were employed in this chapter to draw further value from the obtained signatures, from equivalent circuit model fitting to more complex data mining techniques. Notably, through novel mathematical analysis of early impedance changes, a method of bacterial concentration determination was proposed. Furthermore, for the first time, artificial neural networks enabled bacterial detection and species identification with an accuracy far higher than anticipated. This novel application of AI to bacterial impedance signature analysis was demonstrated to be very promising, with future advancements believed to have the potential to greatly enhance rapid infection diagnostic technology.

7. DISCUSSION

7.1 Introduction

At the beginning of this thesis, project objectives were outlined (Section 1.8). These ultimately aimed to advance the development of an *in situ* electrochemical wound infection sensor, by exploring different sensor materials, bacterial growth conditions and analysing the resulting bacterial impedance signatures. Within this discussion, the results of these experiments (presented in Chapters 4-6), will be placed into the context of these research goals and relevant literature. Ultimately, within this project a simple screen-printed sensor was selected that enabled the detection of wound pathogens in both culture media and wound bed models. Further, algorithmic approaches were successfully developed which supported this detection and further supported the determination of bacterial load and species.

7.2 Electrode Materials - Assessment and Selection

Within this study, three different screen-printed electrode materials were explored for potential use in a future infection detection device: Ag/AgCl, carbon and platinised carbon. In this section the key findings for each sensor type are discussed, and a rationale for the ultimate choice of the PCE sensor made.

7.2.1 Ag/AgCl Sensor Conclusions

The first sensors investigated, the flexible Ag/AgCl Woundsense electrodes (Ohmedics Ltd) ultimately proved unsatisfactory for bacterial detection (Chapter 4). Despite their evidenced clinical efficacy for *in situ* wound moisture monitoring (117,266), data contraindicating their use for bacterial detection in wounds was obtained.

Firstly, the stability of this sensor was found to be dependent upon applied measurement voltage. Through characterisation experiments performed in 0.9% w/v NaCl solution, it was established that a higher measurement potential (200 mV rms for example) negatively impacted measurement consistency, reproducibility and caused low frequency inductive artefacts (Section 4.2). Conversely, lower measurement voltages (10-20 mV for example) produced far more stable and predictable EIS results in the saline solution studied. Expanding upon the conclusions drawn in Chapter 4, this is believed to be a direct consequence of voltage-induced surface changes. At the surface of these electrodes, quasi-reversible changes were induced by the application of higher voltages. For example, changes to the AgCl layer's physical properties

can be related to the magnitude of the applied electric field, such as thickness and Ag/AgCl bond strength (267). A further factor believed to be influential in the disparity between the high and low voltage impedance responses is the anodic potentiodynamic polarisation behaviour of silver in physiological saline solution, as described by Ha and Payer (2011) (246). By applying potential pulses to a Ag/AgCl electrode at incrementally increasing values, they obtained a plot of current density as a function of potential (termed a Tafel plot (186,246)). Notably, their plot showed that a sharp rise in current density occurred from 50 mV to 200 mV, as the potential was increased away from the corrosion potential of silver. Whilst these specific voltages may not be directly comparable to those used in the experiment presented in Section 4.2 (Figure 4.2) due to different experimental conditions and apparatus, the decreasing impedance with increasing potential observed with the Woundsense electrodes is likely to be a manifestation of their analogous increase in current density with potential (see Section 2.3). A further consideration is the manner in which increasing the voltage and, thus, electric field of the electrode influences the adjacent diffuse double layer (186). The chemical reaction rate for example will be increased by the higher field in the double layer (attenuated from the electrode surface) and the diffusion profile more defined, affecting the EIS response (see Section 2.3.4 for a description of the double layer). Furthermore, the early experiments indicated that using an EIS measurement voltage of 20 mV could produce more desirable results than using a higher voltage in bacterial cultures.

As discussed on numerous occasions throughout this thesis, despite a low measurement voltage being generally preferred for EIS studies (Chapter 2), a higher measurement voltage of 200 mV produces a desirable low noise, stable response when using screen-printed sensors for bacterial impedance studies (168,223). Notably, Farrow et al. (2012) (129) previously used a 200 mV measurement voltage to explore the application of the Ag/AgCl Woundsense electrodes to the detection of *S. aureus*. Their study observed bacterial growth inhibition (attributed to silver release by the electrodes), heightened by the performance of hourly 200 mV EIS measurements. Within this thesis, performing 200 mV EIS measurements was similarly confirmed to have a bactericidal effect upon *P. aeruginosa* (Section 4.3.1). Aiming to limit the bactericidal action of these electrodes, further bacterial growth experiments were performed using a 20 mV measurement voltage in this study. Crucially, for the first time no bacterial growth inhibition was observed in these experiments, confirming the earlier conclusions drawn regarding increased sensor surface stability at lower measurement voltages. Whilst Farrow et al. were able to detect some low frequency normalised phase differences between sterile controls and *S. aureus* cultures with their 200 mV measurements, the statistical significance of these differences was not assessed. Conversely, a significant bacterial signature

was obtained here using the 20 mV voltage. For both low frequency normalised phase and modulus, bacterial impedance changes were statistically significant from the negative controls from the 5-hours measurement point (Figure 4.5). A limitation of this study is that different measurement media and strains of bacteria were used by researchers (when comparing between this study and that carried out by Farrow et al. (2012)), however, the clear benefit of using this lower measurement voltage to reduce bacterial growth inhibition has been evidenced.

Whilst in this project the applied potential was adjusted to achieve optimum bacterial growth during measurement, many studies have previously utilised this phenomena in reverse to reduce biofilm formation on a variety of metal surfaces (268). By controlling the potential applied to the metal surface, cell growth and attachment has been intentionally prevented due to underlying processes such as electrostatic forces and the formation of surface oxidants when applying a DC potential. Harnessing the influence of an electric field in this manner has applications in waste water management for example (269). The knowledge gained in this project could, therefore, be utilised to prevent bacterial biofouling on the surface of a wound sensor which is not intended to detect bacteria. Further, dynamic potential changes which result in controlled silver release could be used in the wound environment to reduce bioburden in a similar manner to antimicrobial dressings (including silver dressings, Section 1.4).

Despite the improvements made to the detection of bacterial growth with these sensors, local bacterial growth inhibition on and immediately surrounding the Ag/AgCl electrode surface was still observed (Section 4.4, Figure 4.6). This is likely a direct consequence of the antimicrobial action of silver ions released from the electrode ink. As this was evident both in the presence and absence of EIS measurements it can be concluded that, despite limiting the bactericidal action of the electrodes by reducing the measurement voltage, these effects cannot be completely removed. Many of the key methods in which bacteria can alter impedance rely upon close contact with the electrode surface, for example biofilm formation and direct cellular or appendage contact (118). By using a sensor which reduces these mechanisms, the diagnostic value of the obtained bacterial signatures is almost certainly diminished. For these reasons, in addition to the unsatisfactory Woundsense electrode WBM results that will be discussed in Section 7.3, these sensors with their current Ag/AgCl ink composition were deemed unsuitable for this rapid wound infection monitoring application.

7.2.2 Carbon Sensor Conclusions

Carbon was the second electrode material to be investigated; the sensors tested were screen-printed in-house using a low-cost carbon ink (Section 3.3). As detailed in Chapter 5, the surface inertness and stability of these sensors was a key factor in their selection for study, aiming to improve upon the Ag/AgCl sensor response observed previously. As anticipated, no bactericidal action was evident during these experiments despite a return to the previously evidenced 200 mV measurement voltage (Section 3.4, (223)). Typically, a cell density increase of at least two orders of magnitude (commonly $10^6 - 10^8$ CFU/mL) over the course of a 24-hours growth experiment was seen for a variety of wound bacteria (Section 5.2). Additionally, biofilm formation directly on the sensor surface was evidenced through CV staining (Figure 5.6). This is an immediate, clear advantage over the previous Ag/AgCl sensors. Furthermore, sensor stability at the higher 200 mV EIS measurement voltage was greatly improved compared to the Woundsense electrodes, with minimal negative control variation despite multiple repeated measurements of the medium (exemplified in Figures 4.3 and 5.1). These carbon sensors did, however, exhibit a higher baseline impedance compared to the Ag/AgCl sensors at 200 mV, being over $10^6 \Omega$ at 0.1 Hz vs $10^3 \Omega$ at 0.1 Hz. The limit of detection of the Solartron impedance analyser is $10^7 \Omega$ at 0.1 Hz according to the instrument manual, thus this upper limit was approached. The carbon sensor impedance falls off with increasing frequency, but the higher baseline impedance may still limit the visibility of some smaller magnitude impedance changes at the carbon sensor surface occurring due to the presence of bacteria. This is a concern similarly noted by Ward et al. (2014) (118). Both the Ag/AgCl and carbon sensor baseline impedance values obtained in this study were comparative to those observed in literature using similar screen-printed electrodes. For example, Farrow (2010) recorded an impedance modulus of $\sim 7000 \Omega$ at 0.1 Hz in Mueller-Hinton broth at 200 mV (higher than the 1000Ω observed in this study due to differences in manufacture and measurement medium, but of the same order of magnitude) (168). For the carbon sensors, Ward et al. (2014) recorded an impedance modulus of $\sim 4 \times 10^6 \Omega$ at 0.1 Hz in Tryptone Soya Broth, very similar to that observed in this study in LB medium (118).

Bacterial impedance experiments conducted in LB medium first confirmed the suitability of the carbon sensors for bacterial detection. Previously Ward et al. (2014) detected *P. aeruginosa* growth in a microaerophilic (reduced oxygen) environment using these carbon sensors and EIS, with characteristic impedance changes detected after 24 hours of growth in LB medium (118). Notably, they observed phase and modulus decreases at frequencies below 1 kHz, and normalised resistance peak formation (with the peak location varying with time from 24 to 69

hours). An electroactive metabolite of this bacterium, pyocyanin was believed to play a fundamental role in the emergence of this impedance signature. Further, when measuring *S. aureus* growth, no significant impedance signature features emerged for Ward et al. Within this thesis, this *S. aureus* growth experiment was repeated due to the clinical importance of this species to wound infection (Section 5.2). The standard air oxygen concentration was not altered in this case, mimicking the exposed wound environment. With this experimental difference, significant normalised impedance signature features emerged for *S. aureus* (NCTC8325). Most notably, a decrease in normalised modulus below 1 kHz and an early normalised (absolute) phase trough around 1 kHz occurred (Section 5.2, Figure 5.2). Furthermore, the use of the custom-built multiplexer system in this study to support regular automated EIS measurements enabled statistically significant normalised impedance changes to be detected within only 30 minutes of growth ($p = 0.007$, normalised phase at 1 kHz). This considerable advancement to the bacterial detection system highlights the promise of this technique for rapid infection detection. Unlike in PCR tests where a specific target is being tested for and multiplexed testing can be used to scan for multiple bacterial species simultaneously (270), it is not envisioned that a multiplexer system would be advantageous to a non-specific impedance-based wound monitoring device in clinical practice. In this application the multiplexer has the sole benefit of increasing measurement throughput and efficiency at the research and testing stage, supporting the collection of large data volumes. Paredes et al. (2014) similarly used a multiplexer system to carry out bacterial impedance measurements with a frequency of 30 minutes, however an initial settlement period of 5 hours was required before significant impedance changes emerged due to the growth of Staphylococci from a starting concentration of 10^6 CFU/mL on their gold-sputtered electrodes (126). This difference in initial stability may be partially due to the difference in sensor composition, but a likely additional factor is the electrode pre-treatment steps adopted in this study to improve the response of the carbon sensors. Namely, electrochemical conditioning in 0.9% w/v NaCl followed by overnight settlement in LB medium (Section 3.6.1).

In addition to *S. aureus*, LB medium growth signatures were obtained for *S. epidermidis* and *P. mirabilis*. As detailed in Chapter 5, these were very similar in appearance, containing the significant decrease in normalised modulus below 1 kHz and early mid-frequency normalised phase trough. These features had, therefore, emerged as defining characteristics of bacterial growth in LB medium. This important finding suggests that processes common to many species of bacteria are responsible for these defining changes in impedance. It may, therefore, be possible to reliably detect the presence of infection via the emergence of these key impedance signature features. Further, the time-based plots in particular highlighted some difference in

the timings and magnitudes of impedance changes between species. Focusing upon normalised phase where significant impedance changes were rapidly visible, the time-based plots emphasised the transient nature of the normalised phase trough for both *S. aureus* and *S. epidermidis*. Whilst the trough maximised for these species at around 2.5 Hours before greatly reducing in magnitude, for *P. mirabilis* the feature had a lesser reduction (see Figures 5.3, 5.4 and 5.5). Further, for the Staphylococci a later high frequency normalised phase peak emerged by 24 hours. When measuring *P. aeruginosa* growth in LB medium with these sensors, Ward et al. (2014) observed reductions in modulus and phase which continued to grow in magnitude throughout the 69 hours of measurements (118). The sustained or transient nature of the impedance response appears to be linked to the species under study, with key differentiators such as cell motility or structure (including Gram-stain) being potentially influential.

Due to these variabilities in the timings and evolutions of the detected impedance changes, greater understanding of their underpinning mechanisms was desired. The additional insight gained from experiments conducted in saline solution and equivalent circuit model fitting led to the belief that the identified normalised impedance changes arose due to a number of parallel processes which take place. From even the earliest bacterial impedance studies, mid-frequency changes (such as the rapidly emerging phase trough in this study) have been related to the breakdown of nutrients within the medium during growth (143,165). Media conductivity is altered as the organism breaks down large macromolecules to produce waste products, by-products and secondary metabolites (150). The chemical properties of these molecules could thus contribute to the observed changes in the impedance through irreversible adsorption to the electrode surface combined with changes in the conductivity of the growth medium (150). Metabolomics studies have begun to uncover the vast diversity of metabolites produced by different species of bacteria under different conditions using a variety of techniques such as mass spectrometry (271). Whilst broad commonalities exist between species which may be the cause of the dominating characteristic impedance signatures (such as the breakdown of the LB medium's tryptone peptides into a usable carbon source), numerous differences in biochemical reactions may give rise to the intricate signature differences observed (such as virulence factor production) (272). Through the experiments conducted with *P. mirabilis* and *S. aureus* cells in saline solution where bacterial growth was inhibited (Section 5.5), the contribution of growth-related process such as these was found to dominate the LB signatures due to the far smaller magnitude of impedance changes in saline. When studying *Bacillus subtilis* and *Shewanella oneidensis* growth via embedded gold micro-interdigitated electrodes, Bonetto et al. (2014) also attributed impedance changes to metabolic means (128). Their belief that ionic changes at

sensor surfaces induced by different metabolic process could be harnessed to differentiate between species could explain the subtle signature variations observed here. Further, Paredes et al. (2014) attributed low frequency impedance changes to *S. epidermidis* growth, with metabolic activity believed to influence resistance and biofilm formation linked to capacitive changes (126). In this study, equivalent circuit modelling suggested that the growth-related impedance changes were associated with a reduction in charge transfer resistance for each species studied in LB medium (Section 5.6). In contrast, no significant change in R_{ct} or any other circuit element was seen in 0.9% w/v NaCl. This supports the hypothesis that these dominant impedance changes (and thus changes to charge transfer resistance) were driven by growth related metabolic processes and not cell-electrode interactions such as adsorption. Evaluations of circuit parameter percentage changes have similarly been made in other studies, with changes in a variety of parameters such as double layer capacitance linked to the presence of bacteria (123,163). In some studies, a decrease in charge transfer resistance has also been found to closely relate to the growth of microorganisms on carbon-based electrode surfaces (258–260). The choice of electrode material is likely to be influential in this particular change.

Even though growth related impedance changes dominated, through measuring a single high concentration of *P. mirabilis* cells (5.0×10^8 CFU/mL) in saline solution over time, cellular adsorption was inferred. Between 30 minutes to 6 hours, normalised modulus (10 Hz) and normalised (absolute) phase decreases (200 Hz) progressively emerged. These are thought to be a result of early cell settlement and attachment onto the electrode surface. Bacterial attachment to surfaces is known to occur in two phases called reversible and irreversible. Initial reversible attachment is affected by the buoyant density and motility of bacteria, whereas electrostatic interactions govern later irreversible attachment over several hours (273). In this experiment, the high motility of *P. mirabilis* potentially influenced the adsorption time. Cellular adhesion has been observed in a number of other studies evidencing a link between impedance and direct cellular interaction with an electrode surface (119,121,123). This gradual impedance change induced by direct cellular contact with the electrode highlights the impedance changes observed in LB medium are a result of multiple complex events.

The saline experiments further contributed to the understanding of processes underlying the impedance spectra by revealing bacterial cell concentration dependant regions of change. In addition to a concentration dependant normalised resistance peak, for *S. aureus* washed cell concentrations of 5.8×10^7 CFU/mL and above an immediately significant 10 kHz normalised

phase peak was observed (Figure 5.16B). A limitation of this result is that the true concentration of cells on the electrode was likely higher than estimated due to the lack of an electrode washing step between each measured concentration, possibly resulting in a more pronounced peak. The similar high frequency normalised (absolute) phase peak emerging by 24 hours growth in the LB medium staphylococcal signatures was, therefore, believed to be formed due to the settlement and adsorption of bacterial cells on the sensor surface as the concentration of cells increased (Figure 5.2B). Crucially, the shoulder of this peak may have had a broader spectrum influence, resulting in the diminishing magnitude of the mid-frequency staphylococcal normalised phase troughs over time. These high frequency features are believed to have been influenced by bacterial cell membrane polarisations, such as those harnessed in early β -dispersion dielectric spectroscopy studies of bacterial biomass (Section 1.6.1) (148). More recently, Gnaim et al. (2020) harnessed high frequency impedance differences to distinguish between Gram-positive and negative bacteria, with the Gram-negative species displaying larger negative phase values around 50 kHz (274). Whilst in this study it was the Gram-positive staphylococci which displayed the larger high frequency negative phase values, it is clear that the cell wall/membrane structure is likely key to this difference. Further, Esteban-Ferrer et al. (2014) found Gram-positive bacteria to have greater dielectric constant values, indicating higher capacitances (Equation 35) and supporting the observation in this study of larger negative phase values (275). In agreement with this conclusion, equivalent circuit modelling of the 24-hours *S. aureus* LB medium data showed an increase in capacitance (constant phase element magnitude). This was not, however, a rapidly emerging differentiator.

Within these experiments, therefore, several mechanisms were found to impact the bacterial impedance signatures in culture medium (summarised in Table 7.1). Whilst some late inter-species signature differences began to emerge, in particular between the Gram-positive and -negative species studied, a larger range of bacterial species and strains would need to be investigated to confirm this preliminary finding. Overall, the rapid detection of a number of common wound pathogens was successfully achieved, within 30 minutes. This presents a significant advantage over the Ag/AgCl sensor results and previous carbon electrode studies. The normalised impedance changes enabling rapid detection were, however, observed to have a transient nature which could complicate their use as a diagnostic marker. Further, the simultaneous sterile negative control data was very beneficial to the detection of the small magnitude bacterial signature deviations observed here. For an ideal *in situ* wound sensor, no real-time sterile comparison would be required. This may be possible if, for example, the

bacterial signature features were of a larger and sustained magnitude that could be confidently, rapidly be identified. For these reasons, platinised carbon sensors were next explored.

Table 7.1. Summary of key carbon electrode LB medium growth experiment impedance changes for the studied wound bacteria.

Impedance Change	Normalised Modulus Decrease Below 1 kHz	Normalised Phase Trough at 1 kHz	Normalised Phase Peak at Highest Frequencies
<i>S. aureus</i>	Magnitude of feature increasing to 2.5 hours then decreasing to intermediate value.	Trough at around 1 kHz growing in size until 2.5 hours then diminishing.	Late peak emerging by 24 hours.
<i>S. epidermidis</i>	Magnitude of feature increasing to 2.5 hours then decreasing to intermediate value.	Trough at around 1 kHz growing in size until 2.5 hours then diminishing.	Late peak emerging by 24 hours.
<i>P. mirabilis</i>	Magnitude of feature increasing to ~3 hours then sustained.	Trough at around 1 kHz growing in size until 2.5 hours then small magnitude decrease.	No significant change observed.
Proposed Explanation	Feature dominated by cell growth related processes. A significant reduction in charge transfer resistance is associated with these processes. For <i>P. mirabilis</i> cell adherence over time has an additional but small contribution to this feature, possibly influencing its sustained magnitude.	Feature dominated by cell growth related processes. Large reduction in magnitude of the feature for the Gram-positive Staphylococci due to an increasing concentration of cells adhering to the sensor surface over time.	Feature only present for the Staphylococci, due to an increasing concentration of cells on the electrode surface having a capacitive effect. Cell wall/membrane structure thought to be influential – similar changes have been used to distinguish between Gram-positive and negative species in the literature. Motility could additionally influence this species-dependant change.

7.2.3 PCE Sensor Conclusions

The final sensors investigated in this thesis for the rapid detection of wound bacteria were screen-printed platinised carbon electrodes. Platinum supports the electro-catalysis of a wide range of small organic molecules and is one of the metals most frequently used to modify

carbon screen-printed electrodes (262). Cited applications for platinum modified electrodes include hydrogen peroxide sensing (with applications in glucose monitoring, for example Fu et al. (2017) detected glucose in serum samples via platinum “nanoflower” modified carbon electrodes (276)) and alcohol monitoring, with the platinum modifications enhancing electron transfer at the sensor surface (277). In this thesis, an immediate advantage observed during impedance measurements with the PCE sensors was the greatly reduced baseline impedance (when compared to the basic carbon sensors). Exemplified in Figures 5.1 and 6.1, the PCE sensors showed a baseline impedance magnitude in sterile LB medium of around $10^4 \Omega$ at 0.1 Hz, compared to over $10^6 \Omega$ at 0.1 Hz for the carbon sensors. As discussed in Section 7.2.2, a high baseline impedance can mask smaller impedance changes arising due to bacterial growth, limiting the power of this technique (118). Although a slightly increased negative control instability is visible for the PCE sensors at the lowest and highest frequencies in this data (Figure 6.1), this is an expected consequence of the smaller baseline impedance. Impedance changes of a magnitude around $10^3 \Omega$ for example would appear far larger relative to the $10^4 \Omega$ PCE baseline than the $10^6 \Omega$ carbon baseline magnitude. Despite this slightly more prominent sensor instability compared to the carbon sensors, the stability of the PCE sensors remained far more satisfactory than that seen with the Ag/AgCl sensors (Section 7.2.1).

Bacterial growth experiments in LB medium were again performed to assess the suitability of these impedance-based sensors for rapid bacterial detection. Providing a direct comparison to the previous carbon sensor results, this first involved the use of an initial sterile measurement acting as the normalisation point. Growing *S. aureus* from a concentration of 10^6 CFU/mL to 10^8 CFU/mL, no bactericidal action was evident. With these PCE sensors, clear bacterial signatures emerged during growth. In particular, a decrease in normalised modulus for frequencies below 1 kHz was observed, in a similar shape to that seen with the carbon sensors. Notably, this change was of a larger magnitude with the PCE sensors (around 0.4 vs 0.2 normalised units), increased in magnitude over a longer period (16 hours vs 2.5 hours) and then remained at a sustained level. Sustained normalised phase changes also evolved over a similar time scale, with a broad trough centred around 100 Hz emerging. Despite some differences in the frequencies and timings of these key impedance changes, interestingly they were of the same general form as those reported for the simple carbon sensors. Importantly, once more, they were of a larger magnitude and did not diminish with time- desirable qualities for a predictable and reliable bacterial signal. A key achievement, once more significant normalised impedance changes were detected after only 30 minutes (in this instance via a normalised phase

decrease at 60 Hz, Section 6.2.1). These PCE sensors, therefore, appeared to be just as capable as the carbon sensors of rapid bacterial detection.

Advancing the experimental protocol towards a more realistic *in situ* wound measurement scenario, further LB growth experiments were conducted with *S. aureus* and *P. aeruginosa* without the use of a sterile normalisation point. Crucially, the obtained signatures once again both displayed the characteristic, prominent sustained normalised modulus decreases at frequencies below 1 kHz and normalised phase troughs centred around 100 Hz (Figures 6.4 and 6.5). The earliest time to significant impedance changes emerging increased from 30 minutes to 3.5 hours for *S. aureus*, and 1.5 hours for *P. aeruginosa*. Although an expected consequence of performing bacterial signature normalisation against a non-sterile starting point, the extent of this increase was also influenced by an initial sensor settlement time, seen to be variable between experiments (for example, refer to Figures 6.4D and 6.5D). For both the bacterial and sterile sensors an initial decrease in impedance occurred before any clear deviation between the two conditions occurred. Independent of whether an initial sterile measurement was performed for normalisation, this settlement time is believed to be a result of background surface processes requiring a finite time to decay (186). Despite the sensors being conditioned for at least 16 hours in sterile LB medium prior to the experiment to limit these processes, replacing the medium and applying a potential to the electrode during measurement may have resulted in background currents that required an initial time to settle. Further, the temperature changes induced by placement into the incubator would have impacted ionic diffusion and the electrochemical equilibrium (Chapter 2), which may have caused this initial impedance decrease for both the bacterial and sterile sensors (278). In future, studies to improve the settlement time of these sensors could be conducted, including the trialling of electrochemical pre-treatments such as those detailed by Wei et al. (2007) (232). In the obtained impedance signatures for *S. aureus* and *P. aeruginosa*, some slight feature magnitude and timing differences were observed, however, these experiments were performed at different times. Due to the discussed differences observed in the negative control signatures, the legitimacy of these differences was more appropriately assessed in later SWF and WBM studies where experiments were conducted simultaneously.

Once more, a greater understanding of the processes underpinning these characteristic bacterial impedance signature features was sought. Due to the impedance changes characteristic of bacterial growth being largely similar to those observed with the carbon sensors, it was anticipated that similar mechanisms would be responsible. Supporting this hypothesis, despite

a more complex equivalent circuit model being employed to encompass the low frequency diffusion behaviour observed with the PCE sensors (Section 6.9), once more a significant reduction in charge transfer resistance was attributed to bacterial growth in LB medium. As previously stated, a number of other studies similarly report such an occurrence when using carbon-based sensors, attributing this change to an increase in the number of bacterial cells which facilitate charge transfer across the interface (258–260). This charge transfer change may, therefore, be a consistent indicator of bacterial growth when using carbon-based sensors. Further supporting this conclusion, when performing measurements of *S. aureus* and *P. aeruginosa* in saline solution where growth was inhibited, a significant increase in charge transfer resistance occurred. A similar result has been reported by Li et al 2008, who associated an increase in R_{ct} to the adhesion of *E. coli* to their sensor (279). Via circuit fitting, the impedance coefficient of the Warburg diffusion element was additionally found to significantly decrease during bacterial growth. This may have been induced by bacterial metabolism of media components, breaking them down into smaller molecules. A reduction in radii by this means would result in increased mobility and an increased diffusion coefficient for example, thus decreasing the impedance of mass transfer (Chapter 2). Changes to Warburg impedance may also be associated with biofilm formation (280).

Furthermore, the experiments conducted in 0.9% w/v NaCl (saline) once again highlighted that the bacterial signatures observed in LB medium were dominated by growth related processes. Despite both cellular settlement and attachment to the sensor surface over time and cell concentration dependant normalised impedance changes being observed, these were detected via increases in normalised modulus and phase unlike the characteristic decreases observed in the growth signatures (Section 6.7). Such an increase in impedance is likely a result of electrode surface coverage, similar to that reported by Zikmund et al. (2010) following *E. coli* impedance measurements (131). Further, the increase in normalized absolute phase corresponds to an increasingly capacitive response; bacterial cell attachment to an electrode surface has been linked changes in interfacial capacitance previously (121,123). When using the simple carbon sensors, a normalised phase peak was associated with an increasing concentration of Gram-positive cells, however, with these sensors no clear Gram-positive/negative distinction arose. Ultimately the changes observed here were not the same as those identified to be characteristic of bacterial growth in LB medium. It was, therefore, concluded that the growth medium responses were dominated by mechanisms other than those related to direct cell contact, such as metabolism of available nutrients (as was also concluded for the carbon sensors).

7.2.4 Summary - Electrode Material Selection in the Context of the Project Objectives

Ultimately, based upon the evidence presented in the preceding sections, it was concluded that the PCE sensors were the most suitable for the intended *in situ* wound monitoring application. Both carbon and platinum are widely used in the medical device industry due to their very good biocompatibilities (281,282). Platinised carbon has also been shown to be biocompatible, for example when used *in vivo* to monitor brain activity in rats (283). The toxicology of the PCE sensors would be a regulatory concern going forward, however, these previous assessments indicate that the sensor would be suitable for contact with a wound. Despite continuing to explore the use of each of the three sensors for bacterial detection in the simulated wound bed model (discussed in Section 7.3), the superiority of the PCE sensors was evident from these simple LB medium and saline solution experimental conditions. This decision is placed in the context of the first two research goals (Chapter 1) below.

1. Through testing different electrode materials, determine the most suitable for rapid bacterial detection.

The Ag/AgCl Woundsense electrodes were opposed to this goal, displaying both bactericidal properties and instability during sample measurement, consequently preventing significant impedance changes due to the presence of bacteria from being rapidly detected. With the simple carbon sensors, their greatly improved stability and inertness led to rapid bacterial detection within 30 minutes in LB medium. The comparatively higher baseline impedance of these sensors and the transient nature of the signature features were seen as drawbacks to their use, however. Directly addressing these concerns, with the PCE sensors more pronounced impedance signatures were observed due to their lower baseline impedance. Further, these signatures were sustained, and rapid bacterial detection with 30 minutes was still possible.

2. Identify the key changes to impedance that occur during bacterial growth in culture media.

For both the carbon and PCE sensors normalised impedance changes characteristic of bacterial growth in culture media were identified for common wound pathogens. With the carbon sensors, for all species studied most notably a decrease in normalised modulus below 1 kHz and a normalised (absolute) phase trough centred around 1 kHz emerged. Despite rapidly emerging, for the Gram-positive Staphylococci studied the magnitude of these features diminished over time and a later high frequency normalised phase peak emerged. Whilst no strong species differentiators such as this emerged when using the PCE sensors, the key normalised impedance signature features that rapidly emerged during bacterial

growth were of a far larger and sustained magnitude. Specifically, a decrease in modulus below 1 kHz and a normalised phase trough centred around 100 Hz emerged. Later investigations involving more complex bacterial growth conditions and algorithmic methods found that it was possible to differentiate between bacterial species using the impedance signatures obtained with the PCE sensors- these are discussed in Sections 7.3 and 7.4.

7.3 The Relevance and Importance of the WBM Used to Assess Sensor Performance

7.3.1 Bacterial Growth Detection in SWF

At opposite ends of the nutrient spectrum, the bacterial impedance experiments conducted in LB medium and 0.9% w/v NaCl exemplify in a stark way the influence that the culture environment can have upon the observed impedance spectra. Illustrating this with a smaller step-change, Farrow et al. (2012) noted the dependency of certain normalised impedance peaks upon glucose concentration within their culture medium when growing *S. aureus* using Ag/AgCl electrodes and this impedance technique (129). The creation of additional products because of glucose metabolism was attributed to this difference. Other influences upon impedance signature such as bacterial adaption and growth rates also have a dependency upon culture media composition (255). For this reason, an important first step in the development of a wound bed model in this study was the creation of a simulated wound fluid (SWF): a culture medium which appropriately modelled the nutrients and composition of wound exudate. As detailed in Section 3.2.2, the SWF chosen (a mixture of FBS and Solution A) mimicked the protein content, ionic content and viscosity of wound exudate (215,216).

For the Ag/AgCl sensors alone, normalised impedance changes very different to those observed during LB medium (20 mV) experiments were recorded during the SWF (20 mV) measurements. Highlighting the importance of accurately modelling the wound environment, during *S. aureus* growth a decrease in normalised modulus was seen for example, in contrast to the increase seen in LB medium (Sections 4.3 and 4.6). Now more similar in shape to the LB medium signature seen for *P. aeruginosa* (and each of those later detected with the carbon and PCE sensors), the SWF is believed to have provided a sufficiently different environment to influence this change for *S. aureus*. In addition to the composition of the SWF having the potential to result in different metabolic reactions for this species, the serum component of the SWF may have interacted with the silver particles at the sensor surface, reducing their antimicrobial influence. A reduction in silver nanoparticle antimicrobial activity by serum has previously been observed in vivo by Gnanadhas et al. (2013); a similar occurrence here may

have allowed for greater interaction between the *S. aureus* and sensor surface, resulting in the characteristic impedance decreases being observed (284). *P. aeruginosa* is commonly cited as less susceptible to silver's bactericidal action due to its production of pyocyanin (285), this is a likely reason for the characteristic normalised impedance decreases being observed for *P. aeruginosa* even in LB medium. As *P. aeruginosa* was not additionally measured in SWF, it is not clear if any additional changes to impedance spectrum would have occurred for this species, however, later WBM experiments (discussed in Section 7.3.2) were carried out with both species.

Using the simple carbon sensors, largely similar normalised impedance signatures to LB medium were obtained in SWF. Specifically, decreases in normalised modulus below 1 kHz and a mid-frequency normalised phase trough emerged for all species studied. A notable difference in these signatures, however, was their generally increasing magnitude over time. A potential reason for this is indicated by the comparative magnitude of the impedance changes observed over time. Using *S. aureus* normalised modulus as an example, in LB medium the minimum value observed at 1 Hz was 0.8 normalised units after 2.5 hours. In SWF, however, the minimum 1 Hz value observed was only 0.84 units at 24 hours. This suggests that the maximum change had not yet occurred, and a recession from the maximum may still have occurred later. Whilst the bacteria may have rapidly adapted to growth in the nutrient rich LB medium and moved quickly through the bacterial growth curve stages (Section 2.2.2), in SWF an extended lag phase and slower progression through the growth curve phases may have occurred. Wijesinghe et al. (2019) studied the impact of a range of laboratory culture media upon bacterial growth rates through optical density measurements over 14 hours, finding media composition to influence the growth curves of both *S. aureus* and *P. aeruginosa* (286). The use of similar absorbance measurements or regular colony counting during SWF and LB media measurements in future could similarly confirm differences in growth rates. Also supporting this conclusion, the earliest time to detect statistically significant impedance changes increased in SWF to at least 2 hours (*P. aeruginosa*) from at least 0.5 hours in LB medium (*S. aureus*). Further, the variation in nutrient availability and metabolic reactions in SWF resulted in slight differences in the frequencies and magnitudes of the impedance changes. Once more, a late high frequency normalised phase peak due to the capacitive influence of an increasing concentration of cells on the sensor emerged for *S. aureus* alone (Section 7.2.2), appearing to differentiate between this and the Gram-negative bacteria studied (*P. aeruginosa*, *P. mirabilis*). High frequency noise for *P. mirabilis* was present, however, limiting the significance of this finding for this species. Low frequency noise was also present during both the *P. aeruginosa* and *P. mirabilis* experiments, affecting both the sterile and bacterial sensors. As stated in

Section 5.3, this was thought to be a consequence of an electrode related experimental artefact (256). If not appropriately removed from a future device, noise such as this would adversely affect the detection of early bacterial impedance changes in the low frequency region.

Finally, using the PCE sensors growth signatures were obtained for *S. aureus*, *P. aeruginosa*, *E. coli* and *P. mirabilis* (see Figures 6.10, 6.11 and 6.12). In each instance the characteristic bacterial impedance changes observed in LB medium once more emerged: normalised modulus decreases below 1 kHz and mid-frequency normalised (absolute) phase trough formation. These changes can, therefore, be considered consistent identifiers of bacterial growth. This was a promising indicator that impedance changes like those identified in these laboratory experiments may be detected in a real wound environment. Whilst the key normalised impedance changes were largely similar for each species studies with these sensors, some differences were observed. Focusing upon normalised phase, for *S. aureus* and *P. aeruginosa* which were grown simultaneously (but separately) a difference in the magnitude of the change was evident from 1 hours (Figure 6.10B). The observed differences in bacterial yield are likely to be a key influencing factor in this, with the greater proliferation of *P. aeruginosa* correlating with a larger magnitude of impedance change (Section 6.4, Table 6.2). When comparing the growth curves for these bacteria, Wijesinghe et al. (2019) found (via optical density measurements) that differences in proliferation varied between culture media (286). For both Brain Heart Infusion (BHI) and LB medium, *P. aeruginosa* proliferated more than *S. aureus* over the 14-hour experiments, also reaching a plateau at an earlier time. To be a valid species discriminator, the impact of real wound exudate variabilities (such as white blood cell and protease content (55)) upon bacterial growth rates must be considered in future. Further, the impact of starting concentration upon impedance change evolution is important, and further explored in Section 7.4. Once more focusing on the normalised phase signatures, other subtle differences were seen in the minima frequency and 1 Hz value in particular. Whilst some variations in sterile control signatures were evident between experiments in these regions and, therefore, some caution must be exercised, it was believed these subtle differences could be exploited for species identification. Detailed in Section 6.10 and discussed in Section 7.4, neural networks were employed for this reason. Sheybani and Shukla (2017) observed an impedance shift over time for their sterile uncoated gold sensors when measuring a SWF (containing FBS and an NaCl and Peptone solution) due to protein biofouling (130). To reduce this effect, polymeric coatings were employed. Due to the significant bacterial signatures rapidly detected with the PCE sensors here, such coatings are not considered necessary at this point.

With the PCE sensors providing consistent bacterial signatures in SWF that were identified the most rapidly (after 1 hour (Section 6.4)), the advantage of this sensor material was again indicated. A further benefit of these sensors was their superior performance over the other electrode materials even after the implementation of the dry preparation method (Sections 3.7.3, 6.3). For electrodes with bio-recognition elements such as the paper-based sensors described by Ratajizak et al. (2020), dry storage is preferential for long-term sensor storage due to the decay in performance of these elements as a result of oxidation when stored wet (287). The sensors in this study do not, however, contain any recognition elements such as enzymes or antibodies. Instead, a key motivator for the use of dry room temperature storage in this instance was cost and feasibility for entry to market, driving factors similarly noted by Obaje et al. (2016) in the design of their carbon screen-printed sensors for molecular-based antimicrobial resistance sensing (288).

As summarised by Kadam et al. (2019), various platforms have been developed for modelling the wound environment in vitro (217). As in this section, many of these involve the use of bacteria and a SWF to mimic the nutrients and other chemical constituents of wound exudate. The findings discussed in this section therefore represent an important first step to the wound modelling process, however, a more accurate model of the wound structure was desired. Achieving this, the extracellular matrix of the wound was modelled using a collagen-gel based model adapted from that developed by Werthén et al. (2010): this is discussed in the subsequent section (216).

7.3.2 Bacterial Growth Detection in the WBM

The wound bed model developed by Werthén et al. (2010), containing a 3D collagen gel structure and serum proteins, successfully replicated bacterial growth structures akin to that observed ex-vivo in chronic wounds (216). When studying *S. aureus* and *P. aeruginosa* growth in the model, the authors found that bacteria embedded themselves within the gel in EPS-producing aggregates, signifying biofilm formation (Section 2.2.4). For this reason, a very similar model (with the SWF composition slightly adapted (215)) was employed in this study to assess the bacterial growth and impedance response in a wound-like environment. Each WBM made in this thesis consisted of an electrode in contact with a simulated wound fluid-covered collagen “wound bed”, with the location of the sensor varying based on substrate flexibility as detailed in Chapter 3 (see Figures 3.14 and 3.24).

When using this purpose made WBM, bacterial growth was found to differ to that observed previously in culture medium for the Ag/AgCl sensors at 200 mV. Whereas in LB medium the concentration of *P. aeruginosa* was seen to decrease from around 10^7 CFU/mL to $< 10^4$ CFU/mL over the 24-hour experiment due to the bactericidal action of silver, the wound bed model provided a more protective environment that supported growth from around 10^7 CFU/mL to 10^9 CFU/mL over the same timescale. This observation furthers Werthén et al.'s original finding that bacteria growing within the collagen gel form protective biofilms – in their study the decreased efficacy of antibiotics (ciprofloxacin and rifampicin) against these cells compared to planktonic cells was observed (216). Here, an increased tolerance to silver was observed. Summarised by Joshi et al. (2020), silver (in the form of nanoparticles or ions) has multiple modes of action against bacterial biofilms including cell membrane disruption, enzyme damage and ultimately inhibition of metabolic processes (289). Although the biofilm structure and EPS matrix provides extra protection to the embedded bacteria, silver can interact with and penetrate biofilm material, leading to cellular damage and death. Metal nanoparticles such as silver have emerged as effective bactericidal agents against many multi-drug resistant species of bacteria, however, a number of resistance mechanisms have recently been identified (290). Summarised by Niño-Martínez et al. (2019), these include changes to the biofilm such as greater EPS production, electrostatic repulsion and genetic mutations which increase tolerance to the metal (290). A further resistance mechanism potentially influential in this investigation is the production of pyocyanin by *P. aeruginosa*. In a study by Ellis et al. (2019), *P. aeruginosa* displayed greater tolerance to silver than *S. aureus*, hypothesised to be due to the reduction of Ag^+ ions to Ag by its metabolite pyocyanin (291). Here, clear pyocyanin production by *P. aeruginosa* in the WBM (characterised by green pigmentation) is highlighted in Figure 4.13, supporting this theory. Future studies exploring how the growth of different bacterial species varies between culture medium and the WBM with the Ag/AgCl sensors at 200 mV may provide greater insight into the underpinning resistance mechanisms. This particular result does, however, indicate that silver may not be as bactericidal against *P. aeruginosa* in wound tissue as it would be for planktonic cells within exudate for example. This may have implications for the use of certain silver-based dressings. Mulley et al. (2014) previously noted the influence of human serum upon bacterial tolerance of silver from wound dressings, and that the additional propensity for biofilm formation in the wound bed may be an influencing factor for consideration (249).

Despite the improved growth of *P. aeruginosa*, the impedance signatures obtained with the Ag/AgCl sensors at both 20 mV and 200 mV were unsatisfactory for rapid bacterial detection. In addition to a lack of clear bacterial signatures with these sensors, large inter-sensor variation

in the normalised impedance plots (present as large standard deviation shading) was a key inhibitor of detecting significant changes. This noise was of a large magnitude across all measured frequencies. As the level of noise was not similarly increased in the carbon and PCE sensor plots, this was believed to be due to the unique set-up adopted with the Ag/AgCl sensor WBM. Specifically, these flexible sensors were folded in such a way that the electrodes were on top of the artificial wound, in direct contact with the WBM which was formed in a petri dish (Figure 3.14). Whilst this arrangement was adopted to mimic the anticipated positioning of a sensor on a real wound, the contact of the electrodes with the WBM surface was believed to have been inconsistent and unstable. Due to the mounting evidence against the use of these sensors for wound infection detection however, a new model with the sensors at the base was not explored in this instance.

Conversely, for the carbon and PCE sensors, the sensors were fixed in place at the base of the WBM and no significant increase in normalised impedance plot noise compared to the SWF experiments was observed. Interestingly, both the carbon and PCE sensors did display greater sensor inconsistency (error shading) in the raw, not normalised impedance plots compared to the SWF plots. This is exemplified by comparing Figures 6.9B and 6.13B. The noise was not carried through into the normalised plots, emphasising a key benefit of the normalisation process. As the composition of wounds is highly variable (Chapter 1), it is promising to observe that this may not greatly impact the measured normalised impedance signatures used for bacterial detection. The cause of this noise, most notable at the mid to low frequencies, is believed to be inhomogeneous distribution of the collagen gel on the sensor surface. An expected consequence of the manual collagen-matrix pipetting process, using a larger volume of collagen matrix solution to produce a gel of greater depth may have created a more uniform result. The high cost of the collagen I solution, however, prevented this. Further, the collagen matrix is a viscous solution, prone to retaining air bubbles that decrease the uniformity of the gel (292). Whilst using an agar based in-vitro WBM such as that used by Sheybani and Shukla (2017) may improve the uniformity of the artificial wound formation on the sensor surface, the important clinical and microbiological significance of the collagen-based structure (detailed previously) is not mirrored (130).

The normalised impedance signatures observed for *P. aeruginosa* and *S. aureus* growth in the WBM using both the carbon and PCE sensors were very similar in shape to those obtained in the SWF, once more reinforcing the reliability of the key impedance changes observed with each sensor. Differences between the two species' normalised phase response at high frequencies again made differentiation between them possible when using the carbon sensors.

As discussed in Section 7.2.2, this is believed to be a consequence of the different cell wall/membrane structures between Gram-positive and Gram-negative species affecting capacitance at high frequencies (275). The ability to differentiate between such species in the wound environment could support more targeted antibiotic selection more rapidly than currently possible via laboratory-based analysis. A hospital-based study in Japan found that antibiotic selection based upon Gram-stain resulted in greatly improved broad spectrum antibiotic stewardship, around a 50% reduction in prescribing costs and an equally effective treatment of various infections including SSTIs when compared to the standard Japanese prescribing guidelines (293). Gram-negative bacteria are generally more resistant to antibiotics and careful selection of antimicrobial agents for their effective treatment is necessary (294). This impedance-based species differentiation could have the potential to support treatment selection in future, however, the feature did not emerge until the final 24-hour measurement in these WBM experiments despite general bacterial detection from 3 hours with these carbon sensors (Section 5.4).

A key experimental drawback impacting the PCE sensor WBM results was the use of manual clipping during the experiments to measure multiple working electrodes on a single sensor, rather than automated in-incubator measurements of single electrodes from multiple sensors (as was possible with the carbon sensors). As detailed in Chapter 3, this was due to the high cost of the collagen solution rendering it not possible to use the previous multiple sensor arrangement with these larger sensors. By manually connecting the impedance analyser to the relevant sensor for each measurement, the WBMs were regularly disturbed and did not receive the same duration of incubation at 37 °C as previously. Whilst this is believed to have increased the time to detect significant impedance changes, conducting a manual connection SWF experiment simultaneously to the WBM experiment revealed that very rapid bacterial detection in SWF was still possible despite the reduced incubation (from 1 hour, *P. aeruginosa*). Conversely, significant changes due to the presence of bacteria in the PCE sensor WBM did not emerge until between 5-24 hours (Section 6.5). In future, performing additional more frequent measurements would pinpoint a more precise time to significance, however, the increased time is clear. The collagen gel is believed to be responsible for this. With the placement of the collagen gel on top of the sensor and bacterial aggregation within the gel promoted (216), early direct contact of bacterial cells with the sensor may have decreased, resulting in this increased time to detect bacterial impedance changes (Figure 6.16). This result once more highlights the importance of modelling the wound environment to obtain a more realistic approximation of bacterial detection time and signatures within a real wound. Furthering this, the gravitational influence upon impedance signatures and the impact of

separating a second sensor from the collagen gel is discussed in Section 7.3.3. The normalised impedance signatures obtained with the PCE sensors were again those now known to be characteristic of bacterial growth – a decrease in modulus below 1 kHz and a mid-frequency phase trough. Except for some slight differences in the magnitude of these changes, the signatures obtained for *S. aureus* and *P. aeruginosa* were again very similar in appearance. This method of bacterial detection, therefore, appears to produce a very consistent result despite very different growth conditions. This promising result suggests that it may be possible to detect bacteria via these characteristic changes to normalised impedance in a real wound environment.

7.3.3 The dWBM and Gravitational Influence Upon Single Species Signatures

As discussed previously, forming the collagen gel directly on the PCE sensor surface was believed to inhibit some early interactions between bacterial cells and the electrode that were previously rapidly detected. Further, in a real-world scenario the sensor would be placed onto an exuding wound and not be fully covered by a collagen coating as in the WBM. The sensor must also operate at multiple orientations and cannot rely on the gravity induced settlement of cells on its surface. For these reasons, the double sensor WBM (dWBM) was developed. In this arrangement, an additional sensor face down at the top of the WBM was incorporated (Figures 3.26, 3.27).

Due to the configuration of this model, unfortunately a few additional sources of inconsistency arose which led to larger noise being present than previously observed in the WBM. Factors believed to be influential in these experiments are depicted in Figure 7.1. Firstly, despite holes being cut into the top sensor to allow for air outflow when filling the model with SWF, it is possible that unseen air bubbles were trapped on the top sensor surface. Bubbles at the surface of electrodes have previously been considered in the context of electrochemical reactors by Angulo et al. (2020) (295). Blocking part of the electrode surface, bubbles preferentially form in hydrophobic electrode surface pits. They have a significant (size-dependant) impact upon many electrochemical parameters including mass transport, and can cause increases in both charge transfer resistance and solution resistance (295). Variation in bubbling between the models is, therefore, a likely contributor to the greater inconsistency between top sensors of the dWBM compared to the base sensors (Section 6.5). Secondly, the dWBM arrangement resulted in a more enclosed model with reduced airflow. This is believed to have prevented full ethanol evaporation during model sterilisation, contributing to a lower increase in cell density

for *S. aureus* and *P. aeruginosa* in the dWBM compared to in previous models. Residual ethanol molecules are also believed to have contributed to the overall noise in these experiments. As bacterial broth cultures proliferate well in sealed universal containers during the formation of stock cultures (Section 3.2), it was not believed that the enclosed structure itself directly impacted growth. Thirdly, repeated manual clipping to attach the electrode connectors to the impedance analyser via crocodile clips is believed to have damaged the electrode connectors. Whilst manual clipping was also used for the WBM and the dWBM base sensors, the connectors were not easily visible for the top dWBM sensors, so a greater number of manual adjustments were made. Further, the connection was likely inconsistent between measurements. This is also believed to have contributed to the increased top sensor noise. In future, manufacturing the PCE sensors on flexible substrates would enable a face down sensor WBM such as that used with the Ag/AgCl electrodes to be adopted, negating these specific issues.

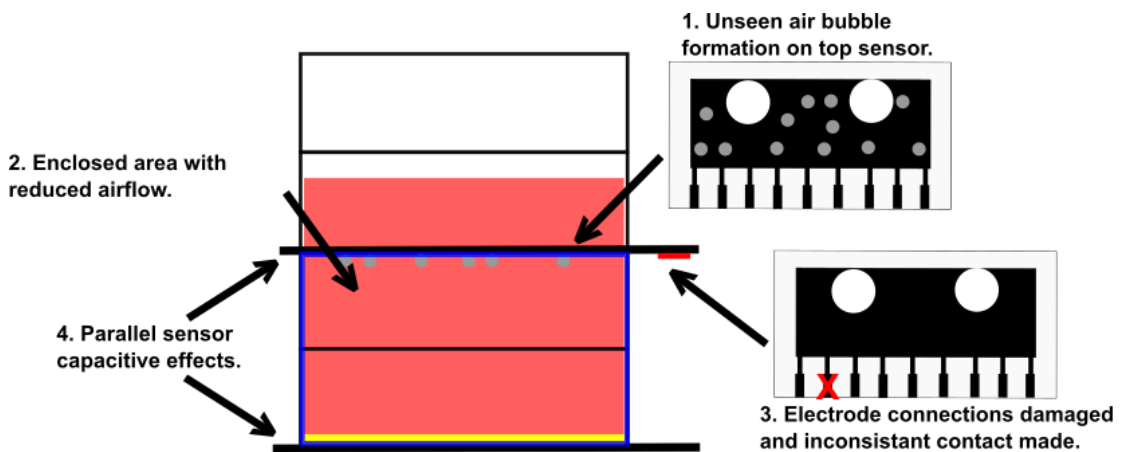


Figure 7.1. Summary of the unique dWBM factors believed to be influential in the quality of experimental results. Namely: trapped air bubbles under the top sensor, the enclosed nature of the model, connection issues due to poor connector visibility and capacitive effects.

A final additional source of noise, placing two sensors in parallel would have had a capacitive effect (Figure 7.1). Using Equation 35 (Section 2.3.8) the magnitude of this capacitance can be estimated. Assuming $\epsilon_0 = 8.854 \times 10^{-12}$ F/m, $\epsilon_r = 80$ (approximately that of water), $A = 60$ mm x 33 mm = 1.98×10^{-3} m² and $d = 0.01$ m:

$$C = \frac{\epsilon_0 \epsilon_r A}{d} = 0.14 \text{ nF}$$

This extra capacitance is negligible when considering the baseline impedance magnitude of 10^3 – 10^4 Ω (Section 6.5), however is likely a key contributor to the increased low frequency negative phase value in the dWBM compared to the WBM (Section 6.5). Further, this parallel

plate arrangement with the conductive SWF acting as the intervening dielectric will have led to leakage resistance in the circuit, with the unintended current flow paths created resulting in additional model noise. This was likely non-uniform, due to collagen coating inhomogeneity for example.

Even with these increases in measurement noise, valuable insight was gained from the dWBM experiments, supporting the use of this novel model for future studies involving a wider range of pathogens with rigid sensors. Firstly, despite being placed face down at the top of the model with a distance of 1 cm between the top sensor and collagen wound bed, clear normalised bacterial impedance signatures emerged during 24 hours of growth (Section 6.5.2). This result supports the idea that the sensors could be used at multiple orientations, as would be the case *in situ*. Further, the result confirms that gravitational settlement is not necessary to obtain a bacterial impedance signature with the PCE sensors. This is of particular interest for the *S. aureus* cells studied: this species is widely regarded as non-motile, with the exception of some spreading and gliding characteristics (296). These cells are, therefore, dominantly affected by gravitational forces in this static wound model and would quickly settle on the base sensor for the duration of the experiment. Conversely, *P. aeruginosa* cells are known to have swimming motility (Section 2.2) and could overcome gravitational forces if necessary to reach favourable growth conditions in other areas of the model. This result also further confirms the earlier conclusion that direct cell/electrode interactions are not the dominant contributor to the normalised impedance signatures obtained during growth (Section 7.2).

Whilst bacterial signatures were obtained for both the top and base sensors, these must be compared to truly assess the effects of gravitational settlement. First considering the base sensors, these signatures could be expected to be identical to the impedance signatures obtained in the simple WBM for *S. aureus* and *P. aeruginosa*. Interestingly, this was not the case. As shown in Figure 6.20, for the first time with the PCE sensors clear differences between these two species emerged by 24 hours. Most notable in normalised phase, clear differences are evident between both the signatures obtained in the WBM (Figure 6.15B) compared to that obtained by the dWBM base sensor (Figure 6.20C), and between the species themselves in the dWBM. These differences are particularly pronounced at 1 Hz and 100 Hz. Whilst *P. aeruginosa* has retained a similar albeit slightly shifted broad trough shape in the dWBM, *S. aureus* displayed a more defined phase trough over a smaller frequency range, minimising at 1 Hz. This difference between the WBM and dWBM base sensor for the *S. aureus* signature in particular may have been caused by the presence of the residual ethanol discussed previously. The ethanol could have directly impacted the impedance, for example via the electro-oxidation

of this substance enhanced by the presence of platinum in the electrodes as was studied by Han et al. (2012) (297). Alternatively, the ethanol or reaction intermediaries may have interacted with molecules produced during *S. aureus* metabolism to create this capacitive response. Not observed during *P. aeruginosa* growth, the ethanol could have fully evaporated in the *P. aeruginosa* dWBM or the ethanol did not interact in the same way with its metabolites for example. Further, the volume of SWF relative to the volume of collagen gel was greater in the dWBM and, as previously discussed, the parallel sensor capacitive effects may have also been influential. Comparisons between the top and base sensor responses revealed the influence of gravity upon the bacterial signatures. For the *S. aureus* model, differences at 1 Hz and 100 Hz normalised phase were evident, with the peak size diminished for the top sensor but the same general shape retained at 24 hours (Figure 6.20D). The far smaller difference for *P. aeruginosa* when comparing between the top and base sensors allows us to reach the conclusion that the bacterial signatures are enhanced by the gravitational settlement, and that bacterial motility impacts the level of this influence. This result is further explored in the context of polymicrobial cultures in Section 7.3.4. Assessing the effects of gravitational settlement upon their bacterial sensor, Sheybani and Shukla (2017) concluded that gravity had a minimal influence upon the measured impedance response (130). Their face down sensor did, however, have direct contact with their agar based artificial wound bed and did not have the extended volume of SWF separating the sensor from the base of the model as in this study. The experiment in this study is therefore a more powerful investigation into the effects of gravity upon sensor response, although further removed from a clinical sensor arrangement.

7.3.4 Multispecies Bacterial Detection in the WBM and Gravitational Influence

As discussed within Chapter 1, the skin and wounds are typically colonised with a wide range of bacterial species. Bessa et al. (2015) found around a quarter of wounds to have a multispecies (polymicrobial) infection (26). *S. aureus* and *P. aeruginosa* are cited as the most common combination of bacteria, commonly found in chronic wounds for example (26,298). Such polymicrobial infections have been associated with increased virulence and delayed wound healing (299). For these reasons, studying this combination of bacteria in the WBM and dWBM was an important step in understanding the response of the bacterial sensor in a wound environment.

During these co-culture experiments, *P. aeruginosa* growth was seen to dominate over *S. aureus*: the increase in cell concentration for *P. aeruginosa* was in line with the parallel single species cultures, whereas the *S. aureus* concentration decreased slightly (Section 6.5). This reflects the “antagonism” of *P. aeruginosa* described by multiple researchers when studying this combination of bacteria in vitro (299–301). *P. aeruginosa* is believed to out-compete *S. aureus* and inhibit its growth in these studies due to factors such as its rapid environmental adaptation and excretion of harmful molecules (300). For example, the electron transport chain of *S. aureus* can be disrupted (Section 2.2.3), forcing the species to use a less successful mode of metabolism – fermentation. When studying wound infections in vivo using mice, Dalton et al. (2011) repeatedly found *P. aeruginosa* to dominate an infection after 2 days, constituting 100% of the bacterial content despite only making up 1% of the starting inoculum with a wide range of other bacterial species (299). Interestingly, within the WBM and dWBM developed here, despite a lack of growth of *S. aureus* over the 24-hours measurement period, the species did survive. DeLeon et al. (2014) note the difficulty that many researchers have in co-culturing these two species of bacteria in vitro, despite their common occurrence together in wound infections (302). Their simulated wound medium, consisting of Bolton broth, bovine plasma and red blood cells, supported the simultaneous growth of both species. The WBM and dWBM used in this thesis have similarly enabled the successful co-culture of these species (albeit without an increase in *S. aureus* cell density) and can serve as an effective wound model for monitoring multispecies infections such as those seen in chronic wounds. The dominance of *P. aeruginosa* over *S. aureus* has previously been associated with changes to antibiotic efficacy. Whilst it has widely been found that these cultures show an increased tolerance to antimicrobial agents, Trizna et al. (2020) found that adding *S. aureus* to a *P. aeruginosa* culture can actually decrease its tolerance to certain antibiotics (300). This could have important consequences for wound treatment in future. Furthermore, understanding the interactions of these species is an important clinical problem, and the ability to rapidly detect a wound infection caused by these species is of critical importance.

The normalised impedance signatures obtained during this multispecies growth provided great insight into the ability of the PCE sensors to detect polymicrobial infections. Firstly, in the WBM the normalised phase signatures reflected the bacterial growth pattern, with the polymicrobial signature closely following the *P. aeruginosa* signature. By 24 hours, the polymicrobial signature was significantly different to the *S. aureus* signature (200 Hz, $p = 0.001$, Section 6.5.1). Within this WBM experiment, it did not appear possible to differentiate between a pure *P. aeruginosa* culture and the polymicrobial culture. In the dWBM however, where clearer signature differences between *S. aureus* and *P. aeruginosa* were observed (as

discussed in Section 7.3.3), further insight could be gained. Once more the normalised phase signatures were of particular interest. Despite the dominance of *P. aeruginosa* in the co-culture, for the base sensor the polymicrobial signature closely followed that of *S. aureus*. This is believed to reflect the gravitational influence upon the non-motile *S. aureus*, with these cells having a dominant presence on the base sensor. This result confirms the earlier conclusion that cell motility can influence the bacterial signature via gravitational influence and can cause identifiable differences in normalised impedance signature to emerge. Conversely, the top sensor recorded a signature for the polymicrobial model which lay at an intermediate location between the *P. aeruginosa* and *S. aureus* signatures. This suggests that both species were influential in the top sensor signal. This top signature may, therefore, be the result of both compositional changes to the SWF (due to both species) and adsorption of *P. aeruginosa* cells. Within the dWBM, therefore, a unique polymicrobial signature was detected. This is of particular importance as it could enable all species responsible for an infection to be detected by the sensor, not just the dominant pathogen. Treating infections containing multiple species can be problematic, especially if (as can be the case with these two species) *P. aeruginosa* causes *S. aureus* to change into small colony variants (SCV) (286,300). SCV are fastidious variants with altered characteristics and can be difficult to detect via current clinical microbiology tests (303). If a rapid bacterial detection device such as this PCE sensor was able to detect these variants, it would be very advantageous.

Previously, Ward et al. (2014) were able to detect *P. aeruginosa* when grown as part of a co-culture with *S. aureus* using a screen-printed carbon sensor and EIS (118). They similarly found the *Pseudomonas* strain PA14 to outcompete *S. aureus* (in this case strain RN4220), however, as they did not see any difference between the polymicrobial and *P. aeruginosa* signatures after 69 hours of growth it was concluded that PA14 alone was responsible for the observed impedance signature. The PCE sensors used here advanced this work, both detecting a significant *S. aureus* impedance signature and detecting a unique polymicrobial impedance signature that could be exploited in future to reveal the complete bacterial content.

7.3.5 The Influence of Wound Dressings Upon Bacteria and Impedance

Assessing the wider influence of the wound environment upon the PCE sensor response, the influences of a range of common wound dressings were determined. The main findings of these studies are summarised in Table 7.2.

Table 7.2. Summary of key wound dressing WBM experiment findings (from Section 6.6).

Dressing	Type	Effect on baseline impedance	Effect on error	Impact on <i>S. aureus</i> growth over 24 hours	Normalised impedance signature
Acticoat absorbent with SILCRYST™	Calcium alginate dressing with nano-crystalline silver	Slight increase	No visible change	Decrease in viable cell count (10^6 to 10^4 CFU/mL)	Increases in low frequency modulus and phase for both sterile and bacterial models, no significant differences found
Advazorb	Non-adherent foam dressing	Large increase across all frequencies due to drying	Large increase in errors	Colony counting not possible due to adsorption	Larger modulus increase for sterile model but large errors prevented significant findings
N-A® Ultra	Silicone coated knitted viscose dressing	Slight increase	Slight increase	No effect	Characteristic bacterial impedance signatures obtained
Activon Tulle	Knitted viscose dressing with Manuka honey	Large increases in mid-low frequency area	No visible change	Decrease in viable cell count (10^6 to $<10^2$ CFU/mL)	No significant bacterial signatures emerged
Mepitel®	Soft silicone coated atraumatic wound contact layer	Large increases in mid-low frequency area	No visible change	No effect	Characteristic bacterial impedance signatures obtained

Whilst each of the dressings resulted in some increase in the baseline impedance of the WBM, this is only believed to have hindered the obtained impedance result when in combination with the very large errors seen with the Advazorb foam dressing. This dressing caused drying of the WBM over the course of the experiment due to its highly absorbent nature, reducing the volume of electrolyte (SWF) available for ion transport. Changes to impedance as a result of moisture changes in the wound environment have previously been exploited by Ohmedics Ltd's Woundsense device (117). The result observed here indicates that this PCE sensor may similarly be able to monitor changes to wound moisture via increases in normalised modulus in particular. The absorption of SWF into the dressing likely resulted in reduced contact and

ion transport between the working and counter electrodes, resulting in far greater resistance. Studied in detail in the context of fuel cells, An et al. (2017) for example describe the increases in solution and charge transfer resistance due to a low electrolyte volume, and suggest a minimum volume for satisfactory electrochemical performance (304). Furthermore, the presence of a highly absorbent dressing in the wound environment may negatively impact the ability of this sensor to detect infection. A foam dressing such as this would typically be applied to a moderately exudative wound, such as a pressure ulcer (67). Future *in situ* measurements to assess the remaining level of moisture in the wound after foam bandage application, and determine the appropriateness of an electrochemical sensor, would need to be performed. Further, future experiments using a dynamic WBM where the SWF is replenished may provide a more realistic model of a moist wound. This particular result could have further implications for the use of this sensor on very dry wounds, again *in situ* measurements would be required. It may be necessary to apply a saline soaked contact layer between the dressing and sensor in this situation to mitigate any negative effects of drying.

For the N-A® Ultra and Mepitel® dressings, bacterial growth was neither inhibited nor enhanced. Crucially, these dressings did not interfere with obtaining the impedance signatures characteristic of bacterial growth. With significant changes to normalised impedance in each case being identified over the same time scale as the dressing free models (from 5 hours), this result promisingly eludes to the suitability of this sensor for operation in close proximity to these dressings. Said et al. (2014) previously indicated that the presence of a wound dressing could affect the growth curves followed by *S. aureus* and *P. aeruginosa* whilst studying an AQUACEL® dressing (ConvaTec Ltd) (305). This did not appear to be the case here, however, as the normalised impedance responses of the dressing and dressing free bacterial models were closely matched.

Conversely, when incorporating the Acticoat (silver) and Activon Tulle (Manuka honey) dressings into the WBM, bactericidal action was observed. Importantly, this was reflected in both the colony counting data and the impedance signatures. No significant differences in normalised impedance between the bacterial models and negative controls were observed, indicating a lack of bacterial growth after 24 hours. This result highlights the applicability of this WBM to studying the efficacy of antimicrobial wound dressings. Said et al. (2014) adopted a SWF composed of FBS and maximum recovery diluent to study the efficacy of the AQUACEL® Ag dressing against *S. aureus* and *P. aeruginosa*, finding this growth medium increased the concentration of silver required to kill the pathogens compared to nutrient broth (305). Accurately modelling the wound environment for such studies is, therefore, an important

task. Future studies involving the use of this WBM could provide further insight into the implications of the wound bed's collagen structures upon antimicrobial susceptibility. Crucially, studies with this PCE sensor and WBM could be expanded to assess, in real time, the effect of antibiotics upon an infected wound environment. Whilst the lack of bacterial impedance signatures for these particular dressings reflects the absence of growth, for the Acticoat silver dressing there still remained around 10^4 CFU/mL viable cells present in the model after 24 hours. Future experiments involving these antimicrobial dressings and a higher starting cell concentration could be carried out to determine if an improving infection can be monitored. As previously stated, a standard definition of bacterial load for a wound infection does not exist, however it has been estimated that a bacterial load of $> 10^5$ CFU/g of tissue would constitute an infection (7). Converting this into an appropriate estimate in CFU/mL, some researchers have acted on the assumption that 10^5 CFU/g is equivalent to 10^5 CFU/mL (39), whereas others have previously estimated equivalence to a lower concentration such as 10^3 CFU/mL from a swab (40). This remaining cell concentration in the Acticoat experiment could still, therefore, be a clinically significant bacterial load that remained undetected by the sensor. The PCE sensor was, however, able to confirm that growth was not occurring.

7.3.6 Summary – Impact of the WBM Studies upon the Project Objectives

The development of an artificial wound bed model proved to be an important step in assessing the suitability of the three different screen-printed sensors for bacterial detection in a wound environment. The experiments discussed within this section ultimately aimed to address the following research objective, as outlined in Chapter 1:

3. Develop and detect bacterial growth in a wound bed model which more accurately simulates a wound environment.

Multiple factors were incorporated into these WBM experiments to incrementally provide a more accurate model of the wound environment: a SWF (consisting of FBS and physiological saline solution); a collagen gel matrix to model the wound bed tissue; co-culture of *S. aureus* and *P. aeruginosa* in the model; inclusion of an additional sensor via the dWBM to explore gravitational effects and the use of the sensor at different orientations; inclusion of a range of common wound dressings. Crucially, these models impacted the growth patterns of the bacteria studied. For example, the collagen based WBM provided more protection for the bacteria against silver when using the Ag/AgCl sensors, and antimicrobial wound dressings prevented growth and impedance signature formation. Notably, bacteria were detected via significant

normalised impedance changes using each of the three sensor types. For the first time, clear signature differences were distinguishable between *S. aureus* and *P. aeruginosa* using the chosen PCE sensors, in addition to unique polymicrobial signatures being detected. The use of the dWBM provided further insight into the interaction of these species with the sensor, and finally the wound dressing experiments highlighted the promise for the generic PCE sensor's operation in close contact with a range of dressings.

7.4 Evaluating the Algorithmic Approaches to Bacterial Signature Differentiation

The final objective of this project was to explore algorithmic methods of exploiting the PCE sensor bacterial impedance data to aid in the detection of infection, identification of bacterial species and assess bacterial load.

7.4.1 Concentration Dependent Signature Differentiation

Within the 0.9% w/v NaCl (saline) experiments, strong evidence of bacterial cell concentration dependant normalised impedance changes was gained (Section 6.7.2). To explore this further, the effects of different *S. aureus* concentrations in LB medium upon impedance were studied. Using cell densities ranging from 10^6 – 10^8 CFU/mL which (as discussed previously) were believed to reflect an established infection, it became apparent that the early impedance changes depended upon the inoculating cell density. Ultimately, it was hypothesised that the early rates of impedance change were proportional bacterial load. This was confirmed via instantaneous rate of change analysis and algorithm validation using additional experimental data (Section 6.9). Ultimately, it was found that using the rate of change (ROC) of 200 Hz normalised phase data gave the most accurate approximation of cell concentration. Further, the ROC values obtained after 1 hour provided a more consistent approximation of cell density than the maximum ROC values. Generating a far larger volume of data to calibrate the obtained ROC to cell density equations would greatly improve their accuracy, beyond the ability seen here to estimate cell density to the correct order of magnitude.

Following early bacterial impedance investigations, Firstenberg-Eden and Eden (1984) developed a detailed mathematical model to link bacterial concentration to various parameters including bacterial metabolic rate, growth medium and generation time (144). A key factor included in their algorithm which draws close parallels with the ROC analysis performed here is time to detection. Within this thesis it has been found that a higher bacterial load causes

larger initial impedance changes, resulting in more rapid detection (for example immediate significant impedance changes compared to a sterile baseline were seen for high bacterial cell concentrations in saline solution in Sections 5.5 and 6.7). Whilst Firstenberg-Eden and Eden's early model provides a far more rigorous exploration of the factors influencing bacterial impedance changes and how the initial cell density can be extrapolated from these, the ROC method proposed in this thesis offers a far simpler calculation for cell density. The algorithm could be calibrated using a large volume of bacterial experiments in the growth medium of interest to improve its accuracy. Adopting this method would, however, likely require prior knowledge of the species being measured due to species differences such as generation time and motility: a proposed species identification approach is discussed within the subsequent section. As detailed in Chapter 1, historically β -dispersion measurements have been applied to bacterial biomass calculations. For example, the "Biomass Monitor" (Aber Instruments) reviewed by Yardley et al. (2000) utilised capacitance measurements of a cell suspension to estimate biomass (148). Specifically, the change in capacitance between measurements performed at high and low frequencies (referred to as the ΔC or capacitance increment of the β -dispersion) was found to increase with an increasing cell density. This method would likely be sensitive to the additional cells present within the wound bed (such as epithelial and blood cells), and further studies would need to be carried out to assess its suitability for use in a wound monitoring device. Conversely, the ROC analysis proposed here would benefit from the background noise reducing normalisation process. Furthermore, Atolia et al. (2020) found (via absorbance measurements and modelling) that the maximum bacterial growth rate for a species is linked to the initial cell density (306). This finding links well to the conclusions drawn here, with growth measured instead via normalised impedance changes. In this case the ROC after 1 hour was found to give a slightly more accurate approximation of starting cell density than maximum ROC (which varied in time point but did most frequently occur at 1 hour (as seen in Section 6.10)). Furthermore, using a defined time such as this 1-hour measurement point would give a consistent, rapid method that is simple to implement in an *in situ* infection monitor. Settu et al. (2015) were similarly able to determine bacterial concentration at defined time points from the observed impedance changes (121). Measuring *E. coli* growth in urine, impedance changes occurring at 10 Hz after 7 hours had the strongest linear relationship to concentration ($R^2 = 0.99$). Much evidence supporting an association between magnitude of impedance change and bacterial concentration, therefore, exists.

7.4.2 Using Artificial Neural Networks for Bacterial Detection and Identification

Applying machine learning to the large volume of bacterial impedance data obtained using the PCE sensors in this project proved very powerful for supporting infection detection. The first time that artificial neural networks have been used in combination with this already powerful bio-impedance approach to bacterial detection, the results reported in this thesis highlight the promise for this approach to greatly improve point-of-care bacterial detection in future. The neural networks developed are summarised in Figure 7.2 below and discussed in the context of wider literature within the following text.

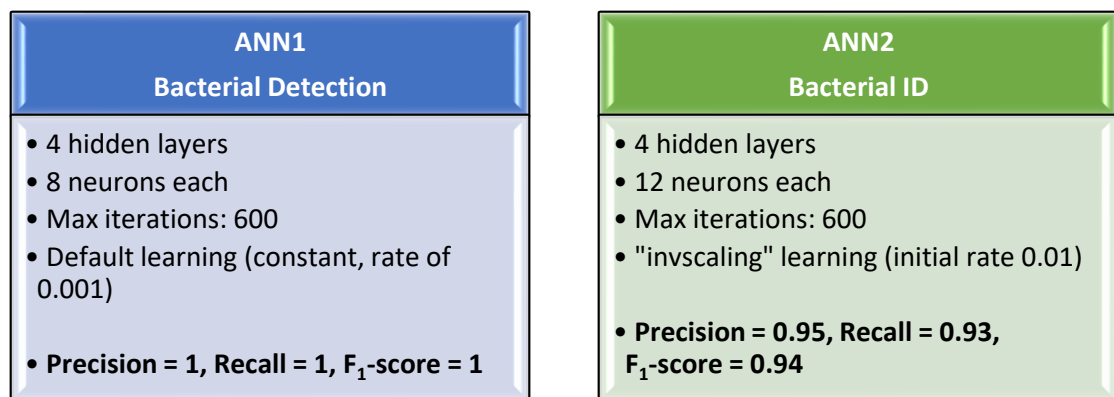


Figure 7.2. Summary of the final ANN1 (bacterial detection) and ANN2 (bacterial identification) key characteristics and average validation scores.

By visually inspecting the normalised impedance signatures obtained in the various growth experiments within Chapter 6, it was possible to easily distinguish between the bacterial and sterile signatures by 24 hours. The power of using ANN1 for bacterial detection is that no simultaneous sterile comparison data is required. The algorithm can, using only the measured signature itself, determine if bacteria is present with a precision and recall of up to 100%. The predictive power of the neural network was more fully realised by ANN2, which was able (for the first time) to confidently identify bacterial species (for *S. aureus*, *P. aeruginosa*, *E. coli*, *P. mirabilis* and limited polymicrobial cultures) with a precision and recall of up to 95% and 93% respectively. This was despite only very subtle differences between species' signatures emerging under specific experimental conditions within Chapter 6. Underrepresentation of certain species in the current dataset (such as *E. coli*, Section 6.10.1) may have a significant negative impact upon the future success of this algorithm. Building a far larger database of signatures with each species equally represented would reduce this classification bias. Whilst only applied to the 24-hour signatures of 4 common wound species within this study to provide a proof of concept, it is promising that similar algorithms could be applied to 1-hour data (for

example) for rapid detection. Further, future exploration of a wider range of cell densities would determine the limit of detection of this approach.

To date, the application of machine learning to bacterial detection has largely focused on imaging techniques. For example, to enhance the bacterial detection power of 3D light sheet fluorescence microscopy detection, Hay et al. (2019) trained a convolutional neural network to analyse the resulting images (307). Convolutional neural networks were similarly adopted in Ho et al.'s (2019) Raman Optical Spectroscopy technique for bacterial detection, with this class of neural network (commonly used in image analysis) shown to have superior performance over the MLP model adopted in this thesis for their image analysis task (308). Appropriate model selection for the specific task undertaken is of vital importance, and future explorations of a wider range of model types and architectures could further increase the classification ability of this impedance-based technology. Within their paper reporting the development of a neural network to detect and classify bacteria from real-time coherent microscopy images, Wang et al. (2020) note the impact of bacterial observation time upon recall (309). For example, a recall of 80% after 6-9 hours increased to over 95% by 12 hours. An important consideration for this work going forward would, therefore, be the likely reduction in power of ANN2 in particular when using earlier impedance data. Greatly increasing the volume of training data and standardising the experimental and measurement conditions would have a positive impact upon on these validation scores.

More closely related to the bacterial impedance sensor developed within this project, Abu-Ali et al. (2019) also employed an ANN within a bacteria-centred electrochemical sensor (310). Instead of aiming to detect bacteria however, their cyclic voltammetry and EIS- based device utilised bacteria immobilised onto screen-printed gold surfaces to indicate the presence of water pollutants such as pesticides. Their ANN architecture consisted of a single hidden layer containing 12 neurons, one for each water pollutant of interest. This structure is quite different to the multiple layer structures adopted in this thesis, where the number of layers and neurons were selected based on an iterative (validation score led) tuning process. As no validation scores were reported by Abu-Ali et al., the rationale for their particular network architecture is unclear. Their ANN was, however, successful in detecting the correct water pollutants from subsequent test data. Further, estimations of concentration were made to an approximate order of magnitude value. This was of a similar power to the ROC method developed in this thesis for target concentration estimation; incorporating this concentration estimation into the bacterial detection and identification ANNs in future could further increase their value.

Although the great potential for these algorithms to benefit bacterial detection is clear, using artificial intelligence within medical applications can be a complex landscape to navigate. There are various ethical and regulatory factors to consider. Aiming to help innovators develop technologies suitable for clinical adoption, the NHS has published “A guide to good practice for digital and data-driven health technologies” (formerly the AI Code of Conduct) (311). The key principles highlighted within this guidance are summarised in Figure 7.3. One crucial consideration which has been widely discussed in the context of artificial neural networks is transparency. The complex non-linear mathematical nature of ANNs means that this type of algorithm can be difficult to interpret and is often referred to as a “black box” algorithm. Methods to improve understanding of ANN model routes to decision making are being developed however, such as the “layer-wise relevance propagation” method described by Montavon et al. 2018 (312). Further, cloud services such as Microsoft’s Azure service have incorporated transparency considerations into their packages, with functions such as “feature importance” supporting model transparency by revealing how much each feature impacted the prediction made (313). By incorporating even simple steps such as revealing the prediction output node weights, more transparency is gained. The safety of the AI algorithm and confidence that it is fit to serve its clinical purpose are similarly crucial considerations. Becker (2019) proposes a method of optimising the safety and reliability of an ANN, using frequent testing both during device use and when in stand-by (314). Further, the sole use of an offline training dataset which has been quality checked is suggested. Ideally, the training dataset should be very large and have been collected from a range of clinical settings to minimise bias and be representative of a broad patient population (315). In the context of the wound infection device developed within this thesis, this would mean deploying a saved algorithm (trained using clinically validated data) to make real-time predictions, and not updating this algorithm with the new data in real time. Subsequent data verification and further model training would be supervised before updated algorithm rollout. This would also support the accessibility principle, allowing for offline use in remote locations. Regulatory compliance is, of course, a vital aspect of AI-supported medical device development. A new area of advancement, in 2020 there were 240 AI and ML-based medical devices which had gained European regulatory approval, but regulatory pathway guidance is limited (316). Liaising with regulatory officials would be of paramount importance.

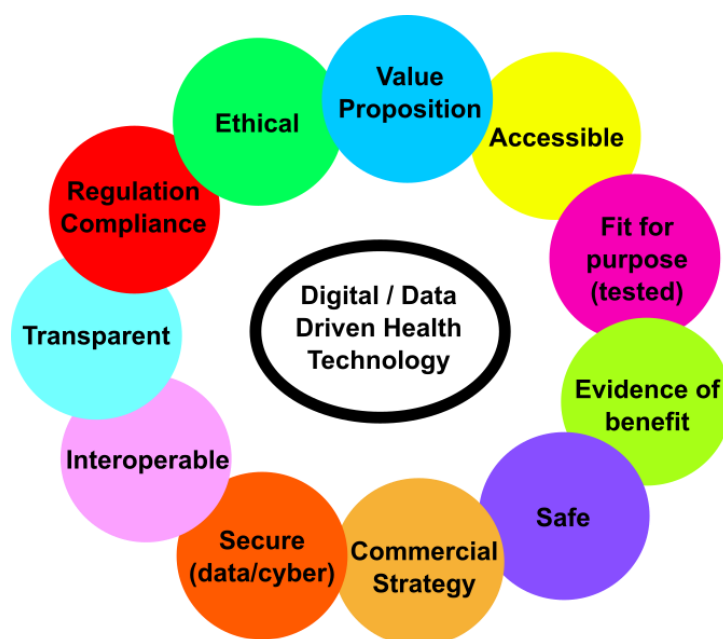


Figure 7.3. Summary of the key considerations for new digital and data driven health technologies (for example AI-based solutions) outlined by NHS guidance (311).

7.4.3 Summary – Algorithmic Approaches to Bacterial Detection in the Context of the Project Objectives

The development of novel algorithmic approaches to support bacterial detection via analysis of impedance signatures greatly enhanced the sensor developed within this project. These algorithms directly addressed the final project objective set in Chapter 1:

4. *Determine methods of identifying infection, different bacterial species and concentrations through differences in the obtained impedance spectra.*

Focusing on data obtained using the PCE sensors, a method for bacterial concentration based upon early rate of normalised impedance change was first proposed. This approach, which was able to approximate *S. aureus* concentration to the correct order of magnitude despite limited calibration data, showed promise for future optimisation. By next developing two artificial neural networks, bacterial detection and identification were shown to be possible with average F_1 -scores of 1 and 0.94 respectively. These approaches proved far more powerful than anticipated and could pave the way for future rapid bacterial detection and identification.

7.5 Conclusions and Future Work

7.5.1 Project Conclusions

As described in Chapter 1, the early detection of wound infection is a clinically important problem. Current gold standard methods of bacterial detection and identification rely upon lengthy laboratory culturing techniques and have a typical turn-around-time of 48 hours. Whilst more recently developed methods of bacterial detection such as PCR have enabled point of care diagnosis at a more rapid rate, these have a number of drawbacks and there are currently no devices suitable for real time wound infection monitoring *in situ*. This project, therefore, focussed upon the advancement of a low-cost sensor for the rapid, *in situ* detection of wound infection with potential applications in both adult and paediatric patient populations. Due to the promise that electrochemical impedance spectroscopy has previously shown for bacterial detection, this analytical method formed the basis of the sensor.

Three different screen-printed sensor materials were investigated: Ag/AgCl, carbon and platinised carbon electrodes (PCE). Through experiments performed under a range of conditions, both the carbon and PCE sensors were found to be suitable for rapid real-time bacterial detection within just 30 minutes via characteristic normalised impedance changes. Further, applying mathematical analysis and machine learning techniques to the large volume of PCE sensor data enabled cell density approximation, bacterial detection, and species determination for a range of common wound pathogens. By developing a wound bed model and simulating various features of the wound environment, the suitability of these particular sensors for operation *in situ* was confirmed. Moreover, each of the key project objectives outlined in Chapter 1 was successfully achieved.

7.5.2 Future Research Recommendations

This research successfully and significantly advanced the development of an *in situ* wound infection sensor. A number of areas for future exploration have been highlighted throughout this thesis; key recommendations for future research are cohesively summarised in Figure 7.4 below, separated into three broad categories.

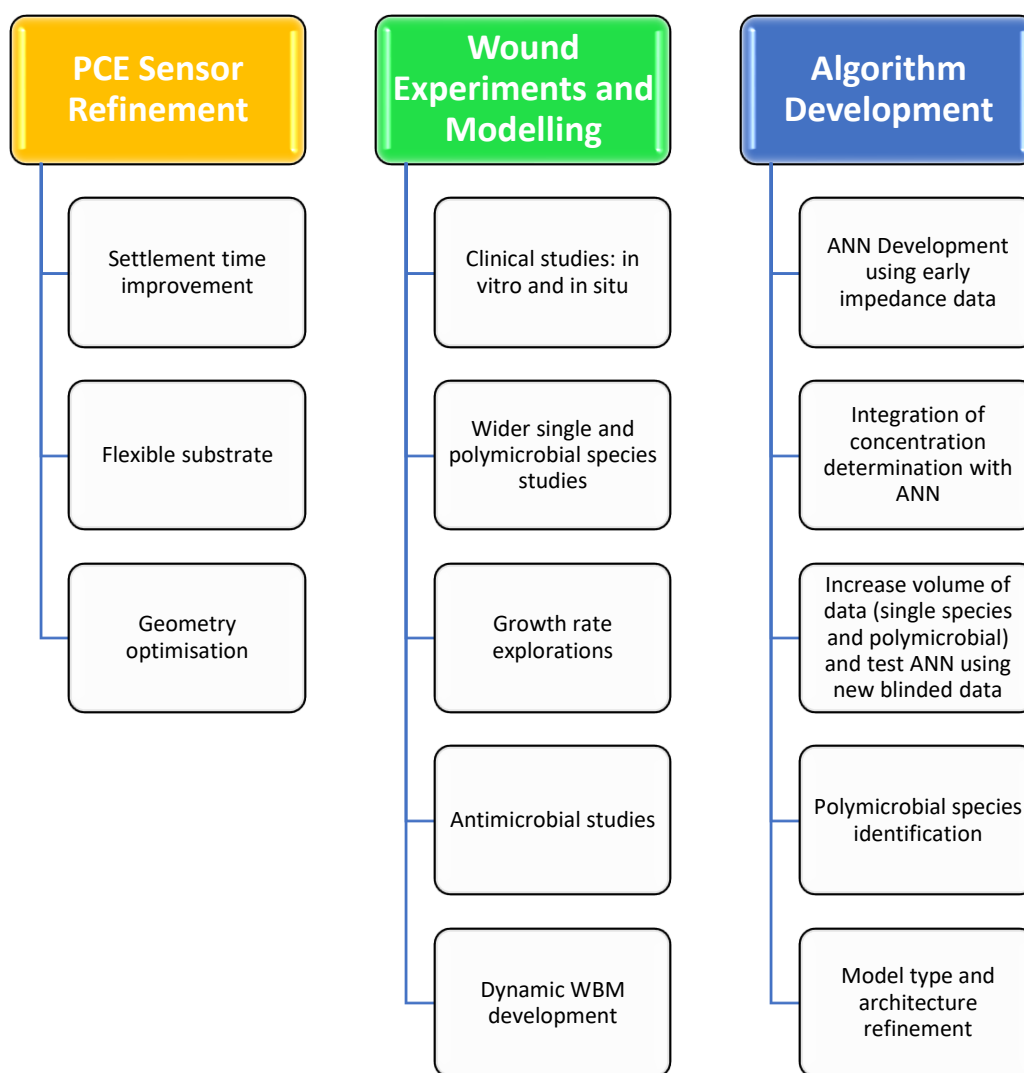


Figure 7.4. Overview of key areas identified for future research.

Firstly, work to further refine the chosen PCE sensors could concentrate upon making improvements to their impedance settlement time in media. Within Section 6.3 a dry preparation method was developed for this sensor, however, some initial changes were evident in the early impedance spectra. Experiments aiming to reduce this instability and accelerate the electrode settlement time could explore the use of additional chemical and electrochemical conditioning procedures for example. Further, printing these sensors onto a flexible substrate more suitable for use on a wound (such as the polyethylene substrate used for the Ag/AgCl Woundsense electrodes) would move these sensors a step further towards clinical relevance. Alternative sensor geometries could also be explored, aiming to optimise the sensor design for wound applications.

The second key area for future work is to advance the wound experiments carried out. The WBM and wound environment studies carried out in Sections 6.5 and 6.6 in particular would be significantly advanced by conducting experiments using clinical wound exudate samples. Such an *in vitro* study could use the novel sensor to measure wound swabs and dressings rehydrated using culture medium for example. This work is already being planned as a follow-on Strathclyde University clinical project. Further, if successful, this study could lead to *in situ* wound measurements being performed on a wide range of wound types. These clinical measurements could provide crucial insight into the suitability of this technology for rapid wound infection detection. In terms of advancing the simulated wound bed model that has been used in this project, further laboratory experiments using a wider range of single species and polymicrobial cultures would greatly enhance the existing database of signatures. Other identified areas for further exploration include assessing in more depth the impact of wound exudate and SWF upon bacterial growth rates, exploring the impact of antimicrobial agents upon the measured impedance signatures and developing a dynamic WBM that models fresh exudate production over time.

The final broad area of further study identified is centred around advancements to the supporting bacterial detection algorithms (developed in Section 6.10). Due to the success of the machine learning approach used for bacterial detection and identification using the 24-hour data, a clear next step would be to train new ANNs using earlier impedance data (such as 1-hour data). This would require a larger volume of data to be obtained under standardised conditions to ensure that this early data is comparable. A wider range of wound pathogens could be measured using the sensor, in addition to a variety of polymicrobial combinations. This could lead to the advancement of the ANNs for accurate polymicrobial species identification. Further, increasing the volume of supporting data underpinning the ROC bacterial concentration analysis and integrating this algorithm with the ANNs would further increase the power of this system. Ultimately, as the quantity and type of data is advanced in future, further investigations into the most appropriate machine learning model, structure, hyperparameters and feature selection will be necessary.

In conclusion, whilst multiple avenues for further exploration have been identified, within this project strong evidence to support the use of a low-cost PCE sensor and machine learning for bacterial detection and identification has been presented. Using a simulated wound environment, the potential for this sensor to rapidly detect a range of wound pathogens has been demonstrated. With further development, this technology shows great promise for adoption into an advanced *in situ* wound infection monitoring device in future.

8. REFERENCES

1. Martini F, Nath JL, Bartholomew EF. *Fundamentals of Anatomy & Physiology*. 11th ed. Pearson; 2019. Available from: <https://books.google.co.uk/books?id=z5j-ngEACAAJ>
2. Takeo M, Lee W, Ito M. Wound healing and skin regeneration. *Cold Spring Harb Perspect Med*. 2015 Jan; 5(1):a023267. Available from: <http://www.ncbi.nlm.nih.gov/pubmed/25561722>
3. Fore J. A review of skin and the effects of aging on skin structure and function. *Ostomy Wound Manage*. 2006 Sep; 52(9):24–35. Available from: <http://www.ncbi.nlm.nih.gov/pubmed/16980727>
4. King A, Stellar JJ, Blevins A, Shah KN. Dressings and Products in Pediatric Wound Care. *Adv wound care*. 2014 Apr; 3(4):324–34. Available from: <http://www.ncbi.nlm.nih.gov/pubmed/24761363>
5. Baharestani MM. An overview of neonatal and pediatric wound care knowledge and considerations. Vol. 53, *Ostomy/wound management*; 2007. p. 34–6, 38, 40. Available from: <http://www.ncbi.nlm.nih.gov/pubmed/17586871>
6. Visscher M, Narendran V. The Ontogeny of Skin. *Adv Wound Care*. 2014 Apr; 3(4):291–303. Available from: <http://www.ncbi.nlm.nih.gov/pmc/articles/PMC3985523/>
7. Bowler PG, Duerden BI, Armstrong DG. Wound microbiology and associated approaches to wound management. *Clin Microbiol Rev*. 2001 Apr; 14(2):244–69. Available from: <http://www.ncbi.nlm.nih.gov/pubmed/11292638>
8. Nunan R, Harding KG, Martin P. Clinical challenges of chronic wounds: searching for an optimal animal model to recapitulate their complexity. *Dis Model Mech*. 2014 Nov; 7(11):1205–13. Available from: <http://www.ncbi.nlm.nih.gov/pubmed/25359790>
9. Sen CK, Gordillo GM, Roy S, Kirsner R, Lambert L, Hunt TK, et al. Human skin wounds: a major and snowballing threat to public health and the economy. *Wound Repair Regen*. 2009; 17(6):763–71. Available from: <http://www.ncbi.nlm.nih.gov/pubmed/19903300>
10. Hess CT. *Skin & wound care*. Wolters Kluwer Health/Lippincott Williams & Wilkins; 2008. 39p.
11. Farooqui MF, Shamim A. Low Cost Inkjet Printed Smart Bandage for Wireless Monitoring of Chronic Wounds. *Sci Rep*. 2016 Jun 29; 6:28949. Available from: <http://www.ncbi.nlm.nih.gov/pubmed/27353200>
12. Guest JF, Ayoub N, McIlwraith T, Uchegbu I, Gerrish A, Weidlich D, et al. Health economic burden that different wound types impose on the UK's National Health Service. *Int Wound J*. 2017 Apr 1; 14(2):322–30. Available from: <https://onlinelibrary.wiley.com/doi/full/10.1111/iwj.12603>

13. Armstrong DG, Boulton AJM, Bus SA. Diabetic Foot Ulcers and Their Recurrence. *N Engl J Med.* 2017 Jun; 376(24):2367–75. Available from: <https://pubmed.ncbi.nlm.nih.gov/28614678/>
14. Paisey RB, Abbott A, Paisey CF, Walker D. Diabetic foot ulcer incidence and survival with improved diabetic foot services: an 18-year study. *Diabet Med.* 2019 Nov; 36(11):1424–30. Available from: [/pmc/articles/PMC6852104/?report=abstract](https://pubmed.ncbi.nlm.nih.gov/36111424/)
15. Turns M. The diabetic foot: an overview of assessment and complications. *Br J Nurs.* 2011 Aug; 20(Sup8):S19–25. Available from: <http://www.ncbi.nlm.nih.gov/pubmed/21841646>
16. Lal BK. Venous ulcers of the lower extremity: Definition, epidemiology, and economic and social burdens. *Semin Vasc Surg.* 2015 Mar; 28(1):3–5. Available from: <http://www.ncbi.nlm.nih.gov/pubmed/26358303>
17. Frykberg RG, Banks J. Challenges in the Treatment of Chronic Wounds. *Adv wound care.* 2015 Sep; 4(9):560–82. Available from: <http://www.ncbi.nlm.nih.gov/pubmed/26339534>
18. Tiwari VK. Burn wound: How it differs from other wounds? *Indian J Plast Surg.* 2012 May; 45(2):364–73. Available from: <http://www.ncbi.nlm.nih.gov/pubmed/23162236>
19. Stylianou N, Buchan I, Dunn KW. A review of the international Burn Injury Database (iBID) for England and Wales: descriptive analysis of burn injuries 2003–2011. *BMJ Open.* 2015 Feb; 5(2):e006184. Available from: <http://www.ncbi.nlm.nih.gov/pubmed/25724981>
20. Abbott TEF, Fowler AJ, Dobbs TD, Harrison EM, Gillies MA, Pearse RM. Frequency of surgical treatment and related hospital procedures in the UK: a national ecological study using hospital episode statistics. *BJA Br J Anaesth.* 2017 Aug; 119(2):249–57. Available from: <http://academic.oup.com/bja/article/119/2/249/4049141/Frequency-of-surgical-treatment-and-related>
21. Noonan C, Quigley S, Curley MAQ. Skin Integrity in Hospitalized Infants and Children. *J Pediatr Nurs.* 2006 Dec; 21(6):445–53. Available from: <http://www.ncbi.nlm.nih.gov/pubmed/17101403>
22. Guo S, Dipietro LA. Factors Affecting Wound Healing. *J Dent Res.* 2010 Mar; 89(3):219–29. Available from: <http://www.ncbi.nlm.nih.gov/pubmed/20139336>
23. Palta S, Saroa R, Palta A. Overview of the coagulation system. Vol. 58, *Indian Journal of Anaesthesia.* Wolters Kluwer - Medknow Publications; 2014. p. 515–23. Available from: <http://www.ncbi.nlm.nih.gov/pubmed/25535411>
24. Rodriguez PG, Felix FN, Woodley DT, Shim EK. The role of oxygen in wound healing:

- A review of the literature. Vol. 34, *Dermatologic Surgery*. 2008. p. 1159–69. Available from: <http://www.ncbi.nlm.nih.gov/pubmed/18513296>
25. Sibbald RG, Elliott JA, Ayello EA, Somayaji R. Optimizing the Moisture Management Tightsheet with Wound Bed Preparation. Vol. 28, *Advances in Skin and Wound Care*; 2015. p. 466–76. Available from: https://journals.lww.com/aswcjournal/Fulltext/2015/10000/Optimizing_the_Moisture_Management_Tightsheet_with.6.aspx
 26. Bessa LJ, Fazii P, Di Giulio M, Cellini L. Bacterial isolates from infected wounds and their antibiotic susceptibility pattern: some remarks about wound infection. *Int Wound J* [Internet]. 2015 Feb 1 [cited 2017 Sep 12];12(1):47–52. Available from: <http://doi.wiley.com/10.1111/iwj.12049>
 27. Sievert DM, Ricks P, Edwards JR, Schneider A, Patel J, Srinivasan A, et al. Antimicrobial-Resistant Pathogens Associated with Healthcare-Associated Infections Summary of Data Reported to the National Healthcare Safety Network at the Centers for Disease Control and Prevention, 2009–2010. *Infect Control Hosp Epidemiol*. 2013 Jan; 34(01):1–14. Available from: <http://www.ncbi.nlm.nih.gov/pubmed/23221186>
 28. Prompers L, Huijberts M, Apelqvist J, Jude E, Piaggese A, Bakker K, et al. High prevalence of ischaemia, infection and serious comorbidity in patients with diabetic foot disease in Europe. Baseline results from the Eurodiale study. *Diabetologia*. 2007 Jan; 50(1):18–25. Available from: <https://link.springer.com/article/10.1007/s00125-006-0491-1>
 29. Guest JF, Fuller GW, Vowden P. Cohort study evaluating the burden of wounds to the UK's National Health Service in 2017/2018: Update from 2012/2013. *BMJ Open*. 2020 Dec; 10(12):45253. Available from: <http://bmjopen.bmj.com/>
 30. Guest JF, Fuller GW, Vowden P. Costs and outcomes in evaluating management of unhealed surgical wounds in the community in clinical practice in the UK: A cohort study. *BMJ Open*. 2018 Dec; 8(12). Available from: </pmc/articles/PMC6303575/?report=abstract>
 31. Sender R, Fuchs S, Milo R. Revised Estimates for the Number of Human and Bacteria Cells in the Body. *PLoS Biol*. 2016 Aug; 14(8):e1002533. Available from: <http://www.ncbi.nlm.nih.gov/pubmed/27541692>
 32. Madigan MT, Bender KS, Buckley DH, Sattley WM, Stahl DA. *Brock Biology of Microorganisms*, Global Edition, 15th Edition. Pearson; 2018.
 33. Grice EA, Segre JA. The skin microbiome. Vol. 9, *Nature Reviews Microbiology*. NIH Public Access; 2011. p. 244–53. Available from: <http://www.ncbi.nlm.nih.gov/pubmed/21407241>

34. Otto M. Staphylococcus colonization of the skin and antimicrobial peptides. *Expert Rev Dermatol.* 2010 Apr; 5(2):183–95. Available from: <http://www.ncbi.nlm.nih.gov/pubmed/20473345>
35. Davis CP. *Medical Microbiology*. 4th ed. Baron S, editor. Chapter 6 Normal Flora. University of Texas Medical Branch at Galveston; 1996. 695–698 p. Available from: <http://www.ncbi.nlm.nih.gov/pubmed/21413249>
36. Byrd AL, Belkaid Y, Segre JA. The human skin microbiome. Vol. 16, *Nature Reviews Microbiology*. Nature Publishing Group; 2018. p. 143–55. Available from: <https://pubmed.ncbi.nlm.nih.gov/29332945/>
37. Dominguez-Bello MG, Costello EK, Contreras M, Magris M, Hidalgo G, Fierer N, et al. Delivery mode shapes the acquisition and structure of the initial microbiota across multiple body habitats in newborns. *Proc Natl Acad Sci.* 2010 Jun; 107(26):11971–5. Available from: <http://www.ncbi.nlm.nih.gov/pubmed/20566857>
38. Grice EA, Kong HH, Conlan S, Deming CB, Davis J, Young AC, et al. Topographical and temporal diversity of the human skin microbiome. *Science* (80-). 2009 May; 324(5931):1190–2. Available from: <http://www.ncbi.nlm.nih.gov/pubmed/19478181>
39. Brunauer A, Verboket RD, Kainz DM, von Stetten F, Früh SM. Rapid Detection of Pathogens in Wound Exudate via Nucleic Acid Lateral Flow Immunoassay. *Biosensors.* 2021 Mar 6; 11(3):74. Available from: <https://www.mdpi.com/2079-6374/11/3/74>
40. Bornside GH, Bornside BB. Comparison between moist swab and tissue biopsy methods for quantitation of bacteria in experimental incisional wounds. *J Trauma - Inj Infect Crit Care.* 1979; 19(2):103–5. Available from: <https://pubmed.ncbi.nlm.nih.gov/368348/>
41. James GA, Swogger E, Wolcott R, Pulcini E deLancey, Secor P, Sestrich J, et al. Biofilms in chronic wounds. *Wound Repair Regen.* 2008 Jan; 16(1):37–44. Available from: <http://www.ncbi.nlm.nih.gov/pubmed/18086294>
42. Tong SYC, Davis JS, Eichenberger E, Holland TL, Fowler VG. Staphylococcus aureus infections: Epidemiology, pathophysiology, clinical manifestations, and management. *Clin Microbiol Rev.* 2015 Jul; 28(3):603–61. Available from: <http://www.ncbi.nlm.nih.gov/pubmed/26016486>
43. Al-Tawfiq JA, Tambyah PA. Healthcare associated infections (HAI) perspectives. *J Infect Public Health.* 2014 Jul; 7(4):339–44. Available from: <http://www.ncbi.nlm.nih.gov/pubmed/24861643>
44. Health Protection Scotland. Scottish National point Prevalence Survey of Healthcare Associated Infection and Antimicrobial Prescribing 2016. 2017. Available from: <https://www.nhsggc.org.uk/media/242579/hai-snpss-2016-full-report.pdf>

45. Cheng K, Li J, Kong Q, Wang C, Ye N, Xia G. Risk factors for surgical site infection in a teaching hospital: a prospective study of 1,138 patients. *Patient Prefer Adherence*. 2015; 9:1171–7. Available from: <http://www.ncbi.nlm.nih.gov/pubmed/26316722>
46. Healy B, Freedman A. ABC of wound healing: Infections. *BMJ*. 2006 Apr; 332(7545):838–41. Available from: <http://www.ncbi.nlm.nih.gov/pubmed/16601046>
47. Azzopardi EA, Azzopardi E, Camilleri L, Villapalos J, Boyce DE, Dziewulski P, et al. Gram Negative Wound Infection in Hospitalised Adult Burn Patients-Systematic Review and Metanalysis. *PLoS One*. 2014 Apr; 9(4):e95042. Available from: <http://dx.plos.org/10.1371/journal.pone.0095042>
48. Holmes AH, Moore LSP, Sundsfjord A, Steinbakk M, Regmi S, Karkey A, et al. Understanding the mechanisms and drivers of antimicrobial resistance. Vol. 387, *The Lancet*. 2016. p. 176–87. Available from: <http://dx.doi.org/10.1016/S0140-6736>
49. O’Neill J. Tackling Drug-Resistant Infections Globally: Final Report and Recommendations the Review on Antimicrobial Resistance. 2016. Available from: [https://amr-review.org/sites/default/files/160525_Final paper_with cover.pdf](https://amr-review.org/sites/default/files/160525_Final%20paper_with%20cover.pdf)
50. Alam MM, Islam MN, Hossain Hawlader MD, Ahmed S, Wahab A, Islam M, et al. Prevalence of multidrug resistance bacterial isolates from infected wound patients in Dhaka, Bangladesh: A cross-sectional study. *Int J Surg Open*. 2021 Jan; 28:56–62.
51. Alemayehu T, Hailemariam M. Prevalence of vancomycin-resistant enterococcus in Africa in one health approach: a systematic review and meta-analysis. *Sci Rep*. 2020 Dec; 10(1):1–10. Available from: <https://doi.org/10.1038/s41598-020-77696-6>
52. Rice LB. Federal Funding for the Study of Antimicrobial Resistance in Nosocomial Pathogens: No ESKAPE. *J Infect Dis*. 2008 Apr; 197(8):1079–81. Available from: <https://academic.oup.com/jid/article-lookup/doi/10.1086/533452>
53. Costerton JW, Stewart PS, Greenberg EP. Bacterial Biofilms: A Common Cause of Persistent Infections. *Science* (80-). 1999; 284(5418). Available from: <http://science.sciencemag.org/content/284/5418/1318.long>
54. Schultz GS, Sibbald RG, Falanga V, Ayello EA, Dowsett C, Harding K, et al. Wound bed preparation: A systematic approach to wound management. *Wound Repair Regen*. 2003 Mar; 11(SUPPL. 1):S1–28. Available from: <http://doi.wiley.com/10.1046/j.1524-475X.11.s2.1.x>
55. Leaper DJ, Schultz G, Carville K, Fletcher J, Swanson T, Drake Leaper RD. Extending the TIME concept: what have we learned in the past 10 years?. *Int Wound J*. 2012; 9:1–19.
56. Harries RL, Bosanquet DC, Harding KG. Wound bed preparation: TIME for an update.

- Int Wound J. 2016 Sep; 13 Suppl 3:8–14. Available from: <http://www.ncbi.nlm.nih.gov/pubmed/27547958>
57. Sibbald RG, Goodman L, Woo KY, Krasner DL, Smart H, Tariq G, et al. Special considerations in wound bed preparation 2011: an update. *Adv Skin Wound Care*. 2011 Sep; 24(9):415–36. Available from: <https://insights.ovid.com/pubmed?pmid=21860264>
 58. Moore Z, Dowsett C, Smith G, Atkin L, Bain M, Lahmann NA, et al. TIME cdst: An updated tool to address the current challenges in wound care. *J Wound Care*. 2019;28(3):154–61.
 59. Fitzgerald JR. Evolution of *Staphylococcus aureus* during human colonization and infection. *Infect Genet Evol*. 2014 Jan; 21:542–7. Available from: <http://www.sciencedirect.com/science/article/pii/S1567134813001603>
 60. Winter GD. Formation of the scab and the rate of epithelization of superficial wounds in the skin of the young domestic pig. *Nature*. 1962 Jan; 193(4812):293–4. Available from: <http://www.nature.com/doi/10.1038/193293a0>
 61. Oranges T, Dini V, Romanelli M. Skin Physiology of the Neonate and Infant: Clinical Implications. *Adv Wound Care*. 2015 Oct; 4(10):587–95. Available from: <http://www.ncbi.nlm.nih.gov/pubmed/26487977>
 62. Power G, Moore Z, O'Connor T. Measurement of pH, exudate composition and temperature in wound healing: A systematic review. *J Wound Care*. 2017 Jul; 26(7):381–97. Available from: <https://pubmed.ncbi.nlm.nih.gov/28704150/>
 63. Ousey K, Cutting KF, Rogers AA, Rippon MG. The importance of hydration in wound healing: Reinvigorating the clinical perspective. *J Wound Care*. 2016 Mar; 25(3):122–30. Available from: <https://pubmed.ncbi.nlm.nih.gov/26947692/>
 64. Jones V, Grey JE, Harding KG. Wound dressings. *BMJ*. 2006 Apr; 332(7544):777–80. Available from: <http://www.ncbi.nlm.nih.gov/pubmed/16575081>
 65. Dargaville TR, Farrugia BL, Broadbent JA, Pace S, Upton Z, Voelcker NH. Sensors and imaging for wound healing: A review. *Biosens Bioelectron*. 2013 Mar; 41(1):30–42. Available from: <http://linkinghub.elsevier.com/retrieve/pii/S0956566312006355>
 66. Dhivya S, Padma VV, Santhini E. Wound dressings - a review. *BioMedicine*. 2015 Dec; 5(4):22. Available from: <http://www.ncbi.nlm.nih.gov/pubmed/26615539>
 67. Sarabahi S. Recent advances in topical wound care. *Indian J Plast Surg*. 2012 May; 45(2):379–87. Available from: <http://www.ncbi.nlm.nih.gov/pubmed/23162238>
 68. Lansdown ABBG. Silver in Health Care: Antimicrobial Effects and Safety in Use. Basel: KARGER; 2006 p. 17–34. Available from: http://euroband.com/Expert_Opinion_-_Silver_in_Health_Care_-_Affect_%26_Safety.pdf

69. Zbuche A. Up-to-date use of honey for burns treatment. *Ann Burns Fire Disasters*. 2014 Mar 31; 27(1):22–30. Available from: <http://www.ncbi.nlm.nih.gov/pubmed/25249844>
70. Lindberg T, Andersson O, Palm M, Fagerström C. A systematic review and meta-analysis of dressings used for wound healing: the efficiency of honey compared to silver on burns. *Contemp Nurse*. 2015 Nov; 51(2–3):121–34. Available from: <http://www.tandfonline.com/doi/full/10.1080/10376178.2016.1171727>
71. Dumville JC, Gray TA, Walter CJ, Sharp CA, Page T, Macefield R, et al. Dressings for the prevention of surgical site infection. *Cochrane Database of Systematic Reviews*. Chichester, UK: John Wiley & Sons, Ltd; 2016. Available from: <http://doi.wiley.com/10.1002/14651858.CD003091.pub4>
72. Nain PS, Uppal SK, Garg R, Bajaj K, Garg S. Role of negative pressure wound therapy in healing of diabetic foot ulcers. *J Surg Tech Case Rep*. 2011 Jan; 3(1):17–22. Available from: </pmc/articles/PMC3192517/>
73. Kloth LC. Electrical Stimulation Technologies for Wound Healing. *Adv Wound Care*. 2014; 3(2):81–90. Available from: http://epublications.marquette.edu/cgi/viewcontent.cgi?article=1057&context=phys_therapy_fac
74. Thakral G, Lafontaine J, Najafi B, Talal TK, Kim P, Lavery LA. Electrical stimulation to accelerate wound healing. *Diabet Foot Ankle*. 2013 Sep; 4. Available from: <http://www.ncbi.nlm.nih.gov/pubmed/24049559>
75. Hampton S, Collins F. Treating a pressure ulcer with bio-electric stimulation therapy. *Br J Nurs*. 2006 Mar; 15(Sup1):S14–8. Available from: <http://www.ncbi.nlm.nih.gov/pubmed/16628158>
76. Leloup P, Toussaint P, Lembelembe JP, Celerier P, Maillard H. The analgesic effect of electrostimulation (WoundEL) in the treatment of leg ulcers. *Int Wound J*. 2015 Dec; 12(6):706–9. Available from: <http://www.ncbi.nlm.nih.gov/pubmed/24618089>
77. Gardner SE, Frantz RA, Doebbeling BN. The validity of the clinical signs and symptoms used to identify localized chronic wound infection. *Wound Repair Regen*. 2001; 9(3):178–86. Available from: <http://www.ncbi.nlm.nih.gov/pubmed/11472613>
78. Keast D, Swanson T, Carville K, Fletcher J, Schultz G, Black J. Understanding and managing wound biofilm. *Wounds Int*. 2014; 5(2). Available from: www.woundsinternational.com
79. PHE. UK Standards for Microbiology Investigations-Identification of Clostridium species. *Bacteriology*. 2016; (4.1):27. Available from: <https://www.gov.uk/uk>
80. Copeland-Halperin LR, Kaminsky AJ, Bluefield N, Miraliakbari R. Sample procurement for cultures of infected wounds: a systematic review. *J Wound Care*. 2016 Apr;

- 25(Sup4):S4–10. Available from: <http://www.ncbi.nlm.nih.gov/pubmed/27068349>
81. Bissonnette L, Bergeron MG. POC tests in microbial diagnostics: Current status. In: *Methods in Microbiology*. 2015. p. 87–110.
 82. Cooper R, Lawrence JC. The Isolation and Identification of Bacteria from Wounds. *J Wound Care*. 1998 Feb; 7(Sup2):9–12. Available from: <http://www.magonlinelibrary.com/doi/10.12968/jowc.1998.7.Sup2.9>
 83. Stevens DL, Bisno AL, Chambers HF, Dellinger EP, Goldstein EJC, Gorbach SL, et al. Practice Guidelines for the Diagnosis and Management of Skin and Soft Tissue Infections: 2014 Update by the Infectious Diseases Society of America. *Clin Infect Dis*. 2014 Jul; 59(2):e10–52. Available from: <http://www.ncbi.nlm.nih.gov/pubmed/24947530>
 84. Bourassa L, Butler-Wu SM. MALDI-TOF mass spectrometry for microorganism identification. In: *Methods in Microbiology*. 2015. p. 37–85.
 85. Novak-Weekley SM, Marlowe EM. Total laboratory automation in clinical bacteriology. In: *Methods in Microbiology*. 2015. p. 1–35.
 86. Heaney J, Rolfe K, Gleadall NS, Greatorex JS, Curran MD. Low-density TaqMan® array cards for the detection of pathogens. In: *Methods in Microbiology*. 2015. p. 199–218.
 87. Guglielmi G. The explosion of new coronavirus tests that could help to end the pandemic. *Nature*. 2020 Jul 1;583(7817):506–9.
 88. Ahrberg CD, Ilic BR, Manz A, Neužil P. Handheld real-time PCR device. *Lab Chip*. 2016 Feb; 16(3):586–92. Available from: <http://www.ncbi.nlm.nih.gov/pubmed/26753557>
 89. Zanolli LM, Spoto G. Isothermal amplification methods for the detection of nucleic acids in microfluidic devices. Vol. 3, *Biosensors*. Multidisciplinary Digital Publishing Institute (MDPI); 2013. p. 18–43. Available from: <http://www.ncbi.nlm.nih.gov/pubmed/25587397>
 90. Buermans HPJ, den Dunnen JT. Next generation sequencing technology: Advances and applications. *Biochim Biophys Acta*. 2014 Oct; 1842(10):1932–41. Available from: <https://www.sciencedirect.com/science/article/pii/S092544391400180X>
 91. Lau SKP, Teng JLL, Ho C-C, Woo PCY. Gene Amplification and Sequencing for Bacterial Identification. In: *Methods in Microbiology*. 2015. p. 433–64.
 92. Aggarwal D, Kankar T, Narouz M, Azadian BS, Moore LSP, Mughal N. Clinical utility and cost-effectiveness of bacterial 16S rRNA and targeted PCR based diagnostic testing in a UK microbiology laboratory network. *Sci Rep*. 2020 Dec; 10(1):1–9. Available

from: <https://doi.org/10.1038/s41598-020-64739-1>

93. Corrigan DK, Schulze H, Ciani I, Henihan G, Mount AR, Bachmann TT. Improving performance of a rapid electrochemical MRSA assay: Optimisation of assay conditions to achieve enhanced discrimination of clinically important DNA sequences under ambient conditions. *J Electroanal Chem.* 2017 Feb; 786:58–62. Available from: <http://linkinghub.elsevier.com/retrieve/pii/S1572665716307524>
94. Blair EO, Hannah S, Vezza V, Avci H, Kocagoz T, Hoskisson PA, et al. Biologically modified microelectrode sensors provide enhanced sensitivity for detection of nucleic acid sequences from *Mycobacterium tuberculosis*. *Sensors and Actuators Reports.* 2020 Nov; 2(1):100008. Available from: <https://pureportal.strath.ac.uk/en/publications/biologically-modified-microelectrode-sensors-provide-enhanced-sen>
95. Banada PP, Bhunia AK. Antibodies and Immunoassays for Detection of Bacterial Pathogens. In: *Principles of Bacterial Detection: Biosensors, Recognition Receptors and Microsystems.* New York, NY: Springer New York; 2008. p. 567–602. Available from: http://link.springer.com/10.1007/978-0-387-75113-9_21
96. Law JW-F, Ab Mutalib N-S, Chan K-G, Lee L-H. Rapid methods for the detection of foodborne bacterial pathogens: principles, applications, advantages and limitations. *Front Microbiol.* 2014; 5:770. Available from: <http://www.ncbi.nlm.nih.gov/pubmed/25628612>
97. Koczula KM, Gallotta A. Lateral flow assays. *Essays Biochem.* 2016 Jun;60(1):111–20. Available from: <http://www.ncbi.nlm.nih.gov/pubmed/27365041>
98. Niu K, Zheng X, Huang C, Xul K, Zhi Y, Shen H, et al. A colloidal gold nanoparticle-based immunochromatographic test strip for rapid and convenient detection of *Staphylococcus aureus*. *J Nanosci Nanotechnol.* 2014 Jul;14(7):5151–6. Available from: <http://www.ncbi.nlm.nih.gov/pubmed/24757994>
99. Mohd Hanafiah K, Arifin N, Bustami Y, Noordin R, Garcia M, Anderson D. Development of Multiplexed Infectious Disease Lateral Flow Assays: Challenges and Opportunities. *Diagnostics (Basel, Switzerland).* 2017 Sep; 7(3). Available from: <http://www.ncbi.nlm.nih.gov/pubmed/28880218>
100. Crozier A, Rajan S, Buchan I, McKee M. Put to the test: Use of rapid testing technologies for Covid-19. *BMJ.* 2021 Feb; 372. Available from: <http://dx.doi.org/10.1136/bmj.n208>
101. Persaud KC. Medical Applications of Odor-Sensing Devices. *Int J Low Extrem Wounds.* 2005 Mar; 4(1):50–6. Available from: <http://www.ncbi.nlm.nih.gov/pubmed/15860452>
102. Parry AD, Chadwick P., Simon D, Oppenheim B, McCollum CN. Leg ulcer odour detection identifies β -haemolytic streptococcal infection. *J Wound Care.* 1995 Oct;

- 4(9):404–6. Available from: <http://www.magonlinelibrary.com/doi/10.12968/jowc.1995.4.9.404>
103. Boilot P, Hines EL, Gardner JW, Pitt R, John S, Mitchell J, et al. Classification of bacteria responsible for ENT and eye infections using the Cyranose system. *IEEE Sens J*. 2002 Jun; 2(3):247–53. Available from: <http://ieeexplore.ieee.org/document/1021065/>
 104. Sun H, Tian F, Liang Z, Sun T, Yu B, Yang SX, et al. Sensor Array Optimization of Electronic Nose for Detection of Bacteria in Wound Infection. *IEEE Trans Ind Electron*. 2017 Sep; 64(9):7350–8. Available from: <http://ieeexplore.ieee.org/document/7902191/>
 105. Ono S, Imai R, Ida Y, Shibata D, Komiya T, Matsumura H. Increased wound pH as an indicator of local wound infection in second degree burns. *Burns*. 2015 Jun; 41(4):820–4. Available from: <http://www.sciencedirect.com/science/article/pii/S0305417914003593>
 106. Sharp D. Printed composite electrodes for in-situ wound pH monitoring. *Biosens Bioelectron*. 2013 Dec; 50:399–405. Available from: <http://www.ncbi.nlm.nih.gov/pubmed/23893062>
 107. Tamayol A, Akbari M, Zilberman Y, Comotto M, Leshia E, Serex L, et al. Flexible pH-Sensing Hydrogel Fibers for Epidermal Applications. *Adv Healthc Mater*. 2016 Mar; 5(6):711–9. Available from: <http://doi.wiley.com/10.1002/adhm.201500553>
 108. Chen X, Wo F, Jin Y, Tan J, Lai Y, Wu J. Drug-Porous Silicon Dual Luminescent System for Monitoring and Inhibition of Wound Infection. 2017; Available from: <http://pubs.acs.org/doi/pdf/10.1021/acsnano.7b02471>
 109. Sharp D, Davis J. Integrated urate sensors for detecting wound infection. 2008; Available from: https://ac.els-cdn.com/S1388248108000866/1-s2.0-S1388248108000866-main.pdf?_tid=265c3956-b987-11e7-9eec-00000aacb35e&acdnat=1508937757_41a22668fc82ea781d87d408cbfb1a7b
 110. Kassal P, Kim J, Kumar R, De Araujo WR, Steinberg IM, Steinberg MD, et al. Smart bandage with wireless connectivity for uric acid biosensing as an indicator of wound status. *Electrochem Commun*. 2015 Jul; 56:6–10. Available from: <http://www.sciencedirect.com/science/article/pii/S1388248115000946>
 111. Liu X, Lillehoj P. Embroidered electrochemical sensors on gauze for rapid quantification of wound biomarkers. *Biosens Bioelectron*. 2017 Dec; 98:189–94. Available from: <http://www.sciencedirect.com/science/article/pii/S0956566317304396>
 112. Hajnsek M, Schiffer D, Harrich D, Koller D, Verient V, Palen J V.D., et al. An electrochemical sensor for fast detection of wound infection based on myeloperoxidase activity. *Sensors Actuators, B Chem*. 2015 Mar; 209:265–74. Available from:

- <http://www.sciencedirect.com/science/article/pii/S0925400514015202>
113. Schiffer D, Tegl G, Vielnascher R, Weber H, Herrero-Rollett A, Sigl E, et al. Myeloperoxidase-responsive materials for infection detection based on immobilized aminomethoxyphenol. *Biotechnol Bioeng*. 2016 Dec;113(12):2553–60. Available from: <http://www.ncbi.nlm.nih.gov/pubmed/27241438>
 114. Burkitt R, Sharp D. Submicromolar quantification of pyocyanin in complex biological fluids using pad-printed carbon electrodes. *Electrochem commun*. 2017 May; 78:43–6. Available from: <https://www.sciencedirect.com/science/article/pii/S1388248117300917>
 115. Sismaet HJ, Banerjee A, McNish S, Choi Y, Torralba M, Lucas S, et al. Electrochemical detection of *Pseudomonas* in wound exudate samples from patients with chronic wounds. *Wound Repair Regen*. 2016 Mar; 24(2):366–72. Available from: <http://doi.wiley.com/10.1111/wrr.12414>
 116. Mehmood N, Hariz A, Templeton S, Voelcker NH. A flexible and low power telemetric sensing and monitoring system for chronic wound diagnostics. *Biomed Eng Online*. 2015 Mar; 14:17. Available from: <http://www.ncbi.nlm.nih.gov/pubmed/25884377>
 117. Milne SD, Seoudi I, Al Hamad H, Talal TK, Anoop AA, Allahverdi N, et al. A wearable wound moisture sensor as an indicator for wound dressing change: an observational study of wound moisture and status. *Int Wound J*. 2016 Dec; 13(6):1309–14. Available from: <http://www.ncbi.nlm.nih.gov/pubmed/26561281>
 118. Ward AC, Connolly P, Tucker NP. *Pseudomonas aeruginosa* can be detected in a polymicrobial competition model using impedance spectroscopy with a novel biosensor. Beloin C, editor. *PLoS One*. 2014 Mar; 9(3):e91732. Available from: <http://dx.plos.org/10.1371/journal.pone.0091732>
 119. Bayouhdh S, Othmane A, Ponsonnet L, Ben Ouada H. Electrical detection and characterization of bacterial adhesion using electrochemical impedance spectroscopy-based flow chamber. *Colloids Surfaces A Physicochem Eng Asp*. 2008 Apr; 318(1–3):291–300. Available from: <http://linkinghub.elsevier.com/retrieve/pii/S0927775708000216>
 120. Muñoz-Berbel X, Vigués N, Mas J, Jenkins ATA, Muñoz FJ. Impedimetric characterization of the changes produced in the electrode-solution interface by bacterial attachment. *Electrochem commun*. 2007 Nov; 9(11):2654–60. Available from: <http://linkinghub.elsevier.com/retrieve/pii/S1388248107003414>
 121. Settu K, Chen CJ, Liu JT, Chen CL, Tsai JZ. Impedimetric method for measuring ultra-low *E. coli* concentrations in human urine. *Biosens Bioelectron*. 2015 Apr; 66:244–50. Available from: <http://www.sciencedirect.com/science/article/pii/S0956>

566314009166?via%3Dihub

122. Zhu T, Pei Z, Huang J, Xiong C, Shi S, Fang J. Detection of bacterial cells by impedance spectra via fluidic electrodes in a microfluidic device. *Lab Chip*. 2010 Jun; 10(12):1557–60. Available from: <http://www.ncbi.nlm.nih.gov/pubmed/20517558>
123. Kim T, Kang J, Lee J-H, Yoon J. Influence of attached bacteria and biofilm on double-layer capacitance during biofilm monitoring by electrochemical impedance spectroscopy. *Water Res*. 2011 Oct; 45(15):4615–22. Available from: <http://linkinghub.elsevier.com/retrieve/pii/S0043135411003447>
124. Yang L, Li Y, Griffis CL, Johnson MG. Interdigitated microelectrode (IME) impedance sensor for the detection of viable *Salmonella typhimurium*. *Biosens Bioelectron*. 2004 May; 19(10):1139–47. Available from: <http://www.sciencedirect.com/science/article/pii/S0956566303003828?via%3Dihub>
125. Paredes J, Becerro S, Arizti F, Aguinaga A, Del Pozo JL, Arana S. Real time monitoring of the impedance characteristics of Staphylococcal bacterial biofilm cultures with a modified CDC reactor system. *Biosens Bioelectron*. 2012 Oct; 38(1):226–32. Available from: <http://linkinghub.elsevier.com/retrieve/pii/S0956566312003399>
126. Paredes J, Becerro S, Arana S. Label-free interdigitated microelectrode based biosensors for bacterial biofilm growth monitoring using Petri dishes. *J Microbiol Methods*. 2014 May; 100(1):77–83. Available from: <http://www.sciencedirect.com/science/article/pii/S0167701214000621>
127. Pires L, Sachsenheimer K, Kleintschek T, Waldbaur A, Schwartz T, Rapp BE. Online monitoring of biofilm growth and activity using a combined multi-channel impedimetric and amperometric sensor. *Biosens Bioelectron*. 2013 Sep; 47:157–63. Available from: <http://linkinghub.elsevier.com/retrieve/pii/S0956566313001747>
128. Bonetto MC, Sacco NJ, Ohlsson AH, Corton E, Sticker D, Charwat V, et al. Rapid and label-free differentiation of bacterial strains using low frequency electrochemical impedance spectroscopy. In: 2014 IEEE 9th IberoAmerican Congress on Sensors [Internet]. IEEE; 2014. p. 1–4. Available from: <http://ieeexplore.ieee.org/document/6995516/>
129. Farrow MJ, Hunter IS, Connolly P. Developing a real time sensing system to monitor bacteria in wound dressings. *Biosensors*. 2012 May; 2(2):171–88. Available from: <http://www.mdpi.com/2079-6374/2/2/171/>
130. Sheybani R, Shukla A. Highly sensitive label-free dual sensor array for rapid detection of wound bacteria. *Biosens Bioelectron*. 2017 Jun; 92:425–33. Available from: <http://linkinghub.elsevier.com/retrieve/pii/S0956566316311071>

131. Zikmund A, Ripka P, Krasny L, Judl T, Jahoda D. Biofilm detection by the impedance method: Bacteria layer detection on surgical implants. In: Proceedings - 2010 3rd International Conference on Biomedical Engineering and Informatics, BMEI 2010. IEEE; 2010. p. 1432–4. Available from: <http://ieeexplore.ieee.org/document/5639411/>
132. Lasia A. Electrochemical Impedance Spectroscopy and its Applications. 2014th ed. New York: Springer New York; 2014. Available from: <https://link.springer.com/content/pdf/10.1007%2F978-1-4614-8933-7.pdf>
133. Niya SMR, Hoorfar M. Study of proton exchange membrane fuel cells using electrochemical impedance spectroscopy technique – A review. *J Power Sources*. 2013 Oct; 240:281–93. Available from: <http://www.sciencedirect.com/science/article/pii/S0378775313006022>
134. Yadav P, Pandey K, Bhatt V, Kumar M, Kim J. Critical aspects of impedance spectroscopy in silicon solar cell characterization: A review. Vol. 76, *Renewable and Sustainable Energy Reviews*. Pergamon; 2017. p. 1562–78. Available from: <http://www.sciencedirect.com/science/article/pii/S1364032116309509>
135. Westerhoff U, Kroker T, Kurbach K, Kurrat M. Electrochemical impedance spectroscopy based estimation of the state of charge of lithium-ion batteries. *J Energy Storage*. 2016 Nov; 8:244–56. Available from: <http://www.sciencedirect.com/science/article/pii/S2352152X16301359>
136. Fricke H, Morse S. The Electric Resistance and Capacity of Blood for Frequencies Between 800 and 4(1/2) Million Cycles. *J Gen Physiol*. 1925 Nov; 9(2):153–67. Available from: <http://www.ncbi.nlm.nih.gov/pubmed/19872239>
137. Dubuisson M. Impedance changes in muscle during contraction, and their possible relation to chemical processes. *J Physiol*. 1937 Mar; 89(2):132–52. Available from: <http://doi.wiley.com/10.1113/jphysiol.1937.sp003469>
138. Dean DAA, Ramanathan T, Machado D, Sundararajan R. Electrical Impedance Spectroscopy Study of Biological Tissues. *J Electrostat*. 2008 Mar; 66(3–4):165–77. Available from: <http://www.ncbi.nlm.nih.gov/pubmed/19255614>
139. Rigaud B, Morucci JP, Chauveau N. Bioelectrical impedance techniques in medicine. Part I: Bioimpedance measurement. Second section: impedance spectrometry. *Crit Rev Biomed Eng*. 1996; 24(4–6):257–351. Available from: <http://www.ncbi.nlm.nih.gov/pubmed/9196884>
140. Foster KR, Schwan HP. Dielectric properties of tissues and biological materials: a critical review. *Crit Rev Biomed Eng*. 1989; 17(1):25–104. Available from: <http://www.ncbi.nlm.nih.gov/pubmed/2651001>

141. Brown B. Electrical impedance tomography (EIT): a review. *J Med Eng Technol.* 2003 Jan;27(3):97–108. Available from: <http://www.tandfonline.com/doi/full/10.1080/0309190021000059687>
142. Cady P, Dufour SW, Lawless P, Nunke B, Kraeger SJ. Impedimetric screening for bacteriuria. *J Clin Microbiol.* 1978 Mar; 7(3):273–8. Available from: <http://www.ncbi.nlm.nih.gov/pubmed/348719>
143. Ur A, Brown DFJ. Impedance Monitoring of Bacterial Activity. *J Med Microbiol.* 1975 Feb; 8(1):19–28. Available from: <http://jmm.microbiologyresearch.org/content/journal/jmm/10.1099/00222615-8-1-19>
144. Firstenberg-Eden R, Eden G. *Impedance Microbiology.* Research Studies Press; 1984.
145. Franklin MJ, Nivens DE, Guckert JB, White DC. Effect of electrochemical impedance spectroscopy on microbial biofilm cell number, viability, and activity. *Corrosion.* 1991 Jul; 47(7):519–22. Available from: <http://corrosionjournal.org/doi/10.5006/1.3585287>
146. Schwan HP. Electrical Properties of Tissue and Cell Suspensions. *Adv Biol Med Phys.* 1957 Jan; 5:147–209. Available from: <https://www.sciencedirect.com/science/article/pii/B9781483231112500080>
147. Fricke H, Schwan Hp, Li K, Bryson V. A dielectric study of the low-conductance surface membrane in *E. coli*. *Nature.* 1956 Jan; 177(4499):134–5. Available from: <http://www.ncbi.nlm.nih.gov/pubmed/13288615>
148. Yardley JE, Kell DB, Barrett J, Davey CL. On-Line, Real-Time Measurements of Cellular Biomass using Dielectric Spectroscopy. *Biotechnol Genet Eng Rev.* 2000; 17(1):3–36. Available from: <http://www.tandfonline.com/doi/pdf/10.1080/02648725.2000.10647986>
149. Valentinuzzi ME. Bioelectrical impedance techniques in medicine. Part I: Bioimpedance measurement. First section: general concepts. *Crit Rev Biomed Eng.* 1996; 24(4–6):223–55. Available from: <http://www.ncbi.nlm.nih.gov/pubmed/9196883>
150. Schröder U, Harnisch F, Angenent LT. Microbial electrochemistry and technology: terminology and classification. *Energy Environ Sci.* 2015; 8(2):513–9. Available from: <http://pubs.rsc.org/en/content/articlepdf/2015/ee/c4ee03359k>
151. Schroder U. Fuel Cells - Exploratory Fuel Cells: Microbial Fuel Cells. *Encycl Electrochem power sources.* 2009;206–16.
152. Koch C, Harnisch F. What Is the Essence of Microbial Electroactivity? *Front Microbiol.* 2016;7:1890. Available from: <http://www.ncbi.nlm.nih.gov/pubmed/27933052>
153. Sydow A, Krieg T, Mayer F, Schrader J, Holtmann D. Electroactive bacteria—molecular mechanisms and genetic tools. Vol. 98, *Applied Microbiology and Biotechnology.*

- Springer Berlin Heidelberg; 2014. p. 8481–95. Available from: <http://link.springer.com/10.1007/s00253-014-6005-z>
154. Donlan RM. Biofilms: microbial life on surfaces. *Emerg Infect Dis*. 2002 Sep;8(9):881–90. Available from: <http://www.ncbi.nlm.nih.gov/pubmed/12194761>
 155. An YH, Friedman RJ. Concise review of mechanisms of bacterial adhesion to biomaterial surfaces. *J Biomed Mater Res*. 1998; 43(3):338–48. Available from: <http://www.ncbi.nlm.nih.gov/pubmed/9730073>
 156. Pringle JH, Fletcher M. Influence of substratum hydration and adsorbed macromolecules on bacterial attachment to surfaces. *Appl Environ Microbiol*. 1986 Jun; 51(6):1321–5. Available from: <http://www.ncbi.nlm.nih.gov/pubmed/2425737>
 157. Marsili E, Baron DB, Shikhare ID, Coursolle D, Gralnick JA, Bond DR. *Shewanella* secretes flavins that mediate extracellular electron transfer. *Proc Natl Acad Sci*. 2008 Mar; 105(10):3968–73. Available from: <http://www.ncbi.nlm.nih.gov/pubmed/18316736>
 158. Daniels JS, Pourmand N. Label-Free Impedance Biosensors: Opportunities and Challenges. *Electroanalysis*. 2007 May; 19(12):1239–57. Available from: <http://www.ncbi.nlm.nih.gov/pubmed/18176631>
 159. Daniele S, Bragato C. From Macroelectrodes to Microelectrodes: Theory and Electrode Properties. In Springer, New York, NY; 2014. p. 373–401. Available from: https://link.springer.com/chapter/10.1007/978-1-4939-0676-5_15
 160. Rowley-Neale SJ, Banks CE. Biosensors-microelectrode design and operation. In: *Encyclopedia of Interfacial Chemistry: Surface Science and Electrochemistry*. Elsevier; 2018. p. 72–80.
 161. Mejri MB, Baccar H, Baldrich E, Campo FJ Del, Helali S, Ktari T, et al. Impedance biosensing using phages for bacteria detection: Generation of dual signals as the clue for in-chip assay confirmation. *Biosens Bioelectron*. 2010; 10(4):1261–67.
 162. Goikoetxea E, Routkevitch D, de Weerd A, Green JJ, Steenackers H, Braeken D. Impedimetric fingerprinting and structural analysis of isogenic *E. coli* biofilms using multielectrode arrays. *Sensors Actuators, B Chem*. 2018 Feb; 263:319–26. Available from: <https://www.sciencedirect.com/science/article/pii/S0925400518302120?via%3Dihub>
 163. Muñoz-Berbel X, Muñoz FJ, Vigués N, Mas J. On-chip impedance measurements to monitor biofilm formation in the drinking water distribution network. *Sensors Actuators, B Chem*. 2006 Oct; 118(1–2):129–34. Available from: <http://www.sciencedirect.com/science/article/pii/S0925400506002802>

164. van Duuren JBJH, Müsken M, Karge B, Tomasch J, Wittmann C, Häussler S, et al. Use of Single-Frequency Impedance Spectroscopy to Characterize the Growth Dynamics of Biofilm Formation in *Pseudomonas aeruginosa*. *Sci Rep*. 2017 Dec; 7(1):5223. Available from: <http://www.nature.com/articles/s41598-017-05273-5>
165. Cady P. Rapid automated bacterial identification by impedance measurement. In: *New approaches to the identification of microorganisms*. London: Wiley; 1975. p. 74–9.
166. Lukaski HC, Moore M. Bioelectrical impedance assessment of wound healing. *J Diabetes Sci Technol*. 2012 Jan; 6(1):209–12. Available from: <http://www.ncbi.nlm.nih.gov/pubmed/22401341>
167. Spence DW, Pomeranz B. Surgical wound healing monitored repeatedly in vivo using electrical resistance of the epidermis. *Physiol Meas*. 1996 May;17(2):57–69. Available from: <http://www.ncbi.nlm.nih.gov/pubmed/8724518>
168. Farrow M. Thesis: A Wound Infection Monitoring System. The University of Strathclyde; 2010.
169. Hayat A, Marty JL. Disposable screen printed electrochemical sensors: tools for environmental monitoring. *Sensors (Basel)*. 2014 Jun;14(6):10432–53. Available from: <http://www.ncbi.nlm.nih.gov/pubmed/24932865>
170. Woese CR, Kandler O, Wheelis ML. Towards a natural system of organisms: Proposal for the domains Archaea, Bacteria, and Eucarya. Vol. 87, *Proc. Natl. Acad. Sci. USA*. 1990. Available from: <http://www.pnas.org/content/pnas/87/12/4576.full.pdf>
171. Young KD. Bacterial morphology: why have different shapes? *Curr Opin Microbiol*. 2007 Dec; 10(6):596–600. Available from: <http://www.ncbi.nlm.nih.gov/pubmed/17981076>
172. Koch AL. What Size Should A Bacterium Be? A Question of Scale. *Annu Rev Microbiol*. 1996 Oct; 50(1):317–48. Available from: <http://www.ncbi.nlm.nih.gov/pubmed/8905083>
173. Bartholomew JW, Mittwer TOD. The Gram Stain. *Bacteriol Rev*. 1952 Mar;16(1):1–29. Available from: <http://www.ncbi.nlm.nih.gov/pubmed/14925025>
174. Greenwood D, Barer MR. Microbiology and medicine- Chapter 2 Structure. In: *Medical Microbiology: Eighteenth Edition*. University of Texas Medical Branch at Galveston; 2012. p. 2–8. Available from: <http://www.ncbi.nlm.nih.gov/pubmed/21413343>
175. Jonson A-B, Normark S, Rhen M. Fimbriae, pili, flagella and bacterial virulence. *Contrib Microbiol*. 2005; 12:67–89. Available from: <http://www.ncbi.nlm.nih.gov/pubmed/15496777>
176. Kearns DB. A field guide to bacterial swarming motility. *Nat Rev Microbiol*. 2010 Sep;

- 8(9):634–44. Available from: <http://www.ncbi.nlm.nih.gov/pubmed/20694026>
177. Alcamo IE, Warner JM, Alcamo IE. Schaum's outlines : microbiology. McGraw-Hill; 2010. 343 p.
178. Doelle HW. Chemosynthesis—Pathways of Carbohydrate Breakdown. In: Bacterial Metabolism. University of Texas Medical Branch at Galveston; 1969. p. 129–98. Available from: <http://www.ncbi.nlm.nih.gov/pubmed/21413278>
179. Jurtschuk P. Bacterial Metabolism. Medical Microbiology. University of Texas Medical Branch at Galveston; 1996. Available from: <http://www.ncbi.nlm.nih.gov/pubmed/21413278>
180. Bjarnsholt T. Biofilm Infection. In: Biofilm Infection. 2011. p. 1–9. Available from: www.springer.com
181. Skariyachan S, Sridhar VS, Packirisamy S, Kumargowda ST, Challapilli SB. Recent perspectives on the molecular basis of biofilm formation by *Pseudomonas aeruginosa* and approaches for treatment and biofilm dispersal. Folia Microbiol (Praha). 2018 Jul; 63(4):413–32. Available from: <http://link.springer.com/10.1007/s12223-018-0585-4>
182. Miller MB, Bassler BL. Quorum Sensing in Bacteria. Annu Rev Microbiol. 2001 Oct; 55(1):165–99. Available from: <http://www.annualreviews.org/doi/10.1146/annurev.micro.55.1.165>
183. Rabin N, Zheng Y, Opoku-Temeng C, Du Y, Bonsu E, Sintim HO. Biofilm formation mechanisms and targets for developing antibiofilm agents. Future Med Chem. 2015 Mar; 7(4):493–512. Available from: <http://www.future-science.com/doi/10.4155/fmc.15.6>
184. Wei D, Zhu XM, Chen YY, Li XY, Chen YP, Liu HY, et al. Chronic wound biofilms: Diagnosis and therapeutic strategies. Vol. 132, Chinese Medical Journal. 2019; p. 2737–44. Available from: [/pmc/articles/PMC6940106/](http://pmc/articles/PMC6940106/)
185. Otto M. *Staphylococcus epidermidis*- the “accidental” pathogen. Nat Rev Microbiol. 2009 Aug; 7(8):555–67. Available from: <http://www.ncbi.nlm.nih.gov/pubmed/19609257>
186. Bard AJ, Faulkner LR. Electrochemical Methods: Fundamentals and Applications. 2nd ed. New York: Wiley; 2001. Available from: <http://xlink.rsc.org/?DOI=C5EE01283J>
187. Orazem ME, Tribollet B. Electrochemical Impedance Spectroscopy. 2nd ed. Hoboken, NJ: John Wiley & Sons, Ltd; 2017.
188. Burgess J. Ions in Solution: Basic Principles of Chemical Interactions. Woodhead Publishing; 1999.
189. Soustelle M. Solvents and Solvation. In: Ionic and Electrochemical Equilibria. Hoboken, NJ, USA: John Wiley & Sons, Inc.; 2016. p. 31–59. Available from:

<http://doi.wiley.com/10.1002/9781119178606.ch2>

190. Andreev M, De Pablo JJ, Chremos A, Douglas JF. Influence of Ion Solvation on the Properties of Electrolyte Solutions. *J Phys Chem B*. 2018 Apr; 122(14):4029–34. Available from: <https://pubs.acs.org/doi/abs/10.1021/acs.jpcc.8b00518>
191. Peskir G. On the diffusion coefficient: The Einstein relation and beyond. *Stoch Model*. 2003;19(3):383–405.
192. Neuman MR. *The Biomedical Engineering Handbook*. 2nd ed. RC Press LLC; 2000.
193. Raicu V, Feldman Y. *Dielectric Relaxation in Biological Systems*. 1st ed. Oxford, UK: Oxford University Press (OUP); 2015. Available from: <https://oxford.universitypressscholarship.com/view/10.1093/acprof:oso/9780199686513.001.0001/acprof-9780199686513-miscMatter-1>
194. Awasthi P, Das S. Reduced electrode polarization at electrode and analyte interface in impedance spectroscopy using carbon paste and paper. *Rev Sci Instrum*. 2019 Dec; 90(12):124103. Available from: <http://aip.scitation.org/doi/10.1063/1.5123585>
195. Koklu A, Mansoorifar A, Beskok A. Effects of electrode size and surface morphology on electrode polarization in physiological buffers. *Electrophoresis*. 2019 Mar; 40(5):766–75. Available from: <http://doi.wiley.com/10.1002/elps.201800303>
196. Lvovich VF. Electrocatalysis Fundamentals. In: *Encyclopedia of Applied Electrochemistry*. New York, NY: Springer New York; 2014. p. 485–507. Available from: http://link.springer.com/10.1007/978-1-4419-6996-5_67
197. Scott K. Electrochemical Principles and Characterization of Bioelectrochemical Systems. In: *Microbial Electrochemical and Fuel Cells: Fundamentals and Applications*. Elsevier Inc.; 2016. p. 29–66.
198. Bird J. *Electrical & Electronic Principles & Technology*. 3rd ed. Oxford, UK: Newnes; 2007. Available from: <http://straniks.ddns.is74.ru/pub/EEL/Data/Теоретические основы электротехники/Bird J. Electrical and Electronic Principles and Technology.pdf>
199. Muñoz-Berbel X, Godino N, Laczka O, Baldrich E, Muñoz FX, del Campo FJ. Impedance-Based Biosensors for Pathogen Detection. In: *Principles of Bacterial Detection: Biosensors, Recognition Receptors and Microsystems*. New York, NY: Springer New York; 2008. p. 341–76. Available from: http://link.springer.com/10.1007/978-0-387-75113-9_15
200. Grossi M, Riccò B. Electrical impedance spectroscopy (EIS) for biological analysis and food characterization: a review. *J Sens Sens Syst*. 2017; 6:303–25. Available from: <https://doi.org/10.5194/jsss-6-303-2017>

201. Ianeselli L, Greci G, Callegari C, Tormen M, Casalis L. Development of stable and reproducible biosensors based on electrochemical impedance spectroscopy: Three-electrode versus two-electrode setup. *Biosens Bioelectron.* 2014 May 15; 55:1–6.
202. Cottis RA, Turgoose S, Neuman R. Corrosion testing made easy: Impedance and noise analysis . 1999. Available from: <https://www.osti.gov/etdeweb/biblio/20050622>
203. Beyenal H, Babauta J. Biofilms in Bioelectrochemical Systems. *Systems: From Laboratory Practice to Data Interpretation.* 2015. p. 1-412.
204. Russell S, Norvig P. *Artificial intelligence: a modern approach.* Global Edition. Pearson Education; 2016. Available from: <https://www.vlebooks.com/Vleweb/Product/Index/861765?page=0>
205. Bini SA. Artificial Intelligence, Machine Learning, Deep Learning, and Cognitive Computing: What Do These Terms Mean and How Will They Impact Health Care? *J Arthroplasty.* 2018 Aug; 33(8):2358–61. Available from: <https://pubmed.ncbi.nlm.nih.gov/29656964/>
206. Helm JM, Swiergosz AM, Haeberle HS, Karnuta JM, Schaffer JL, Krebs VE, et al. Machine Learning and Artificial Intelligence: Definitions, Applications, and Future Directions. Vol. 13, *Current Reviews in Musculoskeletal Medicine.* Springer; 2020. p. 69–76. Available from: </pmc/articles/PMC7083992/?report=abstract>
207. Noorbakhsh-Sabet N, Zand R, Zhang Y, Abedi V. Artificial Intelligence Transforms the Future of Health Care. Vol. 132, *American Journal of Medicine.* Elsevier Inc.; 2019. p. 795–801.
208. Dreiseitl S, Ohno-Machado L. Logistic regression and artificial neural network classification models: A methodology review. *J Biomed Inform.* 2002 Oct 1;35(5–6):352–9.
209. Kennedy MB. Synaptic signaling in learning and memory. *Cold Spring Harb Perspect Biol.* 2016 Feb; 8(2):1–16. Available from: </pmc/articles/PMC4743082/?report=abstract>
210. Aggarwal CC. *Neural Networks and Deep Learning.* Neural Networks and Deep Learning. Springer International Publishing; 2018.
211. Kingma DP, Ba JL. Adam: A method for stochastic optimization. In: 3rd International Conference on Learning Representations, ICLR 2015 - Conference Track Proceedings. International Conference on Learning Representations, ICLR; 2015. Available from: <https://arxiv.org/abs/1412.6980v9>
212. Lawrence S, Giles CL, Tsoi AC. *Lessons in Neural Network Training: Overfitting May be Harder than Expected.* AAAI Press; 1997. Available from: www.aaai.org
213. Char DS, Shah NH, Magnus D. *Implementing machine learning in health care* ’

- addressing ethical challenges. Vol. 378, New England Journal of Medicine. Massachusetts Medical Society; 2018. p. 981–3.
214. Pedregosa F, Varoquaux G, Gramfort A, Michel V, Thirion B, Grisel O, et al. Scikit-learn: Machine Learning in Python. J Mach Learn Res. 2011;12(85):2825–30. Available from: <http://scikit-learn.sourceforge.net>.
 215. Milne SD, Connolly P. The influence of different dressings on the pH of the wound environment. J Wound Care. 2014; 23(2):53–7. Available from: <https://strathprints.strath.ac.uk/48536/>
 216. Werthén M, Henriksson L, Jensen PØ, Sternberg C, Givskov M, Bjarnsholt T. An *in vitro* model of bacterial infections in wounds and other soft tissues. APMIS. 2010 Feb;118(2):156–64. Available from: <http://onlinelibrary.wiley.com/doi/10.1111/j.1600-0463.2009.02580.x/full>
 217. Kadam S, Nadkarni S, Lele J, Sakhalkar S, Mokashi P, Kaushik KS. Bioengineered Platforms for Chronic Wound Infection Studies: How Can We Make Them More Human-Relevant? Vol. 7, Frontiers in Bioengineering and Biotechnology; 2019. p. 418. Available from: </pmc/articles/PMC6923179/?report=abstract>
 218. Oates A, McBain AJ. Growth of MRSA and *Pseudomonas aeruginosa* in a fine-celled foam model containing sessile commensal skin bacteria. Biofouling. 2016 Jan; 32(1):25–33. Available from: <https://pubmed.ncbi.nlm.nih.gov/26727101/>
 219. Price BL, Lovering AM, Bowling FL, Dobson CB. Development of a Novel Collagen Wound Model To Simulate the Activity and Distribution of Antimicrobials in Soft Tissue during Diabetic Foot Infection. Antimicrob Agents Chemother. 2016 Nov; 60(11):6880–9. Available from: <http://www.ncbi.nlm.nih.gov/pubmed/27620475>
 220. Herigstad B, Hamilton M, Heersink J. How to optimize the drop plate method for enumerating bacteria. J Microbiol Methods. 2001;44(2):121–9.
 221. Merritt JH, Kadouri DE, O’Toole GA. Growing and analyzing static biofilms. Curr Protoc Microbiol. 2011;(SUPPL. 22):1–18.
 222. Bruen D, Delaney C, Florea L, Diamond D. Glucose Sensing for Diabetes Monitoring: Recent Developments. Sensors. 2017 Aug; 17(8):1866. Available from: <http://www.ncbi.nlm.nih.gov/pubmed/28805693>
 223. Ward A. Thesis: A Cystic Fibrosis Infection Monitor. The University of Strathclyde. 2015.
 224. Connolly P, Shedden L. A system and method for cell characterisation. 2010. Available from: <https://patents.google.com/patent/EP2271933B1/un>
 225. Albulbul A. Evaluating major electrode types for idle biological signal measurements

- for modern medical technology. *Bioengineering*. 2016 Sep 1;3(3).
226. Venkatratnam C, Farrukh N. Electrode considerations, excitation methods and measurement techniques for electrical impedance tomography. In: *IFMBE Proceedings*. Springer Verlag; 2016. p. 1–5.
 227. Kirby-Bauer Disk Diffusion Susceptibility Test Protocol. 2009. Available from: www.atcc.org
 228. Yamanaka K, Vestergaard MC, Tamiya E. Printable electrochemical biosensors: A focus on screen-printed electrodes and their application. Vol. 16, *Sensors (Switzerland)*. MDPI AG; 2016.
 229. Zhang W, Zhu S, Luque R, Han S, Hu L, Xu G. Recent development of carbon electrode materials and their bioanalytical and environmental applications. Vol. 45, *Chemical Society Reviews*. Royal Society of Chemistry; 2016. p. 715–52.
 230. Wang J, Pedrero M, Sakslund H, Hammerich O, Pingarron J. Electrochemical activation of screen-printed carbon strips. *Analyst*. 1996 Jan; 121(3):345. Available from: <http://xlink.rsc.org/?DOI=an9962100345>
 231. Randles JEB. Kinetics of rapid electrode reactions. *Discuss Faraday Soc*. 1947 Jan;1:11. Available from: <http://xlink.rsc.org/?DOI=df9470100011>
 232. Wei H, Sun J-J, Xie Y, Lin C-G, Wang Y-M, Yin W-H, et al. Enhanced electrochemical performance at screen-printed carbon electrodes by a new pretreating procedure. *Anal Chim Acta*. 2007 Apr; 588(2):297–303. Available from: <https://www.sciencedirect.com/science/article/pii/S0003267007002863>
 233. Morton HE. The Relationship Of Concentration And Germicidal Efficiency Of Ethyl Alcohol. *Ann N Y Acad Sci*. 1950 Aug; 53(1):191–6. Available from: <http://doi.wiley.com/10.1111/j.1749-6632.1950.tb31944.x>
 234. Salvage R, Hull CM, Kelly DE, Kelly SL. Use of 70% alcohol for the routine removal of microbial hard surface bioburden in life science cleanrooms. *Future Microbiol*. 2014 Oct 1;9(10):1123–30.
 235. scikit-learn: machine learning in Python — scikit-learn 0.21.3 documentation [Internet]. [cited 2019 Oct 8]. Available from: <https://scikit-learn.org/stable/>
 236. Piramuthu S. Evaluating feature selection methods for learning in data mining applications. *Eur J Oper Res*. 2004; 156(2):483–94. Available from: www.elsevier.com/locate/dsw
 237. Vieira S, Lopez Pinaya WH, Mechelli A. Main concepts in machine learning. In: Mechelli A, Vieira S, editors. *Machine Learning: Methods and Applications to Brain Disorders*. Elsevier; 2019. p. 21–44.

238. Visalakshi S, Radha V. A literature review of feature selection techniques and applications: Review of feature selection in data mining. In: 2014 IEEE International Conference on Computational Intelligence and Computing Research, IEEE ICCIC 2014. Institute of Electrical and Electronics Engineers Inc.; 2015.
239. Ioffe S, Szegedy C. Batch normalization: Accelerating deep network training by reducing internal covariate shift. In: 32nd International Conference on Machine Learning, ICML 2015. International Machine Learning Society (IMLS); 2015. p. 448–56. Available from: <https://arxiv.org/abs/1502.03167v3>
240. Ibnu Choldun R. M, Santoso J, Surendro K. Determining the number of hidden layers in neural network by using principal component analysis. In: Advances in Intelligent Systems and Computing. Springer Verlag; 2020. p. 490–500. Available from: https://link.springer.com/chapter/10.1007/978-3-030-29513-4_36
241. Géron A. Hands-On Machine Learning with Scikit-Learn and TensorFlow. 1st ed. Sebastopol, CA: O'Reilly Media; 2017.
242. Powers DMW. Evaluation: From Precision, Recall And F-Measure To ROC, Informedness, Markedness & Correlation. J Mach Learn Technol. 2011; 2(1):37–63. Available from: <http://dspace.flinders.edu.au/dspace/http://www.bioinfo.in/contents.php?id=51>
243. Klotz D. Negative capacitance or inductive loop? – A general assessment of a common low frequency impedance feature. Electrochem Commun. 2019 Jan 1;98:58–62.
244. Taibl S, Fafilek G, Fleig J. Impedance spectra of Fe-doped SrTiO₃ thin films upon bias voltage: Inductive loops as a trace of ion motion. Nanoscale. 2016 Aug 7;8(29):13954–66.
245. Deepa P, Padmalatha R. Corrosion behaviour of 6063 aluminium alloy in acidic and in alkaline media. Arab J Chem. 2017 May 1;10:S2234–44.
246. Ha H, Payer J. The effect of silver chloride formation on the kinetics of silver dissolution in chloride solution. Electrochim Acta. 2011 Feb 28;56(7):2781–91.
247. Minhas P, Bansal V, Patel J, Ho JS, Diaz J, Datta A, et al. Electrodes for high-definition transcutaneous DC stimulation for applications in drug delivery and electrotherapy, including tDCS. J Neurosci Methods. 2010 Jul 15;190(2):188–97.
248. Andrews JM. Determination of minimum inhibitory concentrations. J Antimicrob Chemother. 2001 Jul;48(suppl_1):5–16.
249. Mulley G, Jenkins ATA, Waterfield NR. Inactivation of the Antibacterial and Cytotoxic Properties of Silver Ions by Biologically Relevant Compounds. Marr AC, editor. PLoS One. 2014 Apr; 9(4):e94409. Available from: <https://dx.plos.org/10.1371/>

journal.pone.0094409

250. ACTICOAT Antimicrobial Silver Dressings | Smith & Nephew - Corporate [Internet]. [cited 2017 Oct 17]. Available from: <http://www.smith-nephew.com/key-products/advanced-wound-management/acticoat/>
251. Chopra I. The increasing use of silver-based products as antimicrobial agents: a useful development or a cause for concern? *J Antimicrob Chemother.* 2007 Apr; 59(4):587–90. Available from: <http://academic.oup.com/jac/article/59/4/587/677868/The-increasing-use-of-silverbased-products-as>
252. Meija J, Coplen TB, Berglund M, Brand WA, De Bièvre P, Gröning M, et al. Atomic weights of the elements 2013 (IUPAC Technical Report). Vol. 88, *Pure and Applied Chemistry*. Walter de Gruyter GmbH; 2016. p. 265–91.
253. Mondal R, Foote M, Canada A, Wiencek M, Cowan ME, Acevedo C. Efficient Silver Release From Ion Exchange Silver Dressings in Biologically Relevant Media. *WOUNDS.* 2020; 32(1):22–9. Available from: <https://www.woundsresearch.com/article/efficient-silver-release-ion-exchange-silver-dressings-biologically-relevant-media>
254. de la Fuente-Núñez C, Reffuveille F, Fernández L, Hancock RE. Bacterial biofilm development as a multicellular adaptation: antibiotic resistance and new therapeutic strategies. *Curr Opin Microbiol.* 2013 Oct; 16(5):580–9. Available from: <https://www.sciencedirect.com/science/article/pii/S1369527413000891>
255. Ehrenberg M, Bremer H, Dennis PP. Medium-dependent control of the bacterial growth rate. Vol. 95, *Biochimie.* 2013. p. 643–58.
256. Rocha PRF, Schlett P, Kintzel U, Mailänder V, Vandamme LKJ, Zeck G, et al. Electrochemical noise and impedance of Au electrode/electrolyte interfaces enabling extracellular detection of glioma cell populations. *Sci Rep.* 2016 Oct 6;6.
257. You C, Zabara MA, Orazem M, Ulgut B. Application of the Kramers-Kronig Relations to Multi-Sine Electrochemical Impedance Measurements. *J Electrochem Soc.* 2020;167(020515).
258. Manohar AK, Bretschger O, Neelson KH, Mansfeld F. The use of electrochemical impedance spectroscopy (EIS) in the evaluation of the electrochemical properties of a microbial fuel cell. *Bioelectrochemistry.* 2008 Apr; 72(2):149–54. Available from: <http://www.ncbi.nlm.nih.gov/pubmed/18294928>
259. Ramasamy RP, Ren Z, Mench MM, Regan JM. Impact of initial biofilm growth on the anode impedance of microbial fuel cells. *Biotechnol Bioeng.* 2008 Sep; 101(1):101–8. Available from: <http://www.ncbi.nlm.nih.gov/pubmed/18646217>

260. Ren Z, Ramasamy RP, Cloud-Owen SR, Yan H, Mench MM, Regan JM. Time-course correlation of biofilm properties and electrochemical performance in single-chamber microbial fuel cells. *Bioresour Technol.* 2011 Jan; 102(1):416–21. Available from: <http://www.ncbi.nlm.nih.gov/pubmed/20591659>
261. Cardosi MF, Birch SW. Screen printed glucose electrodes based on platinised carbon particles and glucose oxidase. *Anal Chim Acta.* 1993 Apr 15;276(1):69–74.
262. Antuña-Jiménez D, González-García MB, Hernández-Santos D, Fanjul-Bolado P. Screen-Printed Electrodes Modified with Metal Nanoparticles for Small Molecule Sensing. *Biosensors.* 2020 Feb; 10(2):9. Available from: <https://www.mdpi.com/2079-6374/10/2/9>
263. Levi MD, Lu Z, Aurbach D. Application of finite-diffusion models for the interpretation of chronoamperometric and electrochemical impedance responses of thin lithium insertion V2O5 electrodes. *Solid State Ionics.* 2001 Jul 2;143(3–4):309–18.
264. Tyurin RS, Lyalikov YS, Zhdanov SI. Thin-layer Electrochemistry. *Russ Chem Rev.* 1972 Dec 31;41(12):1086–100.
265. Barbero G, Lelidis I. Analysis of Warburg's impedance and its equivalent electric circuits. *Phys Chem Chem Phys.* 2017 Sep 20;19(36):24934–44.
266. McColl D, MacDougall M, Watret L, Connolly P. Monitoring moisture without disturbing the wound dressing. *Wounds UK.* 2009;5(3):94–9.
267. Pargar F, Kolev H, Koleva DA, van Breugel K. Microstructure, surface chemistry and electrochemical response of Ag|AgCl sensors in alkaline media. *J Mater Sci.* 2018 May 1;53(10):7527–50.
268. Sultana ST, Babauta JT, Beyenal H. Electrochemical biofilm control: A review. *Biofouling.* 2015; 31(9):745–58.
269. Czerwińska-Głównka D, Krukiewicz K. A journey in the complex interactions between electrochemistry and bacteriology: From electroactivity to electromodulation of bacterial biofilms. Vol. 131, *Bioelectrochemistry.* Elsevier B.V.; 2020. p. 107401.
270. Poritz MA, Lingenfelter B. Multiplex PCR for detection and identification of microbial pathogens. In: *Advanced Techniques in Diagnostic Microbiology.* Springer International Publishing; 2018. p. 475–93. Available from: https://doi.org/10.1007/978-3-319-95111-9_19
271. Grim CM, Luu GT, Sanchez LM. Staring into the void: demystifying microbial metabolomics. *FEMS Microbiol Lett.* 2019 Jun; 366(11):135. Available from: <https://academic.oup.com/femsle/article/doi/10.1093/femsle/fnz135/5519856>
272. Bonnet M, Lagier JC, Raoult D, Khelaifia S. Bacterial culture through selective and non-

- selective conditions: the evolution of culture media in clinical microbiology. Vol. 34, New Microbes and New Infections. Elsevier Ltd; 2020. p. 100622. Available from: [/pmc/articles/PMC6961714/](https://pubmed.ncbi.nlm.nih.gov/32311114/)
273. Tuson HH, Weibel DB. Bacteria-surface interactions. *Soft Matter*. 2013 May; 9(18):4368–80. Available from: <http://www.ncbi.nlm.nih.gov/pubmed/23930134>
 274. Gnaim R, Golberg A, Sheviriyov J, Rubinsky B, González CA. Detection and differentiation of bacteria by electrical bioimpedance spectroscopy. *Biotechniques*. 2020 Jul; 69(1):26–36. Available from: <https://www.future-science.com/doi/10.2144/btn-2019-0080>
 275. Esteban-Ferrer D, Edwards MA, Fumagalli L, Juárez A, Gomila G. Electric polarization properties of single bacteria measured with electrostatic force microscopy. *ACS Nano*. 2014 Oct; 8(10):9843–9. Available from: <https://pubs.acs.org/doi/abs/10.1021/nn5041476>
 276. Fu L, Wu K, Ji J, Zhang J, Guo X. A highly sensitive disposable glucose biosensor based on platinum nanoflowers decorated screen printed carbon electrode. In: *Proceedings of IEEE Sensors*. Institute of Electrical and Electronics Engineers Inc.; 2017. p. 1–3.
 277. Pereira Silva Neves MM, González-García MB, Bobes-Limenes P, Pérez-Junquera A, Hernández-Santos D, Vidal-Iglesias FJ, et al. A non-enzymatic ethanol sensor based on a nanostructured catalytic disposable electrode. *Anal Methods*. 2017 Sep; 9(35):5108–14. Available from: <https://pubs.rsc.org/en/content/articlehtml/2017/ay/c7ay01078h>
 278. Keefe AS, Dahn JR. Temperature Dependent Electrochemical Impedance Spectroscopy Studies of Lithium Ion Batteries. *ECS Meet Abstr*. 2019 Feb 1; MA2019-03(2):207. Available from: <https://iopscience.iop.org/article/10.1149/MA2019-03/2/207>
 279. Li P, Wang X, Gao W, Yan W, Guan W, Ma Y, et al. Electrochemical method for the quantitative determination of: *Escherichia coli* based on gold functionalized FTO substrate. *Analyst*. 2018 Mar 21;143(6):1462–7.
 280. Sanchez-Herrera D, Pacheco-Catalan D, Valdez-Ojeda R, Canto-Canche B, Dominguez-Benetton X, Domínguez-Maldonado J, et al. Characterization of anode and anolyte community growth and the impact of impedance in a microbial fuel cell. *BMC Biotechnol*. 2014 Dec; 14(1):102. Available from: <http://bmcbiotechnol.biomedcentral.com/articles/10.1186/s12896-014-0102-z>
 281. Smart SK, Cassady AI, Lu GQ, Martin DJ. The biocompatibility of carbon nanotubes. *Carbon N Y*. 2006 May 1;44(6):1034–47.
 282. Cowley A, Woodward B. A healthy future: Platinum in medical applications platinum group metals enhance the quality of life of the global population. *Platin Met Rev*. 2011

- Apr;55(2):98–107.
283. Chatard C, Sabac A, Moreno-Velasquez L, Meiller A, Marinesco S. Minimally Invasive Microelectrode Biosensors Based on Platinized Carbon Fibers for in Vivo Brain Monitoring. *ACS Cent Sci*. 2018 Dec; 4(12):1751. Available from: [/pmc/articles/PMC6311694/](#)
 284. Gnanadhas DP, Thomas M Ben, Thomas R, Raichur AM, Chakravorty D. Interaction of silver nanoparticles with serum proteins affects their antimicrobial activity in vivo. *Antimicrob Agents Chemother*. 2013 Oct; 57(10):4945–55. Available from: <http://dx.doi.org/10.1128>
 285. Muller M, Merrett ND. Pyocyanin production by *Pseudomonas aeruginosa* confers resistance to ionic silver. *Antimicrob Agents Chemother*. 2014 Sep 1;58(9):5492–9.
 286. Wijesinghe G, Dilhari A, Gayani B, Kottegoda N, Samaranyake L, Weerasekera M. Influence of Laboratory Culture Media on in vitro Growth, Adhesion, and Biofilm Formation of *Pseudomonas aeruginosa* and *Staphylococcus aureus*. *Med Princ Pract*. 2019 Apr; 28(1):28–35. Available from: <https://www.karger.com/Article/FullText/494757>
 287. Ratajczak K, Stobiecka M. High-performance modified cellulose paper-based biosensors for medical diagnostics and early cancer screening: A concise review. Vol. 229, *Carbohydrate Polymers*. Elsevier Ltd; 2020. p. 115463.
 288. Obaje EA, Cummins G, Schulze H, Mahmood S, Desmulliez MPY, Bachmann TT. Carbon screen-printed electrodes on ceramic substrates for label-free molecular detection of antibiotic resistance. *J Interdiscip Nanomedicine*. 2016 Sep; 1(3):93–109. Available from: <http://doi.wiley.com/10.1002/jin2.16>
 289. Joshi AS, Singh P, Mijakovic I. Interactions of gold and silver nanoparticles with bacterial biofilms: Molecular interactions behind inhibition and resistance. *Int J Mol Sci*. 2020 Oct; 21(20):1–24. Available from: [/pmc/articles/PMC7589962/](#)
 290. Niño-Martínez N, Orozco MFS, Martínez-Castañón G-A, Mendez FT, Ruiz F. Molecular mechanisms of bacterial resistance to metal and metal oxide nanoparticles. Vol. 20, *International Journal of Molecular Sciences*. MDPI AG; 2019. Available from: [/pmc/articles/PMC6600416/](#)
 291. Ellis DH, Maurer-Gardner EI, Sulentic CEW, Hussain SM. Silver nanoparticle antibacterial efficacy and resistance development in key bacterial species. *Biomed Phys Eng Express*. 2019 Jan; 5(1):015013. Available from: <https://doi.org/10.1088/2057-1976/aad5a7>
 292. Doyle AD. Generation of 3D collagen gels with controlled diverse architectures. *Curr*

- Protoc Cell Biol. 2016; 2016:10.20.1-10.20.16. Available from: /pmc/articles/PMC5030718/
293. Taniguchi T, Tsuha S, Shiiki S, Narita M. Gram-stain-based antimicrobial selection reduces cost and overuse compared with Japanese guidelines. *BMC Infect Dis.* 2015 Oct; 15(1). Available from: /pmc/articles/PMC4623896/
294. Breijyeh Z, Jubeh B, Karaman R. Resistance of gram-negative bacteria to current antibacterial agents and approaches to resolve it. Vol. 25, *Molecules.* MDPI AG; 2020. Available from: /pmc/articles/PMC7144564/
295. Angulo A, van der Linde P, Gardeniers H, Modestino M, Fernández Rivas D. Influence of Bubbles on the Energy Conversion Efficiency of Electrochemical Reactors. Vol. 4, *Joule.* Cell Press; 2020. p. 555–79.
296. Pollitt EJG, Diggle SP. Defining motility in the Staphylococci. Vol. 74, *Cellular and Molecular Life Sciences.* Birkhauser Verlag AG; 2017. p. 2943–58. Available from: /pmc/articles/PMC5501909/
297. Han L, Ju H, Xu Y. Ethanol electro-oxidation: Cyclic voltammetry, electrochemical impedance spectroscopy and galvanostatic oscillation. *Int J Hydrogen Energy.* 2012 Oct 1;37(20):15156–63.
298. Gjødsbøl K, Christensen JJ, Karlsmark T, Jørgensen B, Klein BM, Krogfelt KA. Multiple bacterial species reside in chronic wounds: a longitudinal study. *Int Wound J.* 2006 Sep; 3(3):225–31. Available from: <http://doi.wiley.com/10.1111/j.1742-481X.2006.00159.x>
299. Dalton T, Dowd SE, Wolcott RD, Sun Y, Watters C, Griswold JA, et al. An in vivo polymicrobial biofilm wound infection model to study interspecies interactions. *PLoS One.* 2011 Nov; 6(11):27317. Available from: /pmc/articles/PMC3208625/
300. Trizna EY, Yarullina MN, Baidamshina DR, Mironova A V., Akhatova FS, Rozhina E V., et al. Bidirectional alterations in antibiotics susceptibility in *Staphylococcus aureus*—*Pseudomonas aeruginosa* dual-species biofilm. *Sci Rep.* 2020 Dec; 10(1):14849. Available from: <https://www.nature.com/articles/s41598-020-71834-w>
301. Millette G, Langlois JP, Brouillette E, Frost EH, Cantin AM, Malouin F. Despite Antagonism in vitro, *Pseudomonas aeruginosa* Enhances *Staphylococcus aureus* Colonization in a Murine Lung Infection Model. *Front Microbiol.* 2019 Dec;10. Available from: /pmc/articles/PMC6923662/
302. DeLeon S, Clinton A, Fowler H, Everett J, Horswill AR, Rumbaugh KP. Synergistic interactions of *Pseudomonas aeruginosa* and *Staphylococcus aureus* in an In vitro wound model. *Infect Immun.* 2014; 82(11):4718–28. Available from:

<https://pubmed.ncbi.nlm.nih.gov/25156721/>

303. Proctor RA, von Eiff C, Kahl BC, Becker K, McNamara P, Herrmann M, et al. Small colony variants: A pathogenic form of bacteria that facilitates persistent and recurrent infections. Vol. 4, Nature Reviews Microbiology. Nat Rev Microbiol; 2006. p. 295–305. Available from: <https://pubmed.ncbi.nlm.nih.gov/16541137/>
304. An SJ, Li J, Daniel C, Meyer HM, Trask SE, Polzin BJ, et al. Electrolyte Volume Effects on Electrochemical Performance and Solid Electrolyte Interphase in Si-Graphite/NMC Lithium-Ion Pouch Cells. ACS Appl Mater Interfaces. 2017 Jun; 9(22):18799–808. Available from: www.acsami.org
305. Said J, Dodoo CC, Walker M, Parsons D, Stapleton P, Beezer AE, et al. An in vitro test of the efficacy of silver-containing wound dressings against *Staphylococcus aureus* and *Pseudomonas aeruginosa* in simulated wound fluid. Int J Pharm. 2014 Feb; 462(1–2):123–8.
306. Atolia E, Cesar S, Arjes HA, Rajendram M, Shi H, Knapp BD, et al. Environmental and physiological factors affecting high-throughput measurements of bacterial growth. MBio. 2020 Sep; 11(5):1–19. Available from: <http://mbio.asm.org/>
307. Hay EA, Parthasarathy R. Performance of convolutional neural networks for identification of bacteria in 3D microscopy datasets. PLoS Comput Biol. 2018 Dec;14(12). Available from: [/pmc/articles/PMC6292638/](https://doi.org/10.1371/journal.pcbi.1006638)
308. Ho CS, Jean N, Hogan CA, Blackmon L, Jeffrey SS, Holodniy M, et al. Rapid identification of pathogenic bacteria using Raman spectroscopy and deep learning. Nat Commun. 2019 Dec; 10(1):1–8. Available from: <https://doi.org/10.1038/s41467-019-12898-9>
309. Wang H, Ceylan Koydemir H, Qiu Y, Bai B, Zhang Y, Jin Y, et al. Early detection and classification of live bacteria using time-lapse coherent imaging and deep learning. Light Sci Appl. 2020 Dec; 9(1):2047–7538. Available from: www.nature.com/lsa
310. Abu-Ali H, Nabok A, Smith TJ. Electrochemical inhibition bacterial sensor array for detection of water pollutants: artificial neural network (ANN) approach. Anal Bioanal Chem. 2019 Nov; 411(29):7659–68. Available from: <https://doi.org/10.1007/s00216-019-01853-8>
311. Department of health & Social Care. A guide to good practice for digital and data-driven health technologies - GOV.UK [Internet]. 2021 [cited 2021 Apr 29]. Available from: <https://www.gov.uk/government/publications/code-of-conduct-for-data-driven-health-and-care-technology/initial-code-of-conduct-for-data-driven-health-and-care-technology>

312. Montavon G, Samek W, Müller KR. Methods for interpreting and understanding deep neural networks. Vol. 73, *Digital Signal Processing: A Review Journal*. Elsevier Inc.; 2018. p. 1–15.
313. Interpret & explain ML models in Python (preview) - Azure Machine Learning | Microsoft Docs [Internet]. [cited 2021 May 4]. Available from: <https://docs.microsoft.com/en-us/azure/machine-learning/how-to-machine-learning-interpretability-aml>
314. Becker U. Increasing Safety of Neural Networks in Medical Devices. In Springer, Cham; 2019. p. 127–36. Available from: http://link.springer.com/10.1007/978-3-030-26250-1_10
315. Nsoesie EO. Evaluating Artificial Intelligence Applications in Clinical Settings. *JAMA Netw Open*. 2018 Sep; 1(5):e182658. Available from: <http://jamanetworkopen.jamanetwork.com/article.aspx?doi=10.1001/jamanetworkopen.2018.2658>
316. Muehlematter UJ, Daniore P, Vokinger KN. Approval of artificial intelligence and machine learning-based medical devices in the USA and Europe (2015–20): a comparative analysis. Vol. 3, *The Lancet Digital Health*. Elsevier Ltd; 2021. p. e195–203. Available from: www.thelancet.com/digital-health

9. APPENDIX

9.1 Appendix A

Summary of circuit modelling element values.

Sensor	Medium	Condition	Time	Rct	Wo-R	
Carbon	LB	DSM4479	0 Hrs	7.6E+07	N/A	
			24 Hrs	6.3E+06	N/A	
		Neg Ctrl	0 Hrs	2.7E+07	N/A	
			24 Hrs	1.4E+07	N/A	
	Saline	DSM4479	0 Hrs	7.4E+07	N/A	
			24 Hrs	8.0E+07	N/A	
		Neg Ctrl	0 Hrs	6.3E+07	N/A	
			24 Hrs	6.2E+07	N/A	
	PCE	LB	NCTC8325	0 Hrs	5.7E+07	N/A
				24 Hrs	1.8E+07	N/A
			Neg Ctrl	0 Hrs	9.1E+07	N/A
				24 Hrs	6.8E+07	N/A
Saline		NCTC8325	0 Hrs	5.8E+13	N/A	
			24 Hrs	3.3E+13	N/A	
		Neg Ctrl	0 Hrs	4.3E+13	N/A	
			24 Hrs	4.5E+13	N/A	
PCE		LB	NCTC8325	0 Hrs	1.96E+03	1.81E+04
				24 Hrs	7.41E+02	6.15E+03
			Neg Ctrl	0 Hrs	1.79E+03	1.84E+04
				24 Hrs	1.39E+03	1.46E+04
	Saline	NCTC8325	0 Hrs	3.99E+02	7.68E+03	
			24 Hrs	5.60E+02	7.97E+03	
		Neg Ctrl	0 Hrs	5.29E+02	1.08E+04	
			24 Hrs	4.18E+02	7.24E+03	
	PCE	LB	PA14	0 Hrs	1.46E+03	1.53E+04
				24 Hrs	4.52E+02	4.90E+03
			Neg Ctrl	0 Hrs	1.58E+03	1.52E+04
				24 Hrs	1.52E+03	1.51E+04
Saline		PA14	0 Hrs	3.66E+02	6.96E+03	
			24 Hrs	5.59E+02	6.50E+03	
		Neg Ctrl	0 Hrs	5.29E+02	1.08E+04	
			24 Hrs	4.18E+02	7.24E+03	